



The University of  
**Nottingham**

**Pulsed Laser Ablation (PLA) of  
ultra-hard structures:  
generation of damage-tolerant  
freeform surfaces for advanced  
machining applications**

by Manuela Pacella

Thesis submitted to the University of Nottingham  
for the Degree of Doctor of Philosophy

September 2014

## **Abstract**

The current methods for manufacturing super-abrasive elements result in a stochastic geometry of abrasives with random three-dimensional abrasive spatial locations. This thesis covers the laser generation of novel micro-cutting arrays in ultra-hard super-abrasive composites (e.g. polycrystalline diamond, PCD and polycrystalline cubic boron nitride, PCBN). Pulsed laser ablation (PLA) has been used to manufacture repeatable patterns of micro cutting/abrasive edges onto micro structurally different PCD/PCBN composites. The analysis on the influence of microstructural factors of the composite materials in the use of laser ablation technology has been carried out via a novel technique (Focused Ion Beam/High Resolution Transmission Electron Microscopy/Electron Energy Loss Spectroscopy) to identify the allotropic changes occurring in the composite as a consequence of PLA allowing the laser ablated PCD/PCBN surfaces to be characterized and the nanometric changes evaluated. The wear/failure characteristics/progression of the ultra-hard laser generated micro cutting/abrasive arrays has been studied in wear tests of Silicon Dioxide workpiece shafts and the influence of the microstructural factors in the wear properties of the super-abrasive micro cutting edges has been found. Opposing to these highly-engineered micro cutting/abrasive arrays, conventional electroplated abrasive pads containing diamond and CBN abrasives respectively have been chosen as benchmarks and tested under the same conditions. Contact profiling, Optical Microscopy and Environmental Scanning Electron Microscopy have been employed for the characterization of the abrasive arrays/electroplated tools before/during/after the wear/cutting tests. In the PCD abrasive micro-arrays, the type of grain and binder percentage proved to affect the wear performances due to the different extents of compressive stresses occurring at the grain boundaries. In this respect, the micro-arrays made of PCD with mixed diamond grains have shown slower wear progression when compared to the electroplated diamond pads confirming the combination of the high wear resistance typical of the fine

grain and the good shock resistance typical of the coarse grain structures. While PCD laser manufactured arrays indicated edge break as typical wear mechanism, the abrasive pad confirmed flattening of grits as main wear mechanism. Mixed grained PCD arrays performed 25% better than fine grained arrays. The improved wear performances of laser manufactured arrays when compared to industrial benchmark is proved by the different wear failure mechanism in the array and in the electroplated pad: in the first one the edges break creating new sharp edges during testing, while in the latter grit flattening is the main wear mechanism. This increases up to 60% the life of the laser manufactured array when compared to the benchmarked pads. As for the PCBN abrasive micro-arrays, two are the main wear mechanisms experienced by the arrays: edge flattening for the high CBN content array and edge breaking for the medium CBN content array. The wear performance of the high content PCBN array is directly comparable to the electroplated boron nitride pad, because they both worn out with edge/grit flattening. The increase of metallic binder and the presence of metalloids in the medium content-CBN specimens have shown to produce higher contact pressure with the workpiece when compared to the electroplated specimen, causing fracturing as the main wear mechanism; while the PCBN micro-array with purely a metallic binder phase has shown better wear performances and lower contact pressure in comparison to the electroplated CBN specimen. In particular, the laser manufactured array proved to perform 50% better than the electroplated ones in terms of wear resistance. Among all of the tested arrays, the mixed grained PCD and the purely metallic binder phase PCBN micro-arrays have shown slower wear when benchmarked to the electroplated pads, giving a possible application of their use in the cutting tool industry.

## **Publications**

M. Pacella, P. W. Butler-Smith, D. A. Axinte, and M. W. Fay, "FIB/TEM/EELS micro/nanometric investigations of the effects of laser ablation on the diamond/binder structure in polycrystalline diamond composites," *J. Mater. Process. Technol.*, vol. 214, no. 5, pp. 1153–1161, 2014.

M. Pacella, D. A. Axinte, P. W. Butler-Smith, and M. Daine, "On the Topographical/Chemical Analysis of Polycrystalline Diamond Pulsed Laser Ablated Surfaces," *Procedia CIRP*, vol. 13, pp. 387–392, 2014.

M. Pacella, D. A. Axinte, P. Shipway, P. W. Butler-Smith, M. Daine, C. Wort, "An assessment of the wear characteristics of micro-cutting arrays produced from polycrystalline diamond and cubic boron nitride composites," *Journal of Manufacturing Science and Engineering, Transactions of the ASME*, under review.

## **Related publication**

P. W. Butler-Smith, D. A. Axinte, M. Pacella, and M. W. Fay, "Micro / nanometric investigations of the effects of laser ablation in the generation of micro-tools from solid CVD diamond structures," *Journal of Materials Processing Technology* vol. 213, pp. 194–200, 2013.

## **Acknowledgment**

The author would like to thank Professor Dragos Axinte for all of his support and guidance throughout this research programme, and Element Six for the financial support that enabled this programme to be carried out. In particular, thanks also to: Dr. Paul Butler-Smith for his valuable expertise in diamond materials, Mr Mark Daine for his technical assistance in the use of laser and grinding equipment, Dr. Mike Fay for his expertise in the use of Transmission Electron Microscopy, Mr. Martin Roe for his valuable advices and training in Environmental Scanning Electron Microscopy and my colleagues in the Machining and Condition Monitoring research group at the University of Nottingham for their encouragement over the last three years.

A special and unique thanks to my family, that supported me with love and care although in distance, and to all of my special friends in Nottingham. Thanks to all of you!

<b>Content</b>	<b>Page</b>
<b>Abstract</b>	<b>i</b>
<b>Publications</b>	<b>iii</b>
<b>Acknowledgment</b>	<b>iv</b>
<b>Table of content</b>	<b>v</b>
<b>List of figures</b>	<b>x</b>
<b>List of tables</b>	<b>xxi</b>
<b>Acronyms</b>	<b>xxiii</b>
<b>Nomenclature</b>	<b>xxiv</b>
<b>Chapter 1 Introduction</b>	<b>1</b>
1.1 Research background	1
1.2 Problem definition	4
1.3 Objectives of this study	6
1.4 Outline of this thesis	7
<b>Chapter 2 Literature review</b>	<b>11</b>
2.1 Introduction to ultra-hard materials	12
2.1.1 Synthesis of PCD/PCBN composites	12
2.1.2 Properties of PCD/PCBN composites and benefits for industries	17
2.2 Cutting/abrasive tools made of ultra-hard composites	20
2.2.1 Geometry of the cutting edge in PCD/PCBN composites	20
2.2.1.1 Single-point tools	22
2.2.1.2 Multiple-point tools and ultra-hard electroplated tools	23
2.2.2 Micro-texturing of PCD/PCBN composites	24
2.2.3 Techniques for the manufacture of cutting tools in ultra-hard materials	25
2.2.3.1 EDM	26
2.2.3.2 PLA for generation of tools in ultra-hard materials	27

2.2.3.3 Effects of PLA technique upon PCD/PCBN composites	29
2.3 State of the art: experimental approach in the evaluation of thermal response of ultra-hard materials to PLA	31
2.4 Evaluation of wear progression mechanism of abrasive tools in PCD/PCBN	35
2.5 Gaps in the current PLA technology for PCD/PCBN in academic research and industry	39
<b>Chapter 3 Materials and methodology</b>	<b>42</b>
3.1 Methodology background	42
3.2 Selection of the ultra-hard materials for the generation of the arrays	43
3.3 Selection of workpiece material for the wear progression tests	45
3.4 Pulsed laser ablation of PCD/PCBN structures	47
3.4.1 DOE	48
3.4.2 Laser energy parameters	51
3.4.3 Laser kinematic parameters	53
3.4.4 Identification of extent of ablation in the elemental composition of different composites	54
3.5 Procedure for the evaluation of the thermal response of PCD/PCBN structures to PLA	56
3.5.1 Preliminary procedure for the evaluation of the thermally affected site	57
3.5.2 Approach for the analysis of the thermal response of microstructurally different PCD/PCBN composites	59
3.6 Generation of orderly micro-abrasive arrays in PCD/PCBN structures	63
3.6.1 Influence of the laser path parameters in the design of abrasive geometries	64
3.6.2 Design for the generation of the micro-cutting arrays	67

3.7 Evaluation of wear-resistant properties of micro structurally different PCD/PCBN arrays	71
3.7.1 Selection of the benchmark specimens	71
3.7.2 Setup of the test to evaluate the wear properties of the PCD/PCBN laser generated micro-abrasive arrays	72
3.7.3 Approach for the comparison of the electroplated cutting forces versus the PCD/PCBN micro-cutting arrays	75
3.8 Conclusion and remarks	77
<b>Chapter 4 Optimisation of process parameter for PLA of PCD/PCBN composites</b>	<b>80</b>
4.1 Characterisation of selected materials before PLA	80
4.2 Design of experiment (DOE)	85
4.2.1 Preliminary investigation of process parameters: results of Design of Experiments	86
4.2.2 Observation and discussion	88
4.3 Variation of laser energetic parameters to enable PLA on PCD/PCBN structures	89
4.3.1 Experimental results	89
4.3.2 Observation and discussion	91
4.4 Variation of laser kinematic parameters	92
4.5 EDX chemical environmental analysis	95
4.5.1 Experimental results	95
4.5.2 Observation and discussion	98
4.6 Conclusions and remarks	99
<b>Chapter 5 Thermal response of PCD/PCBN composites to PLA</b>	<b>102</b>
5.1 Thermal response of PCD structures to PLA	102
5.1.1 Results of FIB/HRTEM/EELS analyses of the high fluence ablated site	102
5.1.2 Results of FIB/HRTEM/EELS analyses of the low fluence ablated site	108

5.1.3 Observation and discussion	109
5.2 Thermal response of PCBN structures to PLA	111
5.2.1 Results of FIB/HRTEM/EELS analyses of the high fluence ablated site	112
5.2.2 Results of FIB/HRTEM/EELS analyses of the low fluence ablated site	118
5.2.3 Observation and discussion	121
5.3 Conclusions and remarks	122
<b>Chapter 6 Generation of orderly micro-abrasive arrays in PCD/PCBN structures</b>	<b>125</b>
6.1 Influence of the laser path parameters in the design of abrasive geometries	125
6.1.1 Results of the study of laser path parameters variation	126
6.1.2 Observation and discussion	129
6.2 Design for the generation of the micro-abrasive/cutting arrays	131
6.2.1 Laser generated micro-abrasive arrays in PCD/PCBN	131
6.2.3 Observation and discussions	138
6.3 Conclusions and remarks	139
<b>Chapter 7 Evaluation of wear-resistant properties of microstructurally different PCD/PCBN arrays</b>	<b>141</b>
7.1 Characterisation of the benchmark electroplated pads	141
7.1.1 Selection of the benchmark electroplated pads before the test	142
7.1.2 Observation and discussion	144
7.2 Evaluation of the wear characteristics of the PCD/PCBN laser generated micro-abrasive arrays and electroplated diamond/CBN pads	145
7.2.1 Wear/cutting test of PCD arrays versus electroplated diamond pads	146

7.2.2 Wear/cutting performances of PCBN arrays versus electroplated CBN pads	149
7.2.3 Observation and discussion	153
7.3 Comparison of the abrasive/cutting forces in the electroplated pads and PCD/PCBN micro-cutting arrays	156
7.3.1 Acquired signal/cutting forces for PCD arrays and electroplated diamond pads	156
7.3.2 Acquired signal/cutting forces for PCBN arrays and electroplated CBN pads	162
7.3.3 Observation and discussion	163
7.4 Conclusion and remarks	165
<b>Chapter 8 Research outcomes and future work</b>	<b>169</b>
8.1 Summary of research, findings and conclusions	169
8.2 Future work on the laser generated micro-cutting edges in PCD/PCBN composites	173
<b>References</b>	<b>177</b>

## Figures

Figure 1. 1: Trends of ultra-hard materials application per sector .....	1
Figure 1. 2: Cutting tools and market trends.....	3
Figure 1. 3: Flow chart representing the outline of the thesis and each chapter.....	10
Figure 2. 1: Flow-chart of the main topic of literature review associated with the research and main references for each ones. ....	11
Figure 2. 2: Example of the FCC structure for cBN and diamond [8]. ....	12
Figure 2. 3: Representation of the electronic sp <sup>2</sup> structure in graphite and hBN [12].....	13
Figure 2. 4: Phase diagram of BN and carbon [15], [16]. ....	14
Figure 2. 5: HPHT in capsule process [17].....	15
Figure 2. 6: Schematic of the synthesis process for PCD composites [18].	15
Figure 2. 7: Schematic of the collocation of ultra-hard materials for cutting tool application [48].....	19
Figure 2. 8: Schematic drawing of a cutting tool in: a) single-point and b) multiple-point [53]. ....	21
Figure 2. 9: Schematic of the rake, clearance and edge angles [53].....	21
Figure 2. 10: Image of the electroplated cutting tool [6]. ....	23
Figure 2. 11: Detail of the grit used in the electroplated tool [66].....	24
Figure 2. 12: Orderly CVD single crystal diamond micro-arrays for machining [5].....	25
Figure 2. 13: Drawing of the cutting edge geometry proposed for single crystal diamond from Butler-Smith et al. [5].....	25
Figure 2. 14: SEM micrographs of pulsed laser ablated CVD diamond surfaces [75].....	27
Figure 2. 15: Geometries manufactured in WC/Co via PLA [77]. ....	28
Figure 2. 16: Geometries manufactured in single crystal CVD diamond via PLA [4].....	28
Figure 2. 17: SEM micrograph showing a pulsed laser ablated insert in CBN [60]. ....	29
Figure 2. 18: Typical phase transition during PLA [81]. ....	29

Figure 2. 19: HRTEM image of the interface between graphite and diamond in single crystal diamond as a consequence of PLA [93].	32
Figure 2. 20: HRTEM image of the interface between graphite and diamond in a single crystal CVD diamond as a consequence of PLA [92].	33
Figure 2. 21: Schematic of the preparation of the sample for HRTEM analysis [92].	34
Figure 2. 22: Influence of the grain size on the edge roughness and on the wear rate [98].	35
Figure 2. 23: Set up of the wear test of superabrasive material on a vitrified bonded alumina grinding wheel workpiece [101].	36
Figure 2. 24: Schematic model of the chip formation process during the interaction of a single grain diamond and a stone workpiece [105].	37
Figure 2. 25: Performances of low-CBN PCBN grades in interrupted turning machining of steel [40].	38
Figure 3. 1: Chart diagram showing the methodology used in this research work.	43
Figure 3. 2: Flow chart of the ultra-hard materials selected for the experiments.	44
Figure 3. 3: A schematic explaining the novel procedure of optimisation of laser parameters.	48
Figure 3. 4: Flowchart indicating details of design of experiment an reference to the tables with valued for each DOE.	48
Figure 3. 5: Schematic representation of the procedure used to produce laser ablated grooves starting from single craters, showing the distance between single spots at different feed speeds: $v=500\text{mms}^{-1}$ ( $h=50\ \mu\text{m}$ ), $v=400\text{mms}^{-1}$ ( $h=40\ \mu\text{m}$ ), $v=300\text{mms}^{-1}$ ( $h=30\ \mu\text{m}$ ), $v=200\text{mms}^{-1}$ ( $h=20\ \mu\text{m}$ ), $v=100\text{mms}^{-1}$ ( $h=10\ \mu\text{m}$ )	54
Figure 3. 6: Schematic representation on a Gaussian of the spot diameter versus the power density; numbers 1 to 5 indicate the areas of EDX analysis corresponding to different radial positions di.	55
Figure 3. 7: A schematic of the direction selected for chemical analysis onto different composites.	56

Figure 3. 8: Backscatter ESEM imaging of a polished surface of the selected ultra-hard materials for evaluation of thermal response to PLA: a) PCD CMX850 fine grain diamond with Cobalt as a binder; b) PCBN DCC500 fine grain PCBN showing the CBN grain in the black areas and the ceramic binder in the grey areas.....	58
Figure 3. 9: ESEM backscatter images of the laser ablated continuous groove in the fine grain PCBN specimen: a) top view of the ablated groove showing the high/low fluence areas; b) cross section view showing the corresponding high/low regions in the ablated material. ....	59
Figure 3. 10: A schematic of the surface coating application on a continuous groove ablated composite.....	61
Figure 3. 11: ESEM images of the FIB procedure for lamellas preparation and extraction: a) multiple coating b) milling.....	62
Figure 3. 12: ESEM images of the FIB procedure for lamellas preparation and extraction: a) Tungsten strapping technique in top view b) lift-out of a lamella. ....	62
Figure 3. 13: SEM images of the FIB procedure for lamellas preparation and extraction: a) lamella mounting onto a support grid; b) FIB rastering of the sites of interest corresponding to the sectional locations of the ablated groove.....	63
Figure 3. 14: Flowchart of the process for the manufacture of the orderly micro-abrasive cutting arrays via PLA.....	64
Figure 3. 15: CAD design of the overall abrasive array and insert of desired geometry in term of rake and clearance faces. ....	65
Figure 3. 16: Schematic of the different type of direction of ablation of the laser beam.....	67
Figure 3. 17: Schematic showing the positioning of the ultra-hard specimen to the laser beam.....	68
Figure 3. 18: Example of the dimensions of the ablated abrasives in the CAD design.....	69
Figure 3. 19: Schematic of a CAD design for the variation of the orientation of the specimen to be ablated.....	69

Figure 3. 20: Schematic of the ensembles of the CAD drawings unifying design 1 to 4 .....	70
Figure 3. 21: Geometry of the single abrasive element and identification of the nominal diameter for the selection of the grit.....	71
Figure 3. 22: Schematic of the monitoring equipment for the test set-up and the acquisition of the forces. ....	72
Figure 3. 23: Test set-up: a) positioning of the array in the fixturing system, b) connection of the transducer/fixturing system/array into the grinding machine.....	73
Figure 3. 24: CAD schematic of: a) 3D contact between abrasive array and Silicon dioxide shaft; b) cross section of the contact.....	74
Figure 3. 25: Schematic of the geometry for the theoretical calculation of the area of contact for depths of cut of 1 and 5 $\mu\text{m}$ in the single cutting element.....	75
Figure 3. 26: Schematic of the geometry for the theoretical calculation of the area of contact for depths of cut of 1 and 5 $\mu\text{m}$ in the single grit (assumed spherical).....	76
Figure 4. 1: Backscatter ESEM imaging of PCD polished surfaces before PLA showing the diamond grains in the black areas and Co in the grey areas : a) CMX850 fine grained specimen, b) CTH025 coarse grained specimen; c) CTM302 mix grained specimen.....	81
Figure 4. 2: Backscatter ESEM imaging of PCBN polished surfaces before PLA showing CBN grain in the black areas and binders in the grey areas: a) DCC500 fine grained purely ceramic binder specimen , b) DBW85 metalloid binder specimen; c) DBS900 purely metallic binder specimen. ....	82
Figure 4. 3: Atomic force microscope (AFM) tapping mode imaging of the coarse PCD specimen CTH025: a) large specimen area, b) detail of the large area.....	83
Figure 4. 4: XRD results for the characterisation of CTM302 mixed grained PCD specimen. ....	84
Figure 4. 5: XRD results for the characterisation of DCC500 PCBN specimen.....	85

Figure 4. 6: Optical microscopy imaging of the results from full factorial design described in the methodology in Table 3.3.....	87
Figure 4. 7: Optical microscopy imaging of the results from Full factorial design described in the methodology in Table 3.4.....	87
Figure 4. 8: Optical microscopy imaging of the results from Taguchi design described in the methodology in Table 3.5. ....	88
Figure 4. 9: TALYSURF results for variation on energetic parameters (Table 3.7) in the case of fine grained CMX850 specimen for different laser average power. ....	90
Figure 4. 10: ESEM images showing the effect of variation of laser average power (Table 3.7) onto the coarse grained CTH025 specimen.....	90
Figure 4. 11: ESEM images showing the effect of variation of laser average power (Table 3.7) onto the fine grained CMX850 specimen.....	91
Figure 4. 12: ESEM micrographs of the optimised laser ablated craters in: a) PCD CMX850; b) PCBN DCC500.....	92
Figure 4. 13: ESEM micrograph in PCD CMX850 representative of: a) single ablated craters ( $v=500\text{mms}^{-1}$ ), b) continuous groove ( $v=100\text{mms}^{-1}$ ).....	93
Figure 4. 14: ESEM cross section images on the variation of kinematic parameters: a) $v=500\text{mms}^{-1}$ ; b) $v=100\text{mms}^{-1}$ . ....	93
Figure 4. 15: Talysurf results showing the overlapping between consecutive spots for $v=300\text{mms}^{-1}$ (the values used to achieve this roughness are reported in Table 3.9).....	94
Figure 4. 16: Profilometry of the overlapping between consecutive spots for $v=100\text{mms}^{-1}$ (the values used to achieve this roughness are reported in Table 3.9).....	94
Figure 4. 17: ESEM micrographs of the cross section of the CTH025 specimen showing the areas of analysis of EDX detector for the two different tests: a) optimised single spot achieved with test in Table 3.7; b) optimised continuous groove achieved from test in Table 3.9.....	95
Figure 4. 18: ESEM top view micrograph showing an example of the EDX areas of analysis for CTH025: a) single spot crater; b) continuous groove (Tables 3.7-3.9).....	95

Figure 4. 19: Comparative graph for laser ablated single spots in fine and coarse grained PCD specimens .....	98
Figure 4. 20: Comparative graph for laser ablated continuous grooves in fine and coarse grained PCD specimens.....	99
Figure 5. 1: TEM image of the thin lamella (as presented in Figure 3.13 in Section 3.5.2) in PCD CMX850 from area of high laser fluence region showing the protective coating and underlying PCD substructure and EELS scan length and direction.....	103
Figure 5. 2: EELS low resolution scan results across the green scan length shown in Figure 5. 1. ....	103
Figure 5. 3: High resolution EELS scans of the thinned lamella region showing: a) a signature trace of diamond; b) a reference of diamond structure signature from literature.....	104
Figure 5. 4: High resolution EELS scans of the thinned lamella region showing: a) a signature trace of graphite, b) a reference of graphite structure signature from literature.....	105
Figure 5. 5: HRTEM image of the lamella of the high energy density site showing the allotropic changes into the substructure and the metallic binder pockets.....	106
Figure 5. 6: TEM back focal plane imaging of PCD CMX850 substructure: a) diamond grain intergrowth and binder structure; b) diffraction pattern of an individual diamond grain.....	107
Figure 5. 7: TEM imaging of the voids containing metallic binder: a) Energy Filtered TEM image indicating carbon presence in white areas and cobalt in dark areas; b) Cobalt sensitive Energy Filtered TEM.....	108
Figure 5. 8: HRTEM imaging of the interface graphite/PCD in the upper part of the groove (lowest energy density region). ....	109
Figure 5. 9: HRTEM imaging of the thinned lamella window.....	111
Figure 5. 10: TEM image of the thin lamella in PCBN DCC500 from area of high laser fluence region showing the protective coating and underlying PCBN substructure and EELS scan length and direction. ....	112
Figure 5. 11: TEM image of the thin lamella in PCBN DCC500 from area of high energy density showing the initial areas of analysis for HRTEM. ....	113

Figure 5. 12: HRTEM image of Area1 achieved by the combination of two separate micrographs but unified to show the interface hBN/cBN. ....	113
Figure 5. 13: HRTEM image of Area1 from Figure 5. 10 showing the substructure of DCC500 not affected from the PLA process with areas of the binder TiC and cBN. ....	114
Figure 5. 14: TEM image of the thin lamella in PCBN DCC500 from area of high laser fluence region showing high resolution EELS scan length and direction.....	115
Figure 5. 15: High resolution EELS scan results of the thinned lamella region showing: double energetic peak typical signature of hBN; b) transition between hBN and cBN; c) energetic peak at 200 e V typical of the on the right a reference of the EELS signatures from literature [11].	116
Figure 5. 16: TEM back focal plane overlapping imaging of PCBN substructure showing the diffraction pattern of BN grains in hBN and cBN. ....	117
Figure 5. 17: HRTEM image of interfaces hBN, cBN, $\alpha$ BN in the high energy density area of specimen PCBN DCC500.....	117
Figure 5. 18: TEM image of the thin lamella in PCBN DCC500 from area of low laser fluence region showing the protective coating and underlying PCBN substructure and EELS scan length and direction. ....	118
Figure 5. 19: EDX area of scan for chemical environmental analysis in the area of low fluency for PCBN specimen DCC500. ....	119
Figure 5. 20: TEM image of the voids containing Al and BN; the insert represents a Titanium Sensitive Energy Filtered TEM image indicating that all of the grey areas is Titanium.....	120
Figure 5. 21: HRTEM image of the lamella of the low energy density site showing the abrupt interface between BN and TiC. ....	120
Figure 5. 22: ESEM cross section imaging of the laser generated groove showing a schematic representation of the thermal response of PCBN DCC500 to different laser fluencies in PLA. ....	122
Figure 5. 23: Relationship between laser fluence variation and extent of allotropic presence in PCD materials.....	123

Figure 5. 24: Relationship between laser fluence variation and extent of allotropic presence in PCBN materials.....	124
Figure 6. 1: Optical microscopy image of specimen PCD CTH025 after PLA with: a) border cut, b) no border cut.....	126
Figure 6. 2: Optical microscopy image of specimen PCBN DCC500 after PLA with: a) border cut, b) no border cut.....	127
Figure 6. 3: Optical microscopy image of specimen PCBN DBW85 after PLA with: a) border cut, b) no border cut.....	127
Figure 6. 4: Optical microscopy image of specimen PCBN DBS900 after PLA with: a) border cut, b) no border cut.....	127
Figure 6. 5: Geometry of the array and detail of a single to-be-generated micro-cutting edge.....	128
Figure 6. 6: ESEM images of laser generated (Pm70W, $\tau$ 10 $\mu$ s, f30kHz, v400mms-1) PCD CTH025 specimen with same CAD file but different laser stage direction: a) random direction of ablation, b) 0 $^\circ$ direction of ablation, c) 90 $^\circ$ direction of ablation.....	129
Figure 6. 7: ESEM images of laser generated (Pm70W, $\tau$ 10 $\mu$ s, f30kHz, v400mms-1) PCD CTH025 specimen with different CAD files: a) no overlapping of features in the CAD, b) overlapping of 0.3 mm between features with negative rake angle, c) overlapping of 0.3 mm, 90 $^\circ$ ablation without border cut.....	132
Figure 6. 8: Positioning of the ultra-hard specimen to the laser beam. ....	132
Figure 6. 9: Optical microscopy image of cross section of laser generated array in PCD CTM302: a) tilting of the specimen at 10 $^\circ$ , b) tilting of the specimen at 20 $^\circ$ ; c) tilting of the specimen at 30 $^\circ$ .....	133
Figure 6. 10: Optical microscopy image of cross section of laser generated array in PCD CMX850: a) tilting of the specimen at 10 $^\circ$ , b) tilting of the specimen at 20 $^\circ$ ; c) tilting of the specimen at 30 $^\circ$ .....	134
Figure 6. 11: ESEM images examples of the optimised laser generated arrays in specimens: a) PCD CTM302; b) PCBN DBS900.....	134
Figure 6. 12: ESEM images of a single micro-abrasive edge: a) tilted view of the edge in PCD CMX850 specimen, b) 3D view of the edge in PCBN DBW85 specimen showing the sharpness of the edge.....	135

Figure 6. 13: Repeatability of the achieved rake and clearance angles as a function of the tilting angle onto PCD CTM302.....	136
Figure 6. 14: Repeatability of the achieved rake and clearance angles as a function of the tilting angle onto PCD CMX850.....	138
Figure 7. 1: ESEM image of the benchmark specimens before the test: a) electroplated D501 diamond, b) electroplated B501 CBN.....	142
Figure 7. 2: ESEM image (side view) of electroplated specimens showing the random height of the abrasive grits: a) electroplated diamond specimen; b) electroplated CBN pad.....	143
Figure 7. 3: Example of ESEM image of a single CBN grit in an electroplated abrasive pad: a) tilted and b) top views. ....	143
Figure 7. 4: ESEM micrographs showing the variation in edges/grit density per same surface area of 1 mm <sup>2</sup> : a) 12 micro-edges in the case of the array, b) 7 grits in the case of the electroplated specimen. ....	144
Figure 7. 5: ESEM of wear features for abrasive micro-arrays after 5000 passes (5 μm depth of cut): a) CMX850 fine grained diamond; b) CTM302 mixed grained diamond.....	146
Figure 7. 6: ESEM images proving the fracture of CMX850 fine grained PCD array after 3000 passes (5 μm depth of cut): a) side view, and b) front view of a micro-abrasive edge. ....	147
Figure 7. 7: ESEM images after 3000 passes (5 μm depth of cut) in CTM302 mixed grained PCD array: a) tilted view b) front view.....	147
Figure 7. 8: ESEM images of crack formation and fracture of the CTM302 micro-abrasive edge: a) after 4000 passes, b) after 5000 passes (5 μm depth of cut). ....	148
Figure 7. 9: ESEM micrographs showing chipping as wear progression mechanism on a CTM302 mix grained PCD cutting edge a) after 1000 passes, b) after 4000 passes; c) after 5000 passes.....	148
Figure 7. 10: ESEM micrographs demonstrating the reduction in height (i.e. flattening) of electroplated diamond grits: a) in “fresh” condition b) after 5000 passes (for 5 μm depth of cut). ....	149

Figure 7. 11: ESEM tilted view comparative imaging of the DBS900 in the wear test (1  $\mu\text{m}$  depth of cut): a) before test, b) after 500 passes, c) after 10 m length of cut.....150

Figure 7. 12: ESEM tilted view of the DBW85 during the wear test (1  $\mu\text{m}$  depth of cut): a) before the test, b) after 5 m length of cut, c) after 1000 passes.....150

Figure 7. 13: ESEM micrographs showing the wear progression of the electroplated CBN pad after: a) 250 passes, b) 5 m length of cut, c) 750 passes; d) 10 m length of cut. ....151

Figure 7. 14: ESEM micrographs showing the wear progression of a single grit the electroplated CBN pad: a) before the test, b) after 250 passes (length of cut, 2.5 m), c) after 500 passes (length of cut, 5 m), d) after 1000 passes (length of cut, 10 m).....152

Figure 7. 15: ESEM micrographs showing some detail of unworn/worn grits on the electroplated CBN grain: a) before the test, unworn area b) after 1000 passes (1  $\mu\text{m}$  depth of cut) worn area. ....152

Figure 7. 16: Example of a typical signal acquired in a single pass for the CMX850 fine grained array, the reduced shaft diameter is also shown for each peak; calculation of time and features in contact with the shaft are reported in the insert.....157

Figure 7. 17: Example of the signal acquired in a single pass with the corresponding time of contact of the shaft upon: a) the CMX850 fine grained array; b) the D501 electroplated diamond abrasive.....157

Figure 7. 18: ESEM images of different abrasive edges positioning in the same CMX850 array after 5000 passes: a) most worn surface corresponding to highest contact pressure with the shaft ( $t < 1.25$  s); b) trailing part of the array remained unworn corresponding to time interval of not acquired contact loads ( $t > 1.25$  s).....159

Figure 7. 19: CAD schematic of the manufactured array with dimensions, number of micro-edges in instantaneous contact with the shaft, tested area, untested area, worn and unworn areas.....159

Figure 7. 20 Example of the micro-edges in the abrasive/cutting array and their area of contact with the shaft during test: a) topographical

measurement of a single abrasive element after 250 passes; b) measured area of contact of the single abrasive element via thresholding process after 2.5 m length of cut; c) topographical measurement of a single abrasive element after 5000 passes; d) measured area of contact of a single abrasive element via thresholding process after 50 m length of cut. ....160

Figure 7. 21: Example of a single grit of an diamond electroplated pad and its area of contact with the shaft during test: a) topographical measurement of a single grit after 250 passes; b) measured area of contact of the single grit with the shaft via thresholding process after 2.5 m length of cut; c) topographical measurement of a single grit after 5000 passes; d) measured area of contact of a single grit via thresholding process after 50 m length of cut. ....161

Figure 7. 22: Comparative graph showing the calculated contact pressures, on the vertical Y axis in logarithmic scale.....162

Figure 7. 23: Comparative graph showing the calculated contact pressures for the PCBN/electroplated CBN specimens. ....163

## Tables

Table 2. 1: Atomic separation of BN allotropes, C allotropes and binders.	16
Table 2. 2: Thermal properties of single crystal phases and binders .....	18
Table 2. 3: Values of mechanical properties for different materials .....	18
Table 2. 4: Values of rake and clearance angles for cutting edges in PCD for the machining of different materials .....	22
Table 3. 1: Materials utilised in the experiments and their microstructural properties.....	45
Table 3. 2: Thermo/mechanical properties of SiO <sub>2</sub> , bulk.....	47
Table 3. 3: Example of the full factorial design with 3 factors, 4 levels, 27 runs .....	50
Table 3. 4: Example of the full factorial design with 2 factors, 3 levels and 9 runs .....	50
Table 3. 5: Example of the Taguchi design with 4 factors, 3 levels and 9 runs .....	51
Table 3. 6: Example of the Taguchi design with 3 factors, 3 levels, 9 runs.	51
Table 3. 7: Variation of P <sub>m</sub> for constant values of f, v and τ.....	52
Table 3. 8: Variation of P <sub>m</sub> for constant values of f, v and τ.....	52
Table 3. 9: Variation of beam speed in the experiment.....	53
Table 3. 10: Optimised laser parameters for the generation of micro-abrasive arrays PCD/PCBN composites. ....	66
Table 4. 1: Calculated values for energy density for full factorial experiment reported in Table 3.4 .....	89
Table 4. 2: Results for specimens PCD CMX850 in the test described in Table 3.7.....	92
Table 4. 3: Calculated values of fluence and power density for the chosen areas .....	95
Table 4. 4: EDX results for the continuous groove ablated (P <sub>m</sub> 70W, τ20μs, f10kHz, v100mms-1 ) in CTH025 composite. ....	97
Table 4. 5: EDX results for the single spot ablated (P <sub>m</sub> 70W, τ20μs, f10kHz, v500mms-1) in CTH025 composite.....	97
Table 4. 6: EDX results for the single spot ablated (P <sub>m</sub> 70W, τ20μs, f10kHz, v500mms-1) in CMX850 composite.....	97

Table 4. 7: EDX results for the groove ablated (Pm70W, $\tau$ 20 $\mu$ s, f10kHz, v100mms-1) in CMX850 composite. ....	97
Table 5. 1: Results for EDX scan of Figure 5. 19.....	119
Table 6. 1: Results of rake and clearance angles achieved for different input angle of tilting for PCD CTM302.....	136
Table 6. 2: Results of rake and clearance angles achieved for different input angle of tilting for PCD CMX850. ....	137
Table 7. 1: Measured values of contact area of the micro-edge/grits and the calculated initial and final contact pressures.....	161
Table 7. 2: measured values of contact area of the micro-edge/grits with the shafts and the calculated contact pressures for the PCBN arrays and the electroplated CBN pads. ....	162

## **Acronyms**

$\alpha$ BN: Amorphous Boron Nitride

AFM: Atomic Force Microscope

CAM: Computer-Aided Manufacturing

cBN: Cubic Boron Nitride

CVD: Chemical vapour deposited (diamond)

EDM: Electrical Discharge Machining

EDWM: Electrical Discharge Wire Machining

EDX: Energy Dispersive X-Ray spectroscopy

EELS: Election Energy Loss Spectroscopy

ESEM: Environmental Scanning Electron Microscope

FCC: Face-centered cubic structure

FEPA: Federation of European Producers of Abrasives

FIB: Focused Ion Beam

hBN: Hexagonal Boron Nitride

HPHT: High Pressure High Temperature

HRTEM: High Resolution Transmission Electron Microscope

LASER: Light Amplification by the Stimulated Emissions of Radiation

Nd: YAG: Neodymium-doped Yttrium Aluminium Garnet (laser)

PCD: Polycrystalline Diamond (composite)

PCBN: Polycrystalline Cubic Boron Nitride (composite)

Q-switched: Quality switched giant pulse formation (laser)

rBN: Rhombohedral Boron Nitride

TEM: Transmission Electron Microscope

wBN: Wurtzitic Boron Nitride

WC: Tungsten Carbide

XRD: X-Ray Diffractometer

## Nomenclature

$\alpha'$ : Thermal expansion coefficient ( $K^{-1}$ )

$A_i$ : Contact area array/workpiece after  $i$  passes ( $mm^2$ )

$\alpha$ : Clearance angle ( $^\circ$ )

$\gamma$ : Rake angle ( $^\circ$ )

$r$ : Tool radius of cut (mm)

$v$ : Laser beam traverse speed ( $mm.s^{-1}$ )

$v_f$ : Grinding feed speed ( $mm.min^{-1}$ )

$d_i$ : Radial position on the beam spot diameter (cm)

$e$ : Volumetric strain in the material ( $m^3$ )

$f$ : Laser pulse frequency (Hz)

$F$ : Laser fluence ( $J.cm^{-2}$ )

$F_a$ : Average cutting force (N)

$h$ : Distance between single spots ( $\mu m$ )

$N$ : Number of grit/edges

$P_m$ : Laser average power (W)

$P_L$ : Laser power density ( $W.cm^{-2}$ )

$\tau$ : Laser pulse duration ( $\mu s$ )

$R_a$ : Average surface roughness ( $\mu m$ )

$F_x$ : Cutting force (N)

$T_{amb}$ : Ambient temperature (K)

$T_{process}$ : Process temperature (K)

$V_0$ : Volume prior deformation ( $m^3$ )

# Chapter 1

## Introduction

### 1.1 Research background

In the last few decades, technology widely increased the use of ultra-hard materials for advanced engineering application; Figure 1. 1 depicts a graph containing some of the recent trends of ultra-hard material applications: stone processing representing the wider part of use for those materials, machining and drilling sharing the second place in the scale, and construction being another important part of application. Those are also recently used in glass and ceramic industries and for medical applications.

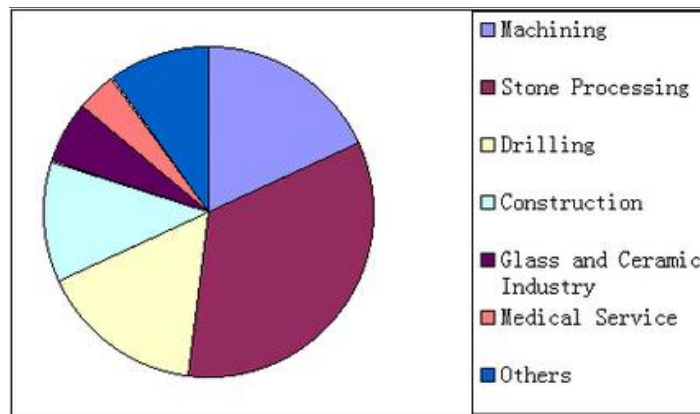


**Figure 1. 1: Trends of ultra-hard materials application per sector [1].**

Among the ultra-hard materials are diamond and cubic boron nitride. The hardest material known in nature is diamond (a carbon allotrope), though the most expensive and valuable among natural materials. Because of its high commercial value, the impossibility of employing natural diamond for industrial applications lead technology to the necessity of synthesising it in the laboratory. The first claim of the conversion of carbon to diamond is dated back to 1880, but the first published literature proving the reproducibility of the transformation of carbon into diamond is dated to 1955 [2], opening a new exciting era for synthetic-diamond industries. In

the same years researches proposed the synthesis of a new compound which could reproduce diamond properties (e.g. high hardness, good thermal and chemical stability, and good thermal conductivity) called cubic boron nitride. Cubic boron nitride (a boron nitride allotrope) is a chemical compound created in 1956 when researchers in General Electric transformed a mixture of Boron and Nitrogen in a cubic crystalline lattice by high pressure and high temperature in capsule process [3]. The similarity between boron nitride and carbon resides not only in the thermal/mechanical properties but also in the similar electronic structure and their comparable allotropic structures: the hexagonal boron nitride is similar to graphite, and the allotrope cubic boron nitride is comparable to diamond. Nowadays, because of the growing innovation on new synthesis technologies, a wide range of diamond and boron nitride is available for industrial application: mono-crystalline chemical vapour deposition diamond (CVD), polycrystalline high pressure high temperature (HPHT) diamond, polycrystalline cubic boron nitride (PCBN) with ceramic or metallic binder. Each synthesis process produces a material with specific properties, crystal structure, binder percentage, grain size; it is nowadays possible to synthesise micro structurally different ultra-hard structures with thermo/mechanical properties for cutting edges applications.

The increased use of those materials can be found in literature: chemical vapour deposition diamond (CVD) has been widely employed for advanced engineering applications (automotive, aerospace, biomedicine where there is a demand for high accurate profiling and high production rates) because of its perfectly oriented crystal structure; a wide range of potential applications have been recently proposed for polycrystalline diamond and polycrystalline cubic boron nitride especially because of the implication that the binder materials give on the mechanical and thermal properties of these composites.

Due to their exceptional mechanical and thermal properties (e.g. hardness, electrical conductivity, thermal stability) diamond and boron nitrides find suitable fields of application in precision manufacturing and cutting tool industries. For this reason, the use of ultra-hard materials for cutting tool

applications has been widened in the recent years (Figure 1.2), leading to increased scientific research on the manufacture of ultra-hard tools for cutting edge applications.

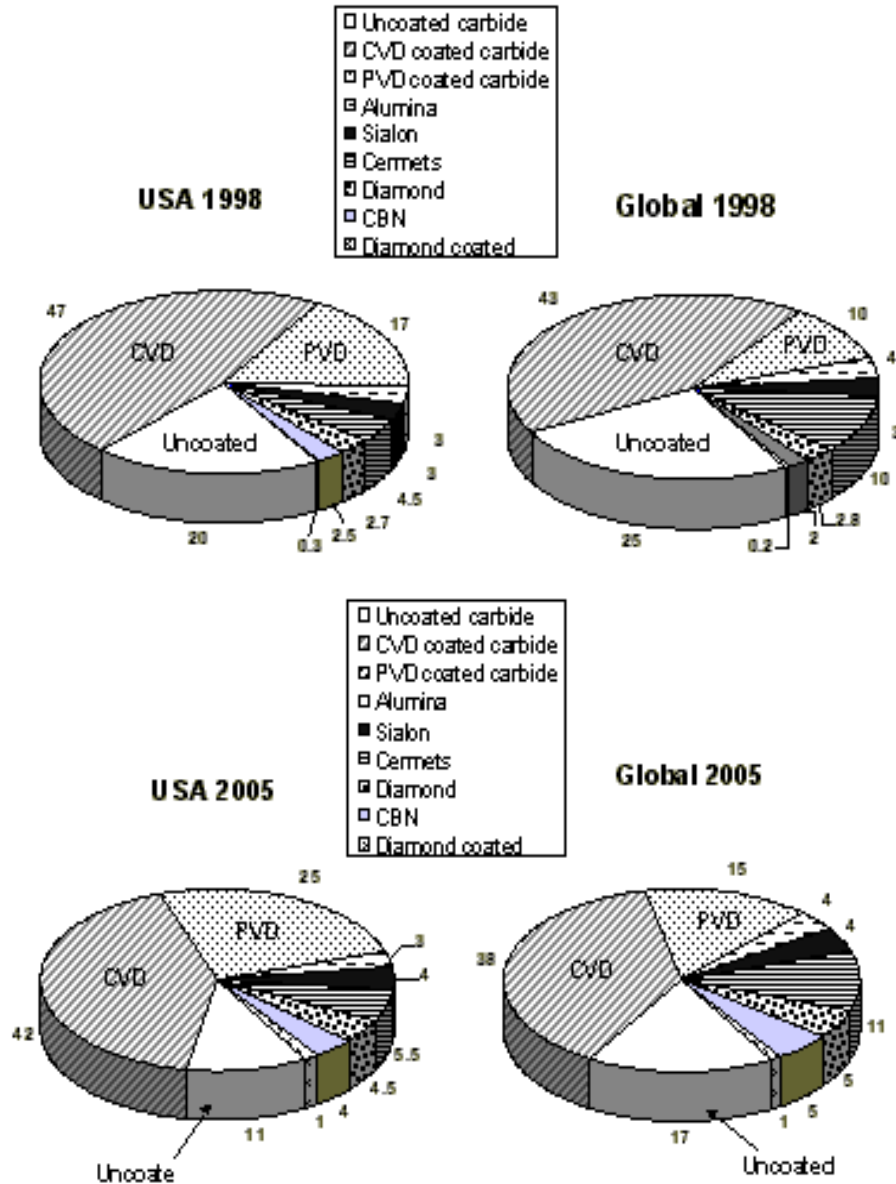


**Figure 1. 2: Cutting tools and market trends (courtesy to MAKINO).**

It is important to note that the extreme hardness of those composites make them classified among the very difficult to shape materials: most conventional materials will have a premature tool failure when used for cutting or machining diamond and boron nitride. The recent trends in manufacturing ultra-hard and super-abrasive grinding wheels/tools via conventional techniques involve mixing random diamond/CBN crystals with a bond material and then this mixture is moulded into a desired

profile. This gives the matrix a strong anisotropic behaviour, and the process giving as a result a time-dependent, stochastic geometry of abrasives, and random three-dimensional abrasive spatial location.

A recent study on single crystal diamond (CVD) has proposed an unconventional technique for shaping a solid diamond surface via material removal with a laser beam, proving that pulsed laser ablation represent a successful technique for shaping single crystal diamond [4]. In fact, the research on CVD diamond proposed laser ablation not only for shaping diamond but also to achieve staggered micro-features showing the validation of the use of laser for the manufacture of high performance micro-grinding wheels in single crystal diamond [5]. These studies open the possibility for the use of laser technology for processing of more complex ultra-hard composites, such as polycrystalline diamond and polycrystalline cubic boron nitride. Up-to date literature has shown that the most common cutting tools in diamond and cubic boron nitride result either in a single cutting point tool (with a single cutting edge in macro dimensions) or in a electroplated tool with random three-dimensional spatial located abrasives. Much research has been done on the performances of electroplated diamond tools for cutting applications [6] on ceramic materials and well known is the use of electroplated boron nitride wheel for grinding of steel [7].

## **1.2 Problem definition**

In material removal via laser ablation, depending on the thermal properties (e.g. thermal expansion coefficient, thermal conductivity) it is very difficult to predict the response of the PCD/PCBN composites to the laser parameters (e.g. energy density, feed speed, and pulse duration) especially because of the variables involved in the process and the influence of those is not evident macroscopically. Although pulsed laser ablation (PLA) has been successfully used for manufacture of single crystal diamond (CVD) tools, no research has been focused on studying the thermal response of PCD/PCBN to laser ablation for manufacture of micro abrasive/cutting arrays/tools. In particular no attention has been given to

the influence of microstructural factors (e.g. binder phase, binder bulk volume percentage, diamond/CBN grain size, binder to grain ratio) in the post ablation workpiece surface integrity; little attention has been given to the allotropic transformations occurring as a consequence of laser ablation because of the thermal excitation at the interface grain/binder. The control of allotropic transformation can possibly enhance the wear performances in ultra-hard cutting tools in specific sites of the edge.

Regarding the use of PCD/PCBN as a cutting tool, considerable research has been conducted on the manufacture of single cutting feature (macro-size, e.g. insert of the order of a few millimeters) and on the cutting performances of electroplated tools; no research has been reported on the manufacture of micro edges in PCD/PCBN materials for enhancing the wear-resistant properties in grinding/cutting machining. In particular, the thermal response of the PCD/PCBN to laser ablation has never been studied in relation to the microstructural composite characteristics (grain size, binder bulk volume percentage, binder type), thus the control of the cutting geometry (including the radius of the micro-edges) via ablation parameters control has not yet been achieved; an experimental approach to enable the control of micro-edge geometry as a function of the binder type, grain size and binder bulk volume percentage has never been proposed.

Well-known is the expected wear behaviour of PCD/PCBN materials as a function of the binder type and diamond grain size, but the influence of microstructural factors (e.g. binder phase, grain size, binder bulk volume) associated to the micro-edge geometry on the wear/cutting performances of PCD/PCBN micro-cutting arrays has never been explored. Proposing a characterisation procedure for understanding the thermal response of the composite is a crucial requirement when it is necessary to enhance the wear-resistant properties of composite materials for a wide range of applications. This could improve the use of laser ablation for manufacture PCD/PCBN and other composite materials which have complex thermal response to an energy beam due to their combination of chemicals.

### 1.3 Objectives of this study

Based on the understanding of the response of composite ultra-hard materials to laser beam, this research work aims at developing novel abrasive/cutting micro-arrays with enhanced wear performances. In particular, the main objectives of the present work are:

- i. Understand the interaction between the laser beam and composite ultra-hard materials (PCD & PCBN): study the material removal mechanisms of ultra-hard structures by PLA, inducing short ( $40\text{fs} < \text{pulse duration} < 50\mu\text{s}$ ) and localized ( $1\mu\text{m} < \text{spot size} < 50\mu\text{m}$ , depth  $< 30\mu\text{m}$ ) thermal transformations including heat flux (controlled by pulse energy), pulse frequency and beam traverse speed as factors. Understand the response surface of the critical characteristics of the beam footprint (depth, width) to enable the identification of the optimal parameters of the PLA process and allow the generation of quality controlled (e.g. roughness, surface integrity) ultra-hard surfaces.
- ii. Understand the causes and quantify the extent of the residual damage to the ultra-hard structures when using PLA. Study the repetitive mechanism of formation & removal of allotropic (graphitic carbon/hexagonal boron nitride) layers during PLA of PCD/PCBN structures. Study the influence of microstructural factors (e.g. percentage of binder phase, crystal intergrowth, texture) of the PCD/PCBN structures upon the material removal mechanism during PLA. Fundamental are the analysis of the microstructural damage and the evaluation of the extent of allotropic change (nanometric layer of graphitic carbon/hexagonal boron nitride). Set up procedures for the examination of the allotropic transformation occurring at atomic level in PCD/PCBN as a consequence of the entity of fluence in a laser pulse.
- iii. Optimise operating parameters (e.g. pulse duration/frequency, power density) and laser paths (e.g. rastering, pocketing) to allow ablation of 3D features with controlled surface quality (roughness, damage level). Identify specific micro-cutting edge arrays to enable

- high wear-resistant properties and cutting/grinding performances; understand the effect of change of laser CAM path parameters (e.g. border cut, direction of ablation, tilt angle, CAD design) onto PCD/PCBN ultra-hard structures. Design (by using CAD package) and optimise specific micro-edges to enable a high control of the edge geometry (i.e. rake and clearance faces, cutting edge radius).
- iv. Understand the wear characteristics and wear progression of abrasive/cutting micro-edges arrays to enable efficient super-abrasive tools; in particular study the different types of wear characteristics (chipping, abrasion, fracture, flattening) of PCD/PCBN structure as a function of the microstructural factors (i.e. binder type, binder bulk volume percentage, grain size) variation and the thermal reaction occurring at the interphase grain/binder.
  - v. Validate the use of ultra-hard micro-edges arrays in cutting/grinding machining applications. In particular, identify the type of failure for diamond and cubic boron nitride electroplated materials and analyse the wear performances of those against the manufactured arrays.

## **1.4 Outline of this thesis**

The structure of this research is described in this paragraph, where each chapter and its content are briefly outlined and the correlation between each chapter analysed. The plan of this thesis is as follows:

- i. The current chapter, *Chapter 1* serves as a general introduction to the background of study; in particular this aims at briefly understanding the research which was already done in the field of study, and evaluating the research gaps which would be beneficial to exploit in order to achieve the aims and objectives of this research.
- ii. *Chapter 2* covers a detailed literature review related to the field of study by including the unconventional techniques to manufacture ultra-hard materials, microscopically different type of ultra-hard

structures and their application to tooling industries; PCD and PCBN cutting and wear performances when machining specific set of soft/brittle materials. In particular this chapter aims at giving to the reader an overview of the technical field of study and a panorama of the most important researches in the field of advanced manufacture of ultra-hard abrasive tools.

- iii. *Chapter 3* includes the methodology, equipment and techniques used throughout the research in order to conduct experiments, design and analysis necessary for the research aims achievements.
- iv. *Chapter 4* contains a detailed study on the effects of variation of laser parameters on the surface integrity of PCD/PCBN structures. In particular, a correlation between laser parameters and micro-structural factors (binder bulk volume percentage, binder phase, binder material and ultra-hard phase grain size) is presented. A generic procedure for finding optimal laser ablation parameters is proposed and the outcome of it reported.
- v. *Chapter 5* includes all of the results of the characterisation work undertaken to understand the thermal response of micro-structurally different composites to the laser beam. In particular, this covers the study of the causes and quantification of the extent of the residual damage to the ultra-hard structures when using PLA. Results from the examination of the allotropic transformation occurring at atomic level in PCD and PCBN as a consequence of the entity of fluence in a laser pulse are presented.
- vi. Based on results included in chapter 5, *Chapter 6* includes the optimisation process for laser operating parameters (e.g. pulse duration/frequency, power density) and laser paths (e.g. rastering, pocketing) to allow ablation of 3D features with controlled surface quality (roughness, damage level). Specifically, it reports about a selected design (via a CAD model) and the related optimisation of the selected micro-edge geometry (i.e. rake and clearance faces, cutting edge radius) manufactured via pulsed laser ablation onto micro-structurally different PCD/PCBN composites.

- vii. *Chapter 7* refers to the design of an unconventional test for evaluating the wear/cutting properties of the manufactured arrays in PCD/PCBN. In particular this chapter aims at presenting a generic methodology applicable for testing the wear performances of ultra-hard micro-edges composites with different geometries in relation to cutting edge applications. This chapter also includes the results of the micro-wear/cutting test performed on a grinding machine to evaluate the performances of the novel micro-cutting arrays; a relation between binder percentage, binder phase, grain size and wear performance is proposed and a predictive experimental model for cutting performances of ultra-hard composites is presented. Furthermore, a comparison of the wear performances of the novel arrays against a benchmark is included and this particularly offers a scientific evidence of the importance of this research work in terms of future perspectives of novel cutting geometries which would improve the tool life and reduce the labour costs in micro-tooling industries.
- viii. *Chapter 8* includes a summary of the discussion of the research work, particularly outlining the outcomes of the project and how those could be beneficial for cutting edge industrial applications. It also includes a conclusion and a future work section.

Figure 1.3 reports a flow chart representing the relation between each chapter. As above mentioned, the optimisation of laser parameters for different ultra-hard materials via analysis of surface integrity at micro/nano level is a necessary step in this research to enable the design and optimisation of the cutting arrays. Once the evaluation of optimal parameters is performed, the manufacture of the array can be achieved and it is then possible to evaluate the wear/cutting progression/characteristics of the arrays in specific tribological tests. The benchmarking of wear progression/characteristics for PCD/PCBN arrays is possible via testing of electroplated diamond/cubic boron nitride specimens under same set up condition. This is an important experimental step which allows designing the production of tools in the studied

materials for cutting edge applications by knowing the wear properties of those (that are provided in this study).

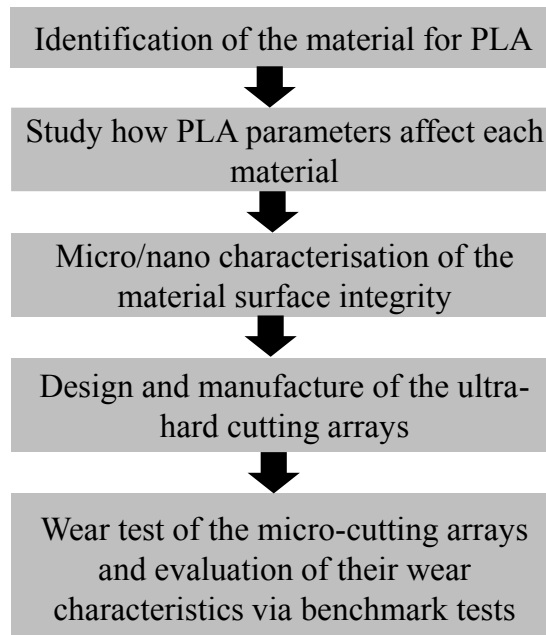


**Figure 1. 3: Flow chart representing the outline of the thesis and each chapter.**

# Chapter 2

## Literature review

As already mentioned in Section 1.4, the literature review chapter contains an in-depth description of the collocation of this research work in the relevant already published literature. It includes an extensive overview of PCD/PCBN materials properties and applications, it describes how the use of super-hard materials has been growing in the years, the main uses of PCD/PCBN in cutting tool industries, the conventional and unconventional manufacture of ultra-hard tools, and the wear characteristics of tools as a function of the microstructural properties of the composites (e.g. binder type, binder bulk volume percentage, type of ultra-hard phase). A flowchart related to the organisation of the literature review, reporting the main researchers that have been working in the related field of study giving a strong contribution to science and technology, is depicted in Figure 2. 1.

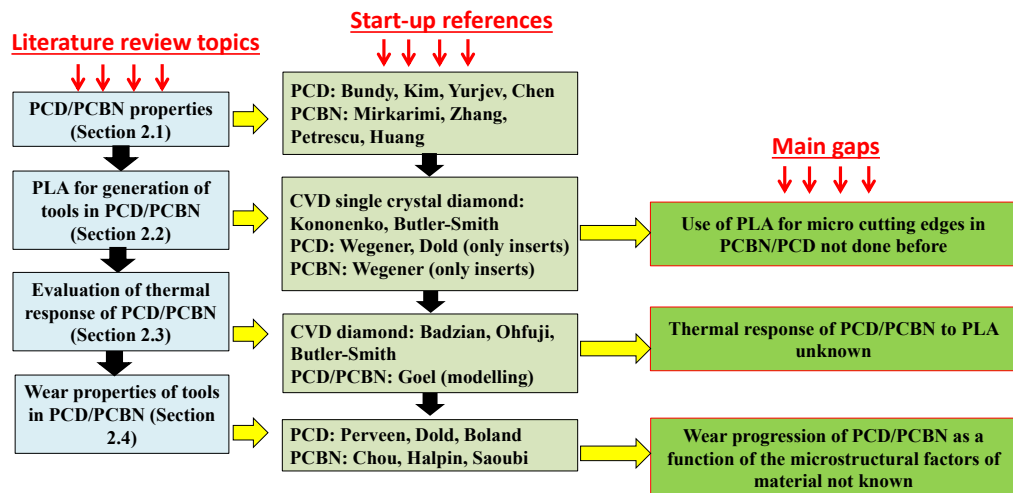


Figure 2. 1: Flow-chart of the main topic of literature review associated with the research and main references for each ones.

## 2.1 Introduction to ultra-hard materials

This section aims at describing the main properties of PCD/PCBN materials, their similarities and main differences. In particular, an in-depth literature review covering the lattice properties of carbon and boron nitride allotropes is here reported for the purpose of the analysis of the thermal response of PCD/PCBN structures to PLA.

### 2.1.1 Synthesis of PCD/PCBN composites

It is well known that [2] diamond and graphite are allotropes of carbon; carbon has an electronic configuration  $1s^2 2s^2 2p^2$ ; the electronic process that allows the transformation of carbon into diamond is the spread of four covalent electrons in the orbitals s and p, thus the s orbital mixes with the three p orbitals to create  $sp^3$  hybridization producing a diamond structure having a face-centered cubic structure (FCC) like the one shown in Figure 2. 2.

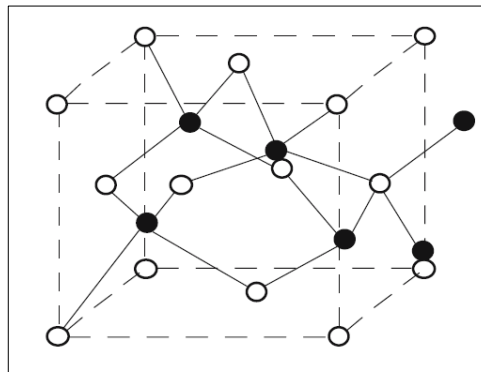


**Figure 2. 2: Example of the FCC structure for cBN and diamond [8].**

In the case of graphite, the s orbital mixes only with two of the three orbitals, producing an  $sp^2$ -bonded structure with hexagonal atomic structure [9], [10] as depicted in Figure 2. 3a. A comparable behaviour is shown from Boron nitride (BN) that is a chemical compound with a carbon like structure existing in different crystalline forms; in particular it has several BN phases (rBN, wBN, hBN, cBN). Among those, the only two equilibrium phases are: the hexagonal  $sp^2$ -structure (Figure 2. 3b) also known as hBN which represents the soft phase and whose layered structure is similar to graphite; the cubic bonded well known as cBN

which is the hard phase, often compared to the diamond phase of carbon shown in Figure 2. 2 [11].

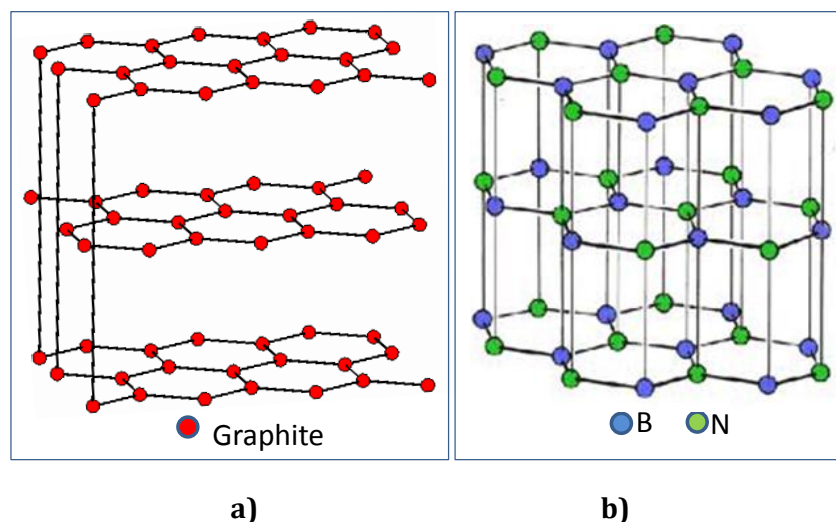


**Figure 2. 3: Representation of the electronic  $sp^2$  structure in graphite and hBN [12].**

The first claim of the conversion of carbon to diamond dates back to 1880, but the first published literature proving the reproducibility of the transformation of carbon into diamond is dated to 1955 [2], opening a new exciting era for synthetic-diamond industries. In the same years researches proposed the synthesis of a new compound which could reproduce diamond properties (e.g. high hardness, good thermal and chemical stability, good thermal conductivity) being only second to diamond in term of hardness, this compound is known as cubic boron nitride [3]. The boron nitride allotrope was firstly synthesized in 1956 when researchers in General Electric transformed a mixture of Boron and Nitrogen in a cubic crystalline lattice by high pressure and high temperature (HPHT) in capsule process [3], [13]. Nowadays cBN is produced by conversion of a mixture of hBN and catalysts (lithium nitride, magnesium nitride, calcium nitride) under high pressures (4-6 GPa) and temperatures (1000-1500 K). Quantities of boron oxide are used to decrease the synthesis pressure which would otherwise be in the region of 18GPa [14]. The pressure-temperature phase diagram of Boron Nitride (Figure 2. 4a) shows the versatility of cubic BN: this is thermodynamically stable in ambient conditions as well as at high pressure and temperature;

while the graphitic BN (hexagonal BN) is thermodynamically stable only in high temperatures conditions [15]. It has been demonstrated that under ambient conditions the transition from  $sp^2$  to  $sp^3$  bonding is impeded by a kinetic barrier [11] which requires a large reaction energy provided by high pressure and temperature conditions to effect the hBN - cBN phase change. To widen the applications field of the monocrystalline cBN, the synthesis of polycrystalline cubic boron nitride (PCBN) has been achieved: this not only allows the achievement of specimens of large size (area up to  $0.01 \text{ mm}^2$ ) but also to increases the fracture toughness beyond that of the single crystal cBN.

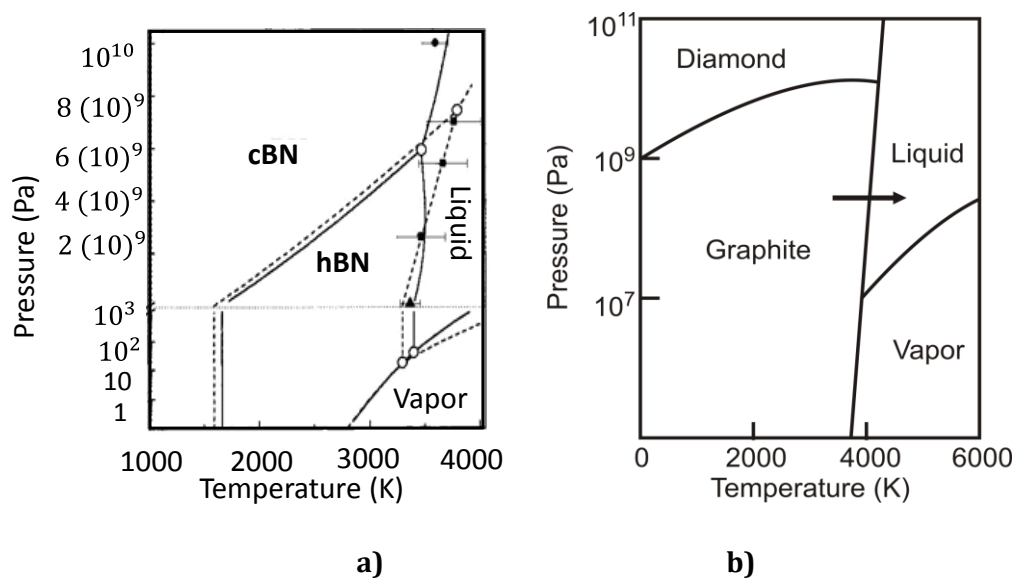


**Figure 2. 4: Phase diagram of BN and carbon [15], [16].**

The physical process of synthesis of PCD/PCBN composites is called “in capsule high pressure-high temperature process” and consists of several phases [16], [17]:

1. The diamond/hBN powders (ultra-hard phase) are mixed with ceramic/metal powders (binder) to produce a homogeneous blend;
2. The achieved powder mix is placed in a metal cup and compacted on a substrate of cemented carbide (WC) to form a green compact;
3. The green compact is then placed in a protective, refractory metal canister called a capsule;
4. The capsule is then assembled from the green compact, ceramic and metal components are used to transmit heat and pressure.

- The achieved capsule is placed in a system where high pressure and high temperature are given to form a polycrystalline compact as shown in Figure 2. 5. The high pressure is produced through the concentration of hydraulic forces on small areas [13].

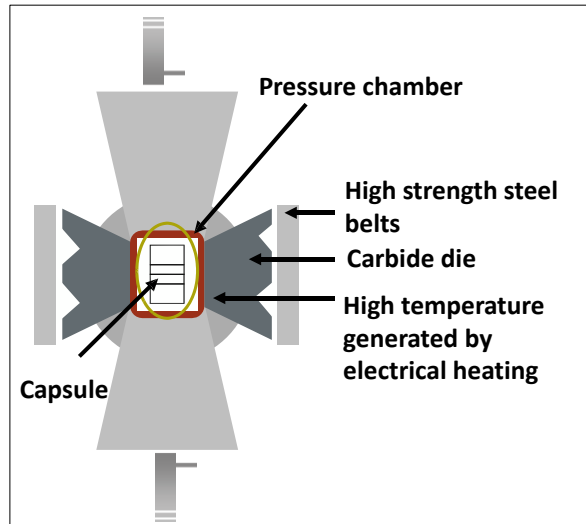


**Figure 2. 5: HPHT in capsule process [17].**

From a material point of view PCD and PCBN synthesis differ because of the intergrowth process which occur in the case of PCD structures: when the diamond crystals are mixed with a catalyst/binder (e.g. Cobalt) and are subjected to high pressures and temperatures (in the vicinity of 5.5 GPa at around 1750 K), diamond intergrowth (i.e. the formation of bridges between individual crystals) take place enabling the molten catalyst/binder to infiltrate the diamond structure, and forming a PCD contiguous hard phase (Figure 2. 6) which incorporates pockets containing the binder phase.

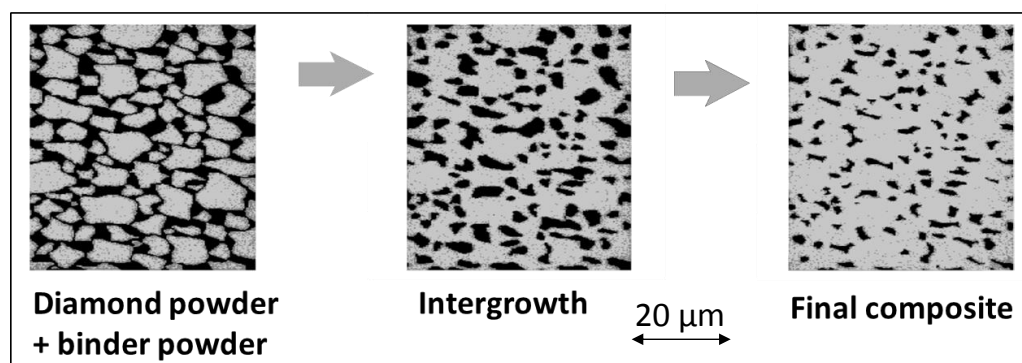


**Figure 2. 6: Schematic of the synthesis process for PCD composites [18].**

The synthesis of PCBN composites is different where the intergrowth process does not occur and the hard phase CBN grains are well defined and separated from the tough phase of binder (TiC, TiN, WC-Co, Ti, TiN-Al). The presence of TiC or TiN reduces the thermal conductivity to 50% that of pure CBN [19]. During the process of synthesis of hBN into cBN there are a number of chemical phenomena taking place, and the formation of different BN structures might occur. It has been demonstrated [10] that the transformation from hBN to cBN take place in a two stage process: at high pressure high temperature a martensitic type of transformation [20] occurs from  $sp^2$ -hBN to  $sp^2$ -rBN (rhombohedral) causing the breaking of the weak Van der Waals bonds between the hBN atomic layers (0.052 eV), then rBN transforms into cBN through a puckering process where the atoms translate perpendicularly to the hexagonal layers.

It has also been proved that in the microstructural evolution of cBN synthesis from hBN, an amorphous BN layer ( $\alpha$ BN) formation might occur due to heat conduction into the substrate [11]. This would explain why research has shown the presence of an  $\alpha$ BN layer during thermo/chemical processes in BN structures [21]. Some of the atomic properties of the main chemicals used throughout this research are reported in Table 2. 1.

**Table 2. 1: Atomic separation of BN allotropes, C allotropes and binders** [10], [11], [22]-[24].

<b>Phase</b>	<b><i>d spacing</i> [Å]</b>
hBN	2.5-3.33
cBN	1.56
TiC	2.50
Diamond	2.
Graphite	3.39
Co	2.13

One of the main differences between the phase changes graphite/diamond and hBN/cBN resides in the energy required to allow the allotropic change taking place: in the case of graphite/diamond, although little difference is in their standard enthalpies values [14], a large reaction energy is

required to make the phase change due to the higher bond energies in carbon (than in boron nitride) because of the ionic bond component [10].

### ***2.1.2 Properties of PCD/PCBN composites and benefits for industries***

In Section 2.1.1 the atomic properties (e.g. atomic spacing, transition between phases) of the allotropes of carbon and boron nitride have been described. This is propaedeutic to the evaluation of the thermo-mechanical properties of PCD/PCBN composites deriving from those allotropes. Essential is the understanding of the role of each allotrope during a thermal excitation phenomenon to allow the identification of the thermal phenomena involved in the processing of PCD/PCBN materials. The thermal properties of single phases elements included in this research are reported in Table 2.2, and their role in the PLA process is described in details in Chapter 5. It has been demonstrated that in ultra-hard composite like structures, the gap in values of thermal expansion coefficient between binder and ultra-hard phase noticeably affect the interface binder/grain because of the different extent in compressive/tensile stresses resulting in the matrix [25], [26]. In the PCD/PCBN composites important material properties such as thermal conductivity, standard enthalpy and melting/vaporization/sublimation temperatures need to be taken into consideration, especially in reference to the processing of composites via thermal processes (such as PLA). As an example, with different values of enthalpy and temperature for vaporization (Table 2.2), diamond and Cobalt will be differently thermally excited: they provide different properties (enthalpy and temperature for vaporization) to the PCD composite structure; with lower values of vaporisation temperature and thermal conductivity, Cobalt will probably melt before the diamond but will act more as a thermal insulator, while diamond will act more as a thermal conductor. Since the Cobalt is embedded in the diamond matrix, the gap in thermal conductivities can possibly provoke important

phenomenon (modification in different extent of binder/ultra-hard grain matrix) during the thermal processes.

**Table 2. 2: Thermal properties of single crystal phases and binders [25], [27]–[33].**

Phase	K [ $\text{Wm}^{-1}\text{K}^{-1}$ ]	$\alpha$ [ $10^{-6}\text{K}^{-1}$ ]	H [kJmol]	$T_v$ [K]
hBN	600	-2.7÷-2.9	-250.6	/
cBN	740	1.2	-247.6	/
TiC	31	7-8.6	/	/
diamond	600-2000	1.2-2.5	-395.4	5100
graphite	390-4180	2-6	-393.5	/
Co	100	13	/	3053

For the purpose of identifying the wear progression mechanisms as a function of the microstructural factors of the composite, it is important to approximately establish the values of hardness and fracture toughness for all of the composites used in this research. In the case of PCD/PCBN all of the values reported in Table 2.3 are experimentally found values [34], [35].

**Table 2. 3: Values of mechanical properties for different materials [34]–[36].**

Specimen	Hardness (GPa)	Fracture toughness ( $\text{MPa}(\text{m})^{\frac{1}{2}}$ )
PCD CTM302	64.0	15.0
PCD CMX850	50.0-60.0	13.2
PCBN DBW85	40.7	6.40
PCBN DBS900	36.0	7.60
SiO <sub>2</sub>	35.4	0.77

The thermo-mechanical properties here described represent the main benefit in the use of polycrystalline ultra-hard materials for industrial applications (Figure 2.7). On the one hand high thermal conductivity and hardness typical of PCD structures, on the other hand high thermal/chemical stability (up to 1573 K) and hardness [37] typical of PCBN materials make PCD and PCBN composites suitable for cutting applications [38] and make reliable their use in micro processing and advanced manufacturing industries [39]. During the last decades the use of ultra-hard materials in the cutting tool industry has been remarkable in

the improvement of precision and productivity in aerospace, automotive and woodworking industries [40], [41].

In particular, since the early 90's PCD and PCBN have been used in a wide range of applications, the most common ones being cutting tools [42]–[44] and polishing pads industries [45]–[47]. The details of those applications and the recent research trends are covered in details in Section 2.2, where an in-depth literature survey is presented on the characteristics of super-abrasive tools for polishing, grinding and cutting applications. As a general rule, PCD are considered as suitable materials for the manufacture of tools for machining abrasive non-ferrous metals, plastics and composites, while PCBN tools are used for machining of hardened tool steels, hard cast irons and as a valuable substitute of solid carbide in machining of hard workpiece materials; PCBN is also recommended for turning, milling and drilling of perlitic iron castings (grey and ductile), but not for ferritic iron castings because of the chemical degradation that might occur because of the high chemical reactivity of ferrite [41], [44]. PCBN is widely used in industry as a ball-nosed type cutter [40] to machine moulds and dies (in several ferrous materials) hard (>55 HRC) or medium hard (<55 HRC).

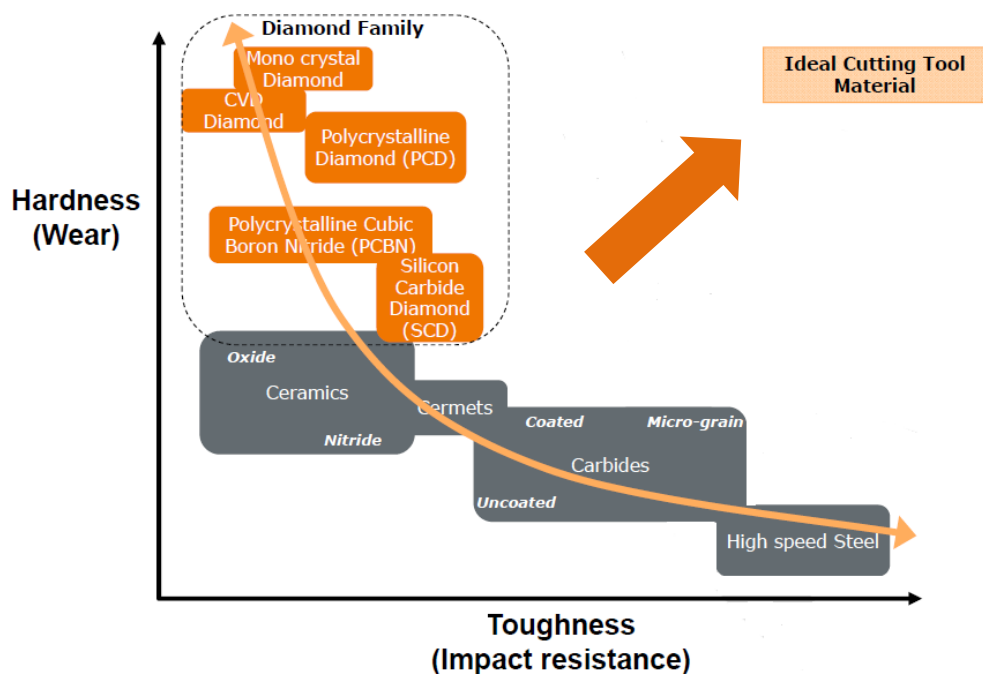


Figure 2. 7: Schematic of the collocation of ultra-hard materials for cutting tool application [48].

## **2.2 Cutting/abrasive tools made of ultra-hard composites**

The recent current methods for manufacturing super-abrasive elements result in a stochastic geometry of abrasives with random three-dimensional abrasive spatial locations or single point abrasive inserts in macrometric dimensions [49]. The literature review covered in this section aims at understanding the development of tools made of ultra-hard materials and the recent trends of research and also at identifying the role of this research work among the different proposed research gaps.

### ***2.2.1 Geometry of the cutting edge in PCD/PCBN composites***

Depending on the type of application, there are many differences in the geometries of cutting inserts already proposed in literature. A sharp cutting edge is a main prerequisite when flawless workpiece machined surfaces are required [50]. Furthermore, rounded cutting edges causes an increase of thermal damages [51], so it is preferable to have a sharp cutting edge.

For definition of the normative ISO 3002/1 [52], conventional cutting tools present a main cutting edge (main edge), but some tools also have a secondary cutting edge (minor edge). There is a classification related to a single-point cutting tool, which is typically used for turning (Figure 2.8a), and a multiple-point cutting tool (Figure 2.8b), which is used for endmilling for instance.

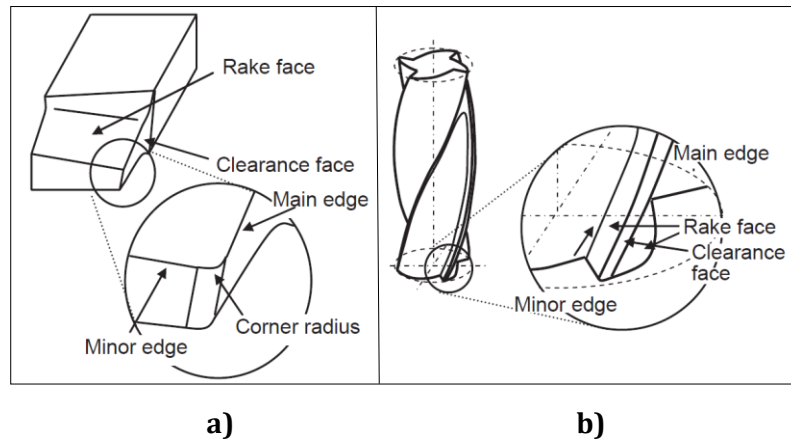


**Figure 2. 8: Schematic drawing of a cutting tool in: a) single-point and b) multiple-point [53].**

One of the characteristics to be considered in the design of cutting tool edge geometry is the ratio clearance/rake faces, together with the edge angle. Typically a positive rake angle is very common, though in hard machining it is preferably negative, this gives a strong cutting edge and it can be used especially for difficult-to-cut materials; the clearance angle is always positive to avoid the rubbing with the surface, and finally the edge radius shown in Figure 2.9 [53].

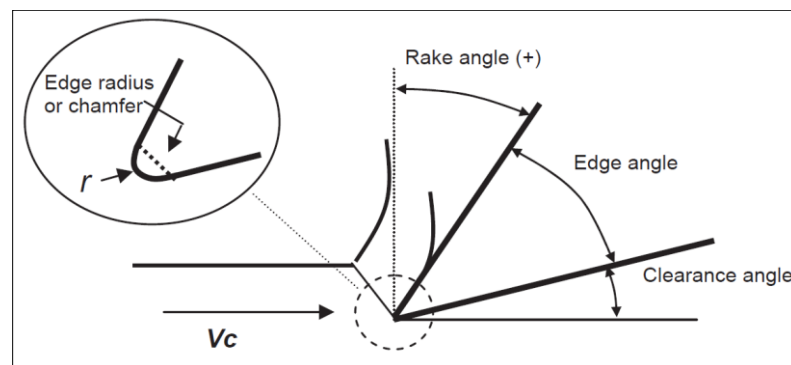


**Figure 2. 9: Schematic of the rake, clearance and edge angles [53].**

The variation of the geometrical characteristics of the macro-cutting edges has been reported in literature for ultra-hard composite materials: negative rake angles in the range  $-6^{\circ}$ / $-10^{\circ}$  are utilised for PCBN [54]–[57] and PCD diamond [4] while rake angles of approximately  $0^{\circ}$  have been used especially for single crystal diamond [58], [59]. Some of the most utilised values of clearance/rake angles are reported in Table 2. 4, here the angles are selected as a function of the material to be machined.

**Table 2. 4: Values of rake and clearance angles for cutting edges in PCD for the machining of different materials [48].**

Rake angle $\gamma$	Clearance angle $\alpha$	Material to be machined	Reference
0°/5°	7°	n.d.	Dold
0°/5°	7°	n.d.	Kyocera PCD cutting tools
0°/5°	11°	n.d.	Kyocera PCD cutting tools
0°/5°	5°	n.d.	Kyocera PCD cutting tools
0°/6°	7°/20°	Non Ferrous Metals	Element Six
0°/6°	7°/11°	Hypereutectic (Si > 12%) aluminium casting alloys	Element Six
0°/+6°	0-7°	Ceramic machining	Element Six
0°/+6°	7-11°	Copper and Magnesium and its alloys	Element Six
0°/+6°	7-11°	Bi-Metals	Element Six
0°/+6°	7-11°	Grey & High Strength Irons	Element Six
0°/+6°	7-11°	Composite Plastics	Element Six
0°/+6°	7-11°	Titanium	Element Six

### **2.2.1.1 Single-point tools**

There are the proposed geometries for single-point cutting tool in PCD and PCBN composites; here some of them are reported from an experimental point of view. In 2003 cutting tools in diamond have been used for the cutting of single crystal silicon; in this case the geometry of the tool was a four-straight nosed diamond with 1.2-1.5 mm main cutting edges and clearance/rake angles of 6°/0° later adjusted to 6°/-20°. A very recent work proposed laser generated inserts on a PCD fine grain composite to achieve a clearance/rake ratio of 7°/0°, as well as inserts in CBN for a tool with diameter dimension 10-15 mm and width 10 mm [60]. PCBN inserts were used in hard-turning of alloy steels [54]; in this case the insert having a negative chamfer normal rake angle (-20°), a chamfer width of 0.1 mm and a normal rake angle also negative (-6°). Another important work on PCBN inserts proposed a clearance/rake ratio of 5°/-30° to evaluate the influence of the binder bulk volume percentage on the wear

characteristics of the PCBN cutting tools [61]. In this regard, relevant work on microstructurally different PCBN composites reported the generation of cutting tools with PCBN macrometric inserts with a clearance/rake ratio of  $20^{\circ}/-6^{\circ}$  to evaluate their wear performances in hard machining [56].

Several models [37], [62]–[64] have been also proposed to understand the influence of variation of clearance/rake faces onto the wear behaviour of cutting inserts. In particular, work conducted in 2012 has proposed the modelling of a diamond tool with a clearance/rake ratio of  $10^{\circ}/-25^{\circ}$  [65].

### ***2.2.1.2 Multiple-point tools and ultra-hard electroplated tools***

All of the recent trends in the use of electroplated tools propose tool in macrometric size with micrometric grit dimensions.

Research published in 2012 proposed a hybrid electroplated diamond abrasive tool for cutting and grinding. The tool looks like a typical endmill or electroplated grinding wheel (Figure 2. 10), but it has a cutting edge and flutes without a radial land and clearance [6].

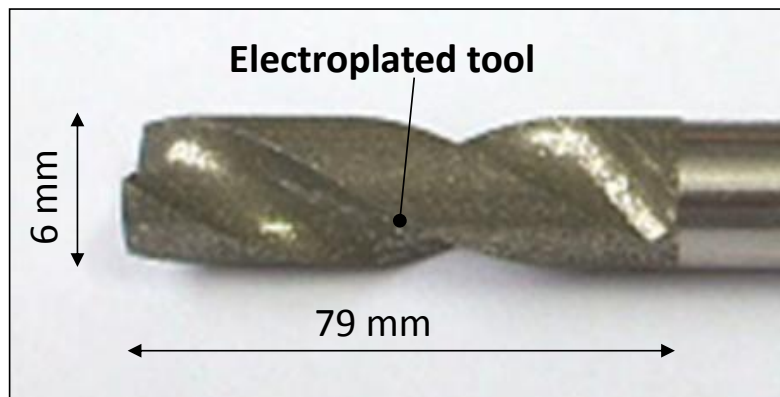


**Figure 2. 10: Image of the electroplated cutting tool [6].**

Electroplated wheels in super-abrasive grains have been widely used over the last decades [6], [38], [66]–[68]; in a recent work proposed by Hwang, an electroplated diamond grinding wheel has been used [63], [64], details of the grit geometry are indicated in Figure 2. 11.

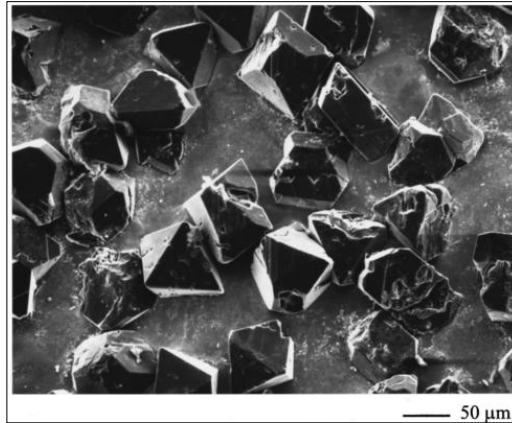


**Figure 2. 11: Detail of the grit used in the electroplated tool [66].**

Regarding CBN electroplated wheels, different works have been done. An investigation is reported on the wear of single-layer electroplated cubic boron nitride (CBN) grinding wheels and how the wear process affects the wheel topography and grinding behaviour. In this case the wheel has a diameter of 50 mm and a width of 16mm, grain size varies from 54 to 252 microns [7].

### ***2.2.2 Micro-texturing of PCD/PCBN composites***

As explained in Section 2.2.1, the current methods for manufacturing super-abrasive elements result either in a single-point tool with ultra-hard inserts in macrometric size, or in a multiple-point tool with a stochastic geometry of abrasives and random three-dimensional abrasive spatial locations, which is the definition of an electroplated tool. There is only one research which proposed a multiple-point array with orderly oriented and equal geometrically abrasives in single crystal CVD diamond [4], [5]. In this work, the technique used to generate the tool is pulsed laser ablation deeply described in Section 2.3. Figure 2. 12 shows some of the multiple-point tools that have been produced in this research in single crystal CVD diamond, and the high control of clearance/rake faces in the tool geometry. The use of multiple edges minimise the contact between each micro-edge and the workpiece material and provide unrestricted chip flow paths in machining [4], [5].

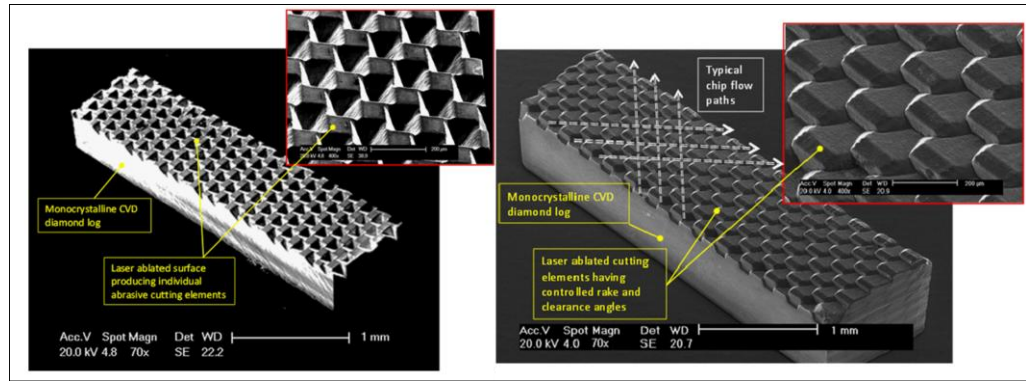


**Figure 2. 12: Orderly CVD single crystal diamond micro-arrays for machining [5].**

The typical tool geometry proposed in 2012 is shown in Figure 2. 13 and represents the starting point for the manufacture of the array in PCD/PCBN materials proposed in this research work: it is evident that the sharpness of the cutting edge is a requirement for a cutting tool which has not been achieved yet.

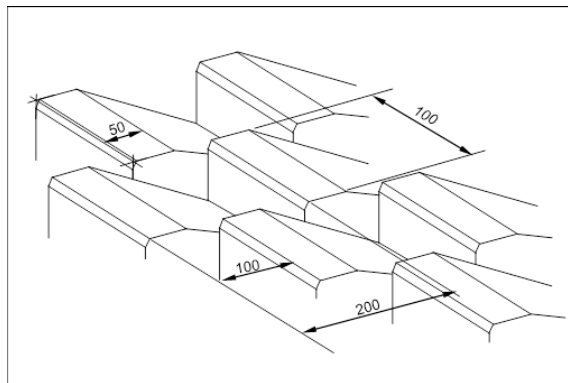


**Figure 2. 13: Drawing of the cutting edge geometry proposed for single crystal diamond from Butler-Smith et al. [5].**

### ***2.2.3 Techniques for the manufacture of cutting tools in ultra-hard materials***

The use of ultra-hard materials in tooling applications (e.g. turning, grinding, drilling, milling and polishing) makes it necessary to profile and texture the composites for the intended applications [4], [40].

Depending on the required dimensions of the cutting tool, different non-contact methods are used for the micro/macro processing of PCD/PCBN tools: in the case of macro geometries mechanical process such as electro discharge machining or grinding is used, where the PCD/PCBN inserts are

brazed or hard soldered to a cutter body [19]; in the case of micro geometries, a recent research has recently proposed laser ablation as a suitable technique to shape diamond-like materials with high precision [4].

### **2.2.3.1 EDM**

In the process of material removal via EDM process, a high current pulsed flow, called spark is created between two electrodes in an electrolyte, the thermal energy on the material causes an erosive effect, producing the material removal [69]. An adaptation of EDM has been done to achieve the so called Electrical Discharge Wire Machining (EDWM), where a wire electrode is incorporated, allowing to improve the accuracy of cut and enabling a better control of surface texturing through the workpiece material also due to the machine controlled guidance of the wire [69], [70]. It has been proved that EDM is a suitable technique to machine PCBN especially for the processing of complex shapes because of the tool electrode simple forming and small loss [71]. Many researches have been focusing on the generation of micro tools in PCD/PCBN via micro-EDM [71], [72]. In all of the ultra-hard composites the metallic binder serves as an electrical conductor [72]. A micro-EDM machining was proposed as technique for processing PCD tools and the effect of a change in energy was studied onto the microstructure of PCD composites: it was proved that depending on the energetic parameters used in the EDM processing, an extent of molten material was deposited on the surface after tool preparation, and this extent was reduced with the decrease in energetic parameters, giving the possibility to produce tool which could improve the surface finishing of the machined material [73]. The main limitation related to the micro processing of PCD and PCBN with the EDM technique is related to the lifetime of the electrodes, to the material restrictions (electrical properties) and to the impossibility to create undercuts.

### ***2.2.3.2 Pulsed laser ablation for generation of tools in ultra-hard materials***

The other technique which has recently shown new developments in micro-processing of ultra-hard materials is the PLA; the unconventional shaping technique of laser ablation has been recognised as a versatile approach among the material removal technologies [74]. The laser ablation removes material via a thermal process, making feasible the generation of micro-features/cutting edges on ultra-hard materials that are normally very difficult to generate with conventional machining processes (such as EDM/EDWM). Laser micro-machining using high intensity, pulsed visible laser radiation, is capable of forming precise micro scale features in diamond in an efficient manner [4], [75], [76]: some examples of the achieved shapes in CVD diamond are depicted in Figure 2. 14.

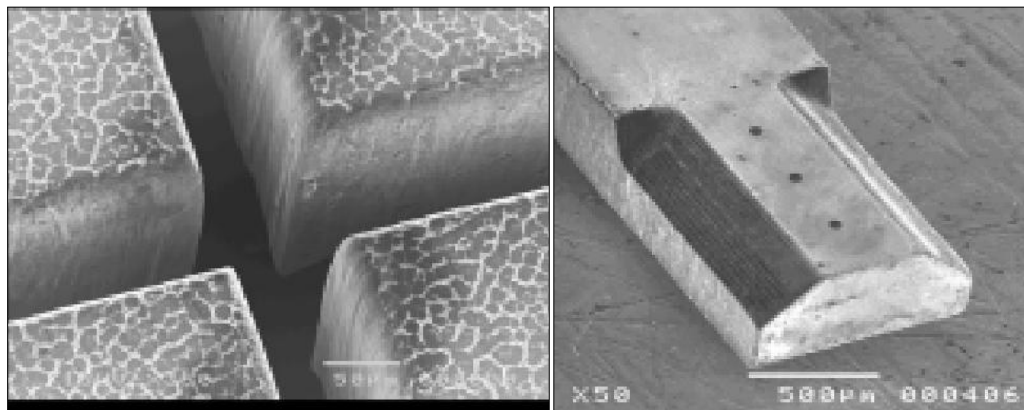


**Figure 2. 14: SEM micrographs of pulsed laser ablated CVD diamond surfaces [75].**

The possibility of using laser ablation to create repeatable micro features onto single crystal diamond materials has been studied in relation to the tribological properties of the features for machining applications [4], [5]. The tribological performances are strictly related to both the geometry of the micro-cutting/polishing elements and the workpiece material utilised. Here reported are some of the tools manufactured via PLA in ultra-hard solid materials: Figure 2. 15 represent the results achieved with the use of PLA on WC/Co solid structures in 2001.

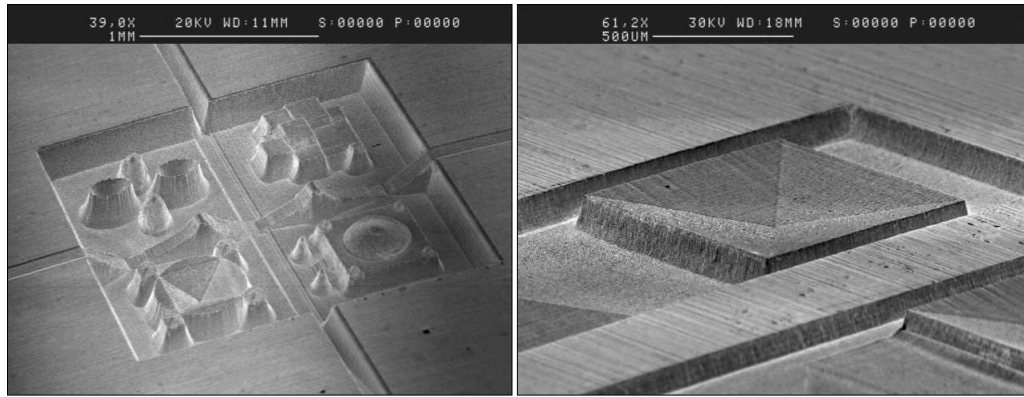


**Figure 2. 15: Geometries manufactured in WC/Co via PLA [77].**

The importance of the clearance/rake faces upon the performance of the abrasive edges has been shown in the production of mono-crystalline CVD diamond micro-arrays patterned to provide chip flow during machining condition [4], [5] and the importance of the geometry of the cutting edge has been extensively explained in Section 2.2. Figure 2. 16 depicts some examples of laser ablated single crystal CVD solid diamond which have been manufactured to provide chip flow.

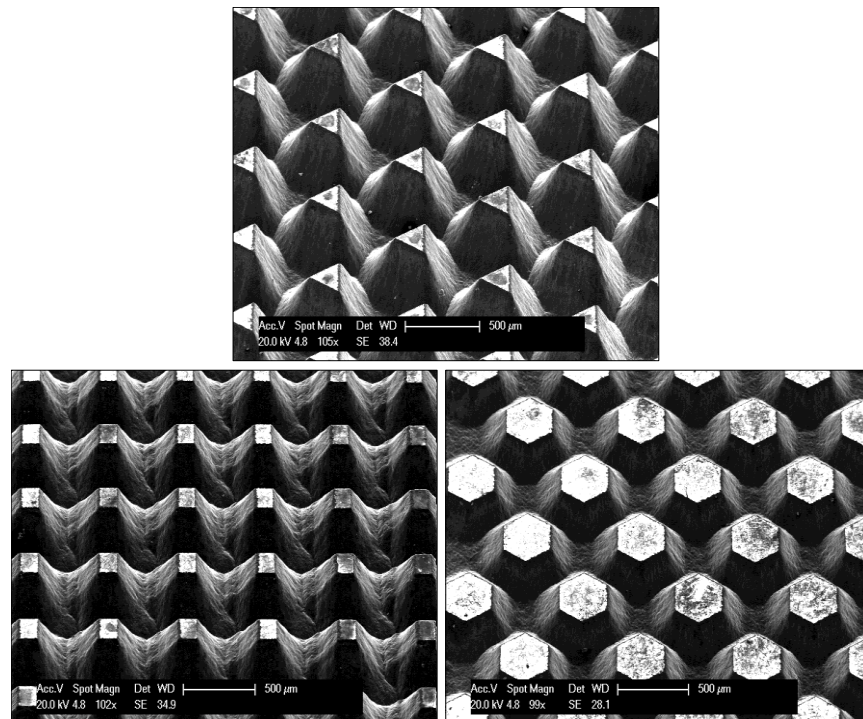


**Figure 2. 16: Geometries manufactured in single crystal CVD diamond via PLA [4].**

While conventional processing of PCD/PCBN tools can be done using grinding processes on a five axis machine depending on the complexity of the tools, some works proposed ultra-short laser pulses (in the regime of

picosecond) have been used in the laser ablation of PCD/PCBN composites for the generation of cutting tool inserts [60], [78]. An example is reported in Figure 2. 17, where a round shape insert has been manufactured on a CBN solid specimen.

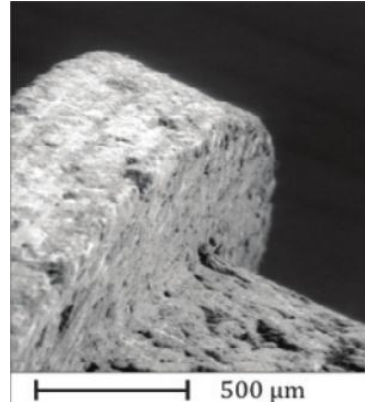


**Figure 2. 17: SEM micrograph showing a pulsed laser ablated insert in CBN [60].**

There are no reported cases of shaping of CBN materials via PLA to achieve tools with reproducible micro-features like in the cases previously shown for CVD diamond in Figure 2. 16.

### ***2.2.3.3 Effects of PLA technique upon PCD/PCBN composites***

Pulsed laser ablation represents a high precision macro/micro removal technique for a wide range of materials; as such a laser beam is focused on a target surface, producing electron excitation resulting in conversion of optical energy into thermal one. As a consequence the surface heats up, melts, vaporizes and expands at atmospheric pressure, forming plasma due to the partial ionization of the expanding plume, with the final ablation cell formed as shown in Figure 2. 18 [79], [80].

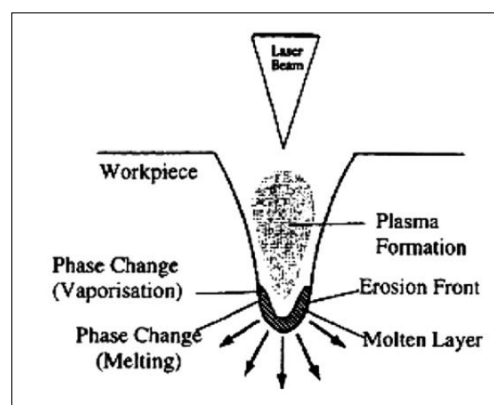


**Figure 2. 18: Typical phase transition during PLA [81].**

More recently, researchers have studied the heat conduction and phase changes in the target material by using a theoretical model of the laser ablation process considering the enthalpy as main affecting parameter in the process, they modelled the laser heating considering different time scales: the lattice heating time, the electron cooling time and the laser pulse duration; hence, they demonstrated that there is a strict relation between enthalpy, pulse duration and surface recession time [82]. In this context it can be commented, that depending on the laser intensity and pulse duration, the effects of laser ablation on the target surface will result in micro craters with different material properties such as optical absorptivity, hardness and hydrophobic properties [80], [83]. In 2010 researchers [84] studied how fluence and pulse frequency affect the ablation rate of different materials, and, by validating the experiments with a theoretical model on PLA they found a decrease of ablation efficiency in the multi-pulse regime mainly due to the reduced incident laser irradiance (laser power density) in the lateral ablated area.

The type of laser for PLA is mainly chosen in relation to material removal rate, optimal surface finishing and cost requirements. Nowadays it is possible to select from Nd: fiber lasers to Nd:YAG lasers in pulse width ranges ms to fs. The pulse duration and the laser wavelength are important parameters involved in the ablation process. A recent study [85] has showed that the variation of pulse duration has the property of dramatically changing the results of laser material removal: nanosecond pulses make possible high power peak with high frequency, causing direct vaporisation of the target material; microsecond pulses enable the highest material removal per pulse despite potentially causing collateral damage to surrounding material. In this regard another researcher commented that the laser wavelength for diamond is not of critical importance since ablation takes place with surface graphitisation that is characterised by high absorption coefficient in all of the wavelength spectra [86], [87].

As deeply described in Section 2.1, in the case of composite materials such as PCD/PCBN, and during their macro/micro processing, important properties such as thermal conductivity and melting/vaporization

/sublimation temperatures need to be taken into consideration. In reference to the laser processing of PCD/PCBN structures, it can be commented that different values of enthalpy, thermal conductivity and thermal expansion coefficient between the binders and the hard phases, causes a peculiar thermal response to PLA.

There are some studies relating the influence of temperature on different grades of PCD materials: it has been reported that the effects of ultra-short pulse (i.e. *ps*) laser ablation has little thermal affected area on the target surface while resulting in little debris and smooth surfaces [88], [89]. However, the presence of a metallic binder can play an essential role in the thermal process during PLA. Larger grain size PCD with smaller content of Cobalt are less affected from the superficial temperature increase and thermal effects [90]. More recently, comments about the thermo-mechanical properties of PCD/PCBN composites demonstrated that, because of the significant differences in thermal expansion coefficients between binder and ultra-hard phase, small temperature variations can provoke expansions of the two materials causing micro cracks/fractures at early stages of temperature increase [34], [91].

### **2.3 State of the art: experimental approach in the evaluation of thermal response of ultra-hard materials to PLA**

As anticipated in Section 2.2.2.2, it is particularly important to understand the thermal response of the composite material to PLA in order to achieve a high degree of process control and to enable macro/micro processing of desired cutting tool geometries. In this contest, some research has been carried out to explain the physical phenomena occurring during PLA: although a good understanding has been achieved for single crystal diamond [92], there is still a lack in understanding the thermal response of ultra-hard composite materials (PCD and PCBN) because of the many variables (binder, ultra-hard phase) and the different thermal properties (thermal conductivity, vaporisation temperature, thermal expansion

coefficient) between hard phase and binders. This section aims at understanding the characterisation techniques used to identify the material behaviour and the methodologies employed to achieve an understanding on the thermal response of PCD/PCBN to PLA.

A few experimental works have been conducted to achieve an understanding of the thermal response of ultra-hard materials to PLA, the most part of them concentrated on single crystal CVD diamond or nano polycrystalline diamond.

A study published in 2010 [93] on both monocrystalline and nano polycrystalline diamond mainly focused on the evaluation of the transition between diamond and graphite during the PLA process. A technique which combined several characterisation methods was used: firstly Raman microspectroscopy was used in selected areas for chemical analysis of the ablated groove, then SEM for the evaluation of surface texture after laser ablation, then a gold deposition on samples with an ion sputter coater. The target area was coated with FIB-assisted carbon deposition, and finally the specimen was then milled in a FIB system for TEM-Foil preparation for further characterisation into the HRTEM.

This research demonstrated that graphitisation always takes place followed by sublimation of the pre-formed graphite; as a consequence of PLA, both in single crystal and polycrystalline diamond, formation and sublimation phenomena of graphite take place. A typical interface which was captured in this research work is depicted in Figure 2. 19.

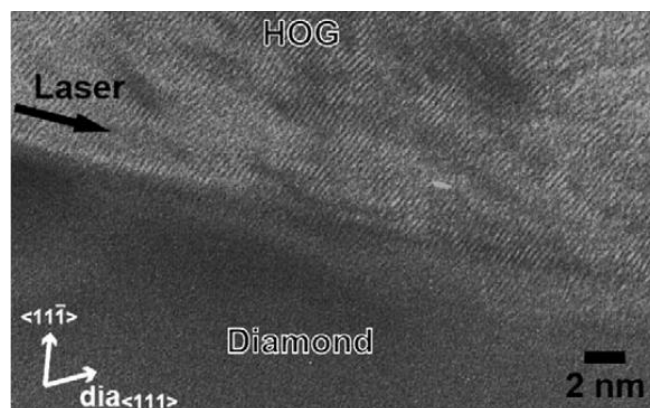


**Figure 2. 19: HRTEM image of the interface between graphite and diamond in single crystal diamond as a consequence of PLA [93].**

Another work [94] studied the ablation process of diamond, hypothesizing that, because of its high transparency and distinct threshold for plasma formation, the initiation of the process starts either from non-linear multi-photon effects (possible at elevated laser power densities) or absorption at an impurity or defect or contamination of the surface. However, in many cases, it is probably a combination of these effects. Once laser absorption begins, then the resulting heat generation locally elevates the diamond to temperatures where it is converted to graphite (see more details in Section 2.1). Another recent work published in 2013 [92] identified both the extent of graphitized layer in PLA of single crystal diamond and a clear interface graphite/diamond (Figure 2. 20).

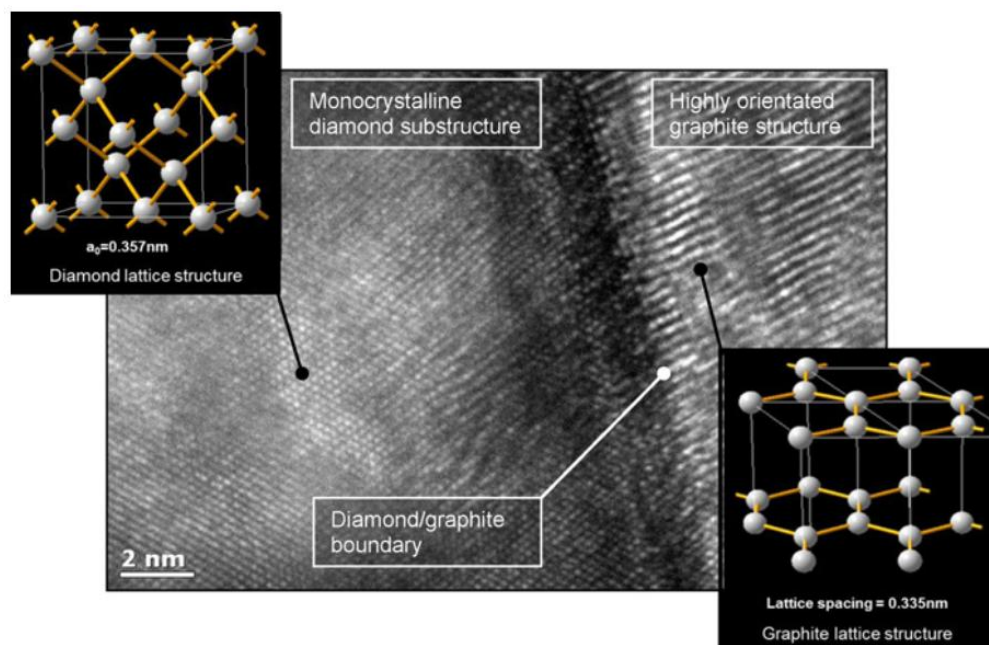


**Figure 2. 20: HRTEM image of the interface between graphite and diamond in a single crystal CVD diamond as a consequence of PLA [92].**

The experimental technique used for the preparation of diamond specimen was composed of four stages (Figure 2. 21): a surface multi coating deposition, the use of a FIB (Focused Ion Beam) miller for preparation of the thin section; an omniprobe nanomanipulator was then adopted to lift out the ultra-thin specimen and to mount the specimen on a support grid for HRTEM analysis.

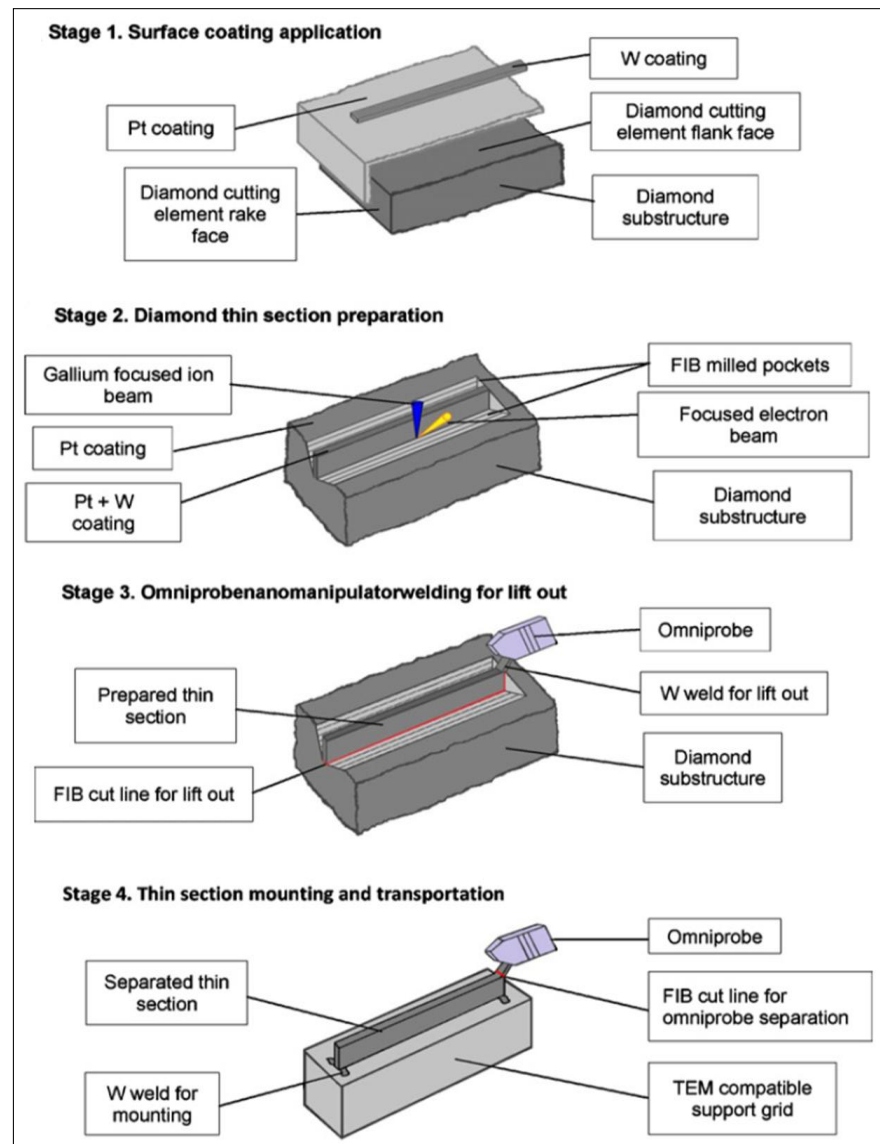


**Figure 2. 21: Schematic of the preparation of the sample for HRTEM analysis [92].**

By using a combined technique FIB /TEM (Transmission Electron Microscopy) /EELS (Electron Energy Loss Spectroscopy) the interface graphite to diamond was captured and the process of formation of graphite in relation to the laser process explained.

In this research, the presence of the metallic binder in the polycrystalline diamond composite structure makes the pulsed laser ablation process more challenging in term of understanding the thermal effects upon the microstructure of the ablated surfaces. Cobalt catalyses the conversion of diamond to graphite at ambient pressure: the finer the diamond grain size of the PCD, the higher the contact area between diamond and Cobalt and hence, the faster thermal degradation occurs [25]. There is no literature

reported in the understanding of the thermal response of ultra-hard composite structures such as PCD/PCBN, mainly because of the complexity of the variables involved in the process. More information about this is reported in Section 2.5, where all of the research gaps are exploited.

## 2.4 Evaluation of wear progression mechanism of abrasive tools in PCD/PCBN

Much research has previously been carried out to investigate ultra-hard tool wear characteristics during machining with different workpiece materials, demonstrating that the severity and mechanism of wear in ultra-hard tools vary with the type of workpiece material selected [93]-[94]. The typical ultra-hard material wear modes have been categorized into four groups: normal wear, chipping, chip dragging and fracture of the cutting edge [97]. It has been demonstrated that with an increase in grain size an improved abrasion resistance can be achieved but the edge quality is higher for finer grain size PCD [40], [98], thus depending on the harsh/moderately harsh test conditions, the fine PCD could be preferred for grinding and polishing applications where better surface quality is required. An example of the effect of the grain size dimension is reported in Figure 2. 22 where the typical abrasive wear rate and tool edge roughness are shown for a fine, medium and coarse grained PCD.

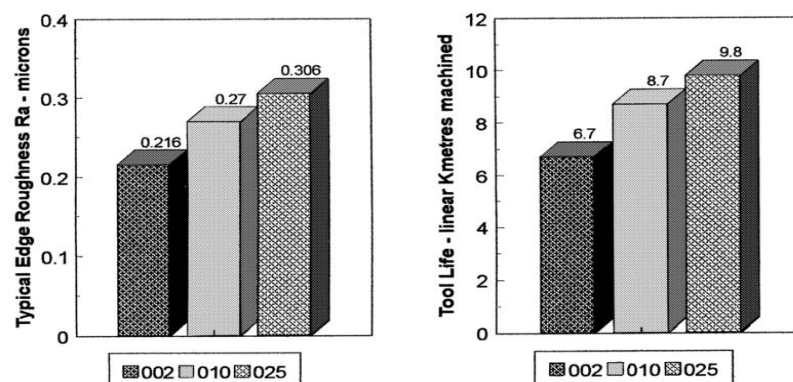
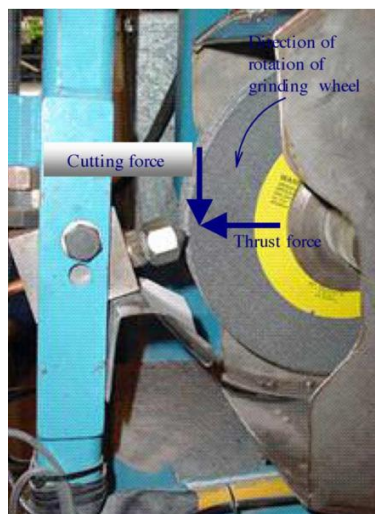


Figure 2. 22: Influence of the grain size on the edge roughness and on the wear rate [98].

Much research has been done on the evaluation of the wear properties of PCD composites, and it was indicated that because of the extreme wear resistance of the composites, standard wear testing procedure were not suitable [99], [100]. A good approach for cutting test of super-abrasive materials has been proposed in 2005; in the proposed set up a vitrified bonded alumina grinding wheel was used as workpiece [101]; during the cutting test (Figure 2. 23), two were the main forces considered between tool and workpiece: the cutting force and the normal force required to maintain the specific depth of cut; the effect of the latter is to accompanying fracturing and cracking wear mechanisms [102]–[105].



**Figure 2. 23: Set up of the wear test of superabrasive material on a vitrified bonded alumina grinding wheel workpiece [101].**

A cutting length up to 4000 m and a depth of cut of 0.3 mm were adopted to test the wear of WC and two different grain size PCD (respectively 13.6 and 15.1 micrometers grain size). In this study the wear was empirically evaluated measuring the weight loss of the workpiece and of the PCD inserts during the test. As well known, PCD is not thermally stable having a complex mix of phases and binder/hard phase bulk volume percentage variable depending on the specimen microstructural factors, for this reason the results of the wear test on PCD have indicated different wear behaviours [102]. This study indicated that two cuts of 75 m were enough to cause abrasive wear onto the insert. In particular, it has been proved that the PCD with finer grain size (13.6 micrometers) worn out quicker than the medium size one (15.1 micrometers). This behaviour has been

explained considering the major factors affecting cutting performance; in particular reaction forces on the tool, stress distribution in the tool and the workpiece, cutting speed and depth of cut, temperature at the tool (if test is performed in dry condition) and removal of swarf in the area in front of the diamond grain [102]. In relation to this, a model on the chip formation in cutting stone with diamond was previously proposed in 2003, and the schematic of the chip formation process is depicted in Figure 2. 24.

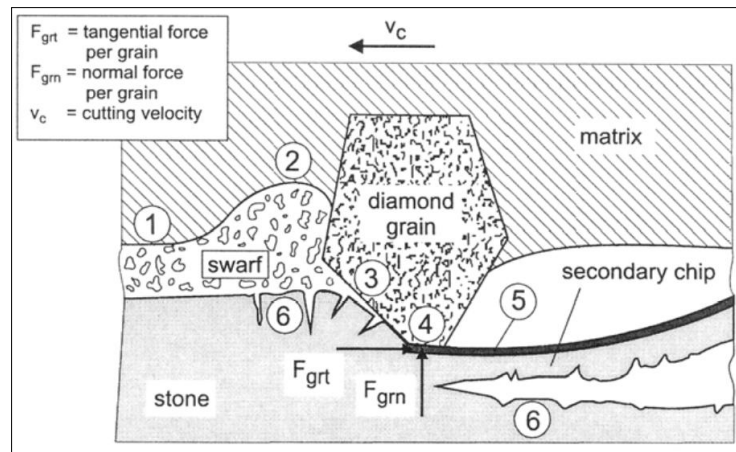


**Figure 2. 24: Schematic model of the chip formation process during the interaction of a single grain diamond and a stone workpiece [105].**

The model for chip formation allowed identifying the main aspects of the wear of diamond tools, indicating that micro-mechanisms are responsible for wear processes: while at the front of an individual diamond grain severe abrasive wear was found [102], [103], [105], less severe abrasive mechanisms occur on the flank/rake surfaces of the cutting element because the force is distributed along the flank surface [102]. Two are the main consequences of wear mechanisms in PCD inserts: either delamination of the PCD composite from its WC substrate (due to weak bonding), or premature abrasive wear with cracking due to defects in the synthesis process [102].

Regarding the reported literature on wear of PCBN tools, some researches have been conducted on the PCBN tool wear mechanisms and this lead to identify five wear mechanisms: abrasion, fatigue, adhesion, dissolution/diffusion and tribochemical processes [106], [107].

Polycrystalline cubic boron nitride (PCBN) has been used as cutting tool in hard turning of steel, producing smooth and uniform finished surfaces,

although deterioration of the tool surface is a commonly encountered problem due to the chip type formation [54]. An example of the performance of a low-CBN PCBN tool is depicted in Figure 2. 25. It has been demonstrated that low-CBN grades found application in continuous and semi-interrupted hard turning because of their reduced flank wear; high-CBN grades tend to resist more to the interrupted machining while wearing rapidly at higher cutting speeds [56]. The type of wear depends upon the continuity or interruption of the test and on the CBN percentage in the PCBN tool: abrasive wear has been found in continuous cutting conditions, while chipping was found as an addition to abrasion in the interrupted cutting [34], [40], [54].

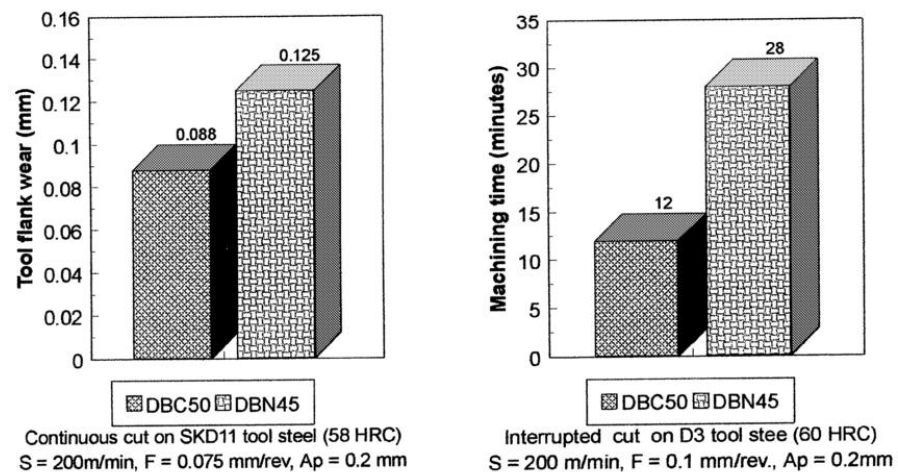


**Figure 2. 25: Performances of low-CBN PCBN grades in interrupted turning machining of steel [40].**

When considering the wear on a PCBN cutting insert, the combination of high temperature and stresses during testing gives a certain severity level of wear depending also on the geometry of the cutting tools, mechanical and thermal loading during testing. As a general guidance, researchers have identified flank and crater wear, chipping, nose wear and thermal shock cracks as frequent wear patterns in cutting insert made of PCBN [108].

While there is still a lack in fully understanding the wear progression mechanisms of composite ultra-hard materials, several researches have reported on the wear performances of electroplated diamond abrasive tools. Most of them have demonstrated a progressive increase in cutting

forces and a dulling of the abrasives mainly caused by attritious wear [38], [66], [67].

In spite of all the reported literature in the performances of both low and high-CBN grades in conventional machining, no study has been done in wear/cutting tests of these grades manufactured at a micro-scale and arranged in arrays, simulating grinding-type operations.

## **2.5 Gaps in the current PLA technology for PCD/PCBN in academic research and industry**

The literature review on PCD/PCBN composites included an extensive description of their thermo mechanical properties, their synthesis methods, their use in industry, and their processing techniques. In particular, it has been found that one of the main fields of application of PCD/PCBN materials is in cutting tool industry; therefore there is a need in optimising the wear performances of cutting tools in ultra-hard materials. Previous researches on single crystal diamond [4], [5] have extensively indicated that PLA is a suitable technique for micro-processing of ultra-hard materials offering the possibility to improve the wear properties of the cutting tool. Despite the information available on the characterisation of ablated single crystal diamond surfaces, no work has been done to evaluate the thermal response of ultra-hard polycrystalline structures (PCD/PCBN) to PLA; in particular, no work has been performed to optimise the wear performances of pulsed laser ablated tool in PCD/PCBN in relation to the microstructural factors of the composite (e.g. binder bulk volume percentage, binder type, ultra-hard grain size).

### ***Research challenge 1 (Refers to objectives i and iii in Section 1.3)***

While laser ablation has been widely employed for straight and profiled cutting of diamond [81] there have not been many studies for generating geometrically controlled micro-features on flat and curved diamond surfaces until recently [4]. The control of the cutting edge radius within a tolerance of few microns together with the high possibility of variation of

rake and clearance faces in micro cutting features on polycrystalline ultra-hard structures seems not to have been reported. Considering ultra-hard polycrystalline structures, an important research challenge is to achieve a high control of PLA laser parameters to enable the generation of desired micro-cutting edges with controlled cutting edge radius.

### ***Industrial/academic benefit 1***

In the case of abrasive tools, the typical cutting surfaces have a stochastic geometry and three-dimensional spatial distributions of the abrasives; as such, the performances of such abrasive tools are difficult to control; novel technologies to provide novel tools incorporating abrasive like features having desired geometry and high repeatability would offer technological advances. As such, using an abrasive tool with repeatable and homogeneous distributed micro-features/abrasives not only facilitates the accommodation of grinding debris and ingress of heat transfer but also achieves consistent performance improving the tool life [5], [92]. In particular, the high geometrical control of micrometric cutting edges in microstructurally different PCD/PCBN materials would enable the control of the wear properties of cutting tools and therefore allow the selection of the desired tool for the specific application.

### ***Research challenge 2 (Refers to objective ii in Section 1.3)***

Although previous researches have been focusing on the thermal response of single crystal diamond [92] and polycrystalline diamond [74], [109], there is still a lack in understanding the thermal response of PCD/PCBN composites to PLA; and the role of the binder in the laser ablation process needs to be investigated, especially its influence in the formation of the thermal affected zone. Though wide research was conducted on the formation of graphite for single crystal diamond, little attention has been given to the allotropic transformation occurring as a consequence of the thermal excitation in PCD/PCBN composites. There is a need in study the transformation occurring at the interface between the cBN/PCD granular interface and binder as a consequence of the thermal excitation. There is also a lack of understanding how a variation in laser energy density affects

the extent of the transformation from  $sp^3$  to  $sp^2$  bonding, if a formation of amorphous phase occurs and the effects on the binder phase in this thermal process.

***Industrial/academic benefit 2***

Proposing a technique for the evaluation of the thermal response of microstructurally different composite materials to PLA would be beneficial not only for industry but also for the academic environment. The possibility to relate the allotropic phase changes to the energetic laser parameter will provide industry to enable the control of phase changes in critical areas of the micro-tool; this in the future could take to a high control of allotropic phase change from graphite/hBN to diamond/cBN enabling to vary the softness/hardness of the tool in specific areas.

***Research challenge 3 (Refers to objectives iv and v in Section 1.3)***

In spite of all the reported literature in the performances of PCD macrometric inserts and low/high-CBN grades tools in conventional machining, no study has been done to evaluate the influence of microstructural factors in the wear behaviour of ultra-hard micrometric cutting edges.

***Industrial/academic benefit 3***

Proposing a general guidance for wear behaviour of PCD/PCBN in relation to their different microstructural properties, would be beneficial for industry to exploit the wear properties and therefore allow the selection of a specific PCD/PCBN grade for cutting edge applications.

# Chapter 3

## Materials and methodology

This is a key chapter for the understanding of the research. It aims at introducing the utilised materials and experimental procedures and research approaches which have been used throughout the development of this research activity in order to achieve the objectives proposed in Section 1.3. In particular, it includes: (i) a novel approach for the experimental optimisation of laser parameters in the generation of micro cutting edges on microstructurally different ultra-hard materials, (ii) a characterisation procedure for the evaluation of the thermal response of different ultra-hard structures to PLA, (iii) a combined procedure/design for laser controlled path geometries; (iv) a test approach for a novel evaluation of wear progression/performance of different micro-cutting geometries in relation to the microstructural factors of the composite (e.g. binder type, binder bulk volume percentage, ultra-hard phase grain size); (v) a procedure for the evaluation of the wear performances of the manufactured arrays against electroplated benchmarked.

### 3.1 Methodology background

As extensively demonstrated in Chapter 2, previous researches have focused on PLA of single crystal CVD diamond for controlled geometry tool manufacture [4], [5]. All of the techniques already recognised in the research for ultra-hard materials have been taken into account in the development of the correct approach for this research work. The already established technology of PLA for shaping difficult to cut materials has been adopted for processing of novel materials such as PCD/PCBN composites. In particular, the literature review described in Chapter 2 has demonstrated a lack in understanding the thermal response of polycrystalline ultra-hard materials to PLA, with particular attention to the influence of microstructural factors in the thermal excitation caused by

PLA. The understanding of thermal response and the effects of microstructural factors are really important when a high control of the tools geometry is needed to achieve a better understanding of wear-resistant properties for the use of PCD/PCBN structures in the cutting/grinding tool industry. Based on the research gaps deeply explained in Section 1.3, Figure 3. 1 reports the different approaches/methodologies adopted for each section of this chapter.

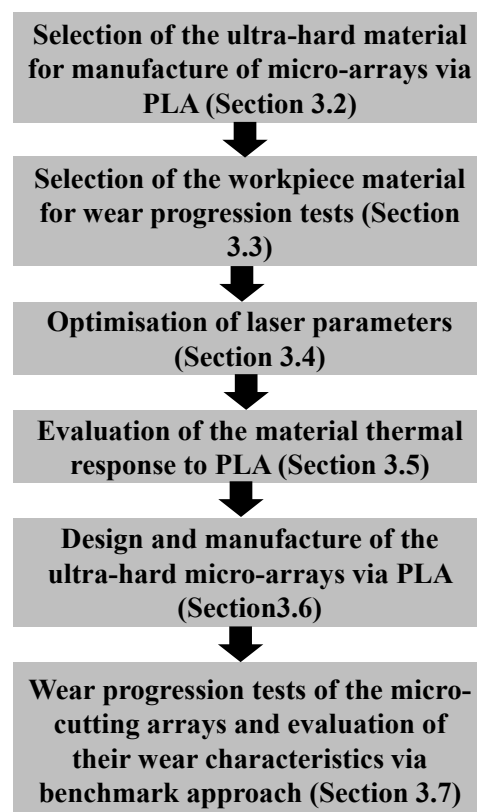


**Figure 3. 1: Chart diagram showing the methodology used in this research work.**

## **3.2 Selection of the ultra-hard materials for the generation of the arrays**

Micro structurally different ultra-hard materials have been selected to accomplish the objectives of this research. In particular, all of the materials chosen for the PLA present differences related to the type of binder (e.g. ceramic, metallic), binder bulk volume percentage (e.g. low, medium, high

content), type of ultra-hard phase (e.g. diamond, cubic boron nitride) and hard constituent grain size (e.g. fine, coarse, mixed). The extensive literature review carried out in Chapter 2 demonstrated a lack in correlating the micro structural factors of ultra-hard materials with their thermal response to PLA; furthermore, a need for evaluating the wear progression of these composites as a function of their micro structural properties is essential when the achievement of a cutting tool with good wear resistance is required. For this reason, the selection of the right material has been carefully carried out. Figure 3. 2 represents a flowchart showing different types of selected materials, which mainly differ for the type of hard-phase (diamond, CBN) or the type of binder and its bulk volume percentage. Only polycrystalline structures (PCD/PCBN) have been chosen because one of the main objectives of this research is the understanding of the role of the binder in the thermal response of polycrystalline matrices as well as in the wear progression characteristics.

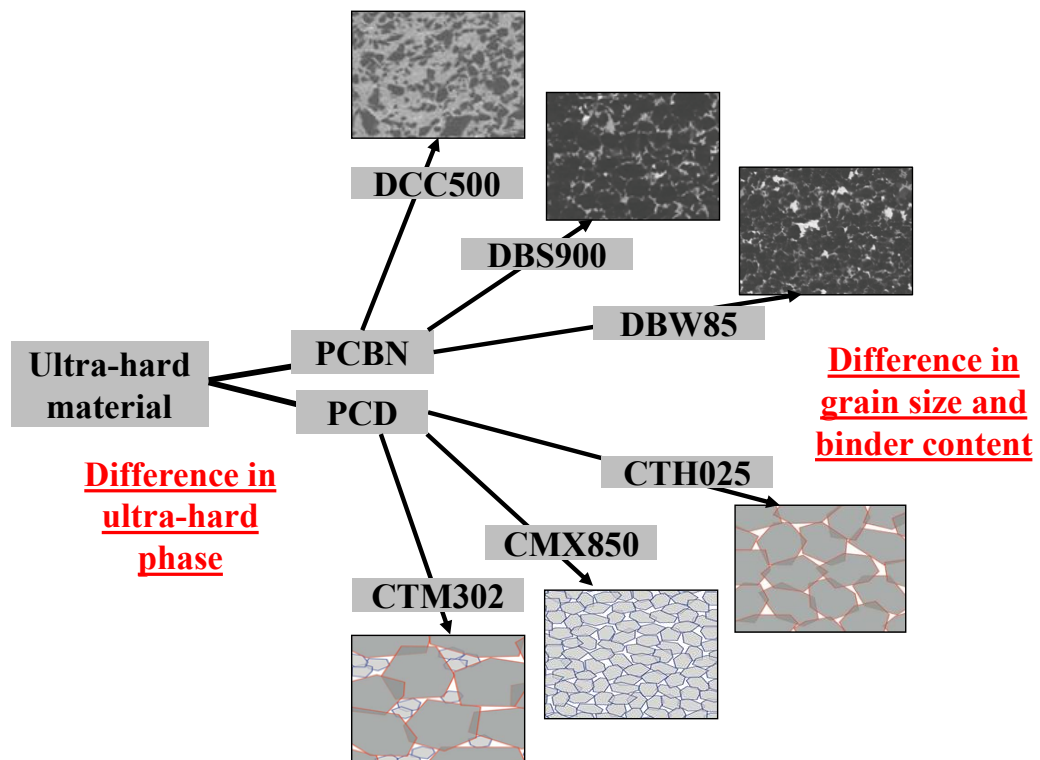


**Figure 3. 2: Flow chart of the ultra-hard materials selected for the experiments.**

PCD thick films (0.5 mm) directly synthesized on a WC substrate (10 mm x 10 mm x 1 mm) have been chosen for the PLA creation of the micro-abrasive arrays (all of the materials selected for the experiments were

provided from Element 6); these are shown in Table 3. 1 where it is evident that in the case of PCD structures the binder type remains the same but the binder bulk volume changes making different materials suitable for different applications. The reason for selecting different binder bulk volume percentage composites and consequently different diamond grain size materials aims at showing the relation between the microstructural factors typical of each material and their wear progression characteristics.

Regarding the PCBN structures, three grades PCBN thick films (0.7 mm) directly synthesized on a WC substrate (10 mm x 10 mm x 1 mm) have been utilized as shown in Table 3. 1. The reason of selection of different grades resides in the already well-established properties of each grade in regard to specific application. DBW85 has been proven to be one of the most versatile high-CBN grades because of its excellent strength and abrasion resistance resulting in high chipping resistance that makes it used in heavily interrupted cutting of a wide range of hard materials. DBS900 with an increase up to 90% of CBN content, is ideal for applications where a long tool life is required [56].

**Table 3. 1: Materials utilised in the experiments and their microstructural properties.**

<b>Material denomination</b>	<b>Binder type</b>	<b>Binder bulk volume (%)</b>	<b>Hard phase grain size (<math>\mu\text{m}</math>)</b>
PCD CTM302	Co	10	2-30
PCD CMX850	Co	15	0.5-1
PCD CTH025	Co	8	20-25
PCBN DBW85	AlWCoB	15	1-3
PCBN DBS900	CoNi	10	2-4
PCBN DCC500	TiC	50	1-2

### **3.3 Selection of workpiece material for the wear tests**

Silicon dioxide ( $\text{SiO}_2$ ) composite material has been selected as workpiece material for the evaluation of the wear progression of PCD/PCBN micro-arrays during the simulated wear/cutting tests. The reason of selection of

this material resides in its properties, which are indicated in Table 3. 2. In particular the choice has been done in consideration of the following:

- Its very low thermal conductivity [110] makes it perfect for machining applications where the cutting condition of low thermally conductive materials (e.g. ceramics) can be replicated and enhanced [62].
- When used against cubic boron nitride tools the silicon dioxide is considered a difficult to machine material [61] offering the possibility of accelerated wear test. In fact, SiO<sub>2</sub> high hardness [111] may reduce the wear progression rate of the tested PCD abrasive arrays but enhance the wear failure of PCBN and therefore providing a tool for comparison and discussion between the two materials [59].
- Because of its lower fracture toughness it exhibits brittle machining behaviour [112], endorsing the possibility of causing materials with higher fracture toughness to fracture in a ductile way: this means that there would be a possibility to see the PCD/PCBN composites to deform elastically/plastically without cracking (depending on the specific binder properties of the composite).
- Although different wear progression rates are expected from the wear tests of PCD and PCBN against silicon dioxide, the same workpiece material has been chosen in order to allow the possibility of comparison of the wear characteristics not only of the PCD/PCBN against their respective benchmarked electroplated, but also of the manufactured PCD arrays against the PCBN ones. In fact, the growth of PCBN tools in the market and their lower cost (see trends in Section 1.1) are enhancing the use of PCBN (replacing PCD) where possible, thus it is important to prove the better wear performance of PCBN tools not only versus the benchmarked sample (e.g. electroplated diamond and CBN), but also against the hardest PCD composite.

**Table 3. 2: Thermo/mechanical properties of SiO<sub>2</sub>, bulk [110], [111].**

Mechanical properties	Value
Hardness (GPa)	35.4
Fracture toughness(MPa (m) <sup>1/2</sup> )	0.77
Thermal conductivity (W/m/K)	1.04-2.51 (depending on temperature)

### 3.4 Pulsed laser ablation of PCD/PCBN structures

As demonstrated in previous research conducted on CVD diamond [5]-[4], it is feasible to use a laser for the shaping of ultra-hard materials. As such, PLA proved its use for surface processing of hard metals and ceramics [5], [84], [113]. In this research work, a laser setup approach was established, using PCD/PCBN described in section 3.2 as platform materials, for the generation of single spot ablated geometry (single crater), multipass ablated geometry (continuous groove) and as a consequence of the optimization process, abrasive micro-arrays. To enable the ablation process to take place, a laser equipment (DMG LASERTEC 60 HSC Q-switched Nd: YAG; wavelength, 1064 nm; max. output power, 100 W; max. pulse frequency, 50kHz; focal point size, Ø 40mm) mounted on linear stages (to allow the motion in 3-axis) has been used. Several experiments have been set up in order to establish the correlation between laser energetic parameters and material extent of ablation/microstructural factors of the materials. In particular, specific set of experiments (repeated five times to check the repeatability) have been performed to allow the identification of extent of ablation and the surface integrity characteristics of microstructurally different materials and to enable the manufacture of PCD/PCBN micro abrasive/cutting arrays. In all the experimental procedures, the influence of laser parameters on the composites has been taken into consideration, thus it was important to identify two main affecting laser parameter categories: (i) energetic parameters such as average laser power ( $P_m$  [W]) and pulse duration ( $\tau$  [ $\mu$ s]); (ii) kinematic parameters such as laser beam frequency ( $f$  [kHz]) and feed speed ( $v$  [mm.s<sup>-1</sup>]). Sections 3.4.1, 3.4.2 and 3.4.3 present the details of the set-up of the experiments.

Because of the various number of laser parameters affecting the ablation process, a DOE (design of experiment) combining a Taguchi design and a full factorial one has been used initially for the evaluation of the optimum laser parameters for each material. The combination of all of the experimental procedures utilized in this research allowed establishing a novel procedure for the optimization of laser ablation parameters for ultra-hard materials; the methodology is shown in Figure 3. 3.

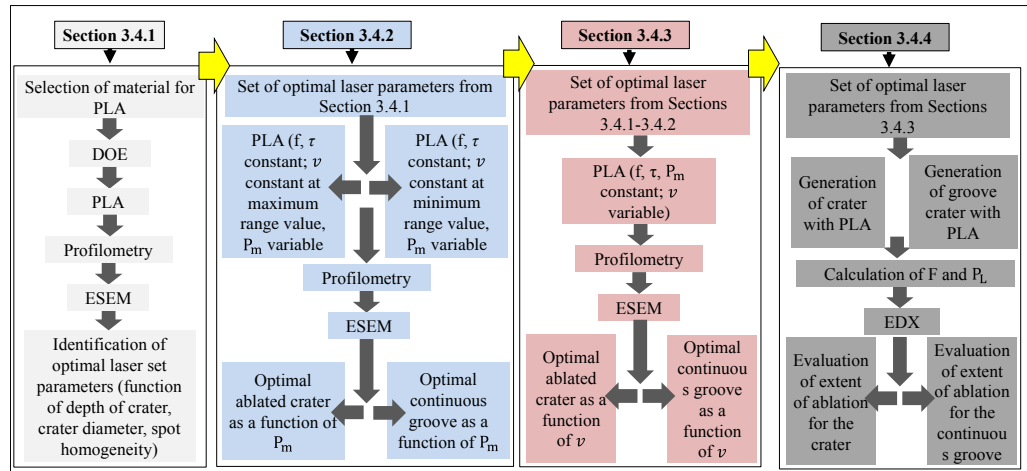


**Figure 3. 3: A schematic explaining the novel procedure of optimisation of laser parameters.**

### 3.4.1 DOE

Because the pulsed laser ablation technique has been previously used on CVD single crystal diamond [4] but never been utilized on the materials selected in this research (see Section 3.2), an initial evaluation of the effect of laser parameters was necessary.

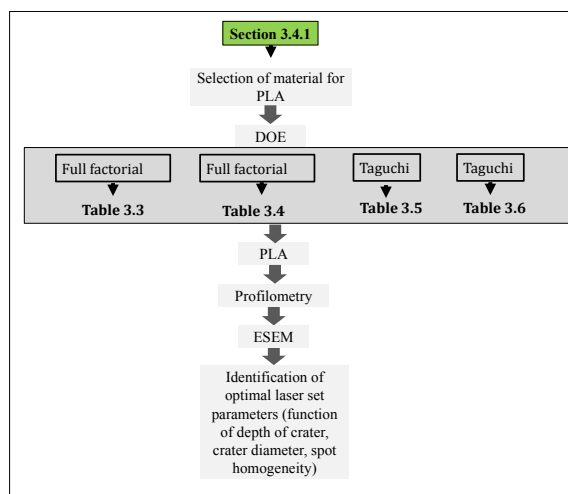


**Figure 3. 4: Flowchart indicating details of design of experiment and reference to the tables (with laser parameters) utilised for each DOE.**

A design of experiments has been used, allowing the identification of possible thermal effects deriving from the combination of more than one variable. In the design of experiments the number of runs depends on the variables involved. The procedure followed for the evaluation of the combination of optimal laser parameters consisted in the use of four statistical design of experiments (Figure 3. 4): 2 set of full factorial design with respectively 3 factors/4 levels and 2 factors/3 levels and 2 set of Taguchi design with respectively 4 factors/3 levels and 3 factors/3 levels. Table 3. 3 includes all of the values which have been employed for the full factorial and the Taguchi design.

**Table 3. 3: Example of the full factorial design with 3 factors, 4 levels, 27 runs.**

$P_m$ [W]	$f$ [kHz]	$v$ [mm.s <sup>-1</sup> ]	$\tau$ [us]
70	30	500	15
100	50	500	15
70	10	100	15
70	30	100	15
50	10	300	15
50	10	100	15
100	30	500	15
90	30	100	15
90	50	100	15
50	50	100	15
50	30	500	15
70	50	300	15
70	50	500	15
50	30	300	15
90	10	100	15
50	50	300	15
70	50	100	15
50	10	500	15
90	30	300	15
70	10	300	15
50	30	100	15
90	10	300	15
70	30	300	15
50	50	500	15
90	10	500	15
70	10	500	15
90	30	300	15

**Table 3. 4: Example of the full factorial design with 2 factors, 3 levels and 9 runs.**

$P_m$ [W]	$f$ [kHz]	$v$ [mm.s <sup>-1</sup> ]	$\tau$ [us]
60	15	800	30
60	5	800	30
90	5	800	30
60	10	800	30
30	15	800	30
30	10	800	30
30	5	800	30
90	15	800	30

**Table 3. 5: Example of the Taguchi design with 4 factors, 3 levels and 9 runs.**

$P_m$ [W]	f [kHz]	v [mm.s <sup>-1</sup> ]	$\tau$ [us]
30	10	100	5
30	30	300	10
30	50	500	15
60	10	500	10
60	30	100	15
60	50	300	5
90	10	300	15
90	30	500	5
90	50	100	10

**Table 3. 6: Example of the Taguchi design with 3 factors, 3 levels, 9 runs.**

$P_m$ [W]	f [kHz]	v [mm.s <sup>-1</sup> ]	$\tau$ [us]
30	10	100	10
30	30	300	10
30	50	500	10
60	10	300	10
60	30	500	10
60	50	100	10
90	10	500	10
90	30	100	10
90	50	300	10

After the laser ablated craters and continuous grooves have been produced by PLA using the parameters indicated in Tables 3. 5, 3. 6, the topography of the ablated surfaces has been evaluated via a Talysurf CSI 1000 contact autofocus profilometer and the surface integrity has been studied via a Philips XL30 Environmental Scanning Electron Microscope (ESEM). The use of a design of experiment represented only a preliminary experimental step to allow the identification of the parameters which really affect the thermal response of the material to PLA.

### ***3.4.2 Laser energy parameters***

PLA is a thermal process, which involves material phase (solid/liquid/gaseous) changes within a very short time interval (pulse duration of the order of microsecond) with a minimum thermal affected

zone, PLA requires a minimum laser energy density threshold depending on the thermal/optical properties of the target material [74], [76].

Thus, it is important to evaluate the influence that a variation of energetic parameters has not only in terms of extent of ablation but also in regards to the surface integrity especially due to the microstructural characteristics of the ablated material. As identified by previous researches [25], [76], [114], an important laser parameter that affects the thermal response of the material is the energy of a single pulse. A first experiment included the variation of  $P_m$  in the range 50-100W, as indicated in Table 3. 7: the selection of  $v = 500\text{mm.s}^{-1}$  and  $f = 10 \text{ kHz}$  using a small aperture mode for the laser beam, allowed the generation of rows of individual craters (e.g. centre separation of  $50 \mu\text{m}$ ).

Optical examination of the ablated craters over a fixed number of assessment of repeatability have been conducted in order to identify the suitable energetic parameters to reduce surface integrity anomalies (e.g. crater inhomogeneity, elongated craters) and to promote geometrically homogeneous craters avoiding double pulses.

**Table 3. 7: Variation of  $P_m$  for constant values of  $f$ ,  $v$  and  $\tau$ .**

$P_m$ [W]	$f$ [kHz]	$v$ [mm.s <sup>-1</sup> ]	$\tau$ [us]	%Overlap
50	10	500	20	0%
60	10	500	20	0%
70	10	500	20	0%
80	10	500	20	0%
90	10	500	20	0%
100	10	500	20	0%

**Table 3. 8: Variation of  $P_m$  for constant values of  $f$ ,  $v$  and  $\tau$  (cfr. Table 3. 3).**

$P_m$ [W]	$f$ [kHz]	$v$ [mm.s <sup>-1</sup> ]	$\tau$ [us]	%Overlap	A. Mode
50	10	100	20	99%	Small
60	10	100	20	99%	Small
70	10	100	20	99%	Small
80	10	100	20	99%	Small
90	10	100	20	99%	Small
100	10	100	20	99%	Small

The contact autofocus profilometer previously mentioned was used for topographical measurements of the extent of ablation (depth of the crater, diameter of the crater, volume of ablation) and the captured data was consequently interpreted. A Philips XL30 Environmental Scanning Electron Microscope (ESEM) was used for the microscopical evaluation of the surface integrity as a function of the variation of  $P_m$ .

This procedure allowed the identification of the optimal  $P_m$  for each material. A chemical composition analysis for the variation of extent of ablation has been conducted in relation to the crater depth and crater diameter by using an INCA EDX system (EDX OXFORD-Inca energy software). This also allowed the identification of the extent of ablation as a function of the energetic parameters and to prepare the specimen for nanometric analysis as reported in Section 3.5.1.

### ***3.4.3 Laser kinematic parameters***

Section 3.4.2 reported about the variation of laser average power for the ablation of single craters with a centre separation of  $50\mu\text{m}$ . In order to evaluate the influence of variation of  $v$  onto the surface topography and surface integrity, an experiment has been performed: a decremented decrease of  $v$  from  $500\text{ mm.s}^{-1}$  to  $100\text{ mm.s}^{-1}$  allowed as well an increased theoretical overlap in the range 0-99%, as shown in Table 3. 9.

**Table 3. 9: Variation of beam speed in the experiment.**

$P_m$ [W]	f [kHz]	$v$ [mm.s <sup>-1</sup> ]	$\tau$ [us]	%Overlap th.	A. Mode
70	10	500	20	0%	Small
70	10	400	20	66%	Small
70	10	300	20	77%	Small
70	10	200	20	90%	Small
70	10	100	20	99%	Small

A schematic of the ablated surfaces as a function of the beam speed variation is shown in Figure 3. 5:  $h$  is an indication of the centre separation and it obviously decreases with the reduction of  $v$ . A  $v$  of  $500\text{ mm.s}^{-1}$  was chosen to achieve a single spot ablation as described in Section 3.4.1; a  $v$  of  $100\text{ mm.s}^{-1}$  was chosen to reduce the distance between single spot ( $h$  [ $\mu\text{m}$ ]) from  $50\ \mu\text{m}$  to  $10\ \mu\text{m}$  and to achieve a continuous groove (ablated

trench). The contact autofocus profilometer (described in Section 3.4.1) was used for topographical measurements of the ablated areas after the ablation test and the ESEM equipment (described in 3.4.1) was used for the microscopical evaluation of the surface integrity as a function of the variation of  $v$  and for the identification of the optimal kinematic parameters for the laser ablation process.

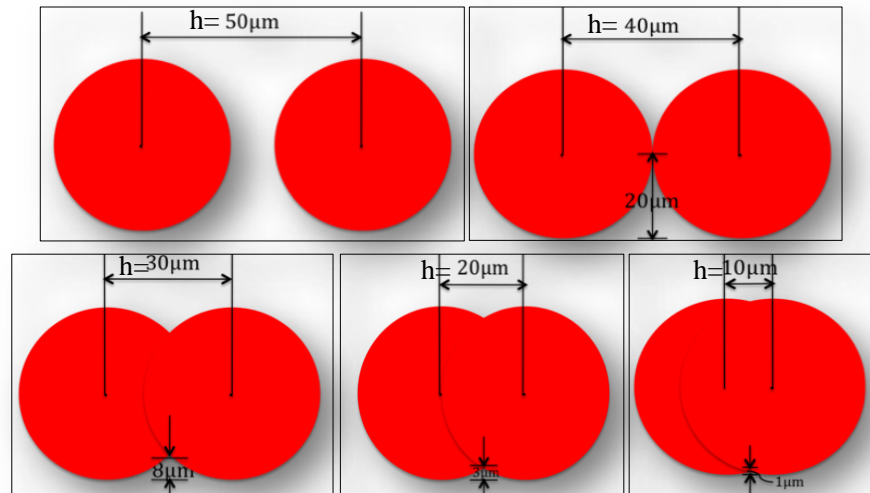


**Figure 3. 5: Schematic representation of the procedure used to produce laser ablated grooves starting from single craters, showing the distance between single spots at different feed speeds:  $v=500\text{mms}^{-1}$  ( $h=50\ \mu\text{m}$ ),  $v=400\text{mms}^{-1}$  ( $h=40\ \mu\text{m}$ ),  $v=300\text{mms}^{-1}$  ( $h=30\ \mu\text{m}$ ),  $v=200\text{mms}^{-1}$  ( $h=20\ \mu\text{m}$ ),  $v=100\text{mms}^{-1}$  ( $h=10\ \mu\text{m}$ ) [74].**

The reported experiment aimed at optimising the kinematic laser operating parameters and enabling the control of the depth of the micro continuous grooves and sharpness of the cutting edges.

### ***3.4.4 Identification of extent of ablation in the elemental composition of different composites***

This Section (Figure 3. 3) is propaedeutic to the procedure for nanometric analysis explained in Section 3.5.1. A methodology for the evaluation of the elemental composition of the composites and their relation to the PLA parameters is proposed here. Initially single ablated craters and continuous grooves were produced onto microstructurally different composites as reported in Sections 3.4.2-3.4.3, preparing the specimens for the experiment. This was aimed at analyzing the chemical composition

of the ablated surfaces at various positions across the spot/trench, characterized by different laser energy densities/fluencies and to evaluate their influence on the local binder bulk volume percentage. Prior EDX analysis, energetic parameters such as laser fluence ( $F$  in  $\text{Jcm}^{-2}$ ) and laser power density ( $P_L$  in  $\text{Wcm}^{-2}$ ) per pulse were calculated using Eq. 1 and 2 [115], [116].

$$F_i = \frac{4P_m}{\pi d_i^2 f} \quad i = 1,2..5 \quad (\text{Eq. 1})$$

$$P_{L_i} = \frac{4P_m}{\pi \tau d_i^2 f} \quad i = 1,2..5 \quad (\text{Eq. 2})$$

Where  $d_i$  [cm] is the radial position on the beam spot diameter which is varying from position 1 to 5 as represented in Figure 3. 6.

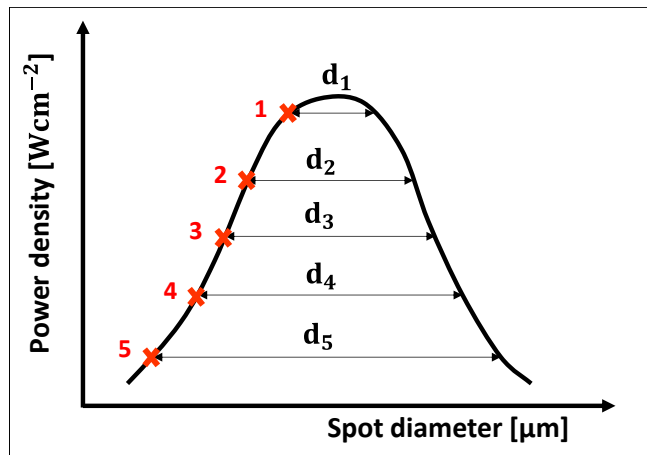


**Figure 3. 6: Schematic representation on a Gaussian of the spot diameter versus the power density; numbers 1 to 5 indicate the areas of EDX analysis corresponding to different radial positions  $d_i$ .**

It is well reported [117] that for a single pulse laser ablation, the laser power density is highest in the centre of the spot, i.e. where the ablation depth is the highest and correspondingly lower towards the sides of the spot (Figure 3. 6).

Then an INCA EDX system (EDX OXFORD-Inca energy software) was employed for the compositional analysis of single pulsed ablated craters and continuous grooves along specific transversal and longitudinal directions shown from the red arrows in Figure 3. 7.

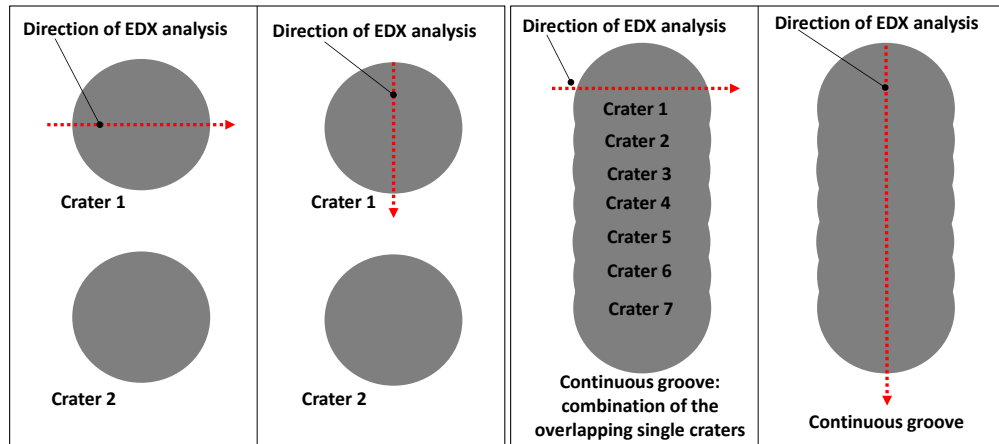


**Figure 3. 7: A schematic of the direction selected for chemical analysis onto different composites.**

This experiment was particularly important to evaluate the extent of ablation in the transversal and longitudinal direction of ablated crater/groove in order to prepare the ablated specimen for the HRTEM analysis which is reported in Section 3.5.1.

### **3.5 Procedure for the evaluation of the thermal response of PCD/PCBN structures to PLA**

PLA produces a massive thermal exposure of the ablated material that causes chemical phase changes in the constituents of the matrix. In ultra-hard structures such as PCD and PCBN, this means that the diamond/cBN occur in the allotropic transformation into graphite/hBN, producing an unfavourable condition in its use as cutting tool because the graphite and hBN soften the surface where the transformation occurs [118]. Previous researches have proposed approaches for the evaluation of the extent of allotropic transformation in a single crystal diamond material [92], [93].

By using some of the concepts proposed in a work on CVD single crystal diamond [92], the study in this section proposes a novel technique for the evaluation of the thermal response of PCD/PCBN composites.

The procedure here proposed has been set up to allow the identification of the thermal response of ultra-hard composite materials PCD/PCBN at sub-atomic level by:

- Identification of the extent of allotropic transformation (e.g. diamond to graphite, cBN to hBN) and the relationship with the laser pulsed energy density (e.g. low energy, high energy).
- Identification of the transition phases (e.g. Co, diamond, graphite, TiC, cBN, hBN) and the interfaces between Co/diamond and TiC/cBN using HRTEM/EELS.
- Evaluation of the undisturbed interface Co/diamond and TiC/cBN and underlying substructure outside the range of high level energy density.

### ***3.5.1 Preliminary procedure for the evaluation of the thermally affected site***

Prior to explaining the set up procedure utilized for the evaluation of the thermal response of the materials to PLA, it is important to understand in which context this experiment has been done and the reasons why. In section 3.4 the methodology used showed that there is a correlation between energetic parameters (in particular energy density) and the microstructural factors of the ablated materials. In particular, the necessity of varying the energetic parameters resides in the different thermal excitation onto the ablated materials. Furthermore, the presence of binder of different chemical composition (see Section 3.2) affects the ablation process and the thermal response, thus it is important to study if there is any influence at the interface binder/hard grain caused by the energy density variation. An understanding of the thermal response of the binder/ultra-hard phase it is necessary at atomic level in order to understand the thermal process of ablation at microscopic level.

Part of the procedures reported in Section 3.4.3 has been used in order to prepare the materials for the nanometric analysis here proposed. In particular, a preliminary experimental procedure has been adopted for the preparation of the samples; this was composed of the following:

1. *Selection of the material for the high resolution transmission electron microscopy (HRTEM) analysis at an atomic level:* in the choice of

materials, particularly important is the need in capturing the interface ultra-hard phase/binder; this led to the selection of fine grain size materials both in the case of PCD and in the case of PCBN. In fact a coarse grain size material (Figure 3. 2 and Table 3.1) would not have allowed the identification of the region of interest (interface grain/binder) due to the lower binder bulk volume percentage (and the big ultra-hard grains). Following these reasons, a fine grain specimen CMX850 (Table 3. 1), shown in Figure 3. 8a, has been selected for the evaluation of the thermal response of PCD composites; a low-CBN content DCC500 specimen (Table 3. 1), shown in Figure 3. 8b, has been chosen as a suitable specimen for the PCBN composites. The latter has been selected also because its low-binder content makes it a difficult material to be ablated without thermal effects (see Section 4).

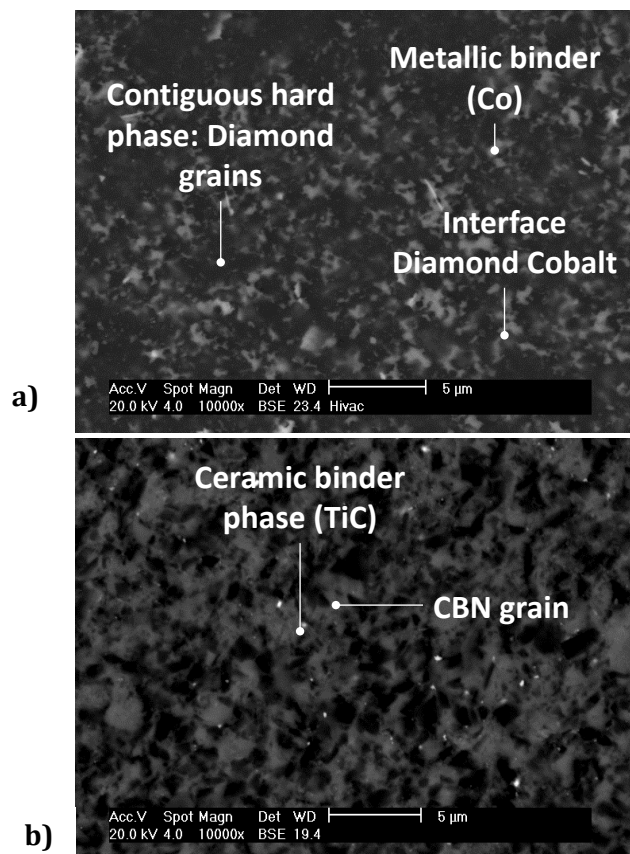


**Figure 3. 8: Backscatter ESEM imaging of a polished surface of the selected ultra-hard materials for evaluation of thermal response to PLA: a) PCD CMX850 fine grain diamond with Cobalt as a binder; b) PCBN DCC500 fine grain PCBN showing the CBN grain in the black areas and the ceramic binder in the grey areas.**

2. Selection of the site of interest of the specific material for the extraction of the lamella via FIB: a relation between energetic parameters and extent of ablation has been explained in Section 3.4.4. The chemical compositional methodology explained in Section 3.4.4 allowed the identification of the site of interest in the area where there was a variation in extent of ablation. This area corresponds to the direction perpendicular to the motion of the laser beam, thus along the cross section of the ablated crater/groove depicted by red line in Figure 3. 9. An additional X-Ray spectroscopy technique (Siemens D500 diffractometer) was used for the characterization of the crystal structure and chemical composition of the selected composites prior the FIB/HRTEM technique.

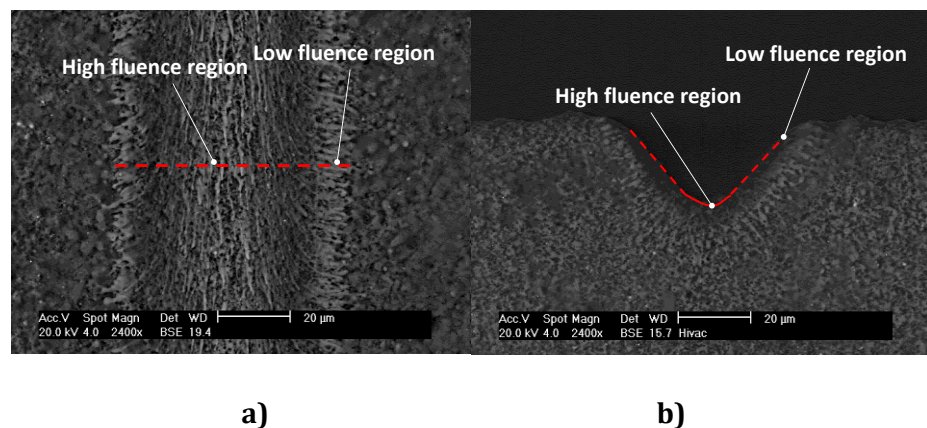


**Figure 3. 9: ESEM backscatter images of the laser ablated continuous groove in the fine grain PCBN specimen: a) top view of the ablated groove showing the high/low fluence areas; b) cross section view showing the corresponding high/low regions in the ablated material.**

### ***3.5.2 Approach for the analysis of the thermal response of microstructurally different PCD/PCBN composites***

Since from the preliminary investigations (whose methodology is reported in Section 3.4.4) it was apparent that the extent of binder was constant along the groove but varied significantly across the section (Figure 3. 9) in all of the materials, the latter provided the direction of interest for FIB extraction and HRTEM evaluation. In this experimental work a groove

generated by using single overlapping pulses provided an opportunity to examine the ablative effects on the PCD/PCBN from both the centre and sides of the pulses. In particular, a combined technique FIB/HRTEM has been used for the extraction of the lamellas from the ablated specimens and the analysis at atomic level. Some steps developed in a previous work on CVD single crystal diamond [92] have been used but the main difficulty in this work was represented by the materials under study: the increased fragility in the extracted thin sections (lamella) both of the fine grain PCD specimen and of the PCBN high binder ceramic content required special attention in the protection of the selected areas. This is a very important step when the stabilisation of the lamellas is required to avoid loss/damage through delamination of the ablated regions during the Focused Ion Beam (FIB) milling and extraction activities [109]. Before establishing the reported procedure in this research, many trials were undertaken to prepare the two lamellas (PCD/PCBN) in the selected sites of the ablated groove which would allow subsequent high-resolution Transmission Electron Microscopy/Electron Energy Loss Spectroscopy (EELS) analyses of the PCD/PCBN exposed to both the high and lower laser fluencies level [109].

The procedure established to successfully carry out the protection/stabilisation of the lamellas (both in PCD and PCBN specimens), FIB milling and extraction of the lamellas from the PCD/PCBN material structures is as follows [109]:

1. In order to stabilise the overall specimen surface prior the FIB milling, the application of multiple coatings was necessary (Figure 3. 10): initially a commercial sputter coater (Quorum technology SC7640) was used to deposit a 50 nm Platinum layer onto the overall specimen in order to reduce the amorphisation of the region of interest by the Gallium ion beam during FIB milling and to prepare the surface for further coatings. Then, a 30 nm layer of Carbon was deposited globally to avoid the charging of the specimen material during electron imaging and ion beam milling activities. A combined scanning electron microscope/Gallium

focused ion beam mill (FEI Quanta 200 3D FIB-SEM) incorporating a Tungsten Precursor Gas Injection System (GIS) has been used for a ion-beam deposition of a Tungsten layer in the selected area of extraction (red area in Figure 3. 10); the Tungsten was deposited in two steps: a 1  $\mu\text{m}$  thin layer deposition applied at a current of 0.5 nA, and a 3  $\mu\text{m}$  thick layer applied at a current of 5 nA.

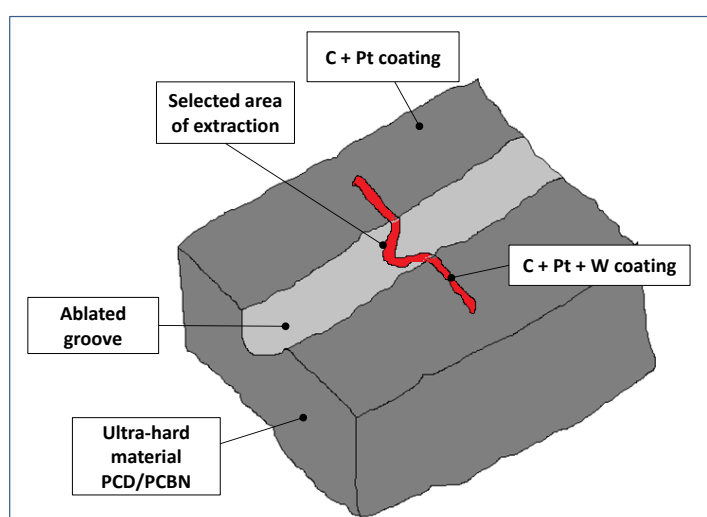
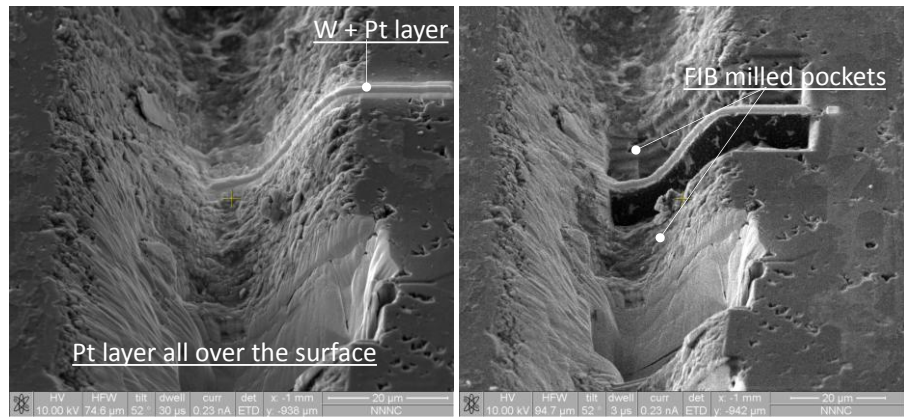


**Figure 3. 10: A schematic of the surface coating application on a continuous groove ablated composite.**

2. The second step involved the most delicate part of the entire experiment: the FIB milling across the ablated groove in the selected site (Figure 3. 11b). Initially the lamellas (both in PCD and in PCBN) were thinned to 3  $\mu\text{m}$  with a Gallium ion beam energy of 30 kV and a current of 5 nA. Then the thickness of the PCD lamella was reduced to 1  $\mu\text{m}$  (width) and then to approximately 300 nm (width) by reducing the ion beam current progressively down to 0.5 nA. The PCBN lamella was thinned till 200 nm to allow the atomic substructure to be capture in HRTEM and to reduce the risk of material amorphisation.

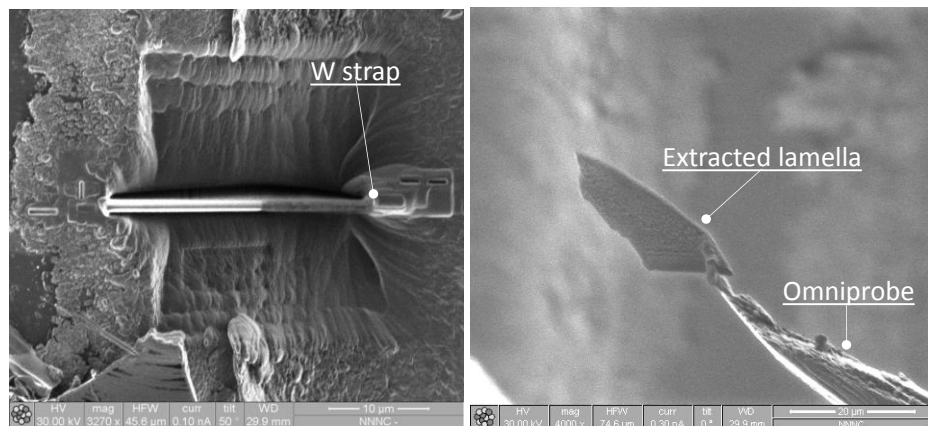


a)

b)

**Figure 3. 11: ESEM images of the FIB procedure for lamellas preparation and extraction: a) multiple coating b) milling [109].**

- The novel part of this procedure, which makes the difference with the previous research conducted on CVD single crystal diamond [92] resides in a special Tungsten strapping technique (Figure 3. 12a) which has been used to enable both the stabilisation of the extracted lamellas (PCD/PCBN) and make therefore possible the connection of them to the support grid. This consisted of a deposition of a Tungsten layer via a gas injection system (GIS) ensuring that the strap completely crosses the graphite/hBN layer, producing a connection between the W layer and the PCD/PCBN substructure of the lamellas [109].



a)

b)

**Figure 3. 12: ESEM images of the FIB procedure for lamellas preparation and extraction: a) Tungsten strapping technique in top view b) lift-out of a lamella [109].**

4. Consequently to the application of the Tungsten strap, the FIB miller was used to separate the lamella from the specimen and another Tungsten welding in four points was made between the lamella and the Omniprobe nanomanipulator (model 100.7) to allow the lift out (Figure 3. 13b) and the transfer to a Copper transportation grid (Figure 3. 13a).
5. In order to allow the atomic level imaging of the extracted lamellas, a final thinning was necessary. This thinning involved only the two areas of interest respectively with high/low laser energy density to approximately 100-150nm thickness (Figure 3. 13b) using a current of 0.10 nA [109].

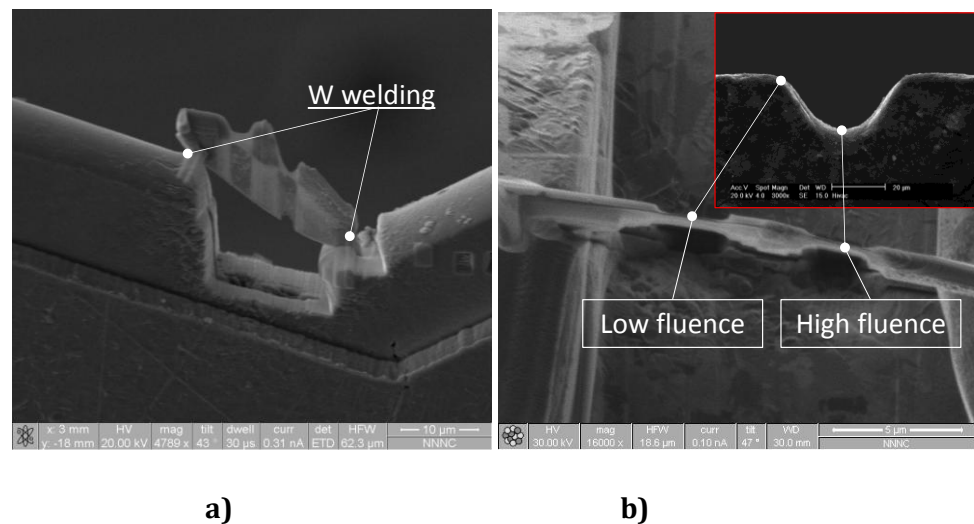


**Figure 3. 13: SEM images of the FIB procedure for lamellas preparation and extraction: a) lamella mounting onto a support grid; b) FIB rastering of the sites of interest corresponding to the sectional locations of the ablated groove [109].**

### 3.6 Generation of orderly micro-abrasive arrays in PCD/PCBN structures

The PLA parameters optimisation process (Section 3.4) and the study of the thermal response of different materials to PLA (Section 3.5) were propaedeutic to the most important generation of micro-abrasive features in the selected materials via PLA technology. This paragraph aims at

explaining the utilised methodology to approach the design and generation of selected geometries onto micro structurally different materials. Many have been the reiteration phases in this process, mainly due to the difficulty in prediction of the PLA results when different laser paths are input in the software. For this reason, Section 3.6.1 shows how this prediction was approached in term of direction of ablation, border cut selection and tilting of the sample to be ablated. Section 3.6.2 explains the process of design for the final achievement of the micro-abrasive arrays. Figure 3. 14 shows a flowchart containing the methodology adopted for the manufacture of the micro-abrasive arrays via PLA technique.

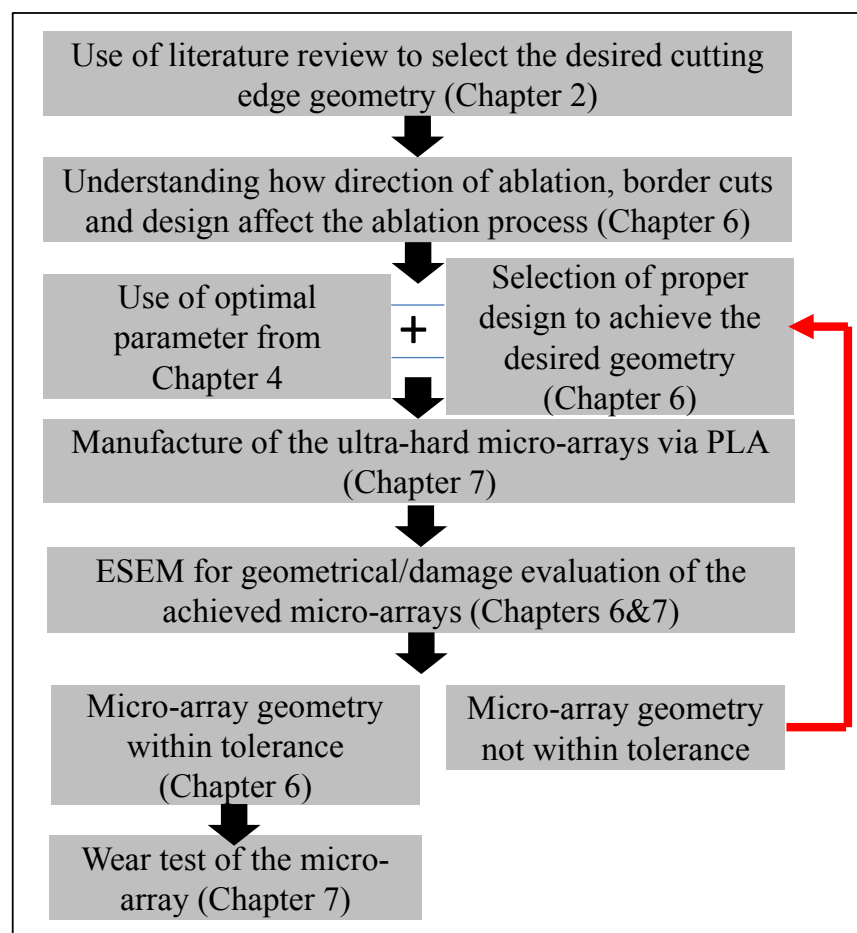


**Figure 3. 14: Flowchart of the process for the manufacture of the orderly micro-abrasive cutting arrays via PLA.**

### ***3.6.1 Influence of the laser path parameters in the design of abrasive geometries***

As shown in the flowchart in Figure 3. 14, the methodology used in this experiment involved an extensive literature review regarding the

clearance/rake angles in abrasive/cutting elements (see Section 2). This is aimed at understanding which cutting edge geometry could have been advantageous in order to study the influence of microstructural factors in the wear tests of different composite materials. Previous work on single CVD crystal diamond already proved the advantages of a tool (in single crystal diamond) whose surface would be composed of many orderly abrasive surfaces [4].

After an extensive literature review (see Section 2.2.1) a cutting edge geometry (insert in Figure 3. 15) with a positive rake angle of  $10^\circ$  (tolerance  $\pm 4^\circ$ ) clearance angle of  $30^\circ$  (tolerance  $\pm 4^\circ$ ) was selected for the following reasons:

- Although negative rake angles are generally preferred to reinforce the abrasive edges, positive rake angles decrease both the amount of cutting forces and the vibration occurring during the wear/cutting test, facilitating the chip flow [19], enabling the wear progression analysis as a function of the microstructural factors of the composite.
- Previous work on single crystal diamond abrasive arrays [4], [5] focussed on the production of staggered pattern of cutting elements but the sharpness of the desired abrasive edges represent (Figure 3. 15) an important novelty of this research work.

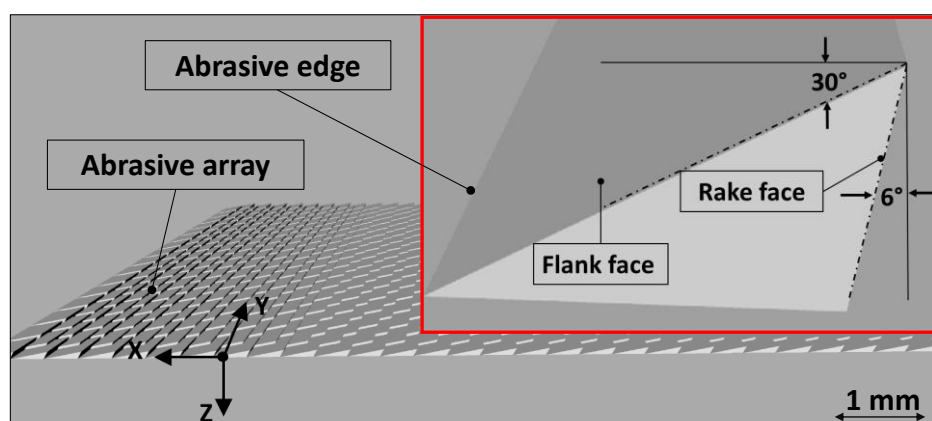


**Figure 3. 15: CAD design of the overall abrasive array and insert of desired geometry in term of rake and clearance faces.**

Once the desired geometry was selected, it was necessary to understand how the laser path parameters (e.g. direction of ablation, use of border

cuts) could affect the PLA process in the manufacture of the desired abrasives. In fact, differently from the laser parameter optimisation methodology described in Section 4.4, it is evident that there are many variables involved in the manufacture of the abrasive arrays, especially when aiming at a complex geometry as the one represented in Figure 3. 15. For this reason, both pulsed laser ablation and laser path parameters were considered in order to understand how these are affected by the design of the to-be-generated arrays. Regarding the understanding of laser path parameters, two experiments were performed: one to evaluate the effect of using border cuts and the other to study the influence of direction of ablation during PLA. This was propaedeutic to the achievement of the selected micro-abrasive arrays, reported in Section 3.6.2.

In Section 3.4.1 a design of experiments was used to see the combined effect of the variation of laser average power ( $P_m=50-100$  W), pulse frequency ( $f=30-50$  kHz) and beam feed speed ( $v= 100-900$  mm.s<sup>-1</sup>) onto PCD (10 mm x 10 mm x 1.5mm) and PCBN (10 mm x 10 mm x 1.7mm) specimens composites.

Experiments in Sections 3.4.2, 3.4.3, 3.4.4 lead to the achievement of optimum laser parameters for both PCD and PCBN (see Table 3. 10).

**Table 3. 10: Optimised laser parameters for the generation of micro-abrasive arrays PCD/PCBN composites.**

Specimen	$P_m$ [W]	$f$ [kHz]	$v$ [mm.s <sup>-1</sup> ]	$\tau$ [us]
PCD	70	30	400	10
PCBN	70	20	300	10

At this point an understanding of the influence of direction of ablation was necessary; for this reason another experiment was set up to evaluate how the angle of the laser beam onto the composite could affect the extent of ablation. This experiment consisted of alternating the direction of ablation among three variants (Figure 3. 16): a random direction of the laser beam respect to the solid specimen (e.g. angles: 0°, 45°, 90°, 135° etc.), a 0° and a 90° orientation of the laser beam to the specimen. For this purpose an initial CAD design reproducing the to-be-generated array geometry has

been input in the laser software. The laser parameters used are the ones reported in Table 3. 10.

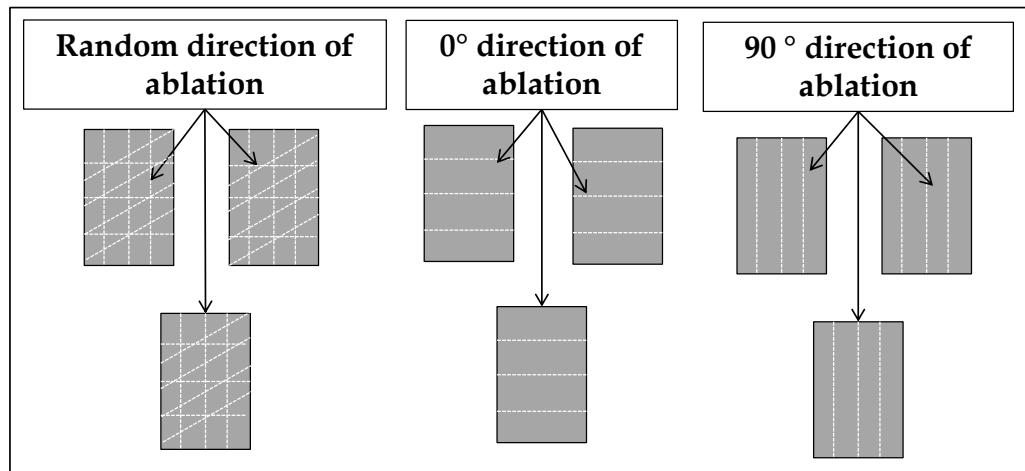


**Figure 3. 16: Schematic of the different type of direction of ablation of the laser beam.**

This experiment was needed in order to select the optimum direction of ablation for the generation of the to-be-generated micro-arrays and to understand how the orientation affects the sharpness of the cutting edges. After selecting the direction of ablation suitable for the specific to-be-generated geometry, another experiment was set up for the evaluation of the influence of using the border cut as the selected option in the laser software. For this purpose, specific geometries whose edge sharpness could be measured (e.g. triangular, hexagonal) were selected to be produced onto the PCD/PCBN composites via the ablation of multiple layer grooves providing a rapid method of generating patterns and allowing to understand the difference in extent of ablation and sharpness of edge between the ablated features with border cut and without border cut.

### ***3.6.2 Design for the generation of the micro-cutting arrays***

Once the influence of the laser path parameters was fully understood through the experiments in Section 3.6.1, the design for the manufacture of the to-be-generated micro-abrasive arrays was optimised. The optimisation procedure for the CAD design to be input in the laser software required an extensive amount of repetition, mainly due to the objective of fully understanding the laser process and to achieve a control

of the use of laser to enable the generation of any geometry. A first experiment was conducted to study the effects of the array orientation in the CAD design onto the generation of the abrasive pads. Because the process of laser ablation for generation of complex 3D geometries requires an approach in three dimensions, previous researchers [4] have shown that it is possible to introduce a tilting of the target material (to be ablated) in order to allow the motion of the beam along one more axis (Figure 3. 17).

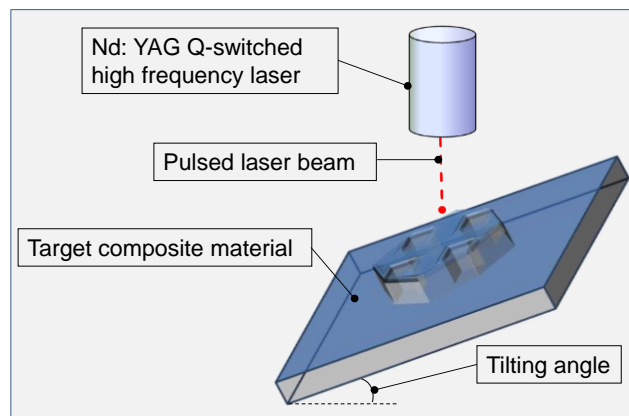


**Figure 3. 17: Schematic showing the positioning of the ultra-hard specimen to the laser beam.**

The experiment was conducted to study the effects of the array orientation in the CAD design onto the generation of the abrasive arrays: using multiple laser passes (overscan) the laser software was programmed in order to generate micro abrasive features (depth, 0.1 mm; length, 0.3 mm; width, 0.3 mm) on PCD/PCBN structures (10 mm x 10 mm x 1.5/1.7 mm) like those represented in Figure 3. 18: single abrasive features to be input in the laser software are depicted, and their dimensions shown.

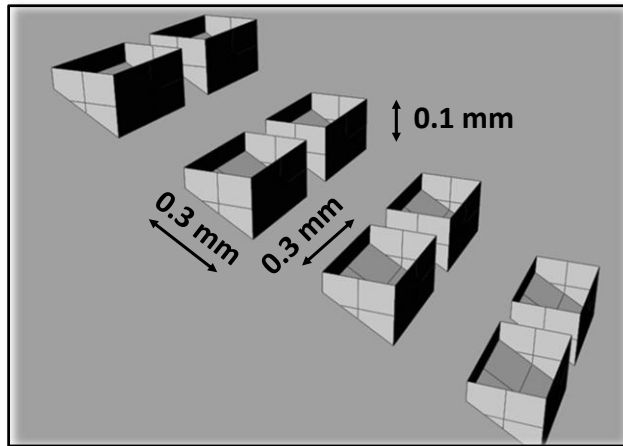


**Figure 3. 18: Example of the dimensions of the ablated abrasives in the CAD design.**

This laser ablation experiment included a variation of design angle orientations, each angle variation resulted into producing geometries with highly controllable clearance/rake faces: the use of an incremental angle variation was done to avoid the grooving effects typical of a multi passes ablation at a fixed angle (Figure 3. 19).

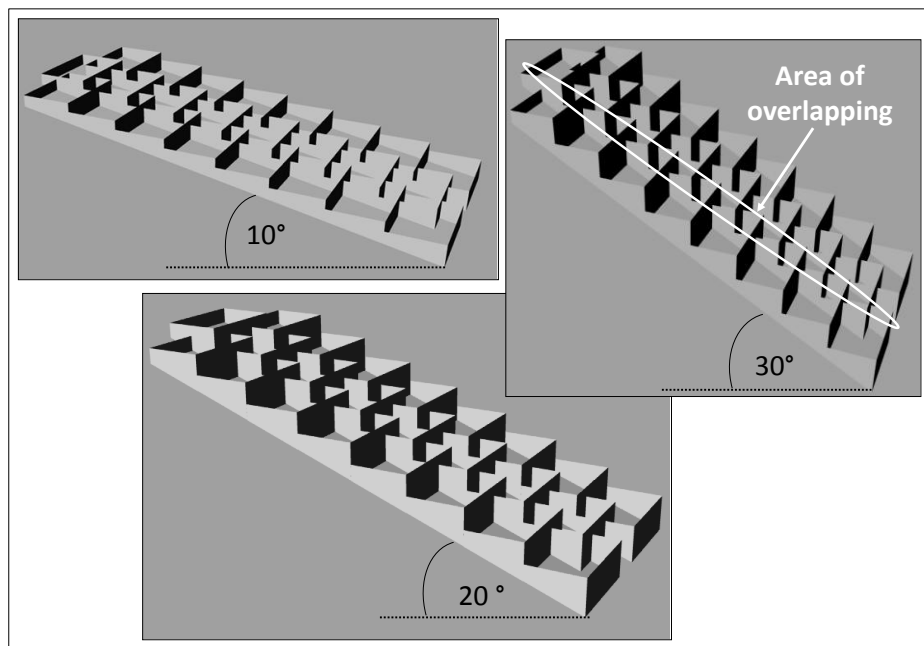


**Figure 3. 19: Schematic of a CAD design for the variation of the orientation of the specimen to be ablated.**

One of the iteration steps in the design of the CAD file to be input in the laser software was related to the spacing between micro-abrasives. As shown in Figure 3.19, the micro-abrasives are homogeneously staggered

and there is an overlapping between each single line. A novel multi-step ablation procedure has been adopted in order to reduce the thermal exposure of the material in the areas of overlapping. This procedure consisted in separating the laser path files (and consequently the CAD drawings) into different files which could be input in the laser software at different stages, enabling to minimise the thermal response in the areas of overlapping (0.05 mm); each file consisted of a group of cutting edges not in contact between each other and with a set distance of 0.3 mm between each feature and each line (Figure 3. 18).

Four separated CAD files (Design 1 to 4) were input in the laser software to programme the laser for minimum thermal exposure in the areas of overlapping (thickness 0.05mm) of the abrasives and Figure 3. 20 depict the ensemble of the four designs.

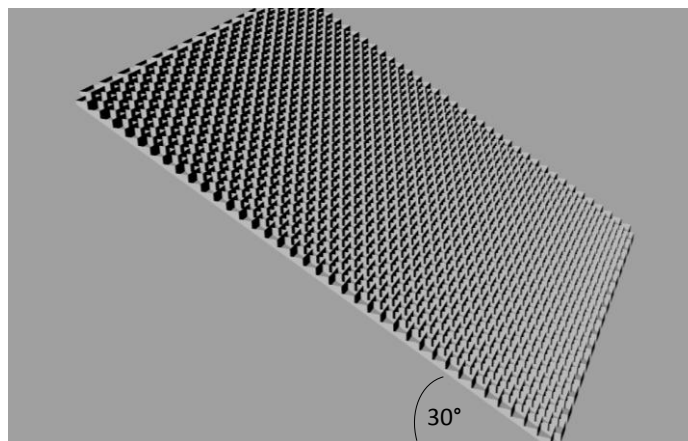


**Figure 3. 20: Schematic of the ensembles of the CAD drawings unifying design 1 to 4.**

After the generation of the laser ablated micro-arrays at every stage of the optimisation process, the following equipment was employed:

- A Talysurf CSI 1000 contact autofocus profilometer was used for topographical analysis of the protrusion height of the abrasives, the evaluation of the repeatability and the measurement of the cutting edge geometry.
- A Philips XL30 Environmental Scanning Electron Microscope (ESEM) was used for the microscopical evaluation of the surface integrity of the micro-abrasives in the areas of overlapping and for the evaluation of the sharpness of the cutting edge which was

measured by positioning the sample in the cross section of the edge (by using a special cross section specimen holder).

The laser ablation technique (multi-step PLA procedure), combined with the optimised design was set up for the generation of the orderly arrays with staggered micro-abrasives elements onto all of the thick film PCD/PCBN materials cited in Section 3.2. The optimal laser parameters achieved by the methodology explained in Section 4.4 were used for the generation of the micro-abrasive arrays (Table 3. 10). Each generated array was composed of overlapped cutting elements (depth, 0.1 mm; length, 0.3 mm; width, 0.25 mm) and had a population of 96 abrasive elements per mm<sup>2</sup>.

### 3.7 Evaluation of wear-resistant properties of micro structurally different PCD/PCBN arrays

#### 3.7.1 Selection of the benchmark specimens

For the selection of the benchmarked specimens, the geometry of a single laser generated abrasive element was considered and a circular geometry was plotted to intersect the rectangle representing the top view of the feature. This lead to the calculation of the approximate nominal diameter for the grit selection: a nominal diameter of 400  $\mu\text{m}$  was calculated as shown in Figure 3.21.

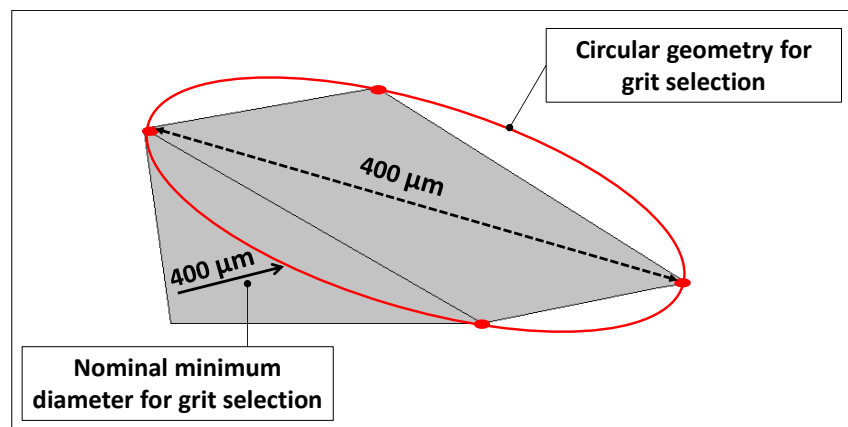
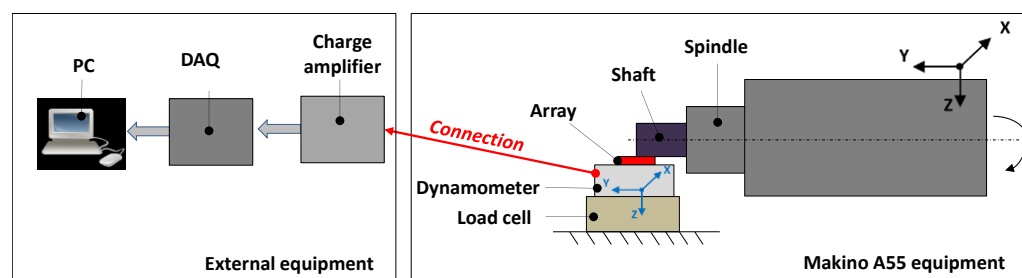


Figure 3. 21: Geometry of the single abrasive element and identification of the nominal diameter for the selection of the grit.

Once the minimum nominal diameter value was calculated, this was then compared to the sizes of the abrasives graded to the Federation of European Producers of Abrasives (FEPA) standards, leading to the choice of an average nominal size of 500  $\mu\text{m}$  to provide a reasonable comparison with the dimensions of the micro-abrasive edges. Once the grit size and type (D501 for the diamond specimen, B501 for the cubic boron nitride specimen), were selected, the base specimens to be electroplated were designed having the same dimensions of the laser generated arrays (10 mm x 10 mm x 1.5 mm). In both cases, the substrate material is boron carbide (thickness 1 mm) and the bonding type is a Nickel electroplating

### ***3.7.2 Setup of the test to evaluate the wear properties of the PCD/PCBN laser generated micro-abrasive arrays***

Once the generation of micro-abrasive arrays was achieved as explained in Section 3.6, a procedure was developed for the evaluation of the wear progression and consequently the wear performance of each generated array. A 5-axis grinding centre (Makino A55; max. spindle speed, 19,000 rpm; spindle power, 30 kW) was used for the wear/cutting tests and the cutting forces were acquired at a sampling rate of 10 kHz. A schematic of the test set-up is represented in Figure 3. 22.



**Figure 3. 22: Schematic of the monitoring equipment for the test set-up and the acquisition of the forces.**

A dedicated fixturing system (Figure 3. 23a) was employed to accommodate a 3-axis miniature dynamometer (Kistler 9317b) connected to three (one for each axis) charge amplifiers (Kistler 5011B10) and then to a data acquisition board (National Instrument BNC-2110) and dedicated

Labview software to save and process the signals (Figure 3. 22). The wear/cutting trials were conducted using a coolant (Houghton 3380, concentration 8-10%) delivered through the nozzle at a pressure of 20 bar.

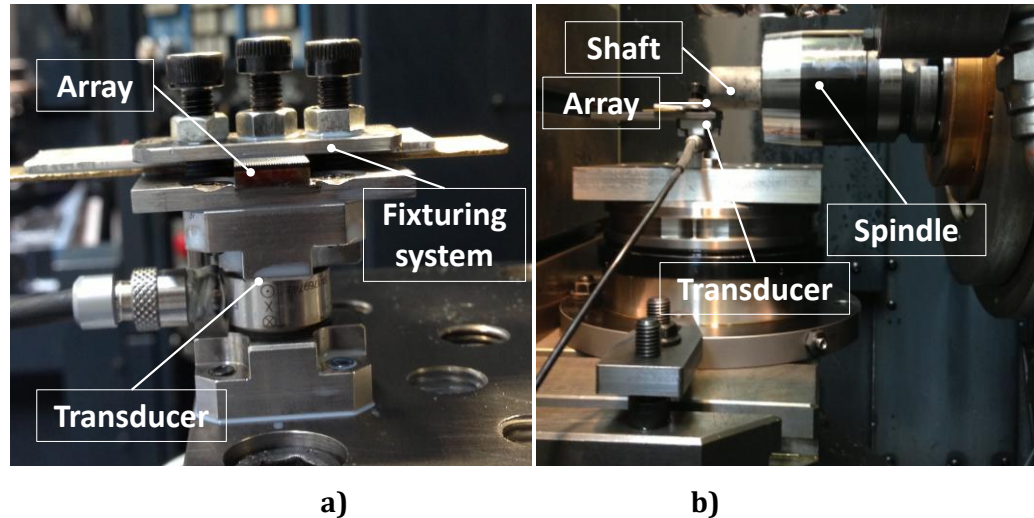


**Figure 3. 23: Test set-up: a) positioning of the array in the fixturing system, b) connection of the transducer/fixturing system/array into the grinding machine.**

The test procedure can be summarised as follows:

1. Initially the nozzle was set to be 100 mm above the abrasive array. Then, the contact between the array and the SiO<sub>2</sub> shaft was verified: this was achieved by using Labview software that was displaying the instantaneous signal acquired along X, Y and Z directions. In particular, the touch between shaft and array was verified when the Labview screen was showing a signal along Z, that corresponds to the direction of depth of cut (Figure 3. 24b).
2. Once the contact was verified, the workpiece (SiO<sub>2</sub> shaft) was subjected to a rotational motion while the laser generated array to a translational motion in Z direction to give a depth of cut and create a contact pressure between shaft and array (Figure 3. 24a). Initially the depth of cut was chosen to be equal to 5% of the total edge height (shown in Figure 3. 15), so 5 μm was used. This depth of cut (in the Z direction) demonstrated to be suitable for PCD arrays since the wear progression was slow enough to be characterised; a different phenomenon occurred in the PCBN

arrays. In this case, the use of a 5  $\mu\text{m}$  depth of cut drastically worn out the micro-edges, not allowing the wear progression to be slowly characterised. For this reason, a depth of cut of 1  $\mu\text{m}$  was selected to repeat the test on the PCBN/electroplated CBN.

3. Once the depth of cut was given to the array, a translational motion was imposed to the abrasive array in the X direction, while rotational motion of  $\text{SiO}_2$  shaft was occurring. The test of each array consisted in a previously established number of passes: 5000 passes (length of cut, 50 m) for the PCD arrays/electroplated diamond, and 1000 passes (length of cut, 10 m) for the PCBN arrays/electroplated CBN. Each pass was a combination of the following motions along the two axes: the touch between array and shaft (with rotation occurring), the depth of cut of the shaft into the array (in the Z direction), the translational motion of the array (in the X direction) covering the length of the array (10 mm), the shaft lift off (in the -Z direction), the translational motion of the array (in the -X direction).
4. At an intermediate set of 250 passes, the abrasive arrays were characterised: an environmental scanning electron microscopy (ESEM Philips XL30) was used for the evaluation of the wear progression of microstructurally different arrays.
5. A Talysurf CL100 was used for the identification of surface topography prior and at the end of each test.

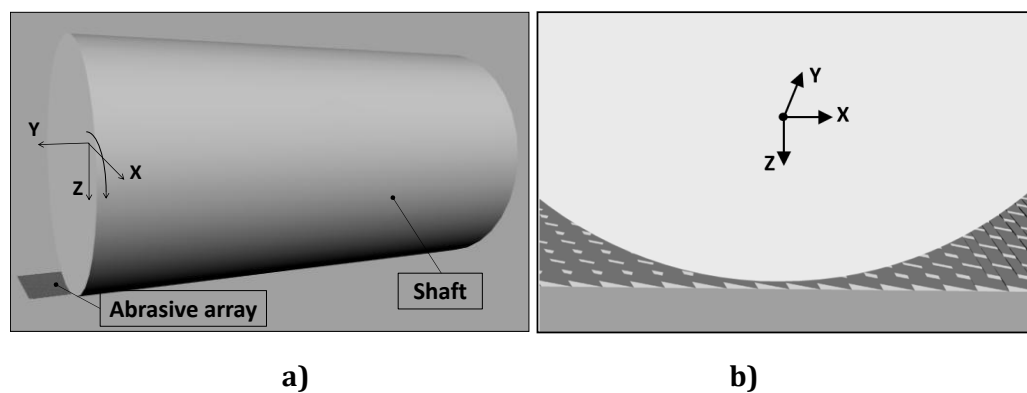


**Figure 3.24: CAD schematic of: a) 3D contact between abrasive array and Silicon dioxide shaft; b) cross section of the contact.**

### ***3.7.3 Approach for the comparison of the electroplated cutting forces versus the PCD/PCBN micro-cutting arrays***

The selected electroplated benchmarks differ from the arrays not only because the grits are randomly oriented on the surface, but also because of the density (number of grits/cutting edges per surface area). As mentioned in Section 3.7.2, a 3-axis dynamometer was used to acquire the forces produced during the wear test, and a Labview was employed to process the forces and convert them into a signal characteristic of each intermediate number of passes. In order to compare the signal acquired from the PCD/PCBN array with the one deriving from the benchmarked specimens, a novel procedure was developed and proposed for the normalisation of the cutting forces and to allow a comparison of the contact pressure produced. Because the cutting force is acquired during the motion of the array/electroplated against the shaft, a procedure was set-up to evaluate the instantaneous contact area between specimen and shaft and the contact pressure per single micro-edge/grit, making possible the comparison. The area ( $A$ ) of contact between single abrasive edge/grit and the shaft was calculated both theoretically and experimentally. The theoretical calculation of the single abrasive element was made by considering the geometry of the cutting edge reported in Figure 3. 25.

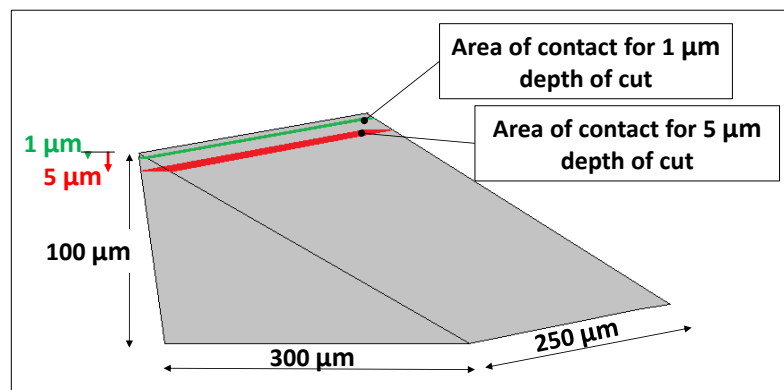


**Figure 3. 25: Schematic of the geometry for the theoretical calculation of the area of contact for depths of cut of  $1\ \mu\text{m}$  and  $5\ \mu\text{m}$  in the single cutting element.**

Because of the random geometry of the grits, the assumption of a spherical profile was made and consequent areas of contact (for  $1\ \mu\text{m}$  and  $5\ \mu\text{m}$  depths of cut) with the shaft were calculated as shown in Figure 3. 26.

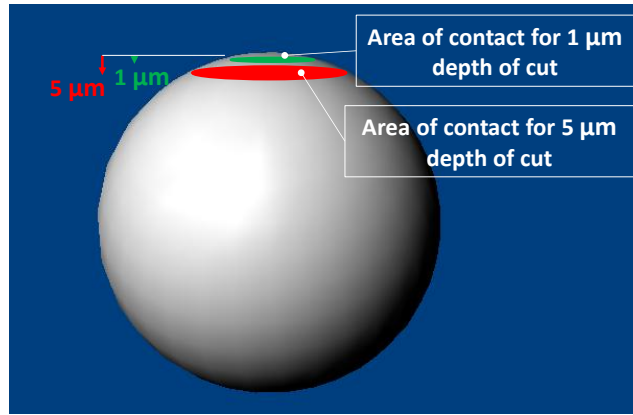


**Figure 3. 26: Schematic of the geometry for the theoretical calculation of the area of contact for depths of cut of 1 and 5 μm in the single grit (assumed spherical).**

The experimental contact areas were measured by using a novel procedure which followed the steps reported as follows:

1. Firstly, both the laser generated arrays and the electroplated specimens were scanned for evaluation of surface topography via the profilometer described in Section 3.4.
2. A thresholding process was used to measure the area of contact at a depth of cut of 1 μm and 5 μm after 250 passes and at the end of the test (1000 passes for PCBN/electroplated CBN, 5000 passes for PCD/electroplated diamond). Since the topographical scan involves the acquisition of a variable number of profiles, the tresholding process consisted of excluding (among all of the profiles) the ones not belonging to the 1 μm depth (for PCBN/electroplated CBN) and 5 μm depth (for PCD/electroplated diamond) in order to identify only the surface at specific depths of cut (1 μm, 5 μm).
3. The acquired cutting forces at the beginning of the test and at the end of it were then transformed to contact pressures by using Eq. 3:

$$p = F_a/NA \quad (\text{Eq. 3}),$$

where A is the area of contact between single abrasive edge/grit and shaft, N is the number of abrasive edges/grits in the instantaneous contact area of 5 mm<sup>2</sup>; F<sub>a</sub> is the average acquired cutting force, p corresponds to the contact pressure of the shaft on the single abrasive edge/grit. This has been calculated taking into account the number of micro-edges/grits present in the

instantaneous contact area of 5 mm<sup>2</sup>. In particular, after a statistical evaluation of the protrusion height of the grits and the calculation of the number of grits in contact with the shaft, it has been considered 45 micro-edges versus a number of 7 grits in the instantaneous contact area.

4. With the calculated contact pressures at the beginning/end of the test, it was possible to find a coefficient of normalisation of the cutting forces acquired at intermediate stages of the test (e.g. 250, 500, 750, 1000 passes for PCBN; up to 5000 for PCD) that allowed to recalculate all of the acquired forces and to compare the contact pressures from the benchmarked specimens with the arrays.

### **3.8 Conclusion and remarks**

The following section aims at summarising the previously described methodology adopted for the achievement of the objectives of this research. In regard to the procedures mentioned in Sections 3.1-3.7, the following considerations could be made:

1. The selection of ultra-hard materials (reported in Section 3.2) for the manufacture of laser generated arrays was done to enable an understanding of the role of the binder in thermal response of polycrystalline matrices as well as in the wear progression characteristics. For this reason, polycrystalline structures (PCD/PCBN) with different binder bulk volume percentage composites and consequently different diamond grain size materials were selected.
2. As widely described in Section 3.3, the properties of Silicon dioxide (SiO<sub>2</sub>) composite material lead to its selection as workpiece material for the evaluation of the wear progression of PCD/PCBN micro-arrays during the simulated wear/cutting tests. In fact, SiO<sub>2</sub> high hardness [111] may reduce the wear progression rate of the tested abrasive arrays and therefore allow the single steps of wear progression to be analysed and discussed [59].

3. In the process of optimisation of PLA parameters (described in details in Section 3.4 and shown in Figure 3. 3), an ensemble of multiple step methodologies has been used. Firstly, a design of experiments (DOE) has been used to produce laser ablated surfaces: topographical scans and environmental scanning electron microscopy were employed allowing the identification of possible thermal effects deriving from the combination of more than one variable. Secondly, the optimal set of parameters in output from the design of experiments (Section 3.4.1, Figure 3. 3) were used as the starting set of parameters to identify the suitable energetic parameters to reduce surface integrity anomalies (e.g. crater inhomogeneity, elongated craters) and to promote geometrically homogeneous craters avoiding double pulses (Section 3.4.2). Thirdly, the effect of variation of beam speed were studied in the generation of laser ablated craters and continuous grooves (Section 3.4.3). Finally, once the methodology proposed in Sections 3.4.1-3.4.3 allowed the identification of a set of optimal laser parameters, an evaluation of the chemical changes occurring in the composite as a function of the laser energy density/fluence was performed via EDX analyses (Section 3.4.4). The latter also allowed preparing the materials for the methodology proposed in Section 3.5.
4. A technique combining FIB, EDX, ESEM, HRTEM and EELS (described in-depth in Section 3.5) has been set up to allow the identification of the thermal response of ultra-hard composite materials PCD/PCBN at sub-atomic level. In particular this procedure allowed: (i) identification of the extent of allotropic transformation (e.g. diamond to graphite, cBN to hBN) and the relationship with the laser pulsed energy density (e.g. low energy, high energy). (ii) Identification of the transition phases (e.g. Co, diamond, graphite, TiC, cBN, hBN) and the interfaces between Co/diamond and TiC/cBN using HRTEM/EELS. (iii) Evaluation of the undisturbed interface Co/diamond and TiC/cBN and

underlying substructure outside the range of high level energy density.

5. Section 3.6 explained the methodology (Figure 3. 14) utilised to approach the design and generation of selected geometries onto microstructurally different materials. In particular, this involved a multiple step procedure which considered at first a wide literature survey for the selection of the to-be-generated cutting edge geometry. Then, the use of ESEM analyses allowed an understanding of the variation of laser path parameters (direction of ablation, use of border cuts) and identification of the optimal design for the to-be-generated arrays (Figure 3. 14).
6. Once the generation of micro-abrasive arrays was achieved, a procedure was developed for the evaluation of the wear progression and consequently the wear performance of each generated array (Section 3.7). A 5-axis grinding centre (described in 3.7.2) was used for the wear/cutting tests and the cutting forces were acquired at a sampling rate of 10 kHz. A dedicated fixturing system was employed to accommodate a 3-axis miniature dynamometer connected to three charge amplifiers and then to a data acquisition board and dedicated Labview software to save and process the signals.

This chapter reported about the methodologies and procedures which have been used for the achievement of the objectives (described in Chapter 1); in particular Sections 3. 4-3. 7 are proposing approaches that have been followed to achieve the results shown from Chapter 4 to Chapter 7.

# Chapter 4

## Optimisation of process parameters for PLA of PCD/PCBN composites

This chapter contains the results achieved in the optimisation process of PLA parameters (energetic and kinematic) necessary to enable the micro-processing of microstructurally different ultra-hard composites. In particular, it contains: (i) the results of characterisation of all of the materials before ablation (Section 4.1) necessary for an in-depth understanding of the materials properties before PLA; (ii) the results from design of experiment (DOE) in Section 4.2 whose details have been described in Section 3.4.1; (iii) topographical and microscopic analysis of the laser ablated spots as a function of the energetic parameters in Section 4.3, whose details of experiments are reported in Section 3.4.2. (iv) Topographical and microscopic analysis of the laser ablation in relation to the variation of kinematic parameters in Section 4.4, whose details of experiments is described in Section 3.4.3. (v) Finally the results of the methodology proposed in Section 3.4.4 to evaluate the extent of ablation in different composites are reported in Section 4.5.

### 4.1 Characterisation of selected materials before PLA

In order to acquire an in-depth understanding of the material microstructural properties (e.g. binder bulk volume percentage, ultra-hard grain size), a characterisation of the materials prior PLA was necessary. It is well known that during the synthesis process of polycrystalline ultra-hard structures, the composite properties change as a function of the bonds created between the ultra-hard grains during the intergrowth process [119] as described in details in Section 2.1.1. In this context, an evaluation of the surface roughness of the polished composites (via

TALYSURF and AFM, Atomic Force Microscope), their microscopic properties (via ESEM), crystal structure (via XRD) and chemical composition (via EDX) is required.

The materials and methodology adopted for experiments/characterisation are described in detail in Section 3.2 and the microstructural properties of the materials are reported in Table 3.1. ESEM microscopic imaging results for the PCD materials before PLA are reported in Figure 4. 1: backscatter ESEM images show the metallic binder (cobalt) in the bright areas and the ultra-hard phase (diamond) in the dark areas.

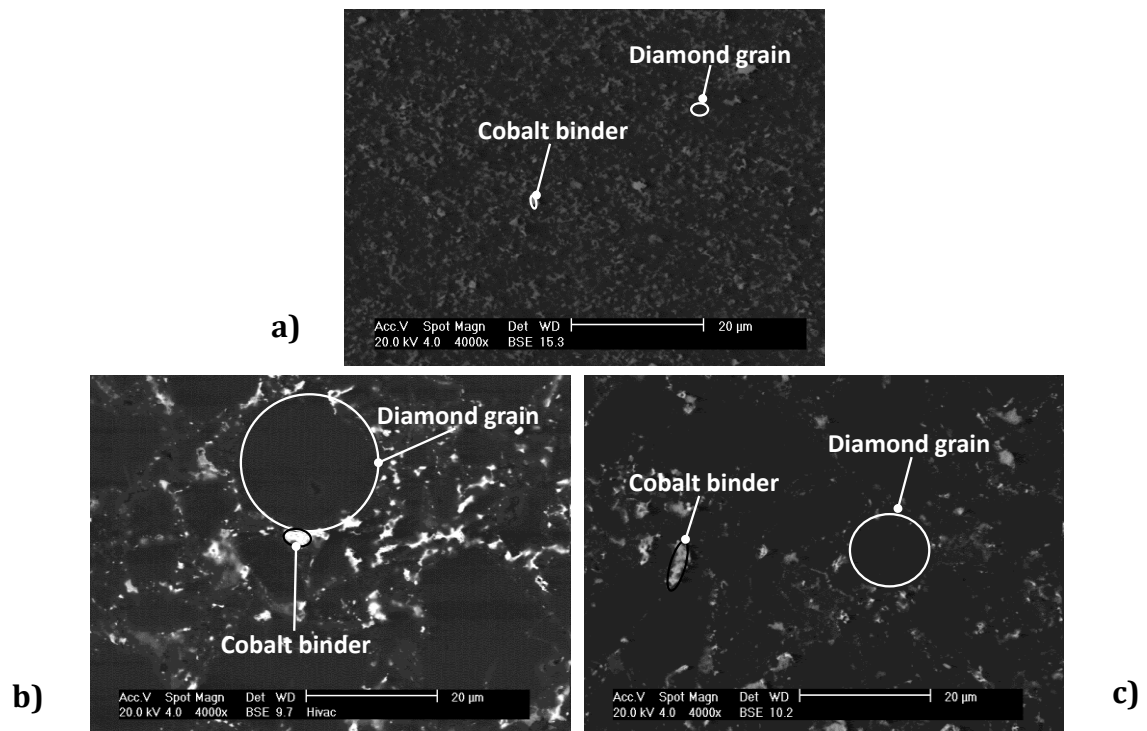


**Figure 4. 1: Backscatter ESEM imaging of PCD polished surfaces before PLA showing the diamond grains in the black areas and Co in the grey areas : a) CMX850 fine grained specimen, b) CTH025 coarse grained specimen; c) CTM302 mix grained specimen.**

The ESEM characterisation is important to understand the difference in diamond grain size between the selected composites: fine (Figure 4. 1a), coarse (Figure 4. 1b) and mixed (Figure 4. 1c) grained structures.

ESEM micrographs for the PCBN composites, whose microstructural properties were described in Table 3.1, are reported in Figure 4. 2; here it is evident the different microstructure in the case of purely ceramic binder (Figure 4. 2a), metallic mixed with metalloids Al and B (Figure 4. 2b) and purely metallic (Figure 4. 2c).

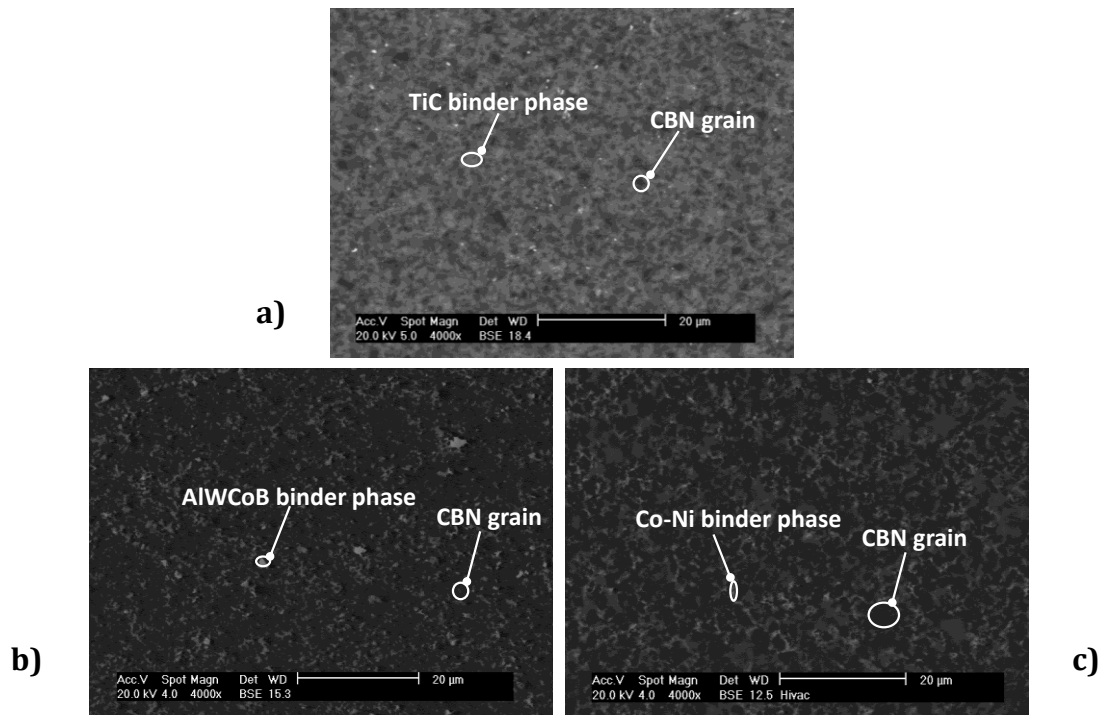


**Figure 4. 2: Backscatter ESEM imaging of PCBN polished surfaces before PLA showing CBN grain in the black areas and binders in the grey areas: a) DCC500 fine grained purely ceramic binder specimen , b) DBW85 metalloïd binder specimen; c) DBS900 purely metallic binder specimen.**

Atomic force microscopy results prior to PLA are depicted in Figure 4. 3 for a coarse grained PCD polished specimen: it can be noticed that: (i) the roughness of the polished sample shows a peak of 108.9 nm in the brightest areas, indicating the good quality of the manufacturer’s polishing on the ultra-hard material: a polished surface is really important for the preparation to micro-processing because it reduces the complication typical of thermal processes; (ii) often the infiltration of metallic binder in the voids created by the diamond bridges formed during the synthesis process (Section 2.3) is not occurring because of the condition of the synthesis. An example of this is depicted in the insert of Figure 4. 3: voids of the order of 200 nm are indicated in the black areas.

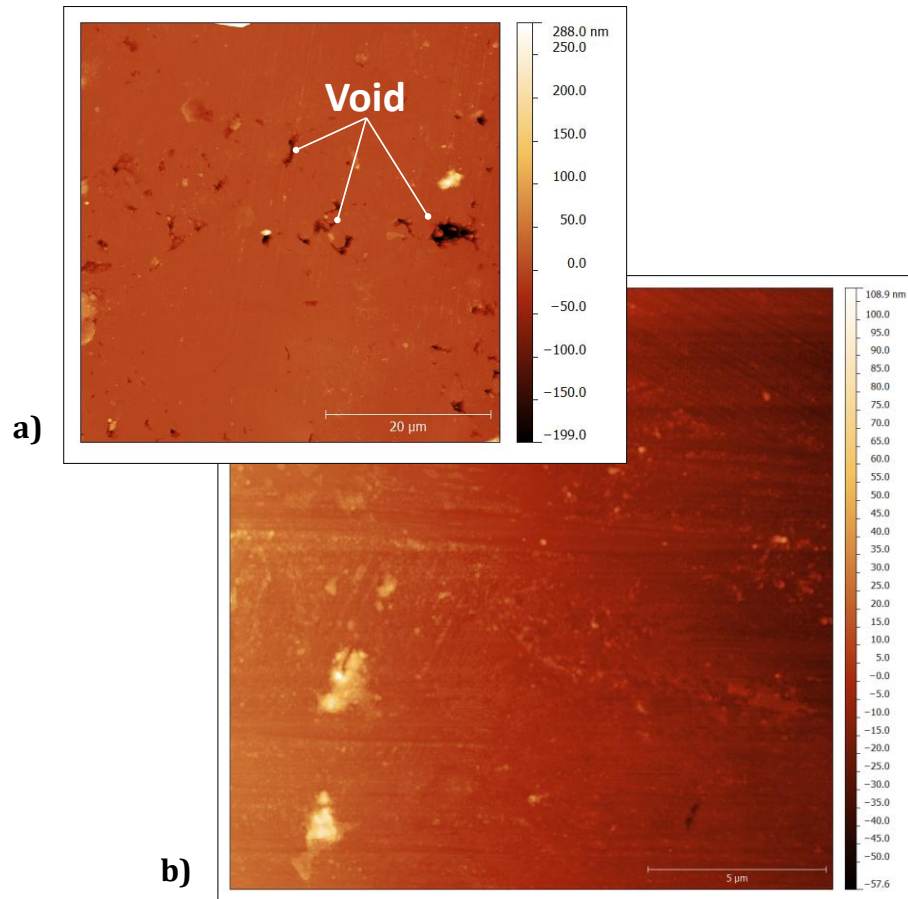


**Figure 4. 3: Atomic force microscope (AFM) tapping mode imaging of the coarse PCD specimen CTH025: a) large specimen area, b) detail of the large area.**

Based on the data provided by the materials manufacturer, it has been necessary to populate the material data information by using different characterisation techniques as widely described in Chapter 3. The use of XRD is particularly important when information on the crystal structure is needed. In this case, this was essential to provide an understanding of the crystal structure for microstructurally different composites, which was unknown when receiving the specimen from the provider. Examples of the results of XRD technique are depicted in Figure 4. 4 (PCD specimen) and Figure 4. 5 (PCBN specimen).

XRD (X-Ray Diffraction Spectroscopy) results provided important information on the material crystal structure. This technique is based on observing the scattered intensity of an X-ray beam hitting a sample as a function of incident and scattered angle, polarization, and wavelength.

Face cubic centred (FCC) of the cobalt and of the diamond are indicated respectively from the blue and red peaks in Figure 4. 4, while the green peak proving the presence of WC in the PCD layer, indicated that the infiltration of WC from the substrate occurred during the synthesis process [17], [119].

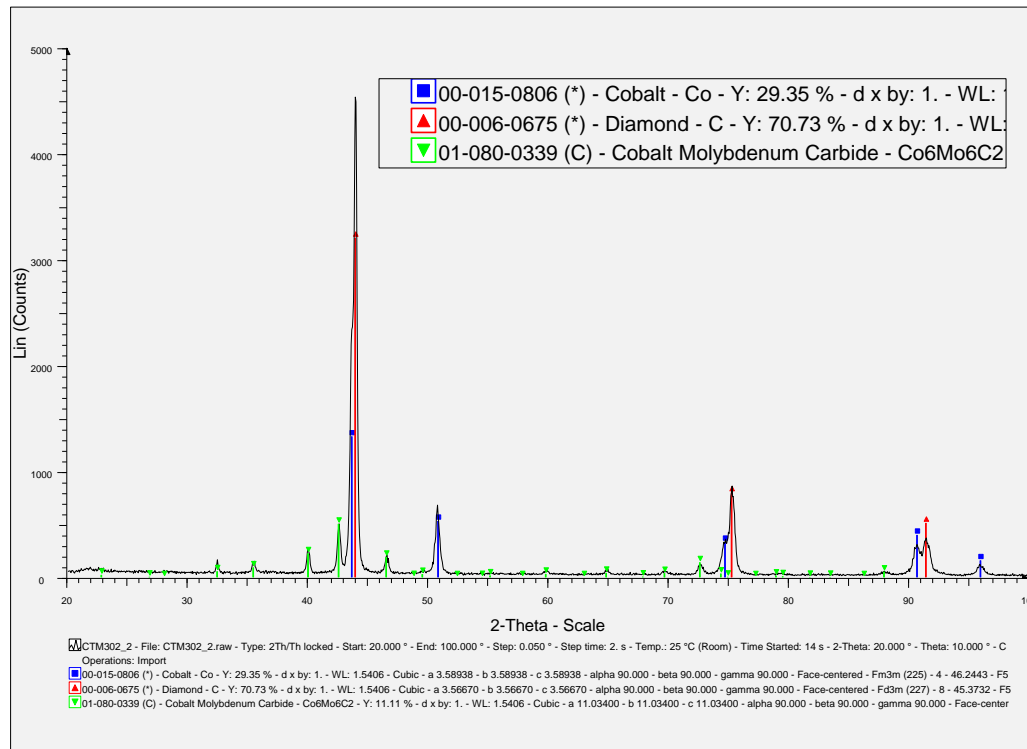


**Figure 4. 4: XRD results for the characterisation of CTM302 mixed grained PCD specimen.**

An example of the XRD characterisation results for the PCBN composite is shown in Figure 4. 5: the red peaks have indicated the presence of a ceramic binder Titanium Carbide (TiC) with cubic lattice structure, while green peaks have shown the presence of BN in a face centred cubic lattice structure. These results confirmed the ones achieved via EDX on the ESEM equipment.

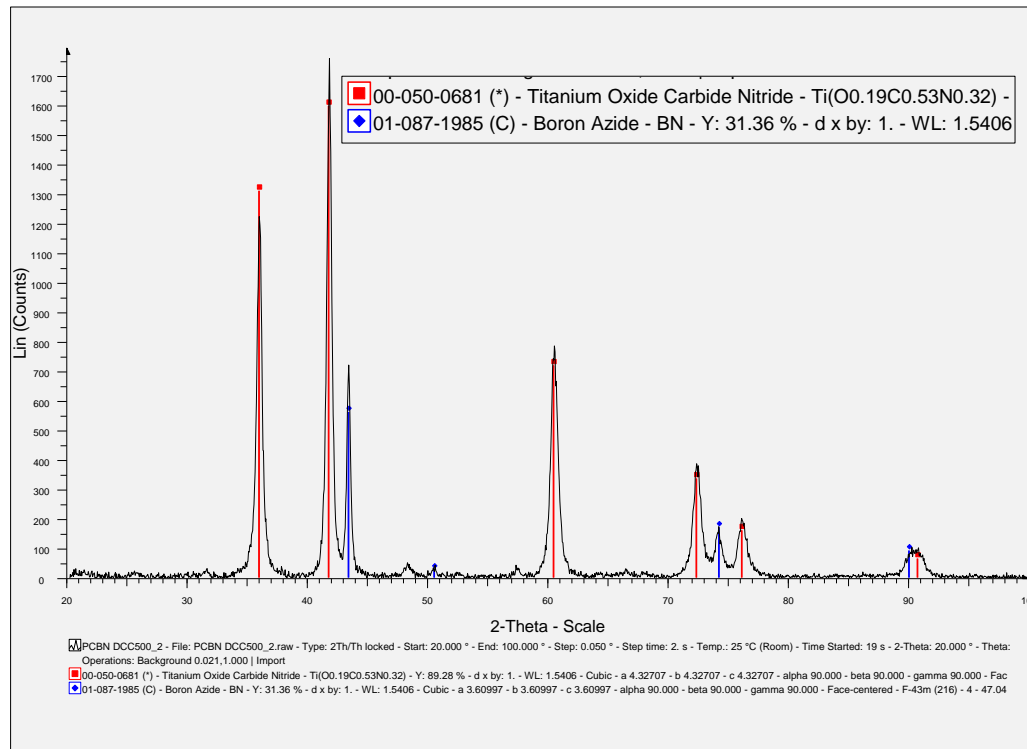


**Figure 4. 5: XRD results for the characterisation of DCC500 PCBN specimen.**

AFM analysis on the PCD structures indicated that the formation of voids of different extent occurred during the synthesis process, this probably occurred because the metallic binder (cobalt) did not infiltrate into the pool created by the intergrowth between diamond grains because in the synthesis process the synthesis of diamond and cobalt powders is difficult to control and the condition (p, T) might have not allowed this to happen [120]. The combination of EDX and XRD allowed characterising the composite chemical composition and crystal structure prior ablation to enable the identification of the change in structure that might occur as a consequence of the thermal excitation during PLA.

## 4.2 Design of experiment (DOE)

As widely described in Section 3.4.1, a DOE was necessary for a pre-optimisation of the laser parameter combination. In fact, since many are the variables involved in the PLA process (beam scanning speed, laser average power, frequency, pulse duration) it is important firstly to gain an understanding of the effect of the variation of multiple variables. This section includes the results of the design of experiments and the main

considerations which allowed proceeding to the second step of optimisation (see Figure 3.3).

#### ***4.2.1 Preliminary investigation of process parameters: results of Design of Experiments***

As widely reported in Section 3.4.1, a sequence of four designs of experiments has been selected as a preliminary step for the evaluation of the optimal parameters in PLA of the selected composites. Two full factorial and two Taguchi experiments have been adopted: in particular it is important to understand the reason of this selection. The first full factorial design ( $P_m$ ,  $f$ ,  $v$  = variable;  $\tau$  = constant) has been performed for a general understanding of the results of combining different parameters, while the second full factorial ( $P_m$ ,  $f$  = variable;  $\tau$ ,  $v$  = constant) specifically focused on the variation of energetic parameters. As a consequence of these two, the first Taguchi ( $P_m$ ,  $f$ ,  $v$ ,  $\tau$  = variable) has been selected for a rapid evaluation of the influence of a variable pulse duration and the second Taguchi ( $P_m$ ,  $f$ ,  $v$  = variable;  $\tau$  = constant) for a confirmation of the trend achieved by the first factorial design. The proposed sequence of DOE is due to the scarce knowledge of PCD/PCBN composites in the PLA process and a need to a rapid approach which represents only the first stage of the optimisation (as proposed in Figure 3.3).

The full factorial design whose selected parameter ranges ( $P_m$  = 50, 70, 90, 100 W;  $f$  = 10, 30, 50 kHz;  $v$  = 100, 300, 500 mm.s<sup>-1</sup>;  $\tau$  = 15  $\mu$ s) are shown in Table 3.3 (Section 3.4.1) employed the use of multiple combinations for a total of 27 runs. Figure 4. 6 depicts the outcome of this full factorial DOE: it can be noticed that specific sets of PLA parameters do not lead to the ablation of the workpiece material. In the case shown in the figure the variables affecting the PLA are mostly energetic ( $P_m$ ,  $f$ ); in fact for  $P_m$  = 100 W,  $f$  = 30 kHz,  $v$  = 500 mm.s<sup>-1</sup> and for  $\tau$  = 15  $\mu$ s and  $P_m$  = 100 W,  $f$  = 50 kHz,  $v$  = 500 mm.s<sup>-1</sup>,  $\tau$  = 15  $\mu$ s the laser did not remove material from the surface. By using Equation 2 in Section 3.4.4, the values of energy density for the ablation that did not occurred have been calculated to be 17.7 MWcm<sup>-2</sup>, 10.6 MWcm<sup>-2</sup> respectively.

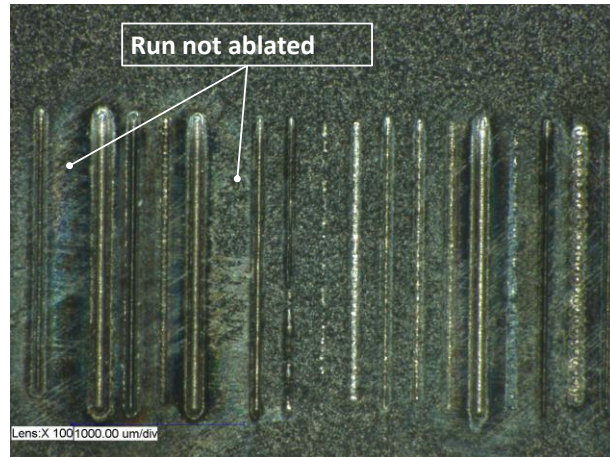


**Figure 4. 6: Optical microscopy imaging of the results from full factorial design described in the methodology in Table 3.3.**

As reported in Section 3.4.1 a second DOE has been utilised Results from the second full factorial design ( $P_m = 30, 60, 90$  W;  $f = 5, 10, 15$  kHz;  $v = 800$  mm.s<sup>-1</sup>;  $\tau = 30$   $\mu$ s) are reported in Figure 4. 7: as in the previous case, laser ablation did not always occur, in particular this happened because of the variation of energetic parameters ( $P_m, f$ ) and the use of a too low value for  $P_m = 30$  W. By using Equation 2 in Section 3.4.2, the values of energy density (corresponding to the site where ablation did not occurred) have been calculated and are equal to  $5.3$  MWcm<sup>-2</sup> (for  $P_m = 30$  W;  $f = 15$ , kHz;  $\tau = 30$   $\mu$ s),  $7.96$  MWcm<sup>-2</sup>(for  $P_m = 30$  W;  $f = 10$ , kHz;  $\tau = 30$   $\mu$ s) and  $15.9$  MWcm<sup>-2</sup> (for  $P_m = 30$  W;  $f = 5$ , kHz;  $\tau = 30$   $\mu$ s).

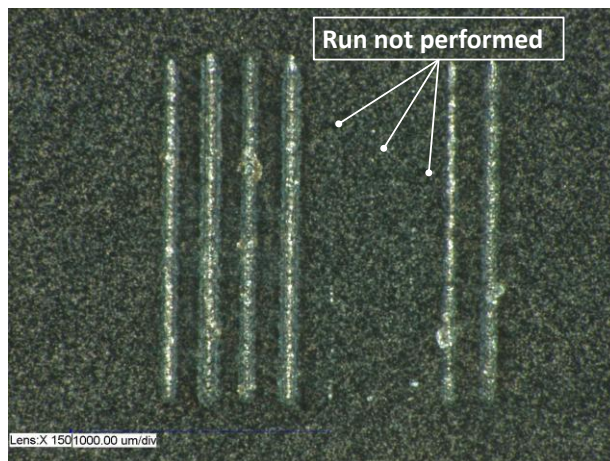


**Figure 4. 7: Optical microscopy imaging of the results from Full factorial design described in the methodology in Table 3.4.**

The Taguchi design was performed using the values reported in Table 3.5 in Section 3.4.1 ( $P_m = 30, 60, 90$ , W;  $f = 10, 30, 50$  kHz;  $v = 100, 300, 500$  mm.s<sup>-1</sup>;  $\tau = 5, 10, 15$   $\mu$ s); the results of this experiment indicated again that

the use of a too low  $P_m$  (30 W) prevented the ablation to occur as shown in Figure 4. 8.

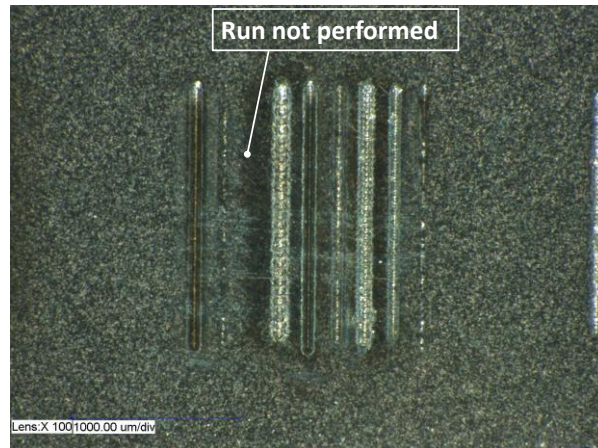


**Figure 4. 8: Optical microscopy imaging of the results from Taguchi design described in the methodology in Table 3.5.**

#### ***4.2.2 Observation and discussion***

In both full factorial designs, the laser did not ablate the surface for values of  $P_m = 30, 100$  W ( $P_L = 17.7$  MWcm<sup>-2</sup>, 10.6 MWcm<sup>-2</sup>); this can be explained considering the lasing threshold: at low energy density the material evaporates/sublimates, at high energy density the material converts to plasma [121]; hence, it was found that in these experimental conditions, if the energy densities are outside the range of energy threshold ( $10.6$  MWcm<sup>-2</sup> <  $P_L$  <  $17.7$  MWcm<sup>-2</sup>) the ablation does not occur. The combination of full factorial design and Taguchi design allowed a first identification of the energy density gaps that enable PLA to occur or not. In particular, it can be commented that it is not solely the energy density that needs to be taken into consideration for the laser ablation to occur because this is a combination of three laser variables ( $P_m$ ;  $\tau$ ;  $f$ ) as indicated in Equation 2. Table 4.1 shows that for same values of energy densities ( $10.6$  MWcm<sup>-2</sup> ablation) did not always occur, and the main differences between these cases were  $P_m$  and  $f$ , thus an in-depth study of the variation of  $P_m$  was conducted and the results are presented in Section 4.3.

**Table 4. 1: Calculated values for energy density for full factorial experiment reported in Table 3.4 in Section 3.4.1.**

$P_m$ [W]	f [kHz]	$\tau$ [us]	$P_L$ [MWcm <sup>-2</sup> ]	Status of ablation
60	15	30	10.6	Occurred
60	5	30	31.8	Occurred
90	5	30	47.7	Occurred
60	10	30	15.9	Occurred
<b>30</b>	15	30	<b>5.30</b>	<b>Not occurred</b>
<b>30</b>	10	30	<b>7.96</b>	<b>Not occurred</b>
<b>30</b>	5	30	<b>15.9</b>	<b>Not occurred</b>
90	15	30	238	Occurred

### 4.3 Variation of laser energetic parameters to enable PLA on PCD/PCBN structures

The experiments reported in this section have been undertaken to gain an understanding of the response of ultra-hard composite structures to the laser energetic parameters, according to the experimental setup discussed in Section 3.4.2.

#### 4.3.1 Experimental results

After the laser was setup as described in Section 3.4.2 to evaluate the influence of the energetic parameters onto microstructurally different PCD/PCBN composite, the redeposited material deriving from PLA process had been cleaned from the craters using an ultrasonic bath technique described previously; and the ablated PCD/PCBN surfaces were introduced to the Talysurf interferometer mentioned in Section 3.4.2 for profile measurements of the generated features. Figure 4. 9 depicts a three dimensional scan of selected craters generated at different  $P_m$  values: dimensional variation of crater topography is evident in the scale labels on each figure.

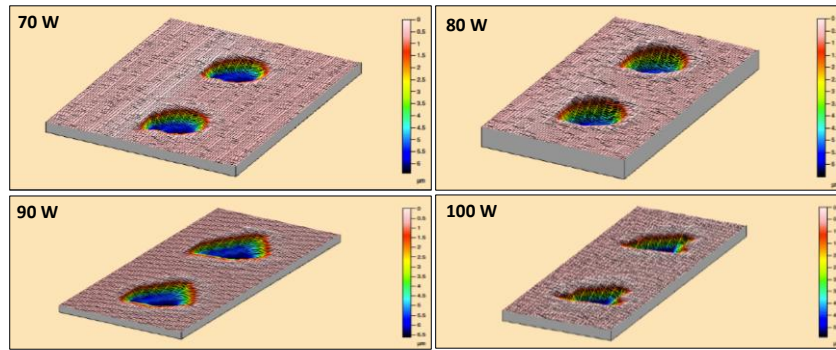


**Figure 4. 9: TALYSURF results for variation on energetic parameters (Table 3.7) in the case of fine grained CMX850 specimen for different laser average power.**

ESEM micrographs depicted in Figure 4. 10, 4. 11 provide a visual representation of the ablated crater generated using selected laser average power. In order to check the repeatability, the craters were created five times with same laser parameters. It has been found that for  $P_m = 70$  W a homogeneous spot with well-defined round circumference was achieved with high repeatability; an increase in  $P_m$  up to 100W led to a variation of the circumference into a triangular shape with a reduction of spot depth and ablated volume (Table 4.2).

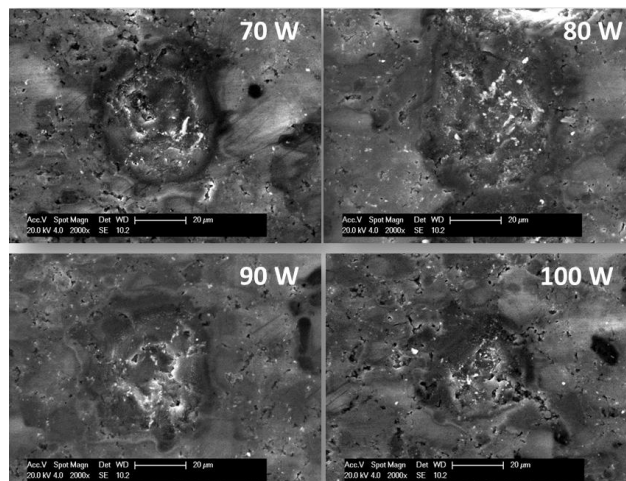


**Figure 4. 10: ESEM images showing the effect of variation of laser average power (Table 3.7) onto the coarse grained CTH025 specimen.**

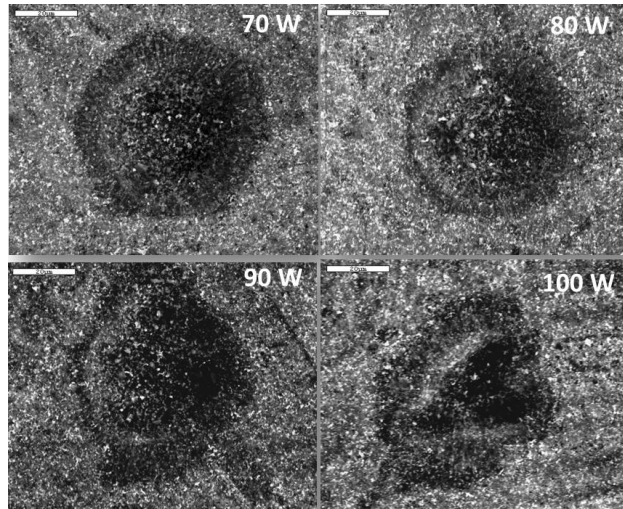


**Figure 4. 11: ESEM images showing the effect of variation of laser average power (Table 3.7) onto the fine grained CMX850 specimen.**

#### ***4.3.2 Observation and discussion***

As previously described in Section 3.4.4 and shown in Figure 3.6, an increase of  $P_m$  caused a decrease of homogeneity in the ablated crater diameter  $d$ , as evident in Figure 4. 10 and Figure 4. 11. This can be explained considering the energy density calculated via Equation 2 in Section 3.4.4: by increasing  $P_m$ , equation 2 has shown to give an increase in  $P_L$ . The lack of homogeneity might arise because the energetic threshold of the target material is exceeded. In fact, when the threshold energy is transferred to the material, ablation takes place and the energy is homogeneously dissipated in the surrounding area of the crater ( $P_m=70W$ ). At high energy density and high  $P_m$  (up to 100W) the material directly converts to plasma [121], producing a thermal affected zone and causing a lack of homogeneity in the spot circumference.

Previous work on CVD single crystal diamond demonstrated that the optimal values in PLA were  $P_m = 60 W$  ,  $P_L = 11.14 MWcm^{-2}$ [4]. Results of this reported experiment (Table 4.2) are partially in agreement with what was indicated in the above mentioned study. On the one hand, the ESEM micrographs allowed the identification of the craters with homogeneity of the spot in the 60 W and 70 W values of  $P_m$ , and to discard all of the other  $P_m$  values resulting in not adequately homogeneous craters (50, 80, 90,

100 W). On the other hand, the topographical scans of the craters allowed achieving the following conclusions: (i) the ablation rate of the spot generated at 70 W is 8% higher than the one at 60 W; (ii) the depth of crater at 70 W is 10% higher than the one generated at 60 W.

**Table 4. 2: Results for specimens PCD CMX850 in the test described in Table 3.7.**

$P_m$ (W)	Depth( $\mu\text{m}$ )	Ablated Area( $\mu\text{m}^2$ )	Ablated Volume( $\mu\text{m}^3$ )
50	5.11	200	1022
60	5.87	161	945
70	6.09	167	1017
80	6.19	202	1250
90	5.10	78.3	399.3
100	3.91	55.8	162.3

As a consequence, the optimal  $P_m$  value was chosen to be 70 W for the above mentioned reasons. An example of craters in PCD/PCBN materials with an optimum laser average power is reported in Figure 4. 12.

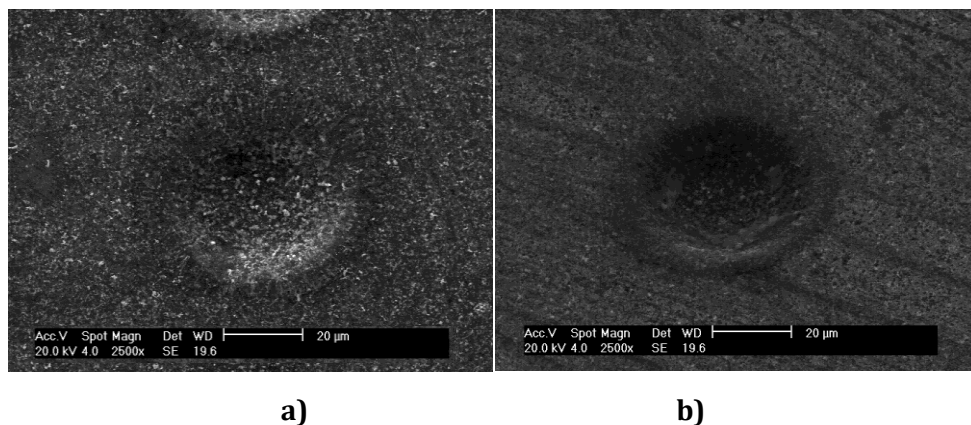


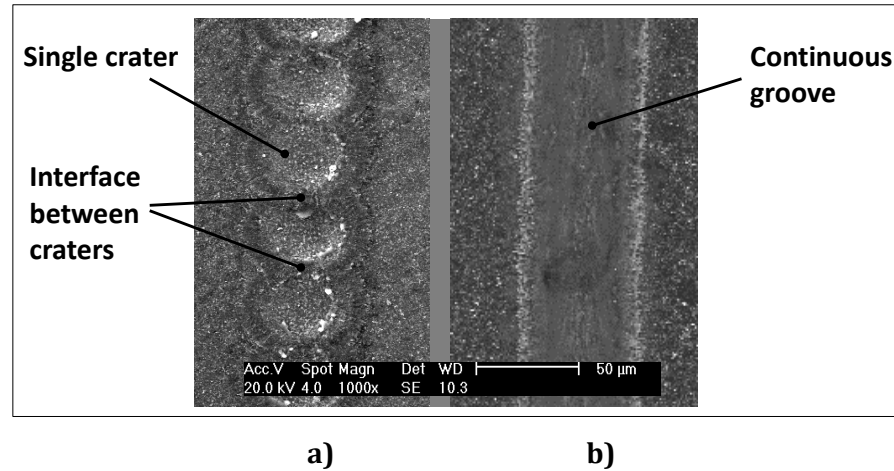
**Figure 4. 12: ESEM micrographs of the optimised laser ablated craters in: a) PCD CMX850; b) PCBN DCC500.**

#### 4.4 Variation of laser kinematic parameters

In Section 4.3 the identification of the optimal  $P_m$  value was achieved and this value was found to be 70 W. This section focuses on the results of experiments performed to evaluate the influence of variation of beam scanning speed, for the considered average power and using the parameters as presented in Table 4.3. Rows of 15 (3 repetitions for each set of parameters) individual craters/continuous grooves were generated

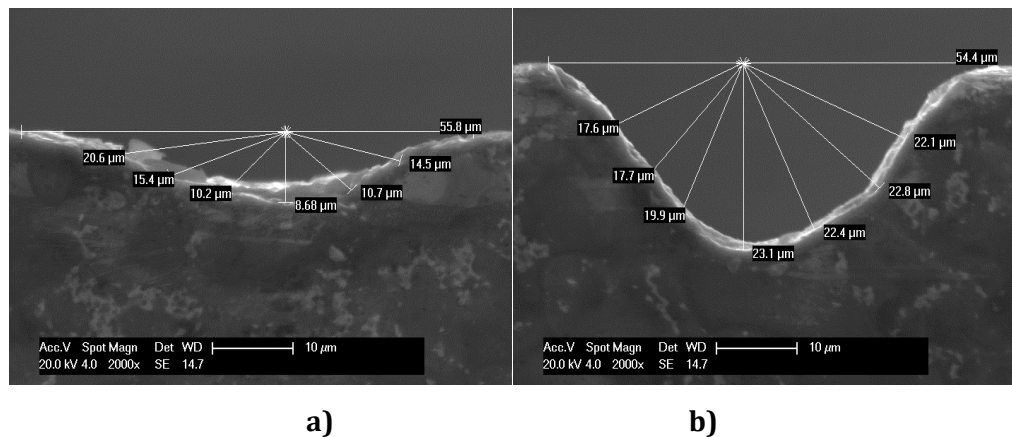
into the surfaces of flat PCD/PCBN specimens and the results are presented here and discussed.

Figure 4. 13 shows selected laser ablated rows, illustrating well defined separated craters (Figure 4. 13a) and a continuous laser groove (Figure 4. 13b) generated using parameters reported in Table 3.9 in Section 3.4.3.



**Figure 4. 13: ESEM micrograph in PCD CMX850 representative of: a) single ablated craters ( $v=500\text{mms}^{-1}$ ), b) continuous groove ( $v=100\text{mms}^{-1}$ ).**

ESEM analysis enabled the evaluation of geometrical differences between minimum ( $100\text{mms}^{-1}$ ) and maximum beam scanning speed ( $500\text{mms}^{-1}$ ) and finding an inverse relation between depths of ablation and scanning speed: it can be commented that by decreasing  $v$  5 times, an increased depth of ablation up to 63% was found (Figure 4. 14).



**Figure 4. 14: ESEM cross section images on the variation of kinematic parameters: a)  $v=500\text{mms}^{-1}$ ; b)  $v=100\text{mms}^{-1}$ .**

The topographical analysis performed as described in Section 3.4.3, have allowed the identification of the actual overlapping percentage between consecutive spots as the decreasing of the scanning speed decreases from

500mms<sup>-1</sup> to 100mms<sup>-1</sup>. The results are reported in Figure 4. 15 ( $v=300\text{mms}^{-1}$ ) and Figure 4. 16 ( $v=100\text{mms}^{-1}$ ): the schematic red craters illustrate the consecutive spots and the blue profile represents the theoretical overlap profile, comparable to the actual overlap profile shown in the topographical measurement.

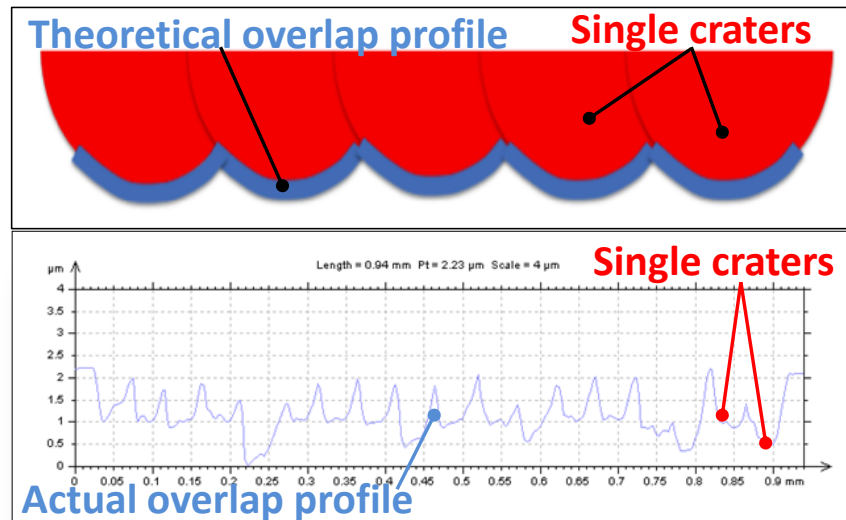


**Figure 4. 15: Talysurf results showing the overlapping between consecutive spots for  $v=300\text{mms}^{-1}$  (the values used to achieve this roughness are reported in Table 3.9).**

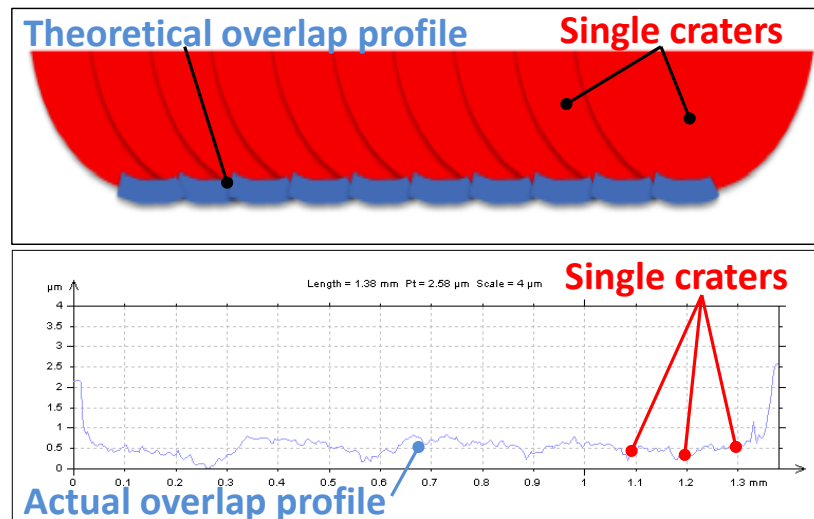


**Figure 4. 16: Profilometry of the overlapping between consecutive spots for  $v=100\text{mms}^{-1}$  (the values used to achieve this roughness are reported in Table 3.9).**

All of the experiments, whose results are presented here, were performed to evaluate the real overlapping profile. As previously anticipated, by

decreasing  $v$  (from  $500\text{mms}^{-1}$  to  $100\text{mms}^{-1}$ ), a 63% increase of ablated depth was found; in fact,  $v$  being a kinematic parameter, when this has been reduced (and  $P_L$  is kept constant) there is a superimposition of energies that continuously overlap each other for every single pulse creating a deeper ablated area and provoking a gap between energies of a single spot and  $P_L$  of the continuous groove [74].

## **4.5 EDX chemical environmental analysis**

In Sections 4.1-4.4 a study on the effects of laser parameters has been achieved for understanding how to approach the PLA process for microprocessing of ultra-hard materials. In this context it is important to identify the ablative effect on the composite microstructure and the experiment reported in this section aims at understanding the effects of PLA onto the chemical composition of microstructurally different PCD/PCBN composites.

### ***4.5.1 Experimental results***

In this section, results from chemical compositional analysis at various positions across the crater/groove, characterized by different laser energy densities are illustrated and their influence on the local binder bulk volume percentage discussed.

The values reported in the methodology Section 3.4.4 were used to create an ablated single crater (Figure 4. 17a) and ablated continuous groove (Figure 4. 17b) in microstructurally different PCD/PCBN specimens.

The chosen areas of EDX analysis (corresponding to different  $d_i$  on the laser spot as shown in Figure 3. 5) are shown in the cross sections depicted in Figure 4. 17, labelled from 1 to 5. The calculated values for  $F$  and  $P_L$  are reported in Table 4. 3: those values are corresponding to different crater/groove positions as shown in Figure 4. 17.

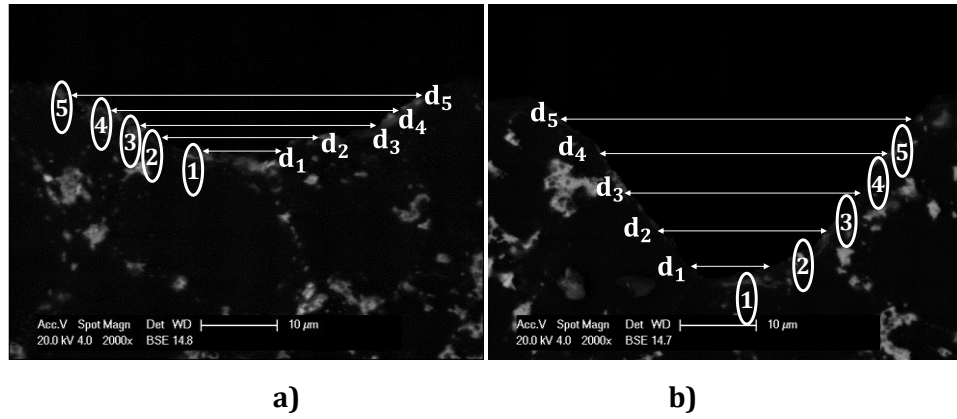


**Figure 4. 17: ESEM micrographs of the cross section of the CTH025 specimen showing the areas of analysis of EDX detector for the two different tests: a) optimised single spot achieved with test in Table 3.7; b) optimised continuous groove achieved from test in Table 3.9.**

It is evident that the material removal rate is proportional to the laser energy density, mainly because of the increased depth of crater for increased energy, as demonstrated in Section 4.4.

**Table 4. 3: Calculated values of fluence and power density for the chosen areas.**

Area of analysis	$d_i(\mu\text{m})$	$F(\text{Jcm}^{-2})$	$P_L(\text{MWcm}^{-2})$
1	10	7369	382
2	15	3395	169
3	25	1222	61
4	30	849	42
5	35	623	31

ESEM micrographs of single crater/groove in top view are illustrated in Figure 4. 18.

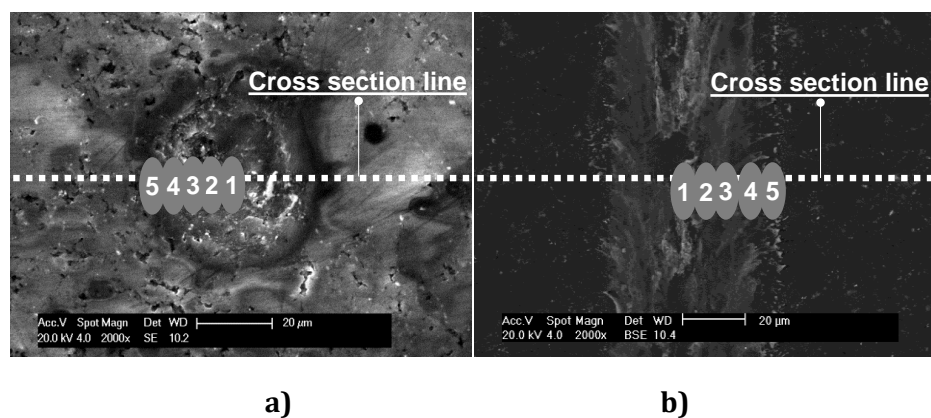


**Figure 4. 18: ESEM top view micrograph showing an example of the EDX areas of analysis for CTH025: a) single spot crater; b) continuous groove (Tables 3.7-3.9).**

Chemical analyses conducted on specimens CTH025 (Figure 4.18) have shown that for the area of higher  $P_L$  (Area 1) a higher presence of cobalt is found (Tables 4.4-4.5), while this is decreasing moving towards Area 5, area with low  $P_L$ . The same result was found for specimen CMX850, where, for higher  $P_L$  the Cobalt bulk volume percentage was higher than in the area with low  $P_L$  (Tables 4.6-4.7).

**Table 4. 4: EDX results for the continuous groove ablated ( $P_m$  70W,  $\tau$ 20 $\mu$ s, f10kHz, v100mms<sup>-1</sup>) in CTH025 composite.**

Element (%)	C	O	Co
Area 1	66.21	3.77	30.02
Area 2	76.96	-	23.04
Area 3	84.29	-	15.71
Area 4	98.43	-	1.57
Area 5	92.08	5.65	1.48

**Table 4. 5: EDX results for the single spot ablated ( $P_m$  70W,  $\tau$ 20 $\mu$ s, f10kHz, v500mms<sup>-1</sup>) in CTH025 composite.**

Element (%)	C	O	Co
Area 1	80.73	-	19.27
Area 2	75.99	3.20	17.23
Area 3	81.81	-	16.88
Area 4	86.58	2.67	8.63
Area 5	89.80	3.37	5.14

**Table 4. 6: EDX results for the single spot ablated ( $P_m$  70W,  $\tau$ 20 $\mu$ s, f10kHz, v500mms<sup>-1</sup>) in CMX850 composite.**

Element (%)	C	O	Co	W
Area 1	50.45	27.40	20.13	2.02
Area 2	79.50	3.29	15.77	1.44
Area 3	74.40	9.68	14.74	1.19
Area 4	81.53	5.49	9.52	3.46
Area 5	62.70	26.98	8.29	2.03

**Table 4. 7: EDX results for the groove ablated ( $P_m$  70W,  $\tau$ 20 $\mu$ s, f10kHz, v100mms<sup>-1</sup>) in CMX850 composite.**

Element (%)	C	O	Co	W
Area 1	45.96	3.80	38.74	11.50
Area 2	54.58	4.64	36.88	3.90
Area 3	56.29	11.83	27.76	4.11
Area 4	75.71	3.25	17.05	3.99
Area 5	83.19	-	15.70	1.11

#### 4.5.2 Observation and discussion

Preliminary chemical analyses (conducted from the manufacturer of the PCD structures, Element Six) indicated that the initial percentage of metallic binder (Cobalt) before PLA is 8% for specimen CTH025 (depicted in the blue line in Figure 4. 19) and 15% circa for specimen CTC002 (depicted in the red line in Figure 4. 19). It has been found that after single spot pulsed laser ablation, the Co percentage is higher than the initial 8% in four of the five analysed areas for specimen CTH025 (points 1, 2, 3, 4 above the blue line in Figure 4. 19); whereas the Co percentage is higher only in 2 of the five analysed areas for specimen CMX850 (points 1, 2 above the red line in Figure 4. 19).

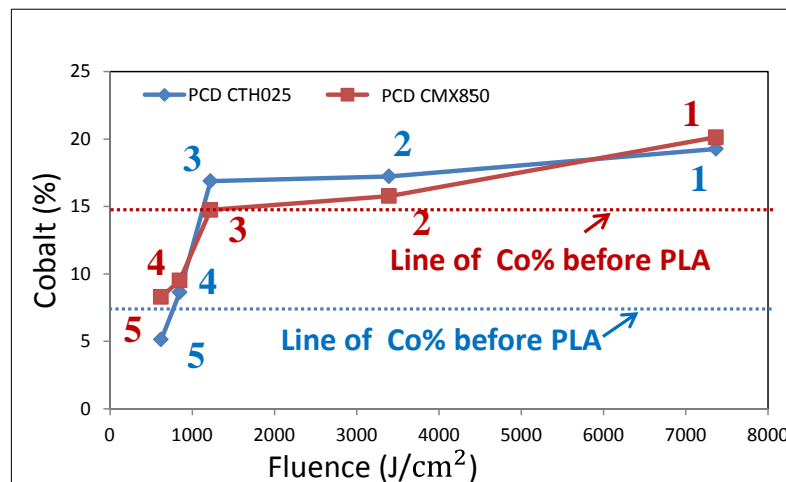


**Figure 4. 19: Comparative graph for laser ablated single spots in fine and coarse grained PCD specimens [74].**

The chemical analyses performed after the continuous groove was generated indicated that the cobalt percentage is higher than the initial 8% in three of the five analyzed areas for specimen CTH025 (points 1, 2, 3 above the blue line in Figure 4. 20); whereas the binder percentage is higher in all of the five analyzed areas for specimen CMX850 (points 1, 2, 3, 4, 5 above the red line in Figure 4. 20).

In all of the cases it was found that the higher percentage of binder after ablation was corresponding to the areas of highest  $P_L$  ( $382 \text{ MWcm}^{-2}$ ). It can be commented that during PLA, for the higher  $P_L$ , the temperature

reached in Area 1 ( $P_L = 382 \text{ MWcm}^{-2}$ ) is higher than the temperature in Area 5 ( $P_L = 31 \text{ MWcm}^{-2}$ ) and this resulted in material ablation through direct vaporization/sublimation [74], [122].

After PLA for the generation of a single spot and based on the evaluation of the beam footprint, the difference in binder percentage between the a coarse and a fine grained specimen decreases. On the one hand, when PLA is performed at high scanning speed ( $500\text{mms}^{-1}$ ) there is no big difference in the ablative effects for fine or coarse grained ultra-hard structures (in term of changes in chemical composition). On the other hand, in PLA at low scanning speed ( $100\text{mms}^{-1}$ ), the difference in binder percentage between the fine and coarse grain ultra-hard specimen is increased with  $P_L$ . In particular, the lower speed, by producing overlapping energies in every single spot, provoked an increased  $P_L$  causing higher quantity of binder to melt and redeposit [74].

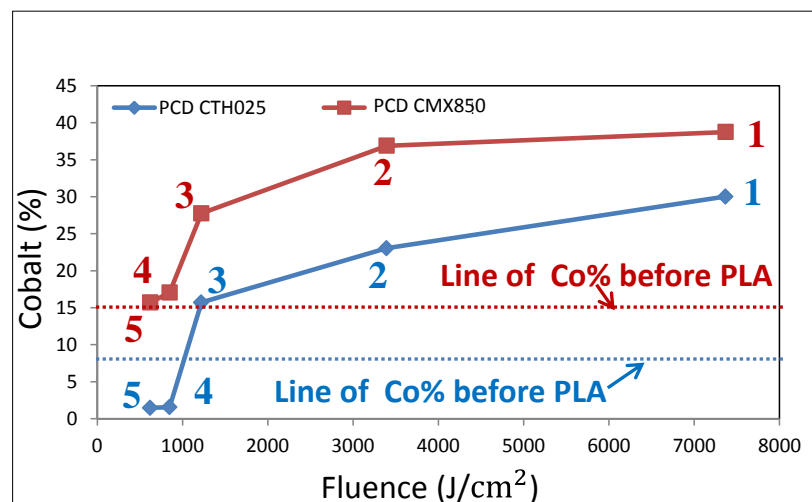


**Figure 4. 20: Comparative graph for laser ablated continuous grooves in fine and coarse grained PCD specimens [74].**

## 4.6 Conclusions and remarks

In this chapter based on an extensive (DOE) testing programme, the influence of energetic and kinematic parameters upon chemical changes in the microstructure were presented and discussed for microstructurally different PCD/PCBN target surfaces. Furthermore results of the

experimental approach (described in Section 3.4) for the identification of optimal laser parameters for PCD/PCBN composites are presented. The results of this study can be summarised as follows:

1. The DOE (Section 4. 2) enabled an understanding of the effect of laser parameters combination on the microscopic changes of PCD/PCBN structures after PLA. This lead to state that the minimum  $P_m$  value for ablation to occur is 40 W, and the interval of energy density to avoid in PLA of PCD/PCBN composites is  $10.6 \text{ MWcm}^{-2} < P_L < 17.7 \text{ MWcm}^{-2}$  .
2. The experiment on variation of energetic parameters (Section 4. 3) allowed to identify the topographical/microscopic changes occurring onto the target material and to relate them to the extent of energy in output from the laser. In particular it has been found that energetic parameters affect noticeably the geometry of craters/grooves: inhomogeneity in spot geometry might arise because of high energy density, thus the material directly converts to plasma. This consideration, together with the discussion on the material removal rate and depth of craters (Section 4.3.2), lead to choose an optimal  $P_m$  value of 70 W.
3. The experiment on variation of kinematic parameters lead to understand the proportion between beam scanning speed and depth of ablation: a speed decrease concentrates the energy in a smaller distance, thus there is a superimposition of energies that continuously overlap each other explaining a deeper ablated spot/groove.
4. The comparative results of chemical analysis before/after PLA have shown an increased percentage of binder in particular in the areas of highest energy density. It has been noticed that the extent of ablation in coarse/fine grained ultra-hard composites differ for low values of beam scanning speed, due to overlapping energies in the target material, provoking an increase of  $P_L$  and higher quantity of binder melting and redepositing.

In conclusion by considering a combination of energetic and kinematic thresholds it is possible to identify the PLA regimes that will yield high controllable pulsed laser ablated crater/grooves in microstructurally different ultra-hard materials. Despite this, there is still a lack in understanding the basic process of PLA when the target material is a polycrystalline ultra-hard composite. Chapter 5 will cover in details the results of a novel technique for the evaluation of the thermal response of any ultra-hard material.

# Chapter 5

## Thermal response of PCD/PCBN composites to PLA

This is an essential chapter for the development of the research work. Results for a combined technique FIB/HRTEM/EELS are presented and discussed for one PCD specimen and one PCBN sample, aiming at understanding the thermal response of the ultra-hard composites as a function of the variable energy density during a single pulse. In particular, allotropic transformation of C (for PCD specimen) and BN (for PCBN specimen) are here reported.

### 5.1 Thermal response of PCD structures to PLA

As described in detail in Section 3.5.1 only one PCD and one PCBN specimen was selected for HRTEM analysis. This is due both to the achievement of the objectives and also to timing problems mainly because the technique FIB/EELS/HRTEM is an extremely time consuming procedure. As mentioned in the methodology Section 3.5.1 there were two main areas on which attention has been paid in the analysis of each specimen: a low fluence region, corresponding to the upper part of the groove, and a high fluence region, corresponding to the lower part of the ablated groove (see Figure 3. 8).

#### *5.1.1 Results of FIB/HRTEM/EELS analyses of the high fluence ablated site*

The results of the FIB technique for the preparation of the lamella (in the area where the peak laser fluence is experienced) is summarised in Figure 5. 1: the white area at the top of the image represents the protective coating described in detail in Section 3.5.2, a distinct boundary with the ablated surface of the PCD is evident; the dark area shows the thinned lamella at a thickness 100-150nm. A low resolution EELS scan (green scale

in Figure 5. 1 indicates direction and length) was initially made in order to identify the characteristics of the PCD CMX850 specimen and the presence of carbonic allotropes at increasing depths under the ablated surface.

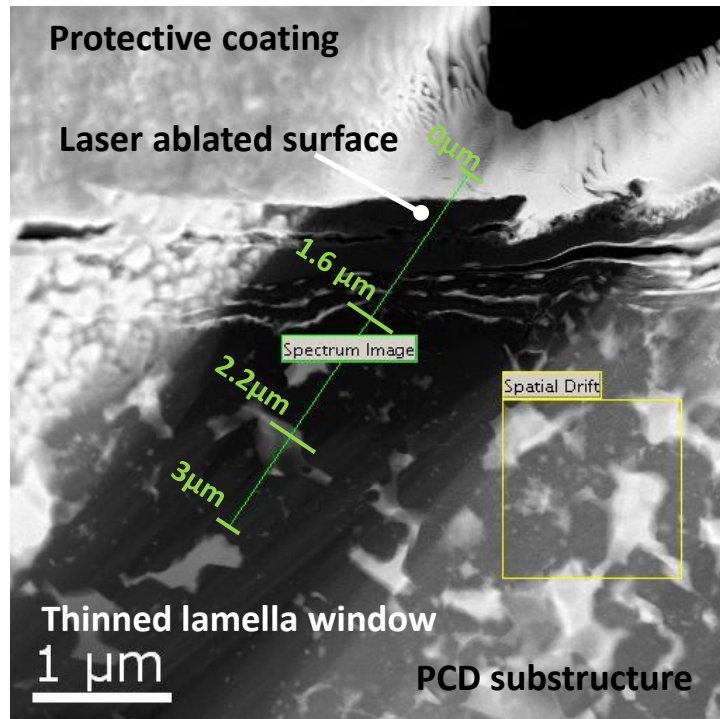


**Figure 5. 1: TEM image of the thin lamella (as presented in Figure 3.13 in Section 3.5.2) in PCD CMX850 from area of high laser fluence region showing the protective coating and underlying PCD substructure and EELS scan length and direction.**

Results from the low resolution EELS scan are refigured in Figure 5. 2: the X axis corresponds to the depth of EELS scan previously shown in Figure 5. 1; the red profile represents the trace sensitive to all carbon allotropes in the region 0.2 – 2.2  $\mu\text{m}$ , while the green profile being the trace sensitive only to graphitic allotropic concentrated in the range 0.2 – 1.7  $\mu\text{m}$  [109].

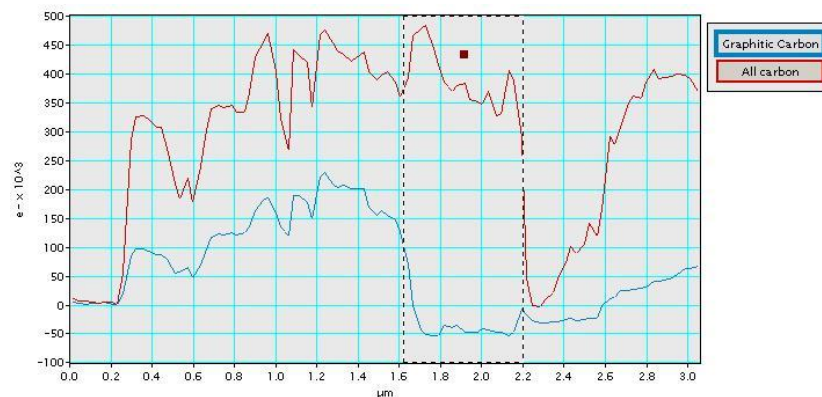


**Figure 5. 2: EELS low resolution scan results across the green scan length shown in Figure 5. 1 [109].**

The low resolution EELS scan did not allow a precise identification of the allotropic forms in specific areas of analysis, for this reason, high resolution EELS scans were subsequently carried out in selected areas, both in the identified graphitic regions of the material and into the regions where the state of the PCD was not expected to have been affected by the intense thermal activity of ablation, to the maximum scan depth of  $3\mu\text{m}$  [109]. While the low resolution EELS scan indicated the presence of all carbon (without specific indication of the type of allotrope) and graphitic traces, results of the high resolution EELS have indicated a clear signature of both allotropes of carbon: diamond and graphite. The scan results showing a graphite signature in the region  $0.2 - 1.7\ \mu\text{m}$  are refigured in Figure 5. 4, while the clear proof of diamond trace in the scan region beyond a depth of  $1.7\ \mu\text{m}$  is indicated in Figure 5. 3. Both images contain a reference graph from the literature for the comparison of EELS peaks spectra or the identification of the correct profile: it is possible to notice a slight gap in energy loss on the X axis between the achieved results and the reference from literature; this can be explained considering the thickness of the prepared lamella, in fact, some superimposition of carbon allotropes and the element signatures of the different materials, might occur producing a deviation of energy loss from the pure allotrope signature.

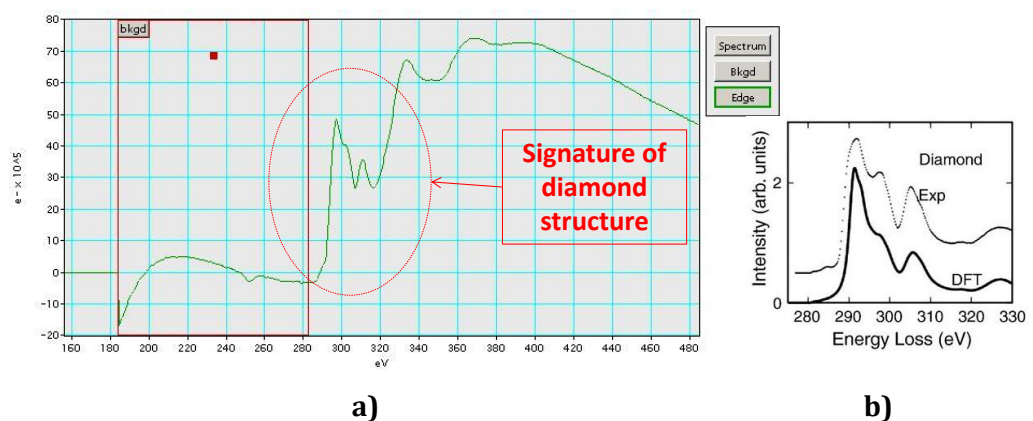


**Figure 5. 3: High resolution EELS scans of the thinned lamella region showing: a) a signature trace of diamond; b) a reference of diamond structure signature from literature [11].**

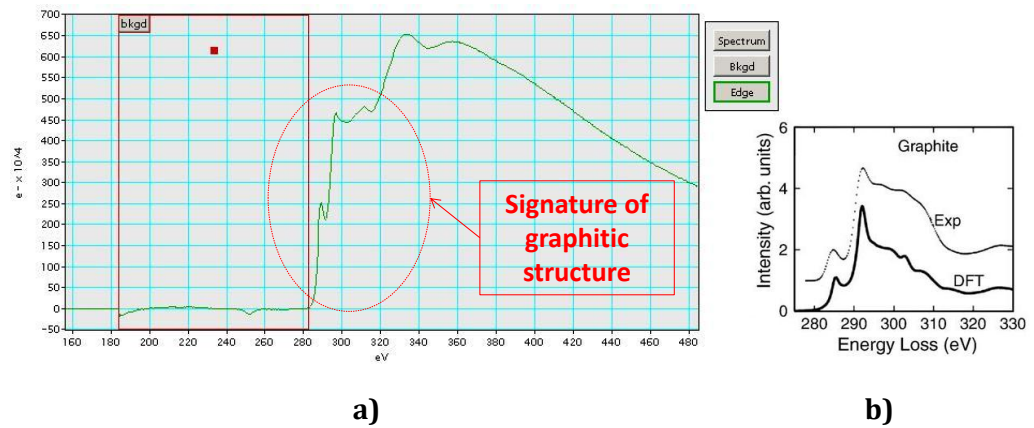


**Figure 5. 4: High resolution EELS scans of the thinned lamella region showing: a) a signature trace of graphite, b) a reference of graphite structure signature from literature [11].**

Once the results from EELS scan were achieved, HRTEM imaging was carried out to identify the crystallographic structures/presence of the EELS identified carbonic allotropes resulting from the intense thermal ablative activity and to determine the presence and form of the Cobalt binder in the underlying material structure [109]. HRTEM results of the most thermally exposed (high fluence region) part of the ablated groove are depicted in Figure 5. 5. The image in the centre at a scale of 0.5 micrometres is a representation of the overall region where the allotropic phases are identified and analysed: immediately below the ablated surface of the PCD a band of amorphous carbon has been found measuring approximately 0.8  $\mu\text{m}$  in depth, as demonstrated in the HRTEM image at 10 nm resolution in the insert in Figure 5. 5.

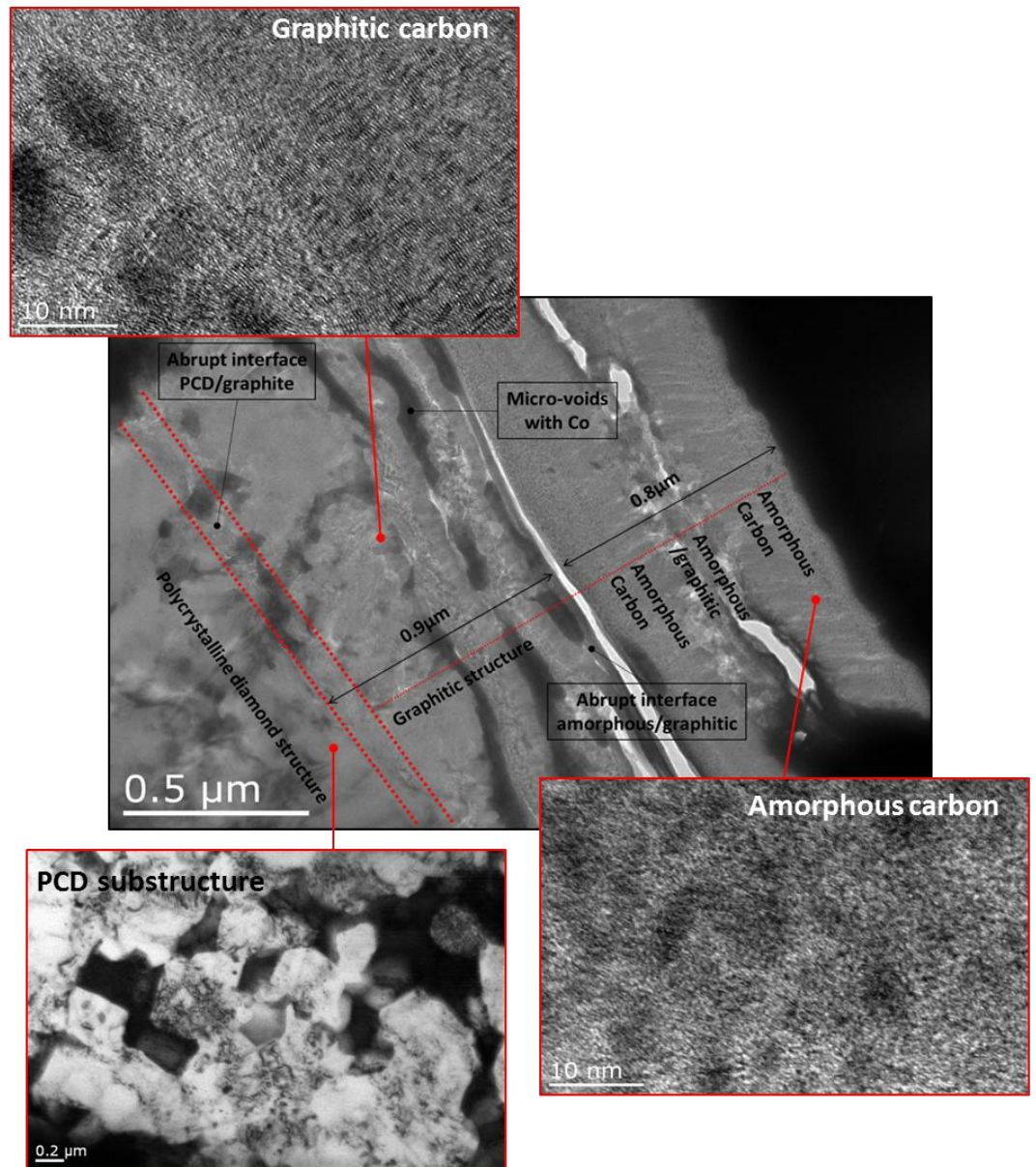


**Figure 5. 5: HRTEM image of the lamella of the high energy density site showing the allotropic changes into the substructure and the metallic binder pockets [109].**

The black voids (Figure 5. 5), that EDX analyses have demonstrated to contain metallic binder (Figure 5. 7), divide the amorphous band from the graphitic, creating an abrupt interface amorphous to graphitic carbon.

The HRTEM image from the latter region is shown in the insert in Figure 5. 5, the presence of a 0.9  $\mu\text{m}$  graphitic band was previously shown by EELS scan (Figure 5. 4). Another abrupt interface between PCD substructure and graphitic band is evident from the TEM image in Figure 5. 5.

The PCD substructure was identified by performing further TEM analyses in the region beyond 1.7  $\mu\text{m}$  on the EELS scan. Selected area diffraction

patterns were utilised to establish the crystallographic integrity of the laser ablated PCD substructure and the results of this are represented in Figure 5. 6a: this presents a clear signature of the crystallographic intergrowth of the diamond grains and the associated infiltrative zones containing cobalt binder.

The use of TEM diffraction pattern (Figure 5. 6b) help to identify the crystallographic lattice structure of the diamond grain in a monocrystallographic structure in the area immediately below the graphitic one, indicating the crystallographic integrity of the diamond grains in the PCD substructure [109].

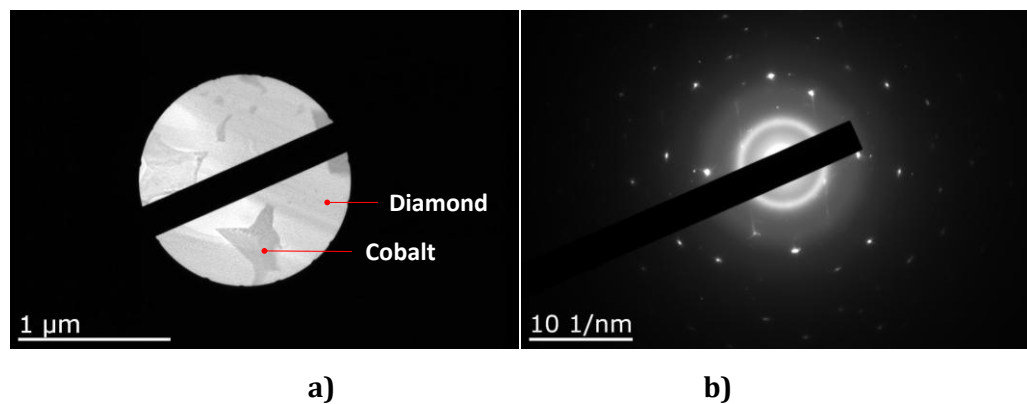


**Figure 5. 6: TEM back focal plane imaging of PCD CMX850 substructure: a) diamond grain intergrowth and binder structure; b) diffraction pattern of an individual diamond grain.**

The presence of cobalt in the voids at the interface amorphous/graphitic carbon was demonstrated by the results achieved both from Energy-Dispersive X ray (EDX) and from Scanning Transmission Electron Microscope (STEM) imaging capabilities (Figure 5. 7). In the latter image bright field imaging (Figure 5. 7a) and energy filtered TEM map for Cobalt (Figure 5. 7b) show the presence of this element in the pockets/elongated features. The TEM investigations performed in all of the investigated voids demonstrated a consistency in the presence of cobalt both in the region of amorphous carbon (depth 0.8 μm) and in the region of graphitic carbon (depth from 0.8 ÷ 1.7 μm), whereas an explanation of such a behaviour could be found in a possible collapse of the ultra-hard matrix and consequent entrapping of metallic binder in the formed elongated areas.

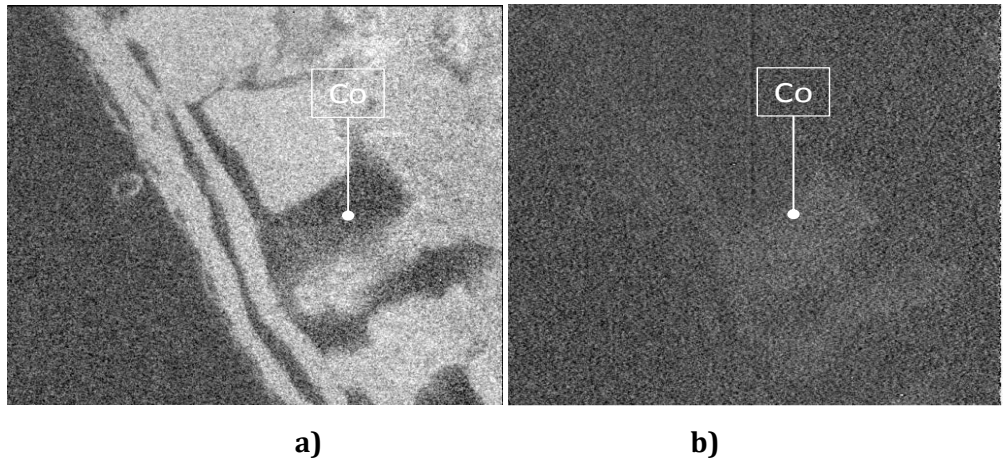


**Figure 5. 7: TEM imaging of the voids containing metallic binder: a) Energy Filtered TEM image indicating carbon presence in white areas and cobalt in dark areas; b) Cobalt sensitive Energy Filtered TEM.**

### ***5.1.2 Results of FIB/HRTEM/EELS analyses of the low fluence ablated site***

The HRTEM/EELS scan analyses performed on the upper part of the groove, corresponding to the ablated area that experienced lower fluence, revealed a similar layered structure from the top of the groove to the PCD untouched substructure. There is a substantial difference in the extent of amorphous and graphitic bands; this is shown in Figure 5. 8: a low resolution image in the insert indicates the area of analysis and the high resolution image (at 50 nm scale), the amorphous band has been reduced to 0.07  $\mu\text{m}$  while the graphitic band to 0.25  $\mu\text{m}$ . Despite of the reduction in thickness of the allotropic bands, it is evident from Figure 5. 8 that also in this case, the PCD structure reacted to the laser pulse with the formation of voids containing the metallic binder as confirmed from the Energy Filtering/Scanning Transmission Electron Microscope investigations. The HRTEM imaging and high resolution EELS scans revealed the polycrystalline diamond boundary with the graphitic carbon exists at a depth of approximately 0.32  $\mu\text{m}$  below the ablated surface [109].

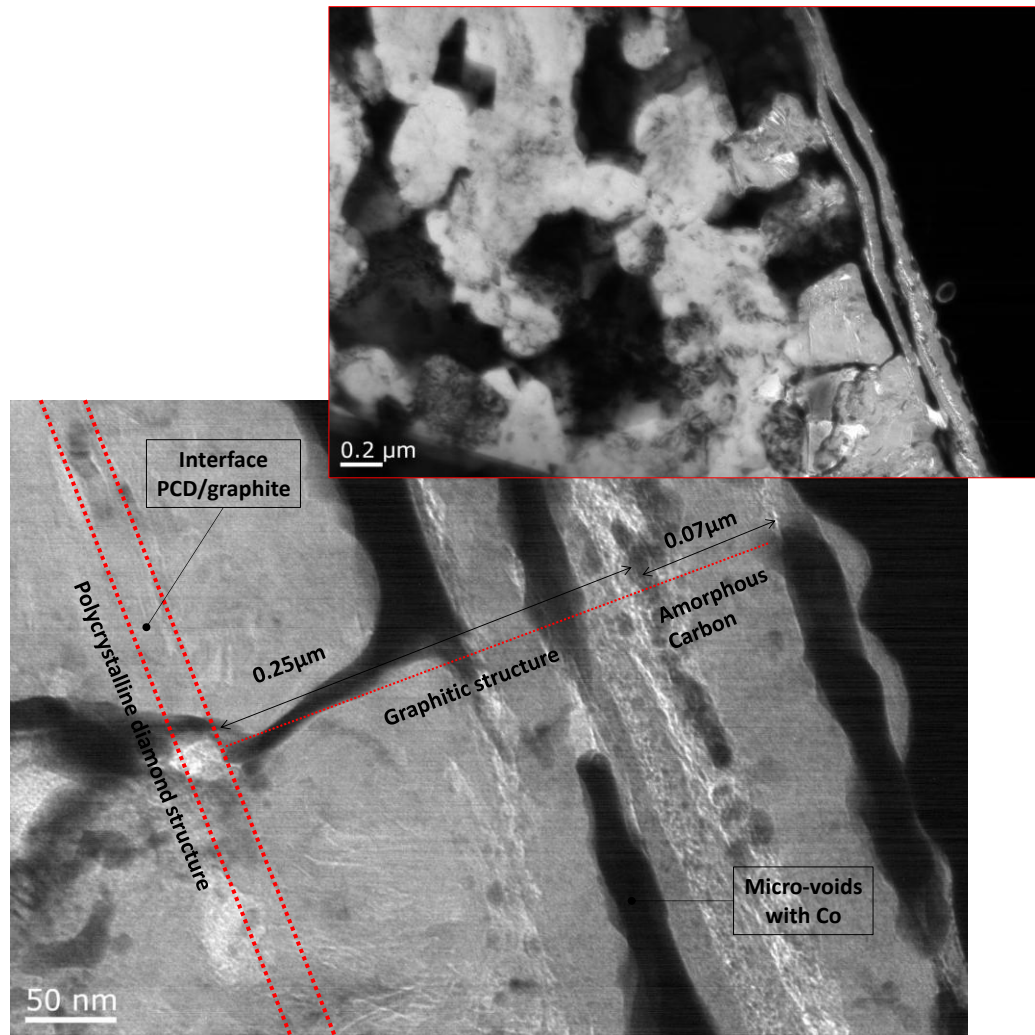


**Figure 5. 8: HRTEM imaging of the interface graphite/PCD in the upper part of the groove (lowest energy density region).**

### ***5.1.3 Observation and discussion***

The novel technique made of the combination of protective multiple surface coating, GIS deposited Tungsten strap extending between the protective coatings and the PCD substructure, allowed extraction and further stabilisation of the laser generated PCD groove to achieve a successful lamella thinning. This allowed the subsequent TEM investigations and the evaluation of the carbon allotropic structures and the interface binder/diamond. The results shown in Sections 5.1.1, 5.1.2 have indicated that both in the area of the lamella with high and low fluence intensity, two interfaces were formed onto the structure as a consequence of PLA: amorphous/graphite and graphite/diamond; a similar result was already found in the single crystal diamond study [92].

This result proved to be repeatable in both of the extracted lamellas. Despite of the formation of two interfaces in both ablated areas, the extents of graphitised and amorphous layers in the two cases were found to be affected by the extent of laser fluence (energy density) experienced, this result confirms what has been described already in literature of PLA of diamond [123]. In particular, it can be commented that in the low fluence ablated site (Figure 5. 8), the measured graphitised layer is 70 % smaller than the one in the high fluence ablated area (Figure 5. 5). This can be explained considering that, for the same pulse duration, PCD experiences higher energy beam density in the lower part of the lamella, therefore the conversion of diamond into graphite is extended [122]. Regarding the formation of an amorphous band in both areas, this could be due to the disordered molecular arrangement associated with amorphous carbon. In fact, it could be that the formation of an amorphous band depends on a phase change during PLA: this region could have entered a liquid phase during the ablation pulse and then rapidly has solidified. The presence of a relative thick layer of graphite below the amorphous region could be caused by the ordered molecular arrangement of the graphite: this region experienced a state change from diamond to graphitic carbon while remaining in the solid state [109]. TEM images (in low/high fluence areas) have shown elongated voids which EDX, Energy Filtered TEM mapping and z-contrast STEM analyses have proved to contain cobalt traces, most probably this is depending on the pulse duration used for PLA of the grooves. The pulse duration utilised in this research is of microsecond type, and this is longer than the Cobalt thermal relaxation time (time used by the target to dissipate 63% of the incident thermal energy) that is in the order of femtosecond [93], [124]; thus vaporisation would have occurred in the laser pulse timeframe, which is in accordance with the theoretical behaviour of this metal as stated in literature [4], [5]. This can be explained considering the high absorption and low vaporisation enthalpy of cobalt ( $382.4 \text{ kJ mol}^{-1}$ ) reported in Section 2.3: during a single ( $\mu\text{s}$ ) laser pulse, the thermal properties of cobalt would have enhanced its quick vaporisation and caused a

consequent ionization, where some of the metal electrons become free [125], absorbing energy directly from the beam and consequently producing higher temperatures, further ionization and absorption [109]. The gap in timing between the pulse duration and the relaxation time of cobalt, would have caused the process of increased temperatures/vaporisation/increased absorption to repeat cyclically with subsequent partially overlapped laser pulses in the formation of the groove [109].

## 5.2 Thermal response of PCBN structures to PLA

The PCBN specimen selected for the HRTEM/EELS analyses is a DCC500, its microstructural properties have been shown in Figure 3.7, Table 3.1, its thermo-mechanical properties reported in Section 2.1; and the reasons for the selection of this specific PCBN specimen have been reported in Section 3.5.1 (see Figure 3.13 b).

Results from the focused ion beam milling activity for the PCBN DCC500 laser ablated specimen are depicted in Figure 5. 9 where a lamella of rectangular geometry is refigured (length, 30  $\mu\text{m}$ ; depth, 5  $\mu\text{m}$ ; thickness, 150 nm); the two regions of HRTEM/EELS analyses are indicated by red arrows and they are representative of the low fluence area in the upper part of the thinned lamella and high fluence area in the lower part of the lamella.

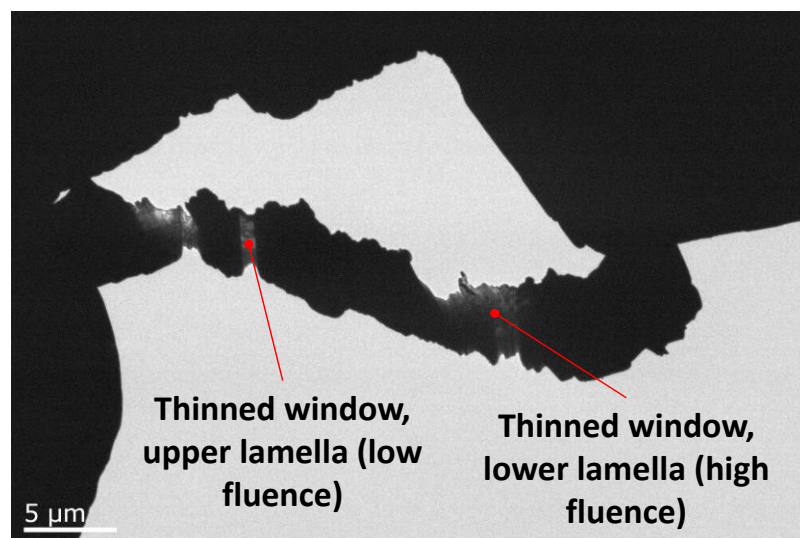
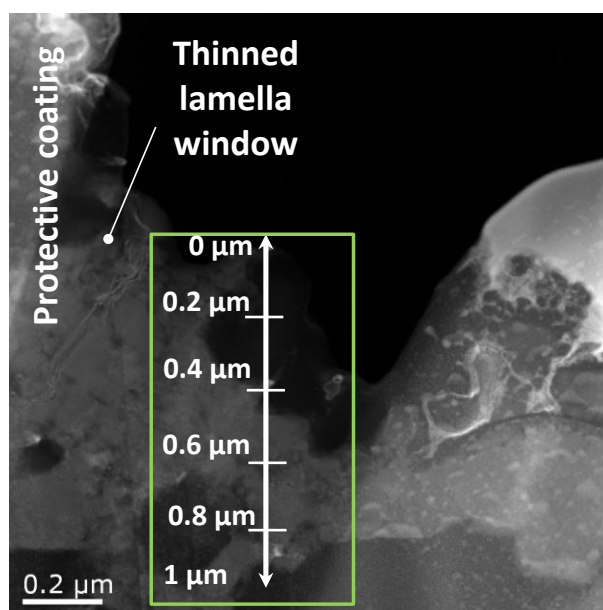


Figure 5. 9: HRTEM imaging of the thinned lamella window (see 3.13.b).

### ***5.2.1 Results of FIB/HRTEM/EELS analyses of the high fluence ablated site***

From the work on the ablative effect of PLA of PCD (Section 5.1) it has been noticed that the PCD specimen revealed a thermal response up to a depth of 2.2  $\mu\text{m}$ . In the case of the PCBN specimen here reported, the material has revealed to be thermally affected up to a depth of 1  $\mu\text{m}$ , where this difference is due to the higher thermal stability of PCBN when compared to PCD; this is better explained in the discussion section.

The thinned lamella results of the FIB technique of the area where the peak laser fluence is experienced is shown in Figure 5. 10: the thinned lamella is represented by the darker thin area representing a thickness of 100-150 nm; the green scale indicates the maximum selected depth of 1  $\mu\text{m}$  for the EELS scan that was initially made in order to identify the characteristics of the PCBN DCC500 specimen and the presence of BN allotropes at increasing depths under the ablated surface.



**Figure 5. 10: TEM image of the thin lamella in PCBN DCC500 from area of high laser fluence region showing the protective coating and underlying PCBN substructure and EELS scan length and direction.**

The areas for preliminary HRTEM analyses are shown in Figure 5. 11: areas from 1 to 3 are representative of the regions where EELS scan has been performed to a depth of 1  $\mu\text{m}$  as shown in Figure 5. 10. Area 1 is the closest to the ablative effects and area 3 the one not affected by PLA.

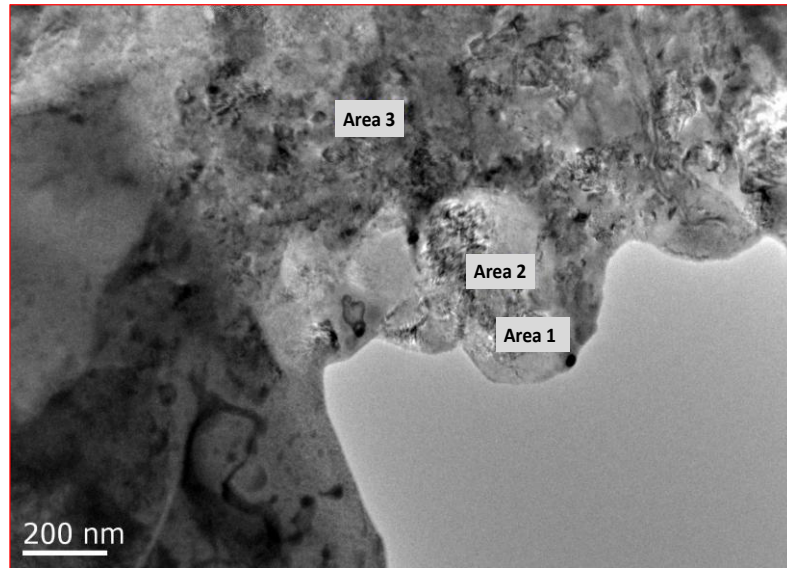


**Figure 5. 11: TEM image of the thin lamella in PCBN DCC500 from area of high energy density showing the initial areas of analysis for HRTEM.**

HRTEM images for area 1 are depicted in Figure 5. 12: the hexagonal allotrope of BN (hBN) has been found from the top of the groove to a depth of 50 nm, while transition from hBN to cBN is revealed in the HRTEM image indicating the cBN atomic spacing beyond a depth of 80 nm. Immediately beyond a depth of 50 nm an area of transition between hBN and cBN seems to appear in the HRTEM image (Figure 5. 12), this has been validated by high resolution EELS scan shown in Figure 5. 15.

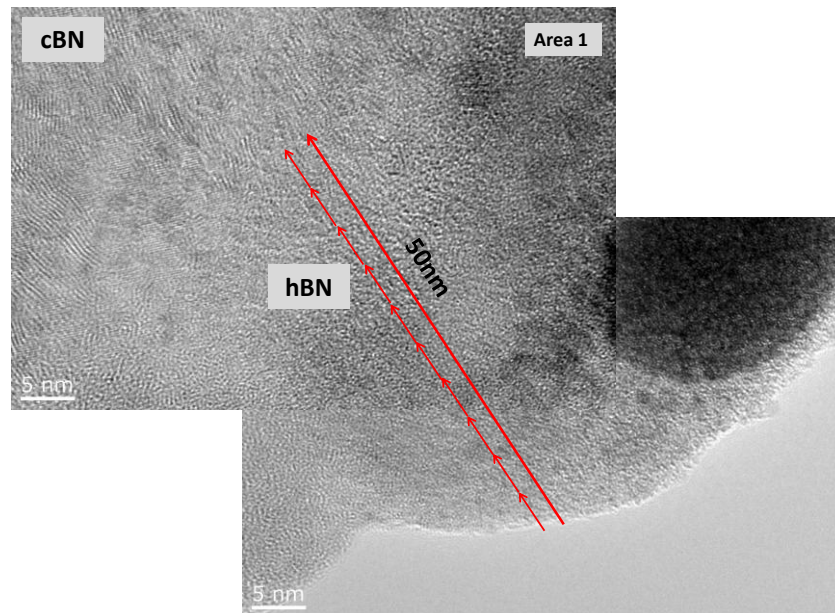


**Figure 5. 12: HRTEM image of Area1 achieved by the combination of two separate micrographs but unified to show the interface hBN/cBN.**

Results for area 2 (previously shown in Figure 5. 11) corresponding to a depth between 50 nm and 80 nm, are reported in Figure 5. 13: the orderly atomic *d spacing* indicated the presence of cBN, while analyses in area 3 showed a 0.27 nm atomic spacing that revealed the presence of the ceramic binder, TiC.

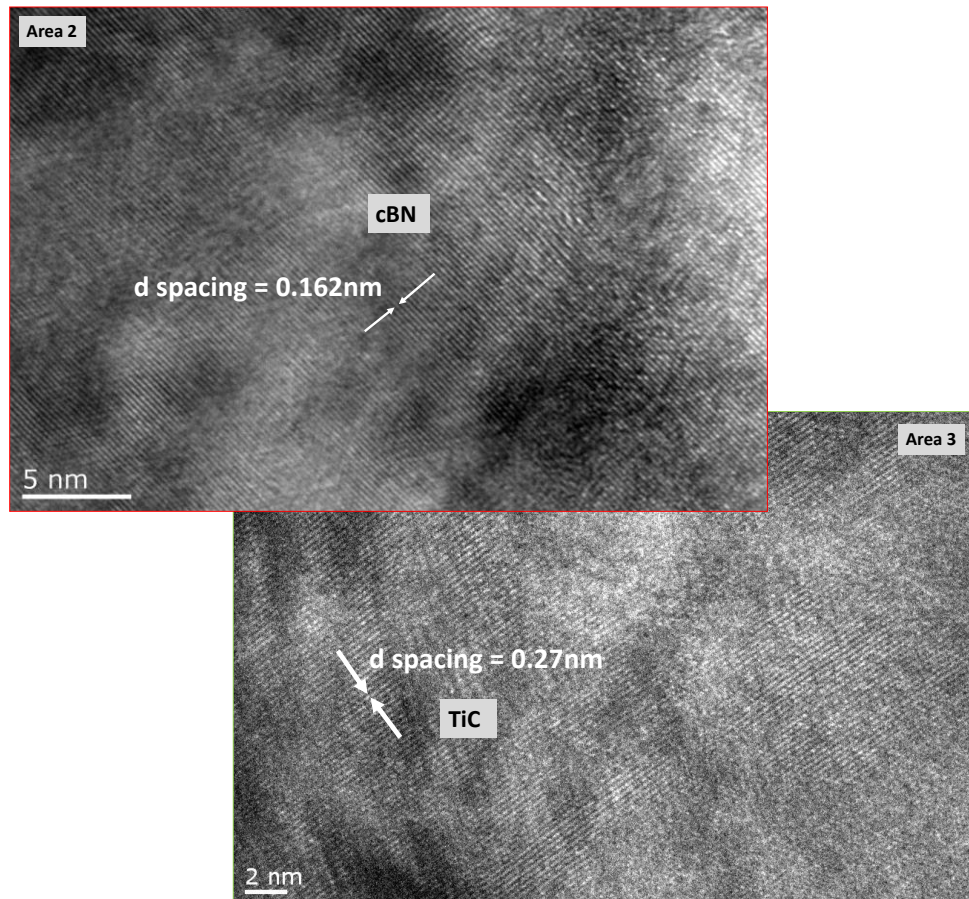


**Figure 5. 13: HRTEM image of Area1 from Figure 5. 10 showing the substructure of DCC500 not affected from the PLA process with areas of the binder TiC and cBN.**

An high resolution EELS scan was made to confirm whether the presence of allotropes cBN and hBN were artefacts due to the superimposition of different crystals in the lamella or they really occurred as a consequence to the thermal excitation during PLA.

The high resolution scan concentrated in a depth up to 0.15  $\mu\text{m}$ , in three single steps of 0.05  $\mu\text{m}$  as shown in Figure 5. 14.

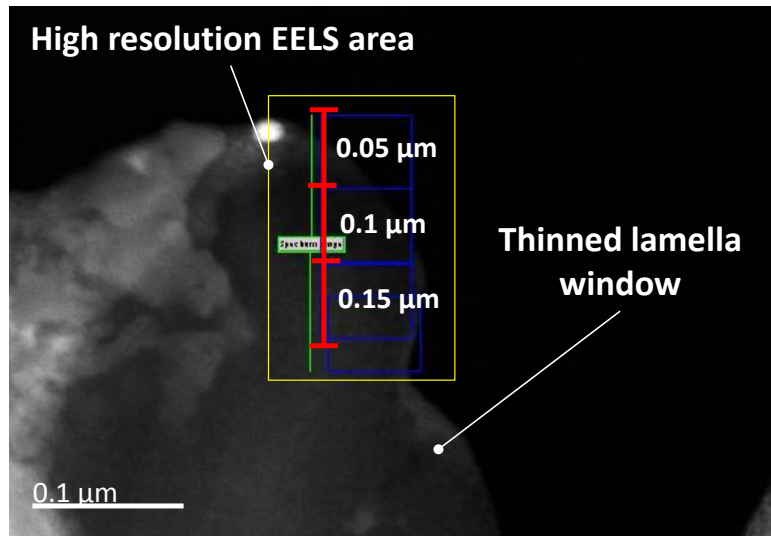


**Figure 5. 14: TEM image of the thin lamella in PCBN DCC500 from area of high laser fluence region showing high resolution EELS scan length and direction.**

Results from high resolution EELS scan have revealed a clear signature of hBN structure in the area of high fluence till a depth of 50 nm (indicated by first gap in Figure 5. 14) as shown from the double energy peak in Figure 5. 15a: the first energetic peak at 190 eV representing a clear sign of hBN, as also confirmed from the hBN peak reported in literature (Figure 5. 15d). EELS scan up to 0.1  $\mu\text{m}$  depth (shown from red arrow in Figure 5. 14) revealed a clear sign of transition between hBN and cBN: a peak is still appearing at 190 eV but this time the peak has a much lower intensity, almost tending to disappear (Figure 5. 15b). The high resolution EELS scan at a depth of 0.1  $\mu\text{m}$  shown in Figure 5. 15c revealed the presence of cBN, validating what has been indicated by the HRTEM analyses.

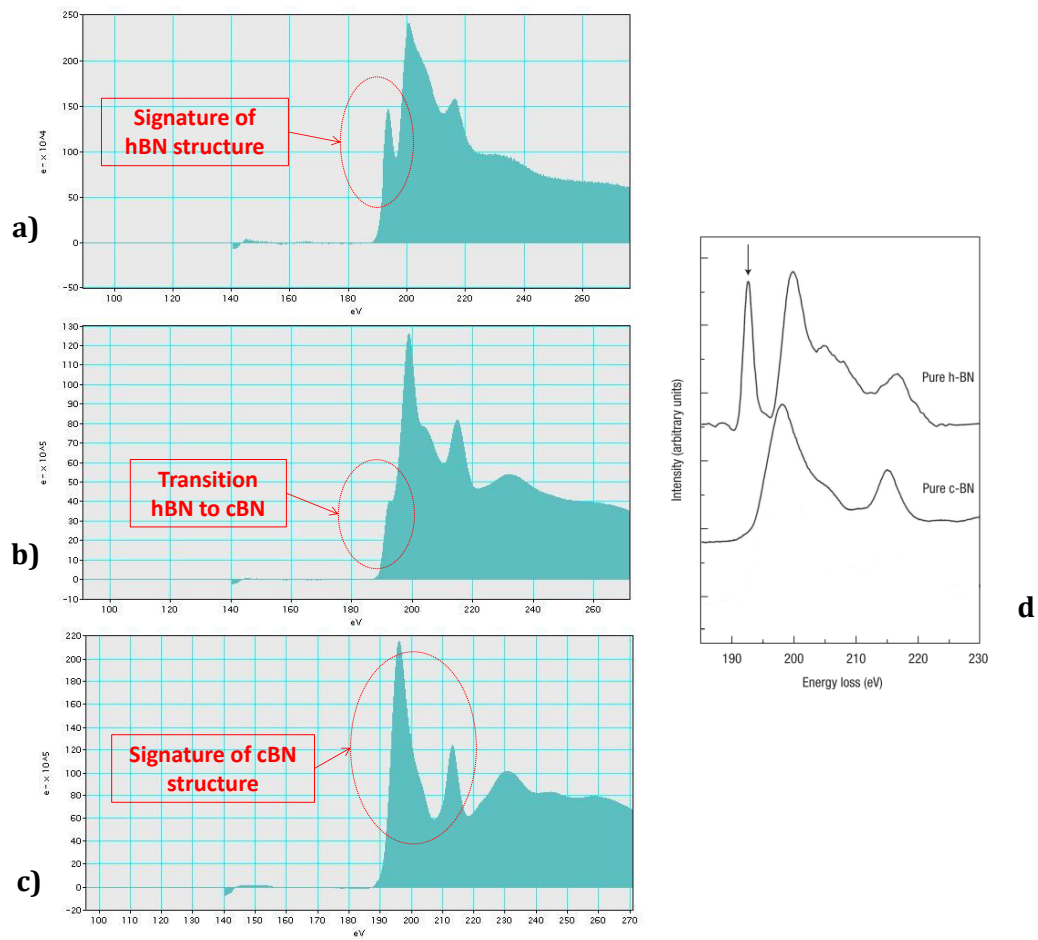


**Figure 5. 15: High resolution EELS scan results of the thinned lamella region showing: double energetic peak typical signature of hBN; b) transition between hBN and cBN; c) energetic peak at 200 e V typical of the on the right a reference of the EELS signatures from literature [126].**

The allotropic transformations of BN were also confirmed by the use of TEM diffraction pattern: two different diffraction patterns were found, indicating the presence of two well defined and separated crystallographic lattice structures of BN. A TEM back focal plane image of the revealed diffraction patterns is depicted in Figure 5. 16: the red and green diffraction patterns are here overlapped to identify the difference in the crystal structures for hBN and cBN.

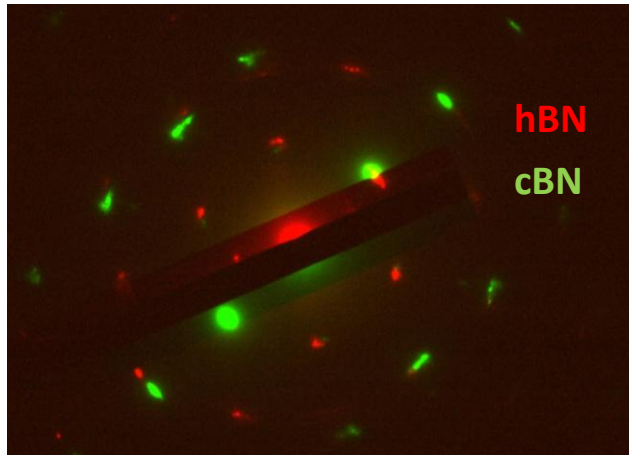


**Figure 5. 16: TEM back focal plane overlapping imaging of PCBN substructure showing the diffraction pattern of BN grains in hBN and cBN.**

After identification via EELS of the signature of BN allotropic changes, an ultimate HRTEM analysis was performed to have a high resolution TEM imaging of the transition between hBN and cBN at a depth of circa 70 nm from the ablated area. The result is shown in HRTEM image in Figure 5. 17: the measured *d spacing* indicated a clear presence of hBN and cBN and an unexpected  $\alpha$ BN (amorphous boron nitride) band has been found, similarly to the case of PCD HRTEM analyses. Based on these results, discussion in Section 5.2.3 widely explains the formation of different allotropes and proposes an experimental thermal response of PCBN structures to PLA.

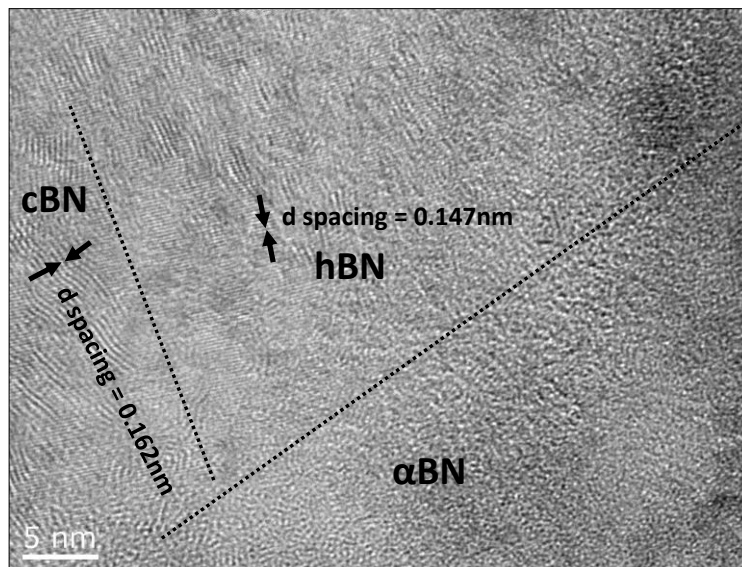


**Figure 5. 17: HRTEM image of interfaces hBN, cBN,  $\alpha$ BN in the high energy density area of specimen PCBN DCC500.**

### ***5.2.2 Results of FIB/HRTEM/EELS analyses of the low fluence ablated site***

The HRTEM/EELS scan analyses performed on the upper part of the groove, corresponding to the ablated area that experienced lower fluence, revealed a different material reaction to the thermal excitation.

Low resolution EELS scan were performed up to a depth of 2  $\mu\text{m}$ , to identify any change in allotropic phase and evaluate the material thermal response to PLA at low fluence. The EELS scan results have not revealed any allotropic phase change and the only allotrope of BN found was cBN, no signature of hBN was found: this is due both to the low energy density transmitted in the target material and to the focused ion beam activity which can possibly remove the upper layer of the lamella corresponding to the area of allotropic phase change (if an allotropic change has occurred, this was of smaller extent in comparison with the area of high energy density). For this reason, this experiment focused on the understanding of the thermal changes affecting the interface cBN/ TiC.

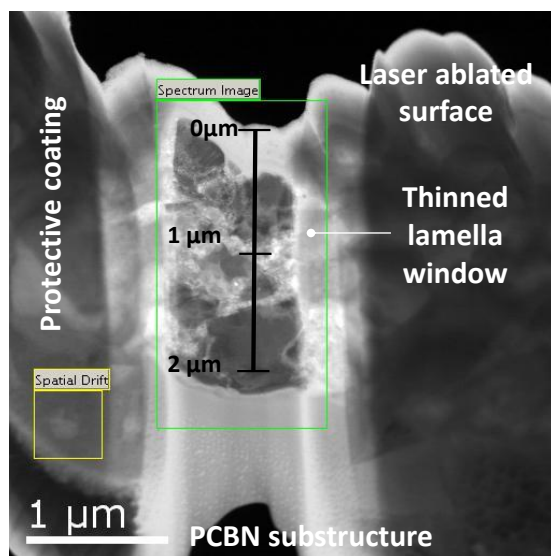


**Figure 5. 18: TEM image of the thin lamella in PCBN DCC500 from area of low laser fluence region showing the protective coating and underlying PCBN substructure and EELS scan length and direction.**

Results from EDX for the considered area at low fluence are reported in Figure 5. 19: individual region of analyses are here shown and the chemical environmental analyses are reported in Table 5. 1.

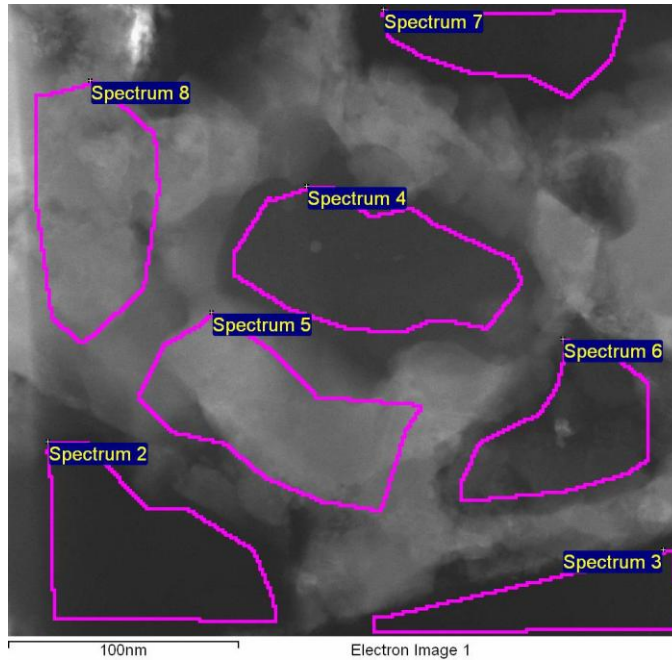


**Figure 5. 19: EDX area of scan for chemical environmental analysis in the area of low fluency for PCBN specimen DCC500.**

**Table 5. 1: Results for EDX scan of Figure 5. 19.**

<b>Spectrum</b>	<b>B</b>	<b>C</b>	<b>N</b>	<b>O</b>	<b>Al</b>	<b>Ti</b>	<b>W</b>
Spectrum 2	40.25	5.15	37.78	2.88	0.27	1.16	4.95
Spectrum 3	35.71	2.06	34.57	1.43	0.97	2.03	12.51
Spectrum 4	-9.73	0.66	0.8	36.28	53.49	2.18	23.22
Spectrum 5	4.31	16.56	-6.93	3.1	2.9	60.96	16.32
Spectrum 6	19.65	0.85	20.3	3.01	5.16	25.56	19.09
Spectrum 7	11.17	5.58	26.08	3.1	-0.26	4.4	25.48
Spectrum 8	4.6	19.16	-4.79	3.31	3.56	61.39	49.93

The bright areas have revealed high percentage of titanium and carbon, indicating the presence of TiC; while the dark areas, rich in boron and nitrogen, indicated the presence of BN. Some dark areas have revealed the presence of aluminium (Figure 5. 20). The EDX analyses have basically indicated a typical PCBN DCC500 structure, with no thermal affected areas or allotropic changes.

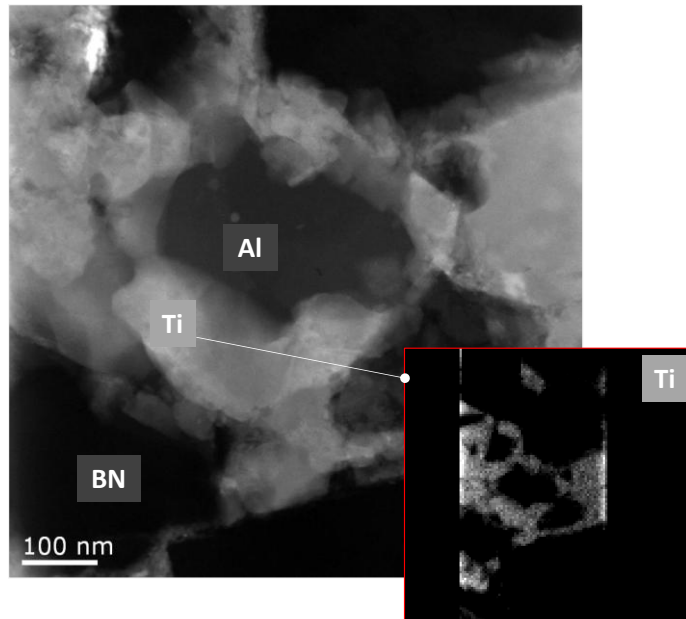


**Figure 5. 20: TEM image of the voids containing Al and BN; the insert represents a Titanium Sensitive Energy Filtered TEM image indicating that all of the grey areas is Titanium.**

Clear sign of an abrupt interface between cBN and TiC were observed in the HRTEM analyses (Figure 5. 21) where the measured *d spacing* indicated the presence of both the ultra-hard phase and the ceramic binder. There is a substantial difference with the region of high fluence in the presence of hexagonal allotrope of BN only when an intense thermal excitation occurs.

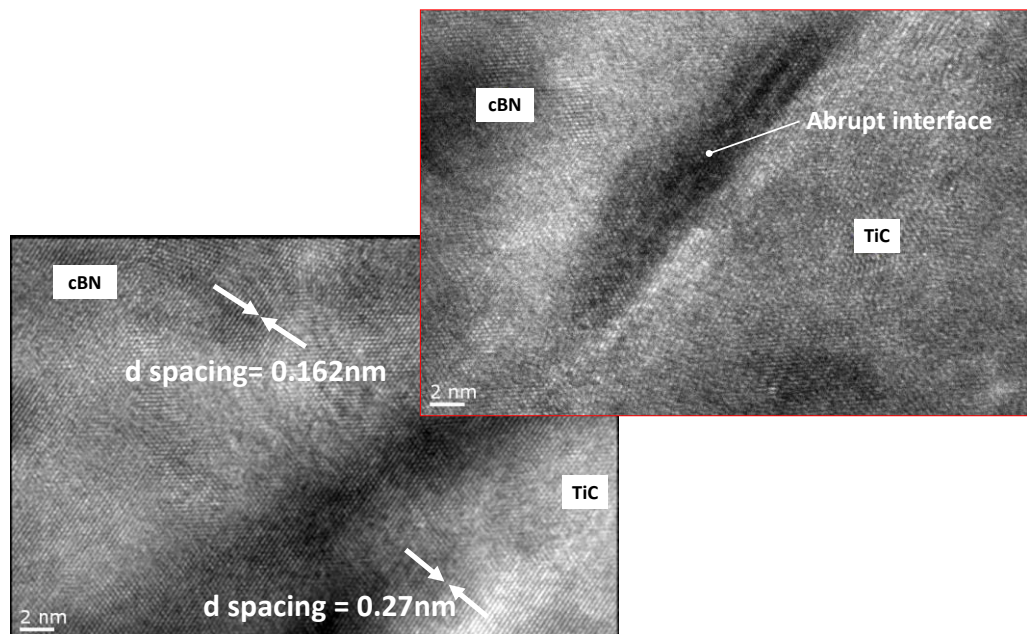


**Figure 5. 21: HRTEM image of the lamella of the low energy density site showing the abrupt interface between BN and TiC.**

### **5.2.3 Observation and discussion**

An experimental model for the thermal response of a low-CBN content PCBN specimen to PLA has been proposed and a summary of results is depicted in Figure 5. 22: the analysed laser generated groove is shown in cross section and the difference in BN allotrope changes/formation is revealed in the low/high fluence areas. HRTEM/EELS/EDX analyses in the high fluence area have shown a layered structure formed by: an  $sp^3$ -hBN structure till a depth of 50nm, followed by a transition phase hBN to cBN up to a depth of 100nm; while an untouched cBN substructure with TiC binder has been revealed beyond a depth of 100nm, indicating that beyond a depth of 1  $\mu$ m, the specimen is not affected from the thermal excitation. Furthermore, in the area surrounding the hBN extent, amorphous boron nitride allotropic ( $\alpha$ BN) traces were found. The transformation of the initial cBN into hBN could be explained considering the thermal excitation caused by intense fluence laser activity. In fact, under ambient conditions the transition from  $sp^2$  to  $sp^3$  bonding is impeded by a kinetic barrier [11] which requires a large reaction energy provided by high pressure and temperature conditions to effect the hBN-cBN phase change; in the case of PLA at high fluence, the achieved reaction energy produced by PLA would have created favorable condition for the allotropic change. This also explains why this transformation did not occur in the area of the groove which experienced low fluence. The formation of amorphous traces in the area surrounding the transformation region can be explained by considering the microstructural evolution of BN transition phases. In fact, many studies in literature have demonstrated that the transition between hBN to cBN does not occur directly, but an amorphous BN layer formation might take place [21] due to heat conduction into the substrate [11]: because of the intense energetic activity and high temperature achieved in the high fluence area the formation of an amorphous BN did not occur in the area that experience low fluence, especially because the formation of an amorphous layer is often connected to the allotropic change hBN to cBN [127]. The transformation hBN to cBN might not have been direct, and this would explain the presence of an

amorphous region ( $\alpha$ BN) in the area surrounding hBN. In fact, there is usually a pre-transformation of hBN to rBN [127] before achieving the cBN allotrope. In the EELS/HRTEM reported results rBN could not be clearly identified, mainly because of peak broadening deriving from weak crystal quality but previous studies already proved that in the low angle range the rhombohedral and hexagonal phase show a similar diffraction pattern, which would explain why this further allotropic change could not be identified [127]. All of the transformations occurring in the high fluence area have shown not to affect the ceramic binder and its interface with the ultra-hard grains, leaving an untouched PCBN substructure already at a depth of 1  $\mu$ m. Different thermal response is the one exhibited by the upper part of the groove, experiencing a low fluence laser. A combination of EDX, EELS, HRTEM revealed an undisturbed PCBN structure, which indicated the possibility of PLA in specific set of fluencies to avoid the thermal effects onto the target material.

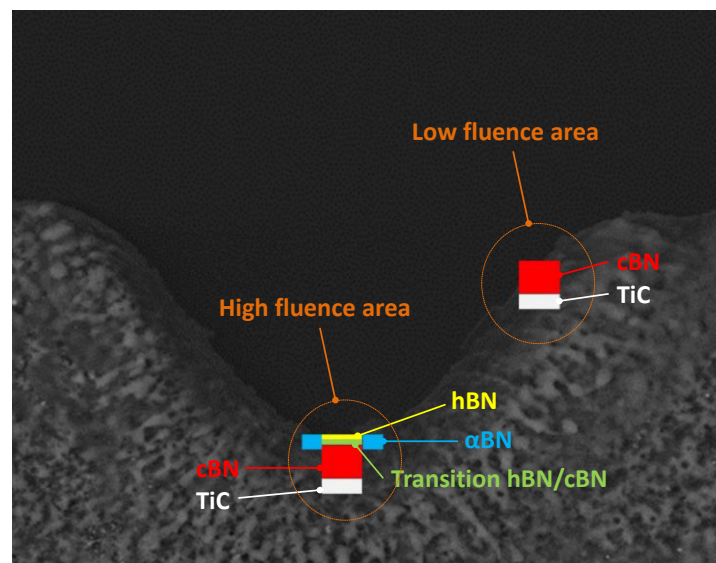


**Figure 5. 22: ESEM cross section imaging of the laser generated groove showing a schematic representation of the thermal response of PCBN DCC500 to different laser fluencies in PLA.**

### 5.3 Conclusions and remarks

This work has enabled a first understanding of the mechanism of formation/removal of allotropic changes during pulsed laser ablation of PCD and PCBN, along with an increased knowledge of the role of the metallic/ceramic binder via the FIB/TEM/EELS analysis. Specifically

developed surface protection multi-coatings along with GIS applied strapping and a focused ion beam procedure enabled to prepare thin lamellas in PCD and PCBN composites. Further thinning of the lamellas in the sites which had experienced high and low fluence during ablation made reliable the EELS/HRTEM analyses of the selected materials. Both in the case of PCD and PCBN materials, a relationship between the graphite/hBN extent and the laser fluence has been found, demonstrating that the material thermal response is affected by the output energy laser. A difference in extent of allotropic transformation occurring in the same PLA condition was found between the PCD and the PCBN specimens. In fact, HRTEM/EELS analyses in the high fluence area revealed an extent of graphite of 0.9  $\mu\text{m}$  in the PCD (Figure 5.23), while an hBN layer of 0.05  $\mu\text{m}$  was found in the PCBN specimen (Figure 5.24), indicating that PCBN composites don't tend to allotropic change during PLA, and thereby confirming the choice of PCBN materials where a better thermal resistance and chemical inertness is required.

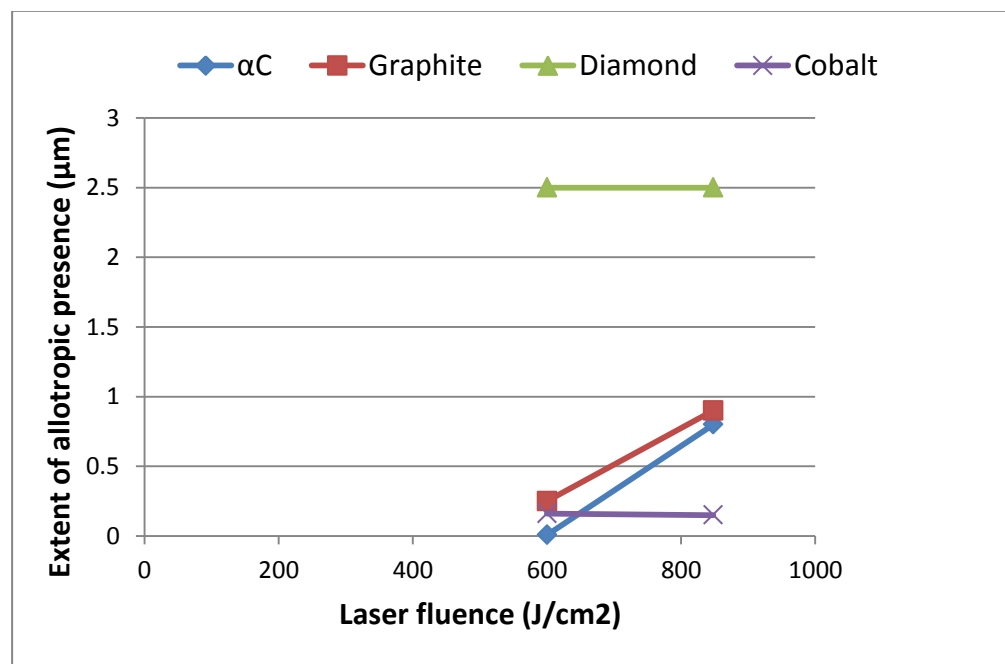


**Figure 5. 23: Relationship between laser fluence variation and extent of allotropic presence in PCD materials.**

This chapter, including an experimental model for the thermal response of PCD/PCBN materials to PLA, is propaedeutic for the work reported in Chapter 6: this will include the optimisation process for laser operating

parameters and laser paths to allow ablation of 3D features with controlled surface quality; thus an in-depth understanding of the thermal response of the material is necessary for optimise the PLA process.

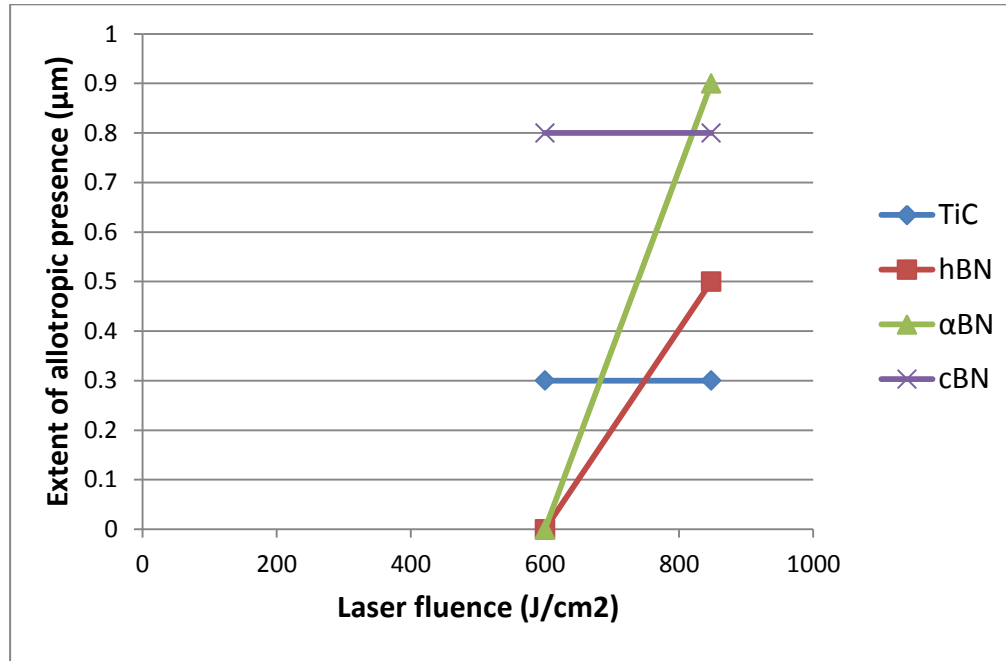


Figure 5. 24: relationship between laser fluence variation and extent of allotropic presence in PCBN materials.

# Chapter 6

## Generation of orderly micro-abrasive arrays in PCD/PCBN structures

Following the findings on the thermal response of ultra-hard composites shown in Chapter 5, this chapter presents the results of PLA to enable the generation of orderly micro abrasive arrays. In particular, it includes the findings of the study of the influence of the laser path parameters (e.g. direction of ablation, use border cuts) for the generation of laser 3D features with controlled surface quality (roughness, damage level); and it reports about design steps for the generation of selected micro-cutting geometries (i.e. rake and clearance faces, cutting edge radius) via PLA technique, for which the methodology is fully described in Section 3.6.2.

### 6.1 Influence of the laser path parameters in the design of abrasive geometries

Chapters 4 and 5 reported on the material thermal response to the PLA process and the optimisation of PLA parameters to enable the manufacturing of selected micro-edge geometries. In order to allow the generation of laser ablated complex geometries within a range of tolerances ( $10\ \mu\text{m} \pm 5\ \mu\text{m}$  for the cutting radius,  $6^\circ \pm 3^\circ$  for the rake angle;  $29^\circ \pm 3^\circ$  for the clearance angle) the methodology reported in Section 3.6.1 has been adopted in order to study the effects of laser path parameters in the design and realisation of micro-abrasive/cutting geometries. The results of the experiments described in Section 3.6.1 are here reported both for PCD and PCBN composites.

### **6.1.1 Results of the study of laser path parameters variation**

Many geometries have been laser generated onto microstructurally different composite materials. Some examples of geometrically complex shapes are here reported. Initially, a triangular shape feature was selected for PLA to enable an easy understanding of the influence of the border cut function onto the edges of the triangle (this means repeated laser overscan on the profile of the selected geometry). When the border cut is selected among the laser options, the laser beam hits repeatedly the profile of the selected geometry in a cutting motion.

The influence of the use of border cuts in the generation of micrometric orderly triangular shapes for a coarse grained CTH025 PCD specimen is reported in Figure 6. 1: a difference in the use or non-use of border cut is evident especially in the edge of the feature, which appear to be not well defined and straight in the case of use of border cuts (Figure 6. 1a).

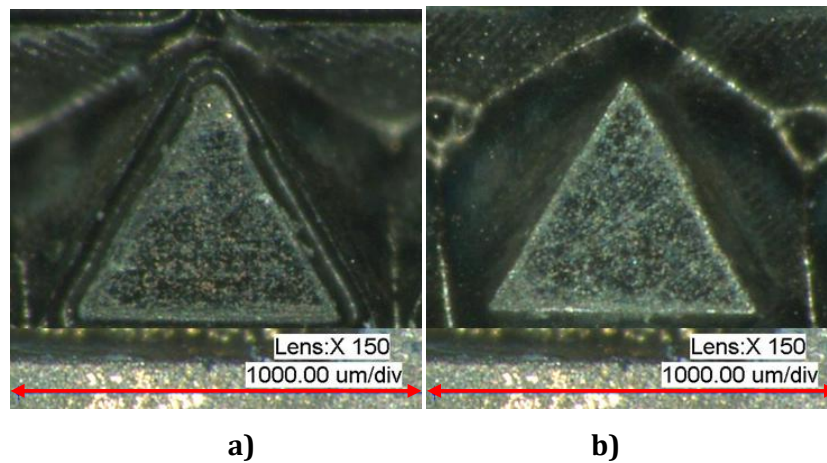


**Figure 6. 1: Optical microscopy image of specimen PCD CTH025 after PLA with: a) border cut, b) no border cut.**

A similar result has been shown in the mix grained CTM302 PCD specimen indicating that the result in the use of border cuts is not affected from the microstructural factors of the material. The use of border cuts in PLA of a low-CBN DCC500 PCBN structure produced triangularly shaped features with irregular borders (Figure 6. 2a) and the extend of edges irregularity is noticeably increased in the selection of border cuts. The generation of orderly triangles onto PCBN structures is shown in Figure 6. 2-6. 4: in all the ablated microstructurally different specimens, the use of border cuts

lead to an increased edge irregularity, especially in the corner of the edges, where an intense energetic activity is experienced due to the path followed by the laser beam.

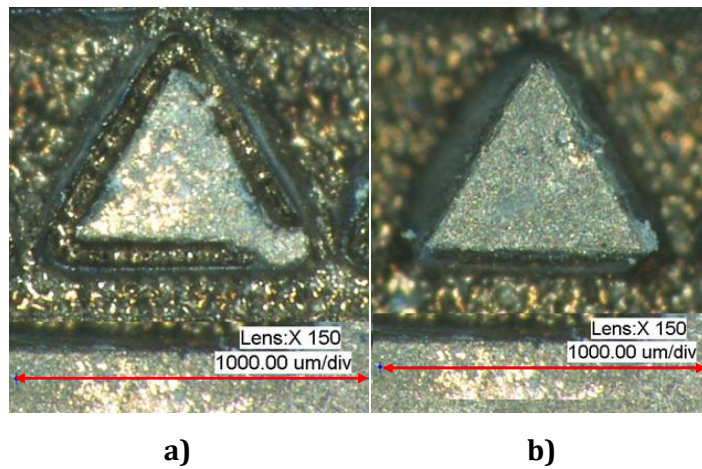


**Figure 6. 2: Optical microscopy image of specimen PCBN DCC500 after PLA with: a) border cut, b) no border cut.**

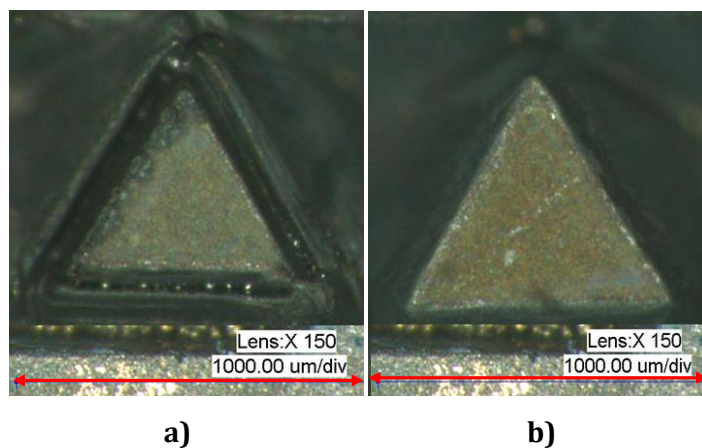


**Figure 6. 3: Optical microscopy image of specimen PCBN DBW85 after PLA with: a) border cut, b) no border cut.**

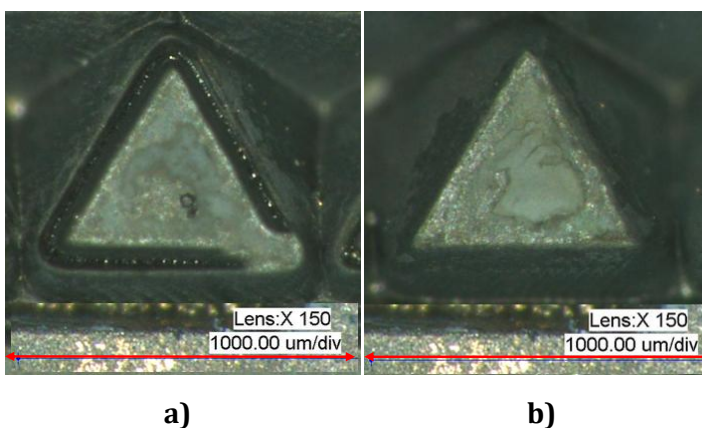


**Figure 6. 4: Optical microscopy image of specimen PCBN DBS900 after PLA with: a) border cut, b) no border cut.**

Another experiment, whose methodology is reported in Section 3.6.1, aimed at understanding the effect of direction of ablation onto microstructurally different materials. Three different directions of ablation have been selected as default of PLA for studying the effect onto the to-be-generated arrays as presented in Figure 3. 16: a random direction of the laser beam respect to the solid specimen (e.g. angles:  $0^\circ$ ,  $45^\circ$ ,  $90^\circ$ ,  $135^\circ$  etc.), a  $0^\circ$  and a  $90^\circ$  orientation of the laser beam to the specimen. It is important to notice that all of the performed experiments were necessary for the achievement of the desired cutting edge whose geometry is reminded in Figure 6. 5 and previously described in details in methodology section (Figure 3.15).

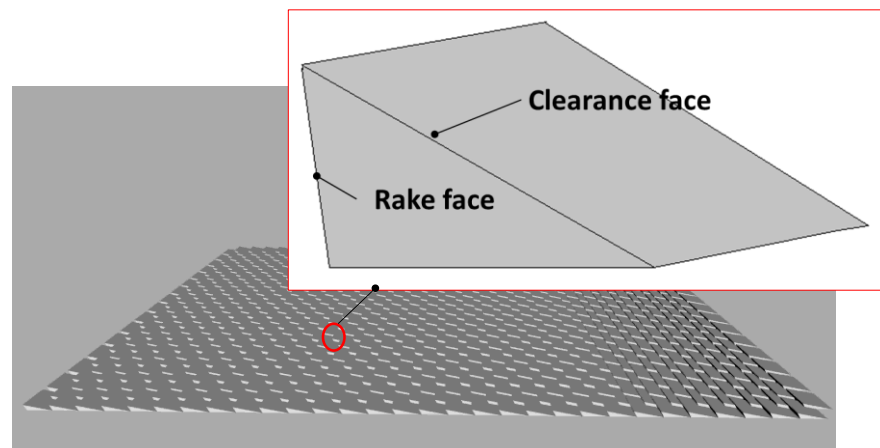


**Figure 6. 5: Geometry of the array and detail of a single to-be-generated micro-cutting edge.**

The parameters used for the influence of direction of ablation are reported in Table 3. 10. An example of the effects of the direction of ablation onto a CTH025 coarse grained PCD specimen, is reported in Figure 6. 6: the CAD design utilised for the generation of the features is the same for images a, b and c; but it is evident that the results are entirely different. An ablation with random direction of ablation (Figure 6. 6a) produced double edges features with re-deposition of possibly melted material in the staggered feature direction; ablation using a  $0^\circ$  angle enabled to achieve very well staggered features with a cutting radius of  $100\ \mu\text{m}$  endorsing the possibility of its use for polishing (Figure 6. 6b). The use of a  $90^\circ$  angle produced the most favourable cutting edge being the cutting radius in the order of  $10\ \mu\text{m}$  (tolerance  $\pm 5\ \mu\text{m}$ ) as shown in Figure 6. 6c. Although the

latter had shown to achieve incomparable cutting edge sharpness, the staggering between features was difficult to achieve because formation of laser generated walls (Figure 6. 6c) appeared and this prevented the generation of staggered micro features that are essential to enable chip path flow as demonstrated in literature [4].

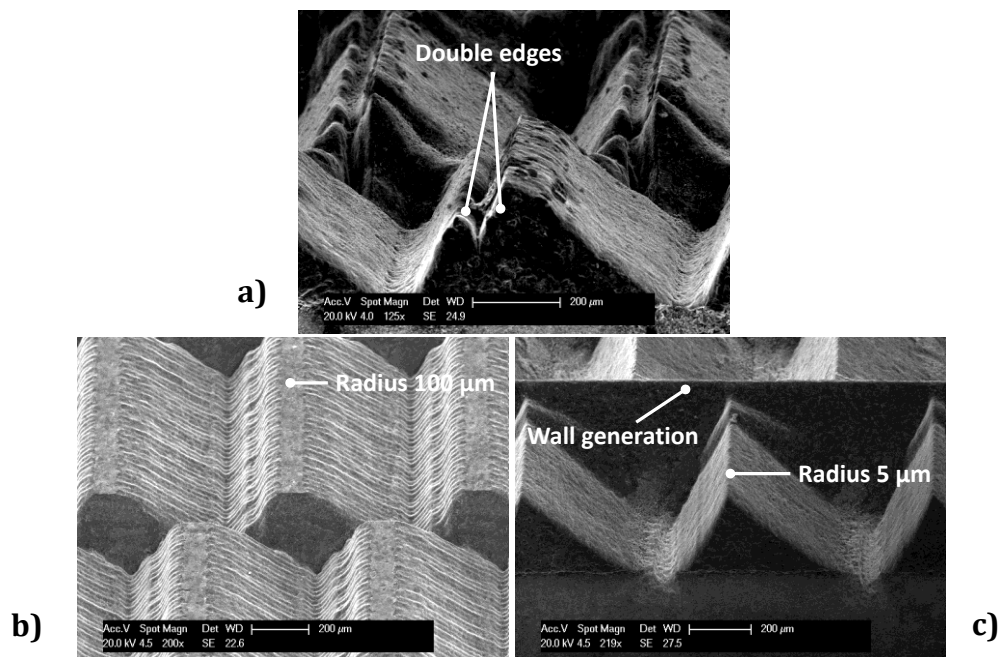


**Figure 6. 6: ESEM images of laser generated ( $P_m 70W$ ,  $\tau 10\mu s$ ,  $f 30kHz$ ,  $v 400mms^{-1}$ ) PCD CTH025 specimen with same CAD file but different laser stage direction: a) random direction of ablation, b)  $0^\circ$  direction of ablation, c)  $90^\circ$  direction of ablation.**

### **6.1.2 Observation and discussion**

The results in Section 6.1.1 have indicated edge irregularity in the ablation with border cuts, which could be explained considering the thermal response of the material. During PLA with border cuts, multiple overlapped single crater ablations are generated onto the base material together with an intense energetic activity, thus producing a favourable condition for melting and re-solidification of material at the edge of the triangular features corresponding to the area where the border cut has been applied. This phenomenon has not occurred in the feature generation without border cuts, therefore indicating that the extent of thermal affected area is noticeably increased in the ablation activity with increased

energy density; this result is in agreement with literature and with the results reported in Chapter 5 [74], [92], [93], [109]. Because of the higher extent of irregularity produced by an intense energetic activity during PLA, the ablation without use of border cuts has been selected as optimal choice for the generation of orderly micro-abrasive arrays.

Results for experiments in the effect of direction of ablation have proven to affect noticeably the cutting edge sharpness and geometry. Random direction of ablation (Figure 6. 6a) produced double edges and irregular geometry possibly caused by melting and re-deposition of binder/ultra-hard phase in different specimen sites: the target material is polycrystalline and the random ablation causes a superimposition of laser fluencies in different sites of the target, thus an intense thermal excitation is produced and high thermal stresses [25] at the interface binder/ultra-hard grain are produced causing what looks like a crack into the edge. Ablation using a  $0^\circ$  angle allowed achieving very well staggered and repeatable features with no sign of thermal effects, but the cutting radius has shown to be of  $100\ \mu\text{m}$  (Figure 6. 6b). In this case, because of the gradient of the thermal field, the thermal excitation onto the target material is occurring in a constant direction, parallel to the designed features, thus not stimulating enough the thermal response of the target at lower distances from the beam (in the upper part of the edge). The  $90^\circ$  angle ablation demonstrated its superiority when sharpness of the edge is the main pre-requisite; although a problem in the formation of laser generated walls appeared (Figure 6. 6c): a possible hypothesis to explain it could be the CAD design which has been fed in the laser path software, but this could be only one of other possible reasons, which could perhaps include thermal gradient field and/or PLA input parameters. Section 6.2.1 aims at showing the results for the removal of the wall by modifying the design in input.

## **6.2 Design for the generation of the micro-abrasive/cutting arrays**

Section 6.1 aimed at understanding the effects of laser path parameters in the generation of laser ablated features via discussion of the results of the experiments from Section 3.6.1. The present paragraph shows the results from the methodology explained in Section 3.6.2 for the generation of optimised orderly micro-abrasive arrays in microstructurally different PCD and PCBN composites. This includes both micro-edge optimisation process and the implementation of the final micro-abrasive/cutting arrays onto microstructurally different composites.

### ***6.2.1 Laser generated micro-abrasive arrays in PCD/PCBN***

Section 6.1.1 has shown the effect of particular types of direction of ablation during PLA. The outcome result was a need of improving the staggering between features because formation of walls was appearing during PLA at 90°. Figure 6. 7a is a representation of the issue appeared in the use of 90° as an angle for ablation. Because the sharpness of the edges is a main requirement in the generation of super-abrasive tools for cutting applications [53], [78], the need of improving the features lead to a modification of the design. In order to remove the walls between each line of features and provide the proper staggering between edges as described in Figure 6. 5, a new CAD drawing was implemented. In the latter overlapping areas were created where the laser generated walls had previously appeared; the methodology adopted is deeply described in Section 3.6.2. Figure 6. 7b and c depict the results of overlapping in the CAD design and the possibility of achieving a high control of clearance/rake angles, producing both negative rake angles (Figure 6. 7b) and positive ones (Figure 6. 7c).

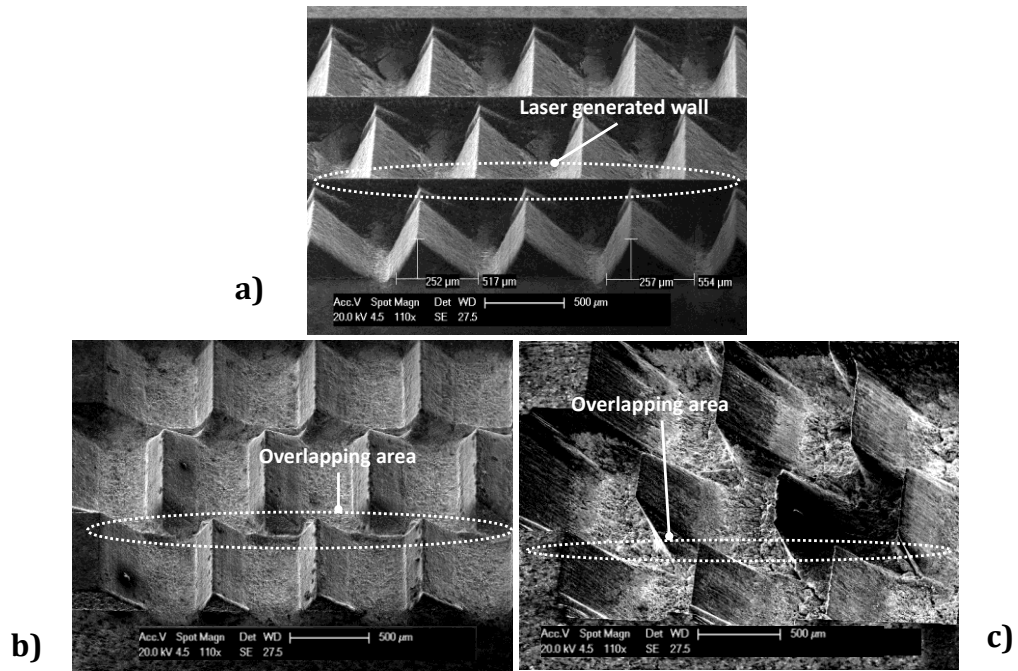


**Figure 6. 7: ESEM images of laser generated ( $P_m 70W$ ,  $\tau 10\mu s$ ,  $f 30kHz$ ,  $v 400mms^{-1}$ ) PCD CTH025 specimen with different CAD files: a) no overlapping of features in the CAD, b) overlapping of 0.3 mm between features with negative rake angle, c) overlapping of 0.3 mm, 90° ablation without border cut.**

As mentioned in Section 3.6.2, a final experiment was set up to evaluate the influence of laser beam tilting angle (angle formed between the laser beam and the target material) on the control of the cutting geometry (e.g. clearance/rake angles, cutting radius). Figure 6. 8 is a schematic of the laser beam respect to the specimen to be ablated.

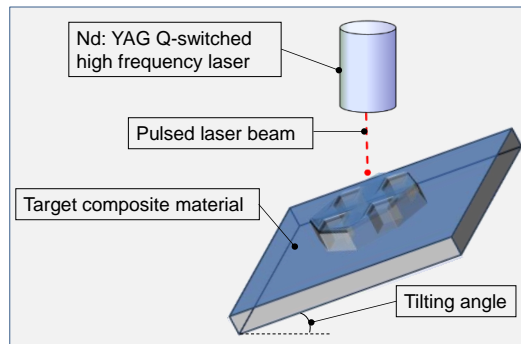


**Figure 6. 8: Positioning of the ultra-hard specimen to the laser beam.**

Results in the production of the to-be-generated arrays using the tested angles ( $10^\circ$ ,  $20^\circ$  and  $30^\circ$ ) onto a mix grained CTM302 PCD specimen are depicted in Figure 6. 9. It is evident that there is a direct relationship (shown in Table 6.1) between tilting of the laser beam respect to the target material and geometry/dimensions of the cutting elements.

By using the same CAD design, a beam tilting of 20° produced deeper features (Figure 6. 9b) when compared to a 10° angle but straightness of the edge is improved at a tilted angle of 30° as indicated in the cross section image of the array (Figure 6. 9c).

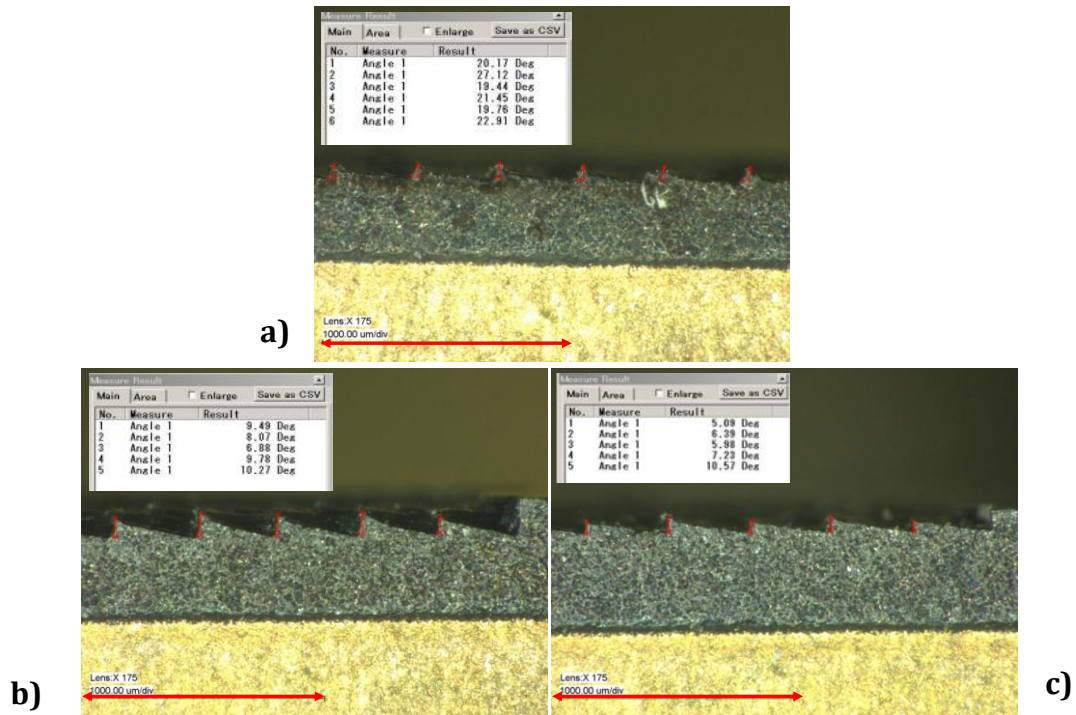


**Figure 6. 9: Optical microscopy image of cross section of laser generated array in PCD CTM302: a) tilting of the specimen at 10°, b) tilting of the specimen at 20°; c) tilting of the specimen at 30°.**

An influence of the beam tilting onto the microstructural properties of the composites has been found. Variable micro-abrasive features and clearance/rake faces were found: Figure 6. 10 is an example of the effect of different tilting angles onto a fine grained CMX850 PCD specimen. By using the same CAD design (as reported in Figure 3.17), a tilting of the beam at 30° (Figure 6. 10c) produced the optimal edge definition in term of edge sharpness and surface integrity as also validated by ESEM analyses (Figure 6. 12a). A tilting angle of 10° (Figure 6. 10a) lead to the generation of arrays with non-straight edges and the use of a tilting angle of 20° produced negative rake angles (Figure 6. 10b) as shown in Table 6.2.

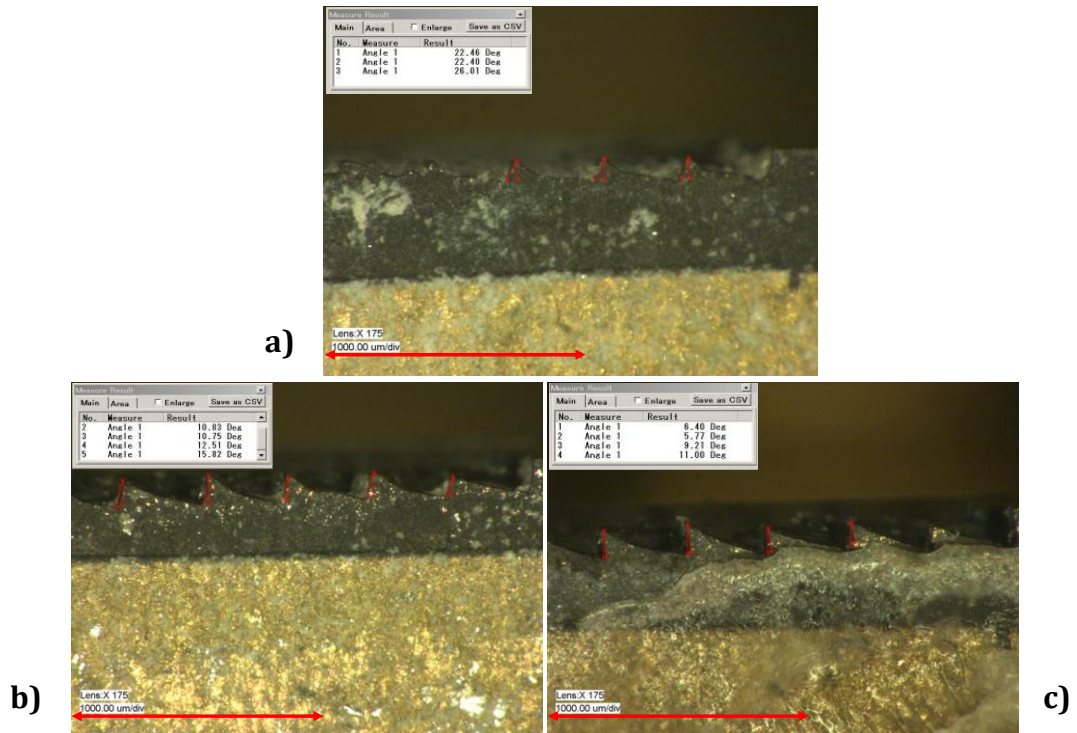


**Figure 6. 10: Optical microscopy image of cross section of laser generated array in PCD CMX850: a) tilting of the specimen at 10°, b) tilting of the specimen at 20°; c) tilting of the specimen at 30°.**

The experiment related to the tilting of the laser beam lead to the identification of the angle (30°) for the manufacture of the to-be-generated arrays. The laser generated orderly arrays are shown in Figure 6. 11 where an example of the micro-abrasive edges is reported both for the mix grained CTM302 PCD specimen and for the high-CBN content DBS900 PCBN sample.

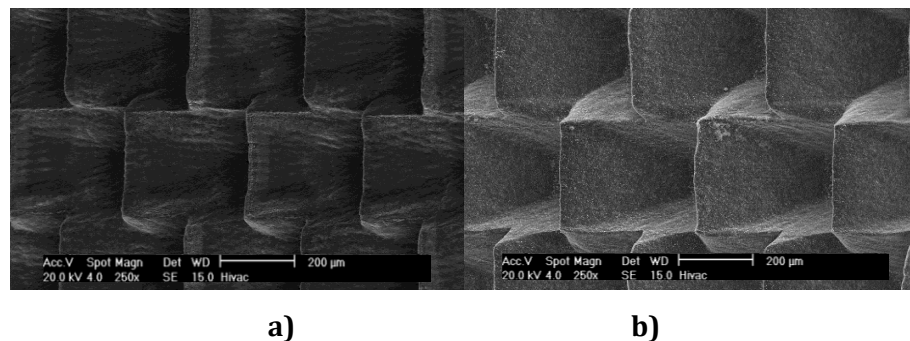


**Figure 6. 11: ESEM images examples of the optimised laser generated arrays in specimens: a) PCD CTM302; b) PCBN DBS900.**

ESEM analyses on the laser generated arrays allowed measurement of the clearance/rake angles for the control of the achieved dimensions within the tolerances reported in Section 3.6.1.

Figure 6. 12a depicts an example of a single micro-abrasive edge in the fine grained CMX850 PCD specimen, where dimensions of the clearance and rake angles have been measured by using the methodology described in Section 3.6.2; the achieved sharpness of the micro-features is evident in Figure 6. 12b for a DBW85 PCBN specimen: the edge radius has shown to be repeatable within features in the range of 10  $\mu\text{m}$  (tolerance  $\pm 5 \mu\text{m}$ ).

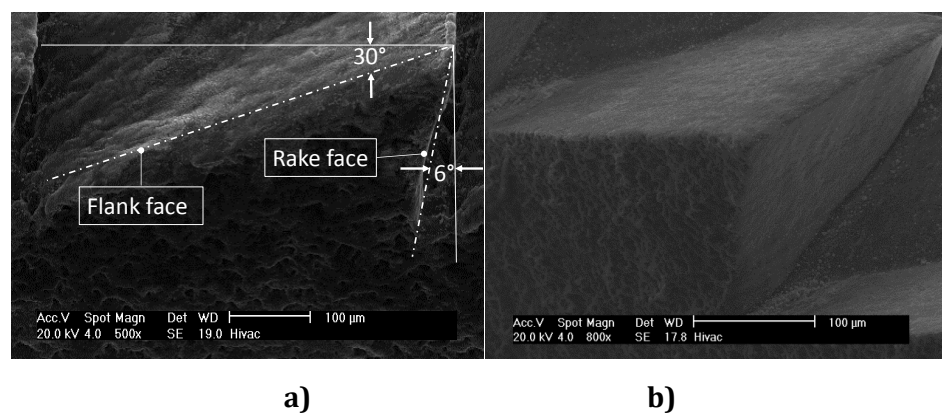


**Figure 6. 12: ESEM images of a single micro-abrasive edge: a) tilted view of the edge in PCD CMX850 specimen, b) 3D view of the edge in PCBN DBW85 specimen showing the sharpness of the edge.**

The possibility of generation of features within a wide range of angles is evident in Tables 6. 1-6. 2 where results from five repetitions for each pulse laser ablated micro-edge are reported. The high variability of the achieved geometry depends upon the tilting angle. Smaller tilting angles should be preferred when a negative rake angle is required, with clearance/rake angles in the range  $9^{\circ}, 13^{\circ} / -22^{\circ}, -20^{\circ}$ ; while bigger tilting angles should be preferred when a positive rake angle is required.

**Table 6. 1: Results of rake and clearance angles achieved for different input angle of tilting for PCD CTM302.**

Angle of tilting [°]	Achieved rake angle[°]	Achieved clearance angle [°]
30	5.09	5.88
30	6.39	7.74
30	5.98	7.61
30	7.23	4.73
30	10.6	5.08
20	-9.49	12.2
20	-8.07	18.2
20	-6.88	15.2
20	-9.78	16.7
20	-10.3	16.9
10	-20.2	10.8
10	-27.1	13.9
10	-19.4	10.6
10	-21.4	11.9
10	-19.8	9.91

The relation between angle of tilting and achieved rake angle is of a direct proportion (as shown in Figure 6.13), thus depending on the type of application where the to-be-generated features are going to be applied (cutting, grinding, polishing), it is possible to select the tilting angle adequate for the desired geometry. Also, the manufactured edges are repeatable in the order of (0-10)° as depicted in Figure 6.13.

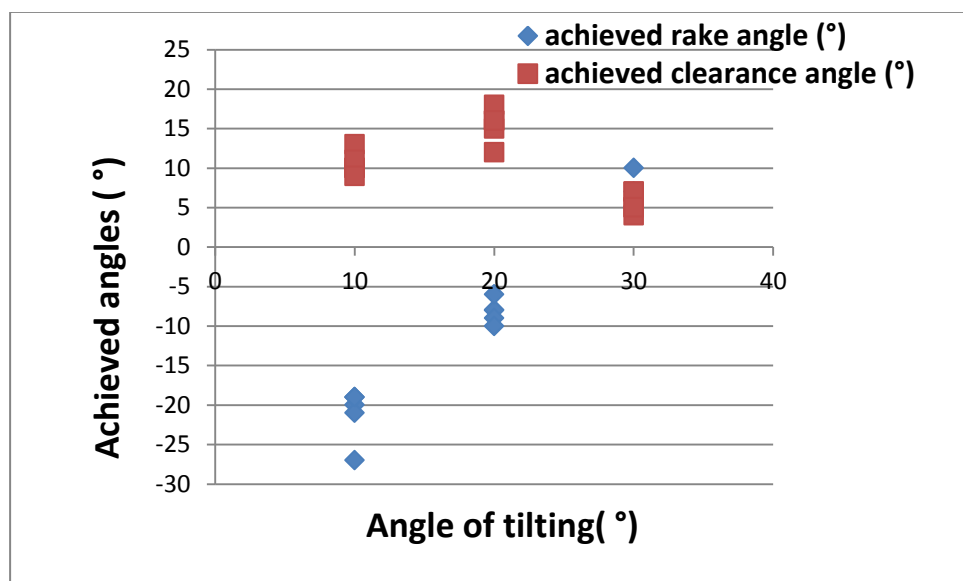


**Figure 6. 13: Repeatability of the achieved rake and clearance angles as a function of the tilting angle onto PCD CTM302.**

Table 6.2 contains all of the achieved rake and clearance angles for specific angle of tilting in input in the case of a fine coarse polycrystalline diamond. The pulsed laser ablation was repeated five times for each tilting angles and a graph of repeatability is reported in Figure 6.14, where it is clear that an increase of tilting angle is able to cause a directly proportional increase in rake angle. In particular, since this effect has been shown both on fine grained and mixed grained PCD structures, the microstructure of the materials does not affect significantly the achieved angles.

**Table 6. 2: Results of rake and clearance angles achieved for different input angle of tilting for PCD CMX850.**

<b>Angle of tilting [°]</b>	<b>Rake angle[°]</b>	<b>Clearance angle [°]</b>
30	6.4	20.6
30	5.7	12.1
30	9.2	21.1
30	11	12.8
30	9.2	15.1
20	-10.8	20.4
20	-10.7	15.2
20	-12.5	14.8
20	-15.8	11.6
20	-10.2	13.2
10	-22.5	12.7
10	-22.4	15.4
10	-26.1	13.6
10	-22.5	15.63
10	-22.4	14.1

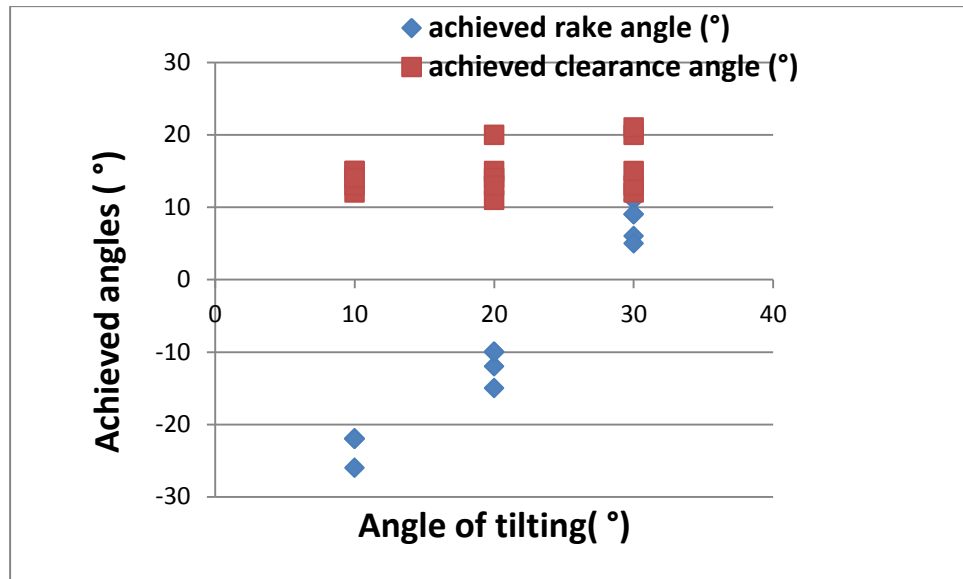


**Figure 6. 14: Repeatability of the achieved rake and clearance angles as a function of the tilting angle onto PCD CMX850.**

### **6.2.3 Observation and discussions**

The results in Section 6.2.1 have shown that it is possible to achieve a high control of clearance/rake angles in the generation of orderly arrays via the PLA process and that design of the to-be-generated arrays is very important in achieving the desired geometry; the influence of design is already well known in the literature for any processing technology [5], [128]–[130]. An important factor which has been studied in this thesis and it has proven to be essential in the control of the micro-abrasive/cutting geometry is the angle of interaction (tilting angle) between the laser beam and the target material. In fact, the introduction of a variable tilting angle has indicated that the control of clearance/rake angles depends upon this angle which allows difficult shapes to be achieved. This can be explained considering the thermal excitation generated in the PLA process: by having a tilting angle the material (in correspondence of the laser beam diameter) is thermally excited at different intensities (following the Gaussian distribution) in a single pulse, and this allows the targeted area to cool down before another excitation, decreasing the thermal affected area and improving noticeably the cutting edge surface integrity. A correlation between the tilting angle and the rake angle has been found as

shown in the results of Section 6.2.2 and this lead to the possibility of generation of specific desired geometry without experimental testing.

### **6.3 Conclusions and remarks**

This chapter included the results for the generation of orderly micro-abrasive arrays via a PLA process. The effect of variation of laser path parameter has been studied; it has been found that in the use of border cuts during the ablative process, a high extent of irregularity was produced by an intense energetic activity onto the target material. This did not occur in the ablation without use of border cuts. For this reason ablation without border cuts has been selected as optimal choice for the generation of orderly micro-abrasive arrays. The study on how the direction of ablation could affect the ablation indicated that random angles are not the best choice for ultra-hard materials due to poor cutting edge surface integrity possibly caused by melting and re-deposition of binder/ultra-hard phase in different specimen sites. Angles of  $0^\circ$  should be used in the achievement of round features and  $90^\circ$  should be used for a good control of the edge sharpness; particularly it has been demonstrated that the variation of angle from  $0^\circ$  to  $90^\circ$  noticeably increased the edge sharpness. For the purpose of this research to generated micro-cutting edges, an angle of  $90^\circ$  was selected. The effects of variable tilting angles of the laser beam respect to the target material has been shown in Section 6.2.1 where results indicated that the variability of the achieved geometry depends upon the tilting angle. In particular, smaller tilting angles should be preferred when a negative rake angle is required, and bigger tilting angles should be preferred when a positive rake angle is needed. In particular, the final laser generated micro-abrasive/cutting features reached values of cutting radius of  $10\ \mu\text{m}$  ( $\pm 5\ \mu\text{m}$ ), values of circa  $6^\circ(\pm 3^\circ)$  for the rake angle and values of  $29^\circ(\pm 3^\circ)$  for the clearance angle. As shown in the flowchart proposed in Figure 3. 14, the generation of micro-abrasive edges within tolerances (reported in Section 3.6.1), whose results were

presented in this chapter, represented a propaedeutic step for the evaluation of the wear characteristics of the laser generated orderly micro-abrasive arrays, which is reported in Chapter 7.

# Chapter 7

## **Evaluation of wear-resistant properties of microstructurally different PCD/PCBN arrays**

The present chapter aims at presenting the results of wear performances of ultra-hard micro-abrasive arrays generated via PLA as described in Chapter 6. A relation between binder percentage/phase, grain size and wear performance is proposed and a predictive experimental procedure for wear-resistant properties of ultra-hard composites is presented. Furthermore, a comparison of the wear performances of the novel arrays against a set of benchmark abrasive pads is included and this particularly offers a scientific evidence of the importance of this research work in terms of future perspective of novel cutting edge geometries which would improve the tool life and reduce the labour costs in micro-tooling industries.

### **7.1 Characterisation of the benchmark electroplated pads**

Electroplated pads with abrasive grits made of diamond and CBN have been selected as benchmarks for the wear tests of PCD and PCBN arrays. The procedure for selection of benchmark specimens is widely described in Section 3.7.1. It is important, when performing comparative tests, to evaluate the similarity and differences between the tested PLA abrasive elements and the benchmark pads; for this reason, the characterisation of the benchmark was necessary for the evaluation of protrusion height and abrasive grit density and further comparison with the ultra-hard PLA generated arrays. This section reports the results for the characterisation

of the electroplated pads; its aims at understanding the main topographical/microscopic differences with the PLA generated arrays to allow a scientifically informed comparison between their performances in terms of wear and cutting forces as main output from the test.

### ***7.1.1 Selection of the benchmark electroplated pads before the test***

As already explained in Section 3.7.2, in order to benchmark the performances of the novel orderly micro-abrasive arrays, two types of electroplated abrasive pads (10mm x 10mm x 0.5mm) have been selected for a comparative test: an electroplated diamond abrasive (grade D501) shown in Figure 7. 1a, and an electroplated CBN abrasive (grade B501) depicted in Figure 7. 1b. In both cases, the substrate material is tungsten carbide in thickness of 1 mm (Figure 7. 2) and the bonding type is a Nickel electroplating.

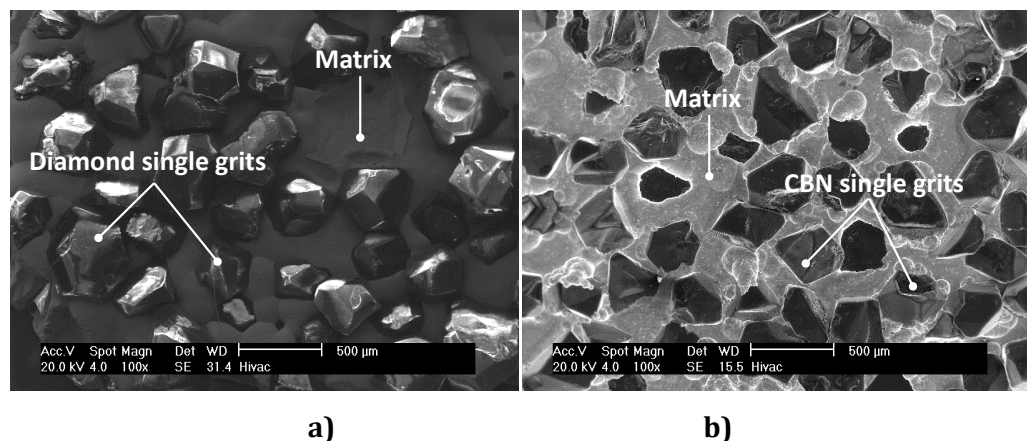


**Figure 7. 1: ESEM image of the benchmark specimens before the test: a) electroplated D501 diamond, b) electroplated B501 CBN.**

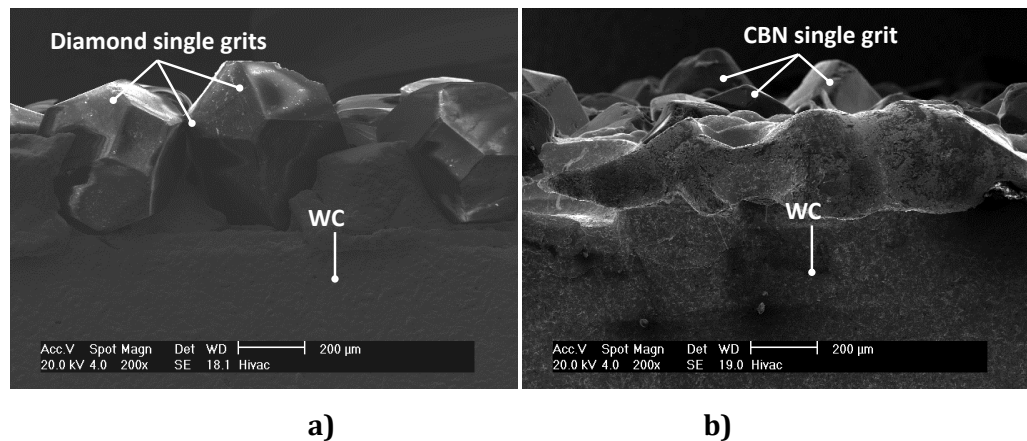


**Figure 7. 2: ESEM image (side view) of electroplated specimens showing the random height of the abrasive grits: a) electroplated diamond specimen; b) electroplated CBN pad.**

The sizes of the abrasives, graded to the Federation of European Producers of Abrasives (FEPA) standards, have an average nominal size of 500  $\mu\text{m}$  (Figure 7. 3b) with circa the same size/volume of the micro-abrasive/cutting edges to provide a reasonable comparison for benchmarked tests.

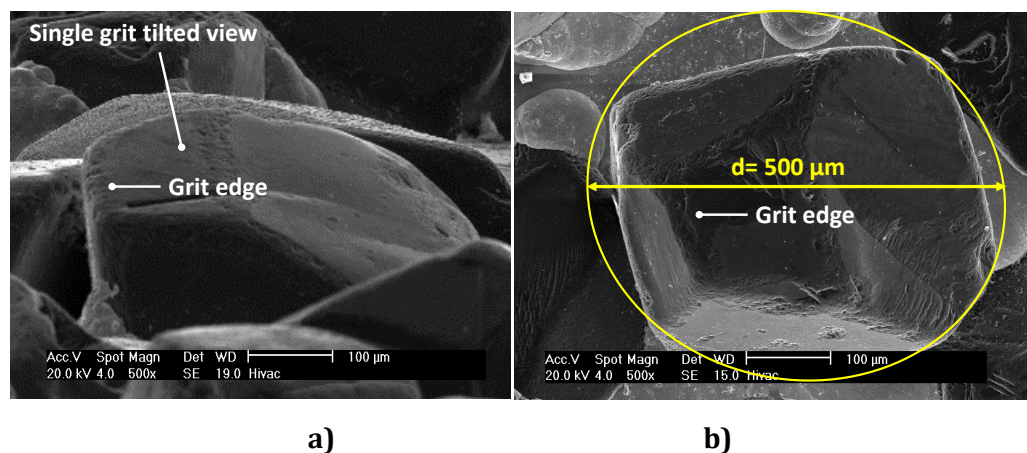


**Figure 7. 3: Example of ESEM image of a single CBN grit in an electroplated abrasive pad: a) tilted and b) top views.**

Figure 7. 4 is representative of the different densities in the case of the micro-edges per array (Figure 7. 4a) and in the case of the grits per electroplated area (Figure 7. 4b). The reason of selecting different densities resides in the choice of a laser generated array which could enhance the wear performances in grinding/cutting applications. Furthermore, the principle of perfectly spatially located features (Figure 7.

4a) is not applicable for the electroplated specimen available in the market, where randomly oriented grits are typically bonded to a substrate in a disorder manner (Figure 7. 4b).

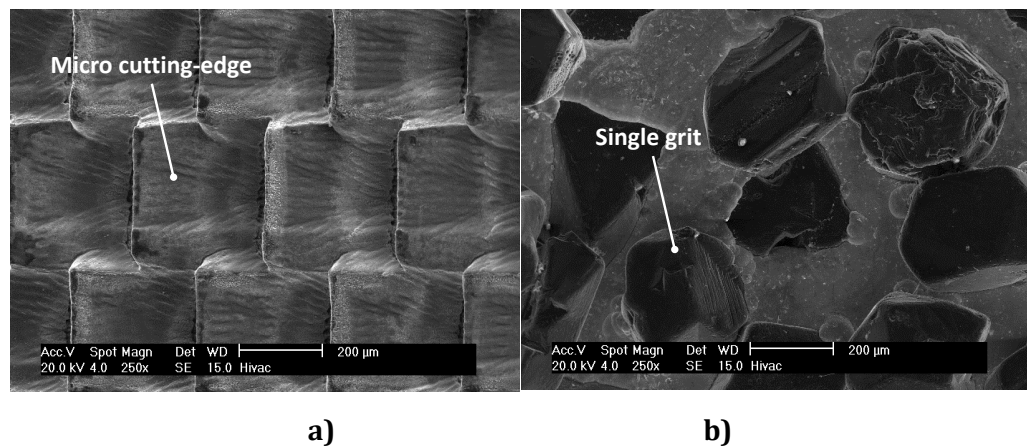


**Figure 7. 4: ESEM micrographs showing the variation in edges/grit density per same surface area of 1 mm<sup>2</sup>: a) 12 micro-edges in the case of the array, b) 7 grits in the case of the electroplated specimen.**

### **7.1.2 Observation and discussion**

The results from the optical analyses on the selected benchmark specimens before testing (Section 7.1.1) are essential for understanding how to approach the comparison of the forces produced during the wear test. In this regard, to calculate and compare the contact loads for the PCD abrasive array and the electroplated diamond pads, two main considerations are necessary: (i) the surface density of the orderly micro-abrasive edges (for orderly arrays) and the abrasive grits (for electroplated elements) are significantly different; approximately the ratio of 12:7 per mm<sup>2</sup> for the orderly micro-arrays and for this reason, the measured forces during the wear test are not directly comparable; (ii) there is a geometrical variability in the grits (e.g. height, shape, orientation/angles of the active cutting edges) of the electroplated pads when compared to the repeatable micro-abrasive edges of the arrays. Figure 7. 1 shows cross section micrographs for the electroplated specimens, indicating that the protrusion height of the grits is variable both for the electroplated diamond specimen and for the CBN one. It can be commented that the variability in height of the grits as well as edge orientation could affect noticeably the results of the cutting test because

the number of grit in contact with the workpiece (i.e. shaft – see Section 3.7.2) would be variable at different length of cut, affecting the acquired force signals and therefore producing an overall signal of lower intensity in comparison with the laser generated micro-cutting arrays (where the homogeneity in height of cutting edges will increase the number of features in contact with the shaft for the same length of cut). Also the density of grits per surface area is an important factor to be considered; in fact, because of the drop in grit density by 42 % for the electroplated pads (Figure 7. 4), less grits (compared to micro-cutting edges) are in contact with the shaft at the beginning of the test therefore representing the main grits responsible of the grinding/cutting process. To avoid problems related to differences in topographical characteristics of the PLA generated arrays and the electroplated specimen, a technical approach has been proposed in Section 3.7.3 for the comparison of cutting forces and wear progression characteristics of the array and corresponding benchmarks.

## **7.2 Evaluation of the wear characteristics of the PCD/PCBN laser generated micro-abrasive arrays and electroplated diamond/CBN pads**

Contemporarily to the evaluation of the cutting forces during test, (reported in Section 3.7.3) an evaluation of the wear progression of the PCD/PCBN arrays and of the benchmarked specimens has been carried out. The wear/cutting tests have been interrupted every 250 passes both in the case of PCD arrays/electroplated diamond pads and for the PCBN arrays/electroplated CBN pads. At every intermediate 250 passes, the ESEM equipment previously described (Section 3.4.2) has been used for the characterisation of the wear characteristics. In particular, any type of cutting edge wear feature (chipping, cracking, flattening) was noted on the microstructurally different composites, and the use of imaging in cross section allowed identification of any change in height/sharpness/integrity both in the electroplated pads and in the wear/cutting arrays. To allow an

easier analysis approach, the same cutting edges/grits have been observed throughout the wear/cutting tests in order to have evidence of the wear progression onto the selected edges/grits. This was done by producing identification signs with special markers onto the selected features.

### ***7.2.1 Wear/cutting test of PCD arrays versus electroplated diamond pads***

The prevalent wear mechanism found in the analysis of the CMX850 fine grained diamond array (after 50 m length of cut) is the slice fracture (Figure 7. 5) indicating the occurrence of a fast wear; while slower wear progression has been shown by the CTM302 mixed grain diamond abrasive array (Figure 7. 5b) whose wear test results indicated that chipping is the prevalent issue found.

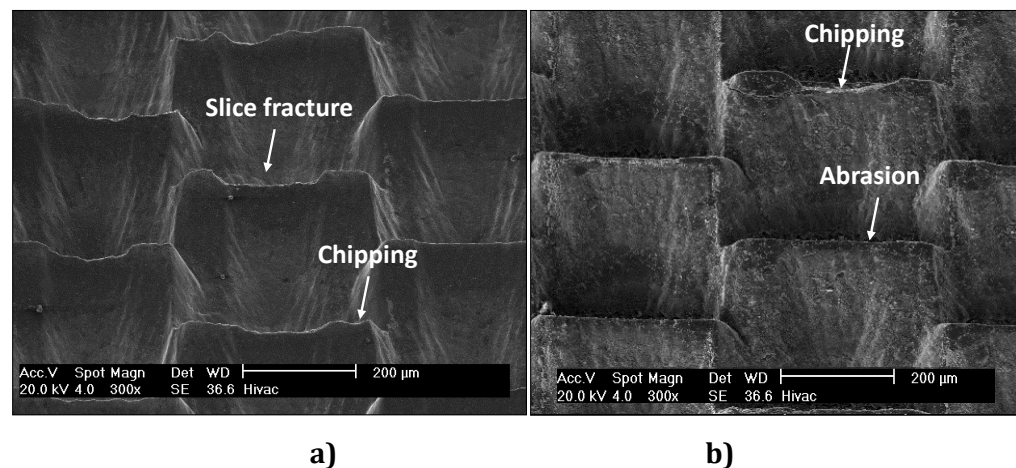


**Figure 7. 5: ESEM of wear features for abrasive micro-arrays after 5000 passes (5 µm depth of cut): a) CMX850 fine grained diamond; b) CTM302 mixed grained diamond.**

ESEM for the CMX850 fine grained diamond array (Figure 7. 6a) has shown that fracture of the micro-abrasive edge occurred already at 3000 passes (compared to 4000 passes for the mixed grained). The typical wear progression for CMX850 mix grained PCD array starts with a micro-damage (chipping) of the single abrasive edge followed by a consequent macro-damage (slice fracture) with the increasing number of passes (length of cut) leading to elevated loads at the micro-edge/grit contact with the workpiece.

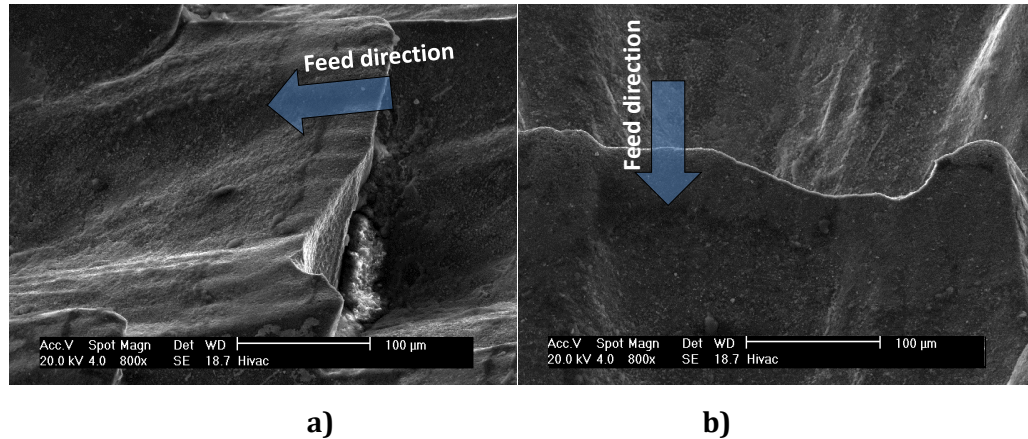


**Figure 7. 6: ESEM images proving the fracture of CMX850 fine grained PCD array after 3000 passes (5 μm depth of cut): a) side view, and b) front view of a micro-abrasive edge.**

The CTM302 mixed grained PCD showed a different type of behaviour when compared to the fine grained material. Figure 7. 7 represents an example of micro-edge after 3000 passes, indicating that no crack or chipping is present after a length of cut of 30 m.

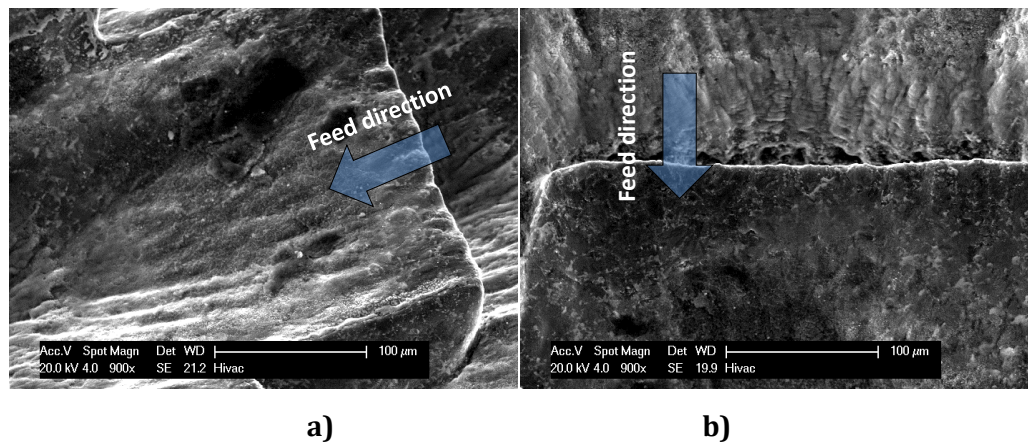


**Figure 7. 7: ESEM images after 3000 passes (5 μm depth of cut) in CTM302 mixed grained PCD array: a) tilted view b) front view.**

Although prevalent wear progression for the CTM302 mixed grained array seems to be of abrasive type, a first appearance of cracking occurred in this composite only at the grain/binder boundary (example of micro-edge - Figure 7. 8a - after 4000 passes). The initial crack started to propagate in the feed direction, and the final result (length of cut, 50 m) is a breaking of part of the cutting edge as shown in Figure 7. 8b.

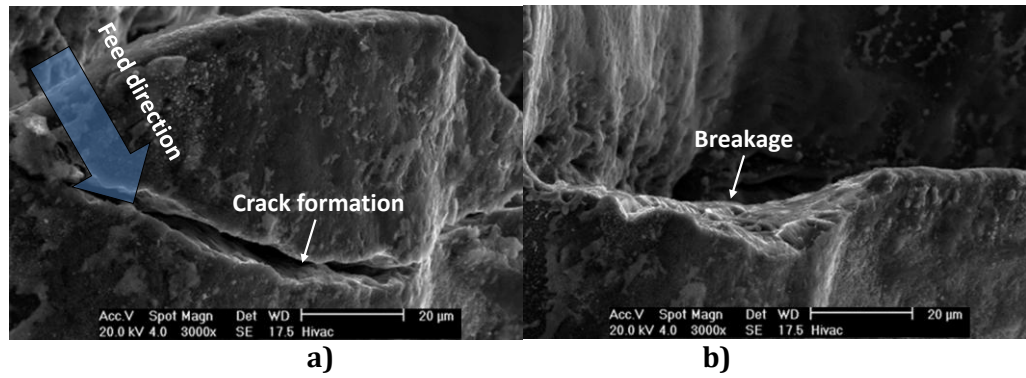


**Figure 7. 8: ESEM images of crack formation and fracture of the CTM302 micro-abrasive edge: a) after 4000 passes, b) after 5000 passes (5 µm depth of cut).**

Figure 7. 9 depicts an example of the wear progression onto a mix grained PCD array, indicating again that the minimum length of cut for chipping to occur is 40 meter in this composite, while being 30 meter in the case of a fine grained PCD array (Figure 7. 6).

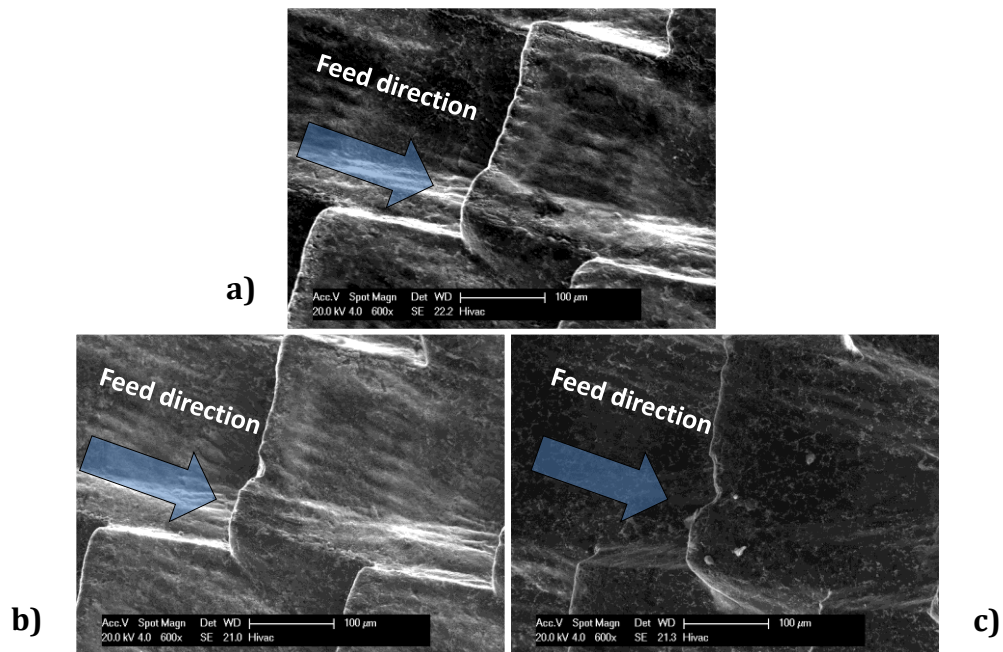


**Figure 7. 9: ESEM micrographs showing chipping as wear progression mechanism on a CTM302 mix grained PCD cutting edge a) after 1000 passes, b) after 4000 passes; c) after 5000 passes.**

The electroplated diamond abrasive pad containing D501 sized abrasives has shown mainly micro-damaged grits (Figure 7. 10b) with consequent flattening of 25-35% of the grits initial height from the beginning of the test (Figure 7. 10a); this indicates a type of abrasive wear similar to that of the mix grained diamond. The wear occurring in the CTM302 mixed grain

PCD array and in the electroplated diamond abrasive pads could be classified as mild abrasive wear [131].

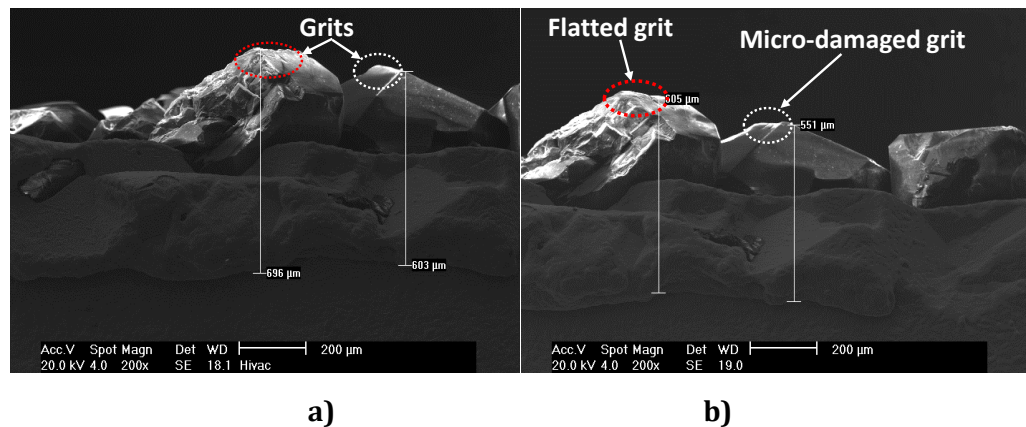


**Figure 7. 10: ESEM micrographs demonstrating the reduction in height (i.e. flattening) of electroplated diamond grits: a) in “fresh” condition b) after 5000 passes (for 5  $\mu$ m depth of cut).**

### ***7.2.2 Wear/cutting performances of PCBN arrays versus electroplated CBN pads***

In the case of high-CBN content array (DBS900), the unworn PCBN abrasive edge is shown in Figure 7. 11a: the white arrows indicate the initial sharpness of the abrasive edge, which has shown a 10 % circa of flattening at intermediate stages of 500 passes (length of cut, 5 m) at 1  $\mu$ m depth of cut resulting in a total height reduction of 20% after a length of cut of 10 m (Figure 7. 11c). The total flank wear from the beginning of the test to the end is 20  $\mu$ m, which represents only the 2% of the total theoretical stock of material removed on the shaft after 1000 passes (length of cut, 10 m).

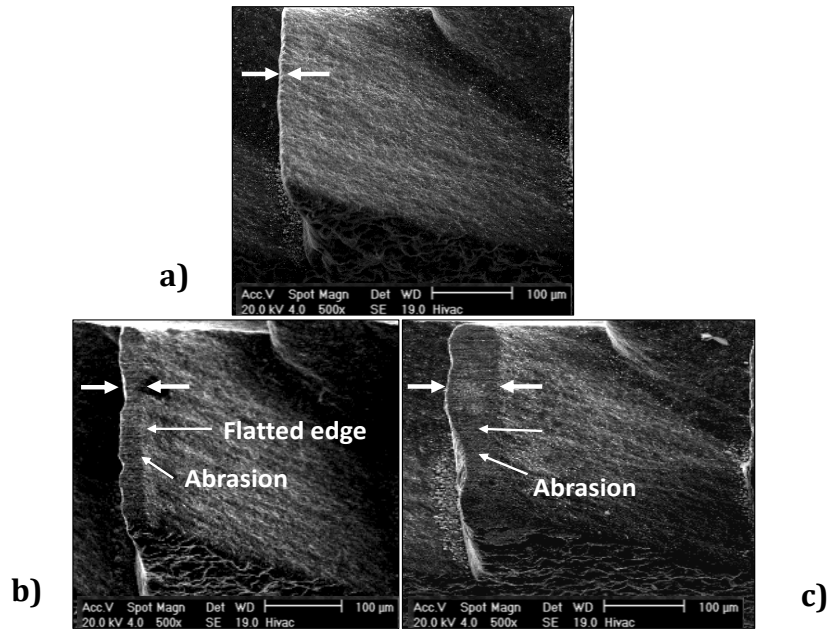


**Figure 7. 11: ESEM tilted view comparative imaging of the DBS900 in the wear test (1  $\mu\text{m}$  depth of cut): a) before test, b) after 500 passes, c) after 10 m length of cut.**

In the case of medium-CBN content array (DBW85), a different wear progression has been found for the unworn area of the abrasive edge (Figure 7. 12a). ESEM micrographs revealed that crack formation caused the side edge of the cutting element to fracture (Figure 7. 12b); this has been followed by a further macro-damage of the abrasive edge probably facilitated by its intermittent contact with the workpiece (Figure 7. 12c).

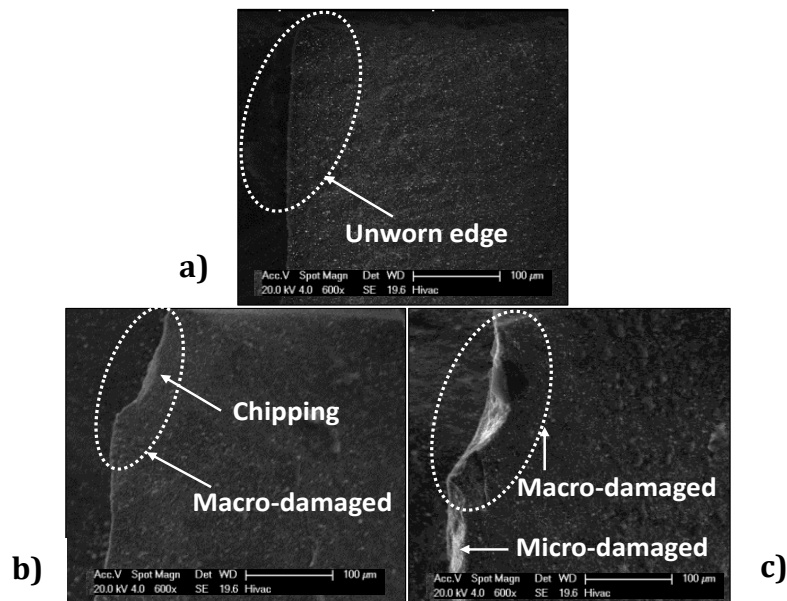


**Figure 7. 12: ESEM tilted view of the DBW85 during the wear test (1  $\mu\text{m}$  depth of cut): a) before the test, b) after 5 m length of cut, c) after 1000 passes.**

The wear phenomenon occurring for the B501 electroplated CBN abrasive has proved to be similar to the one indicated in the purely metallic binder PCBN array (DBS900) mainly showing a flank wear. ESEM images in Figure 7. 13 represent a detail of results of the wear progression in the case of the electroplated CBN specimen: a flattening of grits occurred already at 2,5 m length of cut (Figure 7. 13b) indicating that the 50 % of the total flattening is likely to occur within a length of cut of 2.5 m.

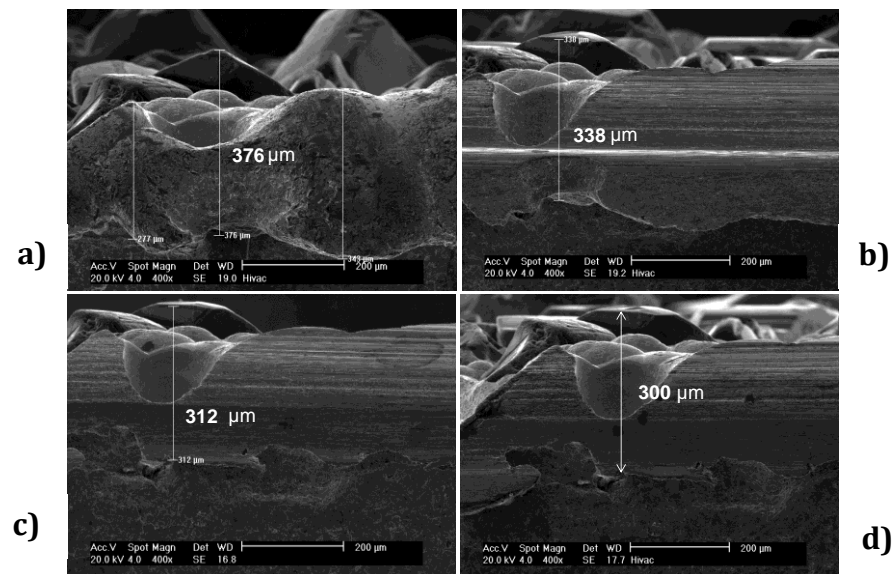


**Figure 7. 13: ESEM micrographs showing the wear progression of the electroplated CBN pad after: a) 250 passes, b) 5 m length of cut, c) 750 passes; d) 10 m length of cut.**

Some examples of grits wear in the electroplated CBN pad are reported in (Figure 7. 14): it is evident that an 80% of grits flattening (Figure 7. 14b) occur already after 2.5 m (length of cut).

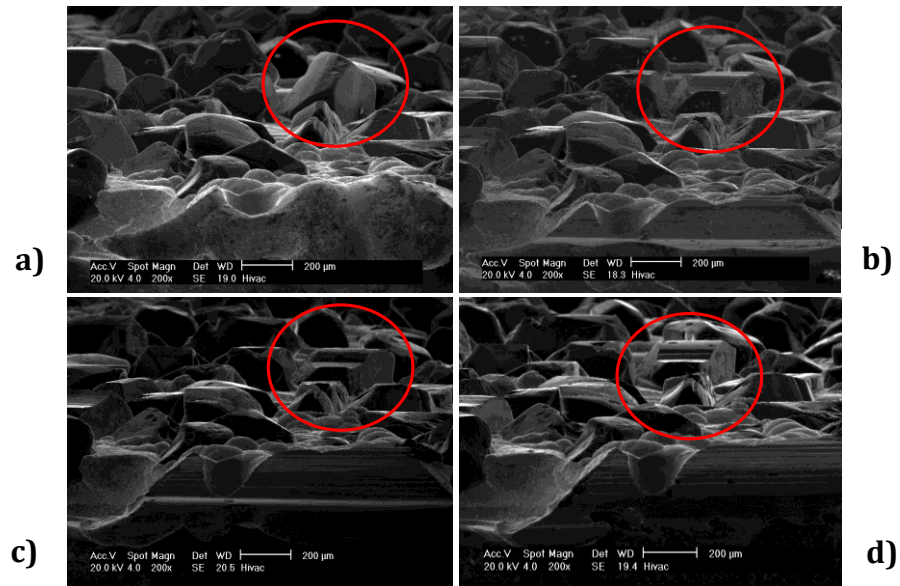


**Figure 7. 14: ESEM micrographs showing the wear progression of a single grit the electroplated CBN pad: a) before the test, b) after 250 passes (length of cut, 2.5 m), c) after 500 passes (length of cut, 5 m), d) after 1000 passes (length of cut, 10 m).**

The height reduction for an average grit after 1000 passes (length of cut, 10 m) is circa 40% of the grit height (Figure 7. 15b); this indicates either that the wear is slower in the case of the laser generated PCBN arrays (20% reduction in height) if compared to CBN electroplated abrasives (40% reduction in height); or that because of the lower density in the electroplated pad, there is an higher load per grit when compared to the PCBN arrays, therefore increasing the wear activity at the grit.

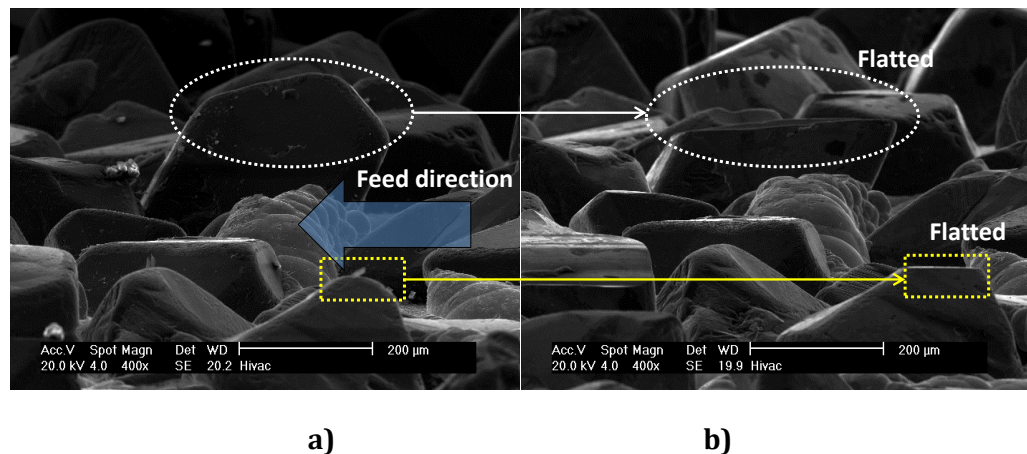


**Figure 7. 15: ESEM micrographs showing some detail of unworn/worn grits on the electroplated CBN grain: a) before the test, unworn area b) after 1000 passes (1 µm depth of cut) worn area.**

### ***7.2.3 Observation and discussion***

#### ***PCD arrays versus electroplated diamond specimen***

The wear occurring during the wear/cutting tests of PCD abrasive micro-arrays and the electroplated diamond abrasives is mainly of a mechanical nature (abrasive wear) combined with thermal effects, previous research has already demonstrated that the main failure mechanism for brittle materials is fracturing [132]. Results shown in Section 7.2.2 indicated that as consequence of the increased length of cut during the test, slice fracture was the prevalent damage mechanism of the CMX850 fine grained diamond arrays (Figure 7. 5a). The fracturing could be caused by a thermal shock, producing the occurrence of a thermal-related wear/damage. For an understanding of the results of the wear test of CTM302 mix grained PCD array, it is necessary to take into consideration a classification reported in wear literature [131] which defined single-cycle deformation mechanisms as those that occur for distortion, displacement and fracture of the material; while repeated-cycle deformation mechanisms those requiring continuous contact for distortion and fracture to occur, such as in fatigue and delamination phenomena. In the wear test (whose results are reported in Section 7.2.2) of PCD arrays, the hardness of abrasive (CTM302 properties in Section 3.2) is higher than the machined material (Silicon dioxide properties in Section 3.3), thus a single-cycle deformation mechanism is expected [131], though the results show that a repeated-cycle deformation mechanisms is necessary for the fracture to be manifested. The damage in the CTM302 mixed grained diamond becomes visible only after multiple cycles (5000 passes corresponding to a length of cut of 50 m) indicating that repeated loading might be the cause of the coalescence and propagation of cracks. The wear progression had shown the occurrence of the following steps: (i) a first appearance of cracks has been found only after 4000 passes (length of cut, 40 m); (ii) the initial crack propagated throughout the edge between 4000 and 5000 passes (length of cut, 40-50 m) possibly because of the repeated cycle deformation mechanism on the single abrasive edge (Figure 7. 8b).

The different wear progression experienced by the fine and mix grained PCD specimen is mainly related to the different extent of cobalt binder percentage. This can be explained by using the physical principle of volumetric strain produced in a material as a consequence of the change in temperature; Eq. 1 was used to study the dependence of the volumetric strain from the change in temperature occurring during the synthesis of PCD composite [25], [26] and for the purpose of this research it has been rearranged in terms of the change in temperature occurring in the abrasive edge during the wear test for every interrupted number of passes:

$$e = \alpha * V_0 * (T_{amb} - T_{process}) \quad (\text{Eq. 1}),$$

where  $e$  is the volumetric strain in the material [ $m^3$ ],  $\alpha$  the thermal expansion coefficient [ $K^{-1}$ ],  $V_0$  the volume prior deformation [ $m^3$ ],  $T_{amb} - T_{process}$  [ $K$ ] the change in temperature occurring during the test. Section 3.2 described the materials thermal properties: in this experiment the mismatch (circa 80%) of thermal expansion coefficient [ $\alpha_{PCD}$  ( $2.5 * 10^{-6}K^{-1}$ )  $<$   $\alpha_{Co}$  ( $13 * 10^{-6}K^{-1}$ )] [25] produces high compressive stress in the diamond grains and low tensile stress in the Co binder, causing internal residual stresses at the interface PCD/Co and thus, leading to material fracture. This phenomenon is likely to occur in the fine grained diamond composites caused by higher Co percentage and the smaller PCD grains, so more expansion of Co and compression of PCD results in an increase of high compressive residual stress in the diamond grains and low tensile stress in the Co binder with a consequent reduced wear resistance; the increased amount of metallic phase in the fine grained PCD also leads to a decreased thermal resistance. These findings are in agreement with literature: a study in 1996 has shown that the fine grain PCD diamond has higher compressive stress when compared to the mixed grained diamond [26]; furthermore, higher amounts of metallic phase is responsible for greater amount of extrusions and reduced thermal resistance [36]. The wear occurring in the CTM302 mixed grain PCD array and in the electroplated diamond abrasive pads is a mild abrasive wear

[131]. A possible explanation of such behaviour could be that the stress is constantly maintained below the elastic limit of the material, causing the repeated-cycle deformation mechanism to dominate.

#### *PCBN arrays versus electroplated CBN specimen*

While polycrystalline diamond proved to have a similar wear progression for the two different grades PCD tested having both a metallic binder (Co), the PCBN arrays were found to have abrasive wear or fracturing mechanism because of the different binder phases and CBN grain dimensions.

PCBN DBS900 has shown a wear progression of abrasive type and it probably occurred because the high thermal conductivity of the metallic binder (reported in Section 3.3) caused the heat to quickly be transferred outside the edge-workpiece interface, thus producing a constant abrasive wear with the increased number of passes (and consequently length of cut).

In the case of the DBW85 cracks formed causing the side edge to fracture (Figure 7. 12b); then, further macro-damage formed on the same abrasive edge: this was possibly caused by the interrupted cycle deformation imposed on the material by its intermittent contact with the workpiece (Figure 7. 12c).

The different wear characteristics identified after the same number of passes between the abrasive array DBS900 and the electroplated CBN abrasive could be due to the following main reasons: (i) the abrasive edge geometry: because of its positive rake angle the edge can not only facilitate the chip flow but also reduce the vibration during machining; (ii) the density of edges/grits in the same area: having less abrasives on the same area might force the taller abrasive to absorb all the impact and vibration of machining, causing a flattening homogeneously distributed in all the protruded grits.

## **7.3 Comparison of the abrasive/cutting forces in the electroplated pads and PCD/PCBN micro-cutting arrays**

The main trend for the signal forces acquired during the wear/cutting test indicated randomly variable signal peaks in the time domain for the electroplated (diamond/CBN) pads and homogeneous signal peaks for the abrasive (PCD/PCBN) arrays. This could be explained by considering what previously said, in regard to the density of the arrays versus electroplated pads (Section 7.1). The lower density and randomness of the grits in the electroplated pads and the different number of micro-edges/grits instantaneously in contact with the SiO<sub>2</sub> shaft during the testing of the different specimens (in the same contact area many edges in the arrays and few grits in the electroplated pads) might have influenced the signal acquired during tests both in term of signal intensity versus length of cut and of signal variation for each edge/grit. Sections 7.3.1, 7.3.2 aim at presenting and discussing the results achieved from the acquired forces in the wear/cutting tests of abrasive arrays and benchmark specimens.

### ***7.3.1 Acquired signal/cutting forces for PCD arrays and electroplated diamond pads***

Section 3.7.3 dealt with the procedure which has been used for the evaluation and comparison of the cutting forces converted from the voltage signal acquired during the abrasive/cutting tests. A typical example of cutting force signal (after acquisition via Labview and processing via Diadem) for a CMX850 fine grained PCD array in a single pass (length of cut, 10 mm) is reported in Figure 7. 16: a reduction of cutting force is shown for each peak along with a reduction of shaft diameter, which has been measured before/after the first 10 mm length of cut.

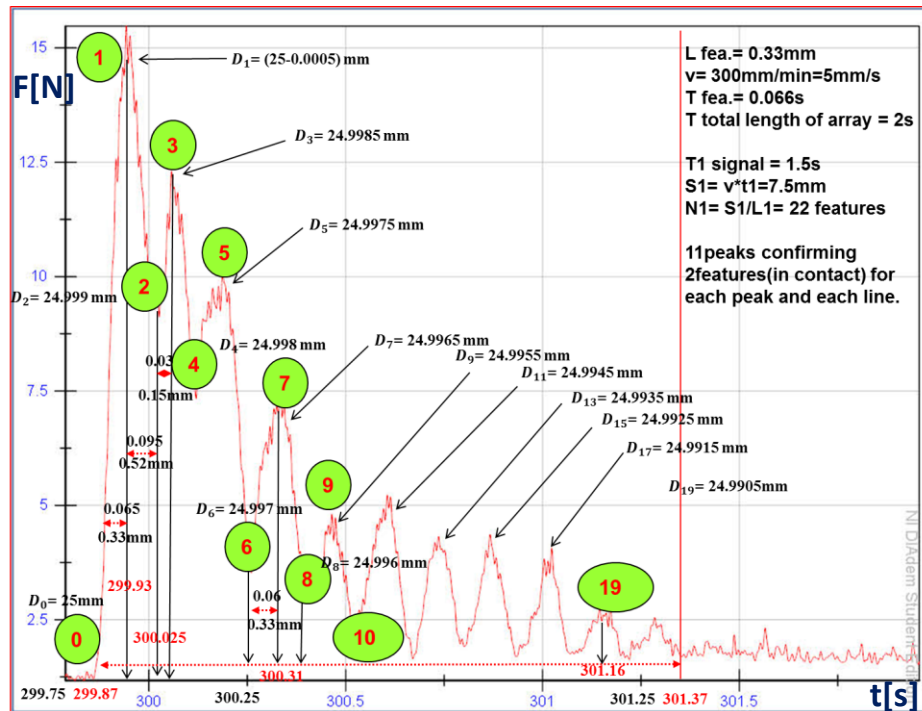


Figure 7. 16: Example of a typical signal acquired in a single pass for the CMX850 fine grained array, the reduced shaft diameter is also shown for each peak; calculation of time and features in contact with the shaft are reported in the insert.

A detailed comparison between a typical cutting force graph for the PCD array and electroplated diamond is depicted in Figure 7. 17. In order to identify the meaning of each peak in the graph, a study has been done.

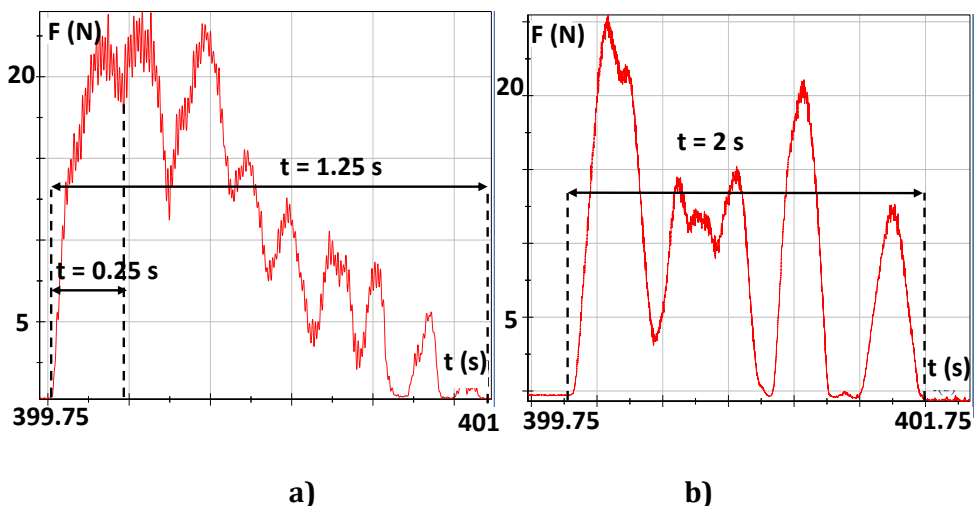


Figure 7. 17: Example of the signal acquired in a single pass with the corresponding time of contact of the shaft upon: a) the CMX850 fine grained array; b) the D501 electroplated diamond abrasive.

The large peaks ( $t=0.25s$ ) of the force diagrams (Fig. 16a) are associated with groups of micro-edges/grits corresponding to the contact between

the array/electroplated abrasives with the shaft during the roto-translational motion and the X axis represents the time domain (with notations for a single pass). As shown in Figure 7. 16, the calculated overall time necessary for the shaft to cover the length of an array/electroplated abrasives (under test condition reported in Section 3.7.2) in a single pass (length of cut, 10 mm) is 2s.

Results from the acquired signal of cutting force have indicated that the experimental time of signal acquisition for each pass is not the same for the array and electroplated pad. Theoretically, if the specimen would be in contact with the shaft for the all length of cut of 10 mm, the time of signal acquisition should be 2 s. Results have shown that in the case of D501 electroplated specimen, the experimental time is 2 s, which means that the electroplated pad is in contact with the shaft during all the test.

In the case of PCD micro-arrays the time of contact with the shaft is not 2 s, but 1.25 s (Figure 7. 17a). This difference in time spent for each pass could be due to the workpiece diameter reduction: the entire depth of cut has been done by the front cutting edges, thus more material is removed from the shaft with the use of the abrasive arrays reducing the contact time in a single pass (from 2s to 1.25s) and provoking only the left side of the array to wear out as indicated also in the ESEM micrographs results (Figure 7. 18a). In fact, in the case of the PCD abrasive arrays, only part of the specimen has been subjected to wear (Figure 7. 18a).

The trailing part (Figure 7. 18b) remained unworn because it has not been in “active” cutting/contact with the shaft, as also demonstrated by the “not acquired forces” in the time interval 1.25-2 s (Figure 7. 17a).

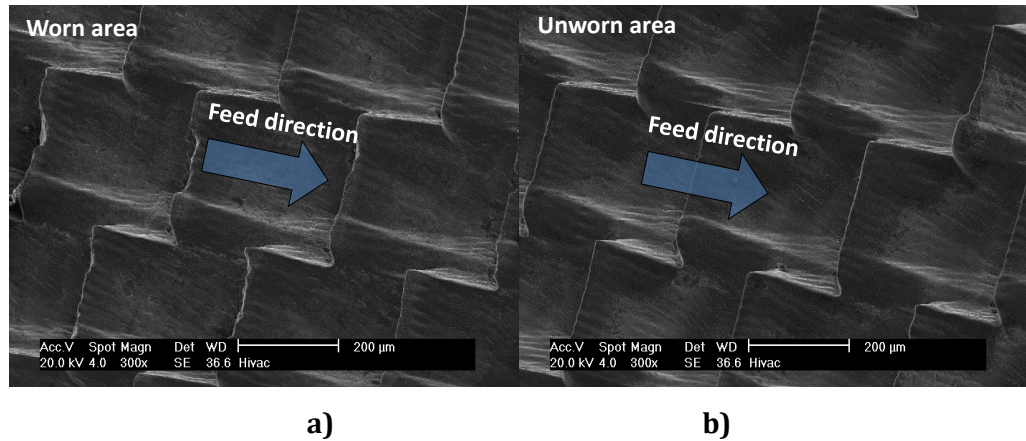


**Figure 7.18: ESEM images of different abrasive edges positioning in the same CMX850 array after 5000 passes: a) most worn surface corresponding to highest contact pressure with the shaft ( $t < 1.25$  s); b) trailing part of the array remained unworn corresponding to time interval of not acquired contact loads ( $t > 1.25$  s).**

Figure 7.19 depicts a schematic representation of the tested array and the resulting worn/unworn surfaces after testing.

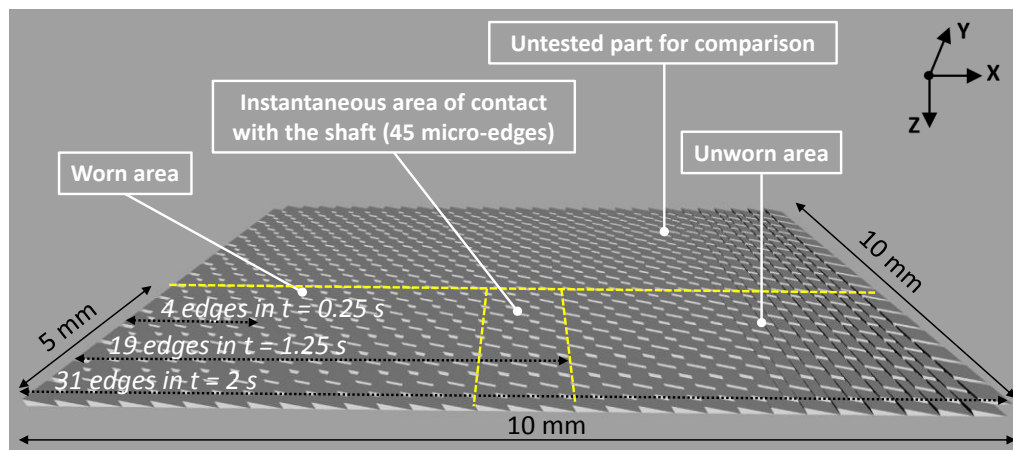


**Figure 7.19: CAD schematic of the manufactured array with dimensions, number of micro-edges in instantaneous contact with the shaft, tested area, untested area, worn and unworn areas.**

To enable the comparison of the specific cutting forces acquired in the abrasive arrays and electroplated diamond pads testing, a normalisation of the forces (initial/final) into contact pressure was made following the methodology reported in Section 3.7.3. Topological scans of the orderly arrays and electroplated pads have been carried out to evaluate the contact surface of representative micro-abrasive edges/grits with the SiO<sub>2</sub> shaft counterpart. Result of the topographical scan of a micro-edge at the

initial stage of the test and its contact area (blue area in Figure 7. 20b) with the rotating shaft is shown in Figure 7. 20. The contact area has been measured following the methodology in Section 3.7.3. For the cutting edge after 250 passes (length of cut, 2.5 m) the contact measured area (Figure 7. 20b) for 5  $\mu\text{m}$  depth of cut is 10.6% of the total area scanned area (Figure 7. 20a). Similarly, the blue area in Figure 7. 20d represents the measured area of contact for a micro-edge after 5000 passes (length of cut, 50 m), which measures 25.8% of the total scanned area (for 5  $\mu\text{m}$  depth of cut).

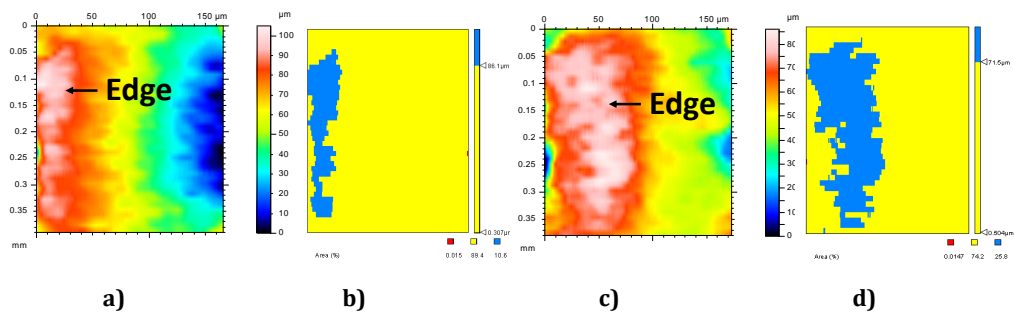


**Figure 7. 20 Example of the micro-edges in the abrasive/cutting array and their area of contact with the shaft during test: a) topographical measurement of a single abrasive element after 250 passes; b) measured area of contact of the single abrasive element via thresholding process after 2.5 m length of cut; c) topographical measurement of a single abrasive element after 5000 passes; d) measured area of contact of a single abrasive element via thresholding process after 50 m length of cut.**

The same procedure has been used to evaluate the contact areas of an average grit size of the electroplated abrasive pads with the shaft at different stages of the test: Figure 7. 21a represents the topographical profile of a single grit after 250 passes while the blue area in Fig. 20b depicts the measured contact area between grit and shaft; similarly, Figure 7.20c indicates a worn grit after 5000 passes (length of cut, 50 m), whose contact area is represented in Figure 7. 21d.

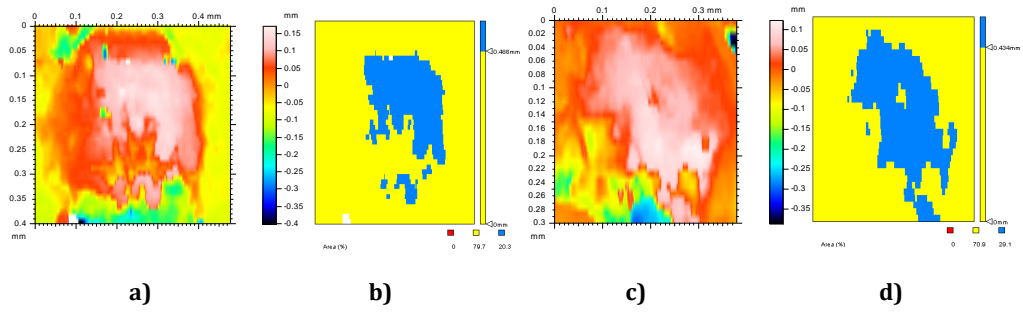


**Figure 7. 21: Example of a single grit of an diamond electroplated pad and its area of contact with the shaft during test: a) topographical measurement of a single grit after 250 passes; b) measured area of contact of the single grit with the shaft via thresholding process after 2.5 m length of cut; c) topographical measurement of a single grit after 5000 passes; d) measured area of contact of a single grit via thresholding process after 50 m length of cut.**

The cutting forces have been transformed into contact pressure per single edge/grit and the resulting contact pressures (see Eq. 2) between a single grit/edge and shaft have been calculated using Equation 2 in Section 3.7.3. Table 7. 1 contains all of the measured values for A and the calculated value for p after 250 passes (length of cut, 2.5 m) and after 5000 passes (length of cut, 50 m).

**Table 7. 1: Measured values of contact area of the micro-edge/grits and the calculated initial and final contact pressures.**

Specimen	$A_{250}$ [ $mm^2$ ]	$A_{5000}$ [ $mm^2$ ]	$p_{250}$ [ $N*mm^{-2}$ ]	$p_{5000}$ [ $N*mm^{-2}$ ]
PCD CTM302	0.012	0.061	26.9	5.33
PCD CMX850	0.012	0.061	29.3	8.60
Electroplated D501	0.003	0.018	336	135

The calculated contact pressures are shown in Figure 7.22 (with a Y axis in logarithmic scale) as a function of the length of cut, the general wear performances are depicted for all of the three specimens: both PCD micro-cutting arrays (CTM302 and CMX850) have proved their superior wear-resistant properties when compared to a benchmarked electroplated diamond pads (D501). Despite the fact that a positive rake angle results in a weaker cutting edge and increases tendency of edge breakage [19], these results demonstrate that the orderly micro-cutting edge arrays produced 70% lower contact pressures in comparison with the negative rake angle

typical of the grits in the electroplated specimens. This being corroborated with the better wear performance, represents a step change in replacing electroplated pads (with stochastically distributed abrasives) with arrays of micro-cutting edges for grinding/polishing operations.

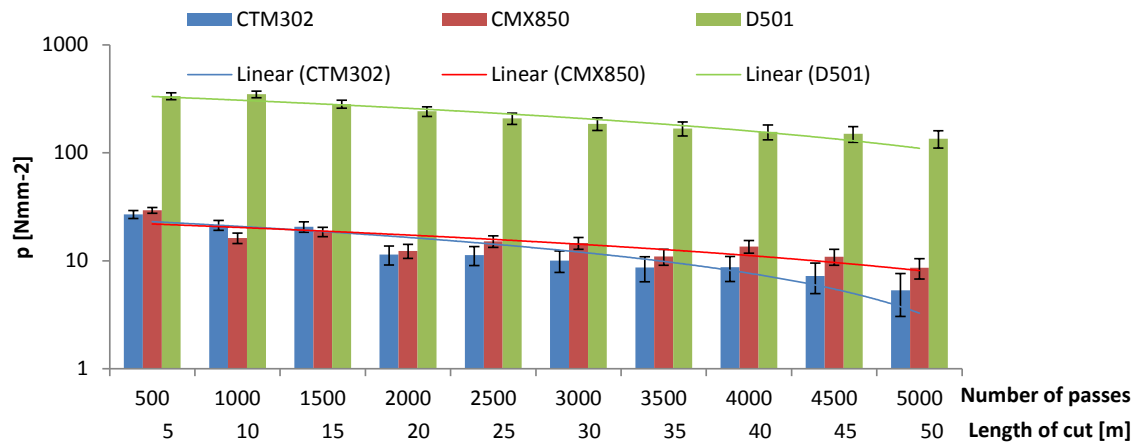


Figure 7.22: Comparative graph showing the calculated contact pressures, on the vertical Y axis in logarithmic scale.

### 7.3.2 Acquired signal/cutting forces for PCBN arrays and electroplated CBN pads

Using the procedure explained in Section 3.7.3, also adopted for the case of PCD abrasive arrays/electroplated diamond specimen, the contact pressures have been calculated for the PCBN abrasive/electroplated CBN pad; and Table 7. 2 include the results for experimental contact area and the relative contact pressures respectively after 250 passes (length of cut, 2.5 m) and 1000 passes (length of cut, 10 m) in the case of the PCBN abrasives and electroplated CBN pads.

Table 7. 2: measured values of contact area of the micro-edge/grits with the shafts and the calculated contact pressures for the PCBN arrays and the electroplated CBN pads.

Specimen	$A_{250}$ [mm <sup>2</sup> ]	$A_{1000}$ [mm <sup>2</sup> ]	$p_{250}$ [N*mm <sup>-2</sup> ]	$p_{f1000}$ [N*mm <sup>-2</sup> ]
PCBN DBS900	0.007	0.017	53.14	48.93
PCBN DBW85	0.007	0.017	209.8	99.45
Electroplated	0.032	0.035	104.3	92.28

As shown in the graph of pressure for the three specimens under test depicted in Figure 7.23, it is evident that the electroplated pad B501 worn out quicker than pure metallic binder specimen (DBS900) but slower than DBW85. The latter has in fact shown fracturing as main deformation mechanism (as previously demonstrated by ESEM analysis) which can explain the reason of very high contact pressures with the workpiece material during testing [5], and therefore it cannot be directly compared to the other two tested pads. A direct comparison between one of the two manufactured micro-cutting array and a benchmarked specimen was made possible especially thanks to similar wear (flattening) experienced between B501 and PCBN DBS900. In this regard, it is essential the result of contact pressures measured during test and reported in Figure 7.23: the lower pressures of the micro-array with purely metallic binder (DBS900) against the electroplated specimen are the evidence of wear resistance property of this novel material. The saddle shape evident in the electroplated CBN (Figure 7. 23) is mainly due to a variation of grits height and it is explained in details in Section 7.3.3.

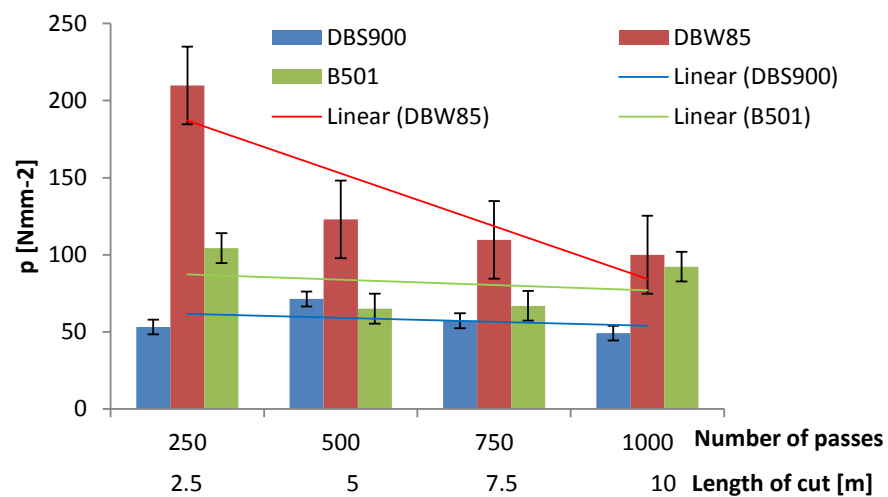


**Figure 7. 23: Comparative graph showing the calculated contact pressures for the PCBN/electroplated CBN specimens.**

### **7.3.3 Observation and discussion**

#### PCD arrays versus electroplated diamond specimen

The wear progression of the micro-arrays manufactured on different PCD composites as well as of electroplated diamond pads have been examined:

the slower wear (better wear resistance) achieved in the CTM302 mix grained PCD array has been analysed by microscopic technique and also been confirmed from the calculated contact pressure per abrasive edge. In particular, analyses on the signal acquired during testing of PCD arrays and electroplated diamond pads lead to find a difference in the signal acquisition time and intensity. Results in Section 3.7.2 have shown a gap in time spent for each pass and the variation of signal acquired are possibly due to the following reasons: (i) workpiece diameter reduction: the entire depth of cut has been done by the front cutting edges, thus more material is removed from the shaft with the use of the abrasive arrays reducing the contact time in a single pass (from 2s to 1.25s) and provoking only the left side of the array to wear out (Figure 7.18); (ii) edges height homogeneity: the random height typical of the electroplated pad does not guarantee constant contact with the shaft producing variable force peaks (Figure 7.17b). The trend-lines for the two PCD arrays and the electroplated diamond pad have shown a reduction of contact pressure with the testing time due to the decreased edge sharpness vs. cutting time; this is in agreement with the published literature [5]. Despite the fact that a positive rake angle results in a weaker abrasive edge and increases tendency of edge breakage [19], these results demonstrate that the orderly micro-cutting edge arrays produced 70% lower contact pressures in comparison with the negative rake angle typical of the grits in the electroplated specimens. This, being corroborated with the better wear performance, represents a step change in replacing electroplated pads (with stochastically distributed abrasives) with arrays of micro-cutting edges for grinding/polishing operations.

#### *PCBN arrays versus electroplated CBN specimen*

In the case of the purely metallic binder specimen (DBS900), the high thermal conductivity of CBN rapidly takes the heat away from the cutting zone [131], and this results in: lower contact pressures (Figure 7.23), less softening of the material at the interface abrasive/workpiece and mainly flank wear as a typical wear mechanism. The presence of the metalloids

boron and aluminium in the medium-CBN content PCBN array (DBW85): (i) makes the mechanical structure more brittle; (ii) reduces the thermal conductivity of CBN by 50% [19], thus the heat concentrates in the shear zone producing higher contact pressures, as depicted in Figure 7. 23. (iii) Furthermore boron and aluminium cause a favourable softening of the material (at the interface abrasive/workpiece) which reduces the flank wear on the abrasive edge, leaving fracturing as main wear mechanism. The presence of metalloids (B and Al) in the DBW85 PCBN specimen might have affected the wear progression of the medium-content abrasive array producing higher contact pressures, and for this reason one of the two manufactured abrasive arrays (DBW85) has shown the occurrence of a quicker failure mechanism. The results widely presented in Section 7.3.2 have demonstrated that there is at least one manufactured PCBN micro-abrasive array (DBS900) that has shown better wear performance with respect to the benchmarked specimen containing B501.

## **7.4 Conclusion and remarks**

The wear progression of PCD/PCBN micro-abrasive edges has been studied and benchmarked against electroplated diamond/CBN pads; the results are summarised in the following key points:

- For the PCD abrasive micro-arrays, the size of diamond grain and binder percentage affect the wear performances because of different extent of residual stresses (compressive in the diamond, tensile in the binder) occurring at the grain boundaries. An 80% mismatch of thermal expansion between ultra-hard grain and binder coefficient produces higher internal stresses in the material with higher binder bulk volume percentage (CMX850) leading the material to fracture quicker.
- In the CTM302 mix grained PCD array, the bigger grain dimension (90%) and the decrease of binder percentage (5%) compared to the CMX850 fine grained specimen are the main causes of the slower wear of the CTM302 mix grained array: the compressive stresses in the diamond grains are smaller and cause lower residual

stresses in the matrix if compared to the CMX850 fine grained material.

- The CTM302 mix grained PCD showed slower failure mechanism (in terms of time for crack formation) when compared to the CMX850 fine grained PCD: for CTM302 the length of cut for crack formation was 40 m, while for CMX850 30 m. This confirms that the mixed grained diamonds combine the high wear resistance typical of the fine grain and the good shock resistance typical of the coarse grained PCD.
- The wear occurring in the CTM302 mixed grain PCD array and in the electroplated diamond abrasive pads could be classified as mild abrasive wear: the electroplated diamond abrasive pad containing D501 sized abrasives has shown mainly micro-damaged grits with consequent flattening of 25-35% of the grits initial height from the beginning of the test. This result, along with the contact pressures produced during test (70% lower contact pressures in the case of the array), indicated the better wear-resistant properties of the orderly micro-cutting edge arrays.
- For the PCBN DBW85 the presence of a medium-CBN content (and the reduction of thermal conductivity) together with the metalloids binders causes fracturing as main wear/failure mechanism and as a consequence high contact pressures are experienced because new sharp edges are continuously generated onto the cutting edge.
- The PCBN DBS900 array has shown a total flank wear of 15% of the total height of the cutting edge, and this represents only the 2% of the total theoretical stock of material removed on the shaft after a length of cut of 10 m. When compared to the DBW85 specimen, DBS900 has proved to have slower wear and a lower trend-line of contact pressures due to the quick heat transfer which caused mainly flank wear without cracking of the micro-edges.
- After a length of cut of 10 m, the B501 electroplated abrasive has shown micro damaged grits with a flank flattening between 25%

and 35% of the total grit height. This height flattening is circa double the value achieved for the PCBN arrays (15%).

- Both PCD and PCBN abrasive arrays have shown higher wear resistance when benchmarked to the most used abrasive electroplated pads (D501, B501); the orderly micro-cutting edge arrays produced 70% lower contact pressures in comparison with the negative rake angle typical of the grits in the electroplated specimens. This being corroborated with the better wear performance it represents a step change in replacing electroplated pads (with stochastically distributed abrasives) with arrays of micro-cutting edges for grinding/polishing operations.
- Despite the fact that presence of metalloids (B and Al) might affect the wear progression of the medium-content abrasive array producing higher contact pressures, and for this reason one of the two manufactured abrasive arrays has shown the occurrence of a quicker failure mechanism; the results have demonstrated that there is at least one manufactured specimen that has shown better wear performance with respect to the benchmarked specimen containing B501, this is the pure metallic binder DBS900 whose better wear performance during the performed wear test.

The superior wear-resistant properties of micro-cutting arrays produced by pulsed laser ablation have been demonstrated via benchmarked grinding/cutting test of silicon dioxide rods. It has been demonstrated that the binder is the main factor responsible of the wear performance. As expected, both of the polycrystalline specimens containing metallic binders (mix grained and fine grained) have shown lower contact pressure with the workpiece when compared to a benchmark, therefore endorsing the possibility of introducing these micro-features in the generation of tools for advanced engineering applications. Polycrystalline cubic boron nitride arrays exhibited different wear behaviours in function of the type of binder. In particular, the specimen containing purely metallic binder (DBS900) has proved its wear-resistant characteristics when compared to

a benchmark and to an array with no purely metallic binder (containing metalloids).

# Chapter 8

## Research outcomes and future work

This chapter aims at presenting a summary of the results achieved in this research and discuss them for use in future research. In particular, the findings on pulsed laser ablation for the generation of complex geometry micro-cutting edge arrays for advanced machining/grinding applications in terms of thermal response of particular group of tool materials, i.e. ultra-hard composites, are summarised thus offering some key points research applications for future research perspective.

### 8.1 Summary of research, findings and conclusions

Based on understanding the thermal response of composite ultra-hard materials to laser beam, this research work aimed at developing novel micro-cutting/abrasive arrays with enhanced wear performances for advanced engineering applications. The aims and objectives of this research work were presented in Chapter 1, while the methodology steps utilised to undertake all of the research work and to achieve the proposed objectives were reported in Chapter 3. The research activity conducted for the achievement of each objective (reported in Section 1.3) is presented below and their respective outcomes in relation to the specific research objectives are summarised as follows:

- i. **Research activity:** An understanding of the interaction between laser beam (Nd: Yag laser) and microstructurally different ultra-hard materials (PCD & PCBN) along with a study of the material removal mechanisms in laser ablation are carried out, by generating quality controlled (e.g. roughness, surface integrity) ultra-hard surfaces from individual laser pulses over a range of energy/kinematic parameters.

**Research outcome:** Chapter 4 revealed that energetic parameters affect noticeably the geometry of craters/grooves: inhomogeneity in spot geometry might arise because of high energy density. The comparative results of chemical analysis before/after PLA indicated an increased percentage of binder (Cobalt) in particular in the areas of highest energy density. It has been noticed that the extent of ablation in coarse/fine grained ultra-hard composites differ for low values of beam scanning speed, due to overlapping energies in the target material, provoking an increase of laser power density and higher quantity of binder melting and re-depositing.

- ii. **Research activity:** An understanding of the thermal response of microstructurally different PCD/PCBN composites is carried out, by using procedures for the examination of the allotropic transformation occurring at atomic level in PCD/PCBN as a consequence of the extent of fluence in a laser pulse. The use of a novel technique combining ESEM, FIB, HRTEM and EELS allowed to study the repetitive mechanism of formation & removal of allotropic (graphitic carbon/hexagonal boron nitride) layers occurring in PCD/PCBN structures as a consequence of the thermal excitation.

**Research outcome:** HRTEM/EELS/EDX results (presented in Chapter 5) revealed a different thermal response of PCD and PCBN composites to the same thermal excitation. Both in the case of PCD and PCBN materials, a relationship between the graphite/hBN extent and the laser fluence was discovered and a difference in extent of allotropic transformation occurring in the same PLA condition was found between the PCD and the PCBN specimens.

High resolution transmission microscopy analyses in the high fluence area have shown a layered structure formed by: an  $sp^3$ -hBN structure till a depth of 50nm, followed by a transition phase hBN to cBN up to a depth of 100nm; while an untouched cBN

substructure with TiC binder has been revealed beyond a depth of 100nm, indicating that beyond a depth of 1  $\mu\text{m}$ , the specimen is not affected from the thermal excitation. Furthermore, in the area surrounding the hBN extent, amorphous boron nitride allotropic ( $\alpha\text{BN}$ ) traces were found. The transformation of the initial cBN into hBN in the case of PLA at high fluence, the achieved reaction energy produced by PLA would have created favorable condition for the allotropic change. In the case of PCD, two interfaces were formed onto the structure as a consequence of PLA: amorphous/graphite and graphite/diamond. Despite of the formation of two interfaces in both ablated areas, the extents of graphitised and amorphous layers in the two cases were found to be affected by the extent of laser fluence (energy density) experienced; in particular, it can be commented that in the low fluence ablated site, the measured graphitised layer is 70 % smaller than the one in the high fluence ablated area.

In conclusion, HRTEM/EELS analyses in the high fluence area indicated an extent of graphite of 0.9  $\mu\text{m}$  in the PCD, while an hBN layer of 0.05  $\mu\text{m}$  was found in the PCBN specimen, therefore showing that PCBN composites don't tend to allotropic change during PLA, and thereby confirming the choice of PCBN materials where a better thermal resistance and chemical inertness is required.

- iii. **Research activity**: An optimisation of laser operating parameters (e.g. pulse duration/frequency, power density) and laser paths (e.g. direction of ablation, use of border cuts) is carried out onto PCD/PCBN ultra-hard structures by designing and producing specific micro-edges with controlled edge geometry via CAD software and pulsed laser ablation technology.

**Research outcome**: In Chapter 6 it was found that in the use of border cuts during the ablative process, a high extent of edge irregularity (corner of the triangle in case of triangular shape, sharpness of the edges in the case of cutting features) was

produced by an intense energetic activity onto the target material. For this reason ablation without border cuts has been selected as optimal choice for the generation of orderly micro-abrasive arrays. On the other hand, the study on how the direction of ablation could affect the ablation indicated that well defined angles (e.g. 0°, 90°) should be used for a good control of the edge sharpness; particularly it has been demonstrated that the variation of angle from 0° to 90° noticeably increased the edge sharpness. Smaller tilting angles of the laser beam with the target specimen should be preferred when a negative rake angle is required, and bigger tilting angles should be preferred when a positive rake angle is needed. A novel approach has been proposed for the creation of edges with desired rake/clearance faces via laser ablation and this represents an important step for the scientific community when it is important to manufacture features in specific range of tolerances.

- iv. **Research activity:** A study on the wear-resistant characteristics and wear progression of micro-cutting arrays to enable efficient super-abrasive tools is effectuated; and there is a need to find a correlation between microstructural factors (i.e. binder type, binder bulk weight, grain size) variation and wear resistant properties. These objectives have been achieved by performing wear/cutting test of the laser generated orderly micro-arrays.

**Research outcome:** Results reported in Chapter 7 revealed that for the PCD abrasive micro-arrays, the size of diamond grain and binder percentage affect the wear performances. The CTM302 mix grained PCD showed slower wear when compared to the CMX850 fine grained PCD: in the CTM302 the compressive stresses in the diamond grains are smaller and cause lower residual stresses in the matrix facilitating the quicker failure mechanism of the fine grained CMX850 array. The presence of metalloids binders in the PCBN DBW85 array caused fracturing as main wear/failure mechanism, while the presence of a purely metallic binder in DBS900 is the

reason of slower wear due to the quick heat transfer which caused mainly flank wear without cracking of the micro-edges.

- v. **Research activity**: A validation of the wear-resistant properties of ultra-hard micro-cutting arrays (tested in research activity iv) along with a comparison of those against benchmark specimens is carried out. The objective has been achieved by performing wear/cutting test onto electroplated CBN/diamond pads under the same test condition of the wear/cutting test of the orderly arrays.

**Research outcome**: Results (presented in Chapter 7) revealed a similar wear behaviour (abrasive wear) between CTM302 mix grained PCD array and electroplated diamond abrasive pad. Nevertheless, the electroplated diamond abrasive pad containing D501 sized abrasives has shown mainly micro-damaged grits with consequent flattening of 25-35% of the grits initial height from the beginning of the test, while the orderly micro-cutting edge arrays revealed 70% lower contact pressures with the silicon dioxide workpiece, thereby indicating the better wear-resistant properties of the laser generated arrays. Regarding the benchmark test of PCBN, the B501 electroplated abrasive has shown micro damaged grits with a flank flattening between 25% and 35% of the total grit height, this height flattening is circa double the value achieved for the PCBN arrays, whose results have revealed a total flank wear of 15% of the total edge height.

## **8.2 Future work on the laser generated micro-cutting edges in PCD/PCBN composites**

This research allowed the identification of important research gaps existing in the use pulsed laser ablation technology on polycrystalline ultra-hard structures and their use for developing innovative cutting/grinding tools. In particular, because of the many chemical components which compose PCD and PCBN structures (e.g. ultra-hard

phase, binders), it is very difficult to predict the thermal response of polycrystalline composites to a thermal excitation such as the one produced onto the target material by a laser beam. This research programme allowed introducing some new advances into the topic of behaviour of binders and allotropic transformation occurring into the composite as a consequence of the thermal excitation. Some interesting results are especially proposed in Chapter 5, where some important findings in the use of an experimental approach for understanding the thermal response of PCBN composites are proposed for the first time in literature. The main findings proposed in this thesis open new perspective for future research. In particular, some of the main future possible application/research programme is here listed:

1. A theoretical model (for polycrystalline ultra-hard composites: PCD, PCBN) could be approached for an in-depth study of the influence of laser energetic parameters onto PCD/PCBN materials. In particular, what has been experimentally demonstrated in this research programme could be validated with the introduction of a model. This has not yet been proposed for PCD/PCBN structures because of the many variables involved in the process and the different thermal properties of binders and ultra-hard phases but it could be easier if a combined theoretical/experimental approach would be followed. The findings of this research programme could be initially used in the first stage of the achievement of the model.
2. Results from Chapter 5 regarding the material thermal response to pulsed laser ablation directly lead into another idea of future work: a control of hardness/softness in selected sites of the cutting edge could possibly be achieved. By considering the main findings of this research, it has been demonstrated that it is reliable to find a relationship between laser energetic parameters and extent of allotropic transformation occurring in specific sites of laser generated crater/groove. A research approach utilising pulsed laser ablation as a technology for simple cutting edge generation (proposed in Chapters 4 and 6) and the use of the technology

FIB/EELS/HRTEM (proposed in Chapter 5) would lead to study in-depth the extent of allotropic transformations (hexagonal boron nitride into cubic boron nitride, graphite into diamond and viceversa) in selected areas of the cutting edge and therefore allowing a control of softness/hardness of the cutting edge (and consequently of the overall tool). This would result in a high control of the properties of laser generated cutting edges, allowing a big scientific step change to be realised and thereby offering advantages for industries and academia.

3. Results in Chapter 7 have revealed that microstructural factors play an essential role in the wear-resistant properties of PCD and PCBN composites. Although a first approach onto the study of wear progression properties of PCD/PCBN is proposed in this thesis, the found results suggest interesting future research perspective into this topic. In particular, an in-depth study could be performed to evaluate if allotropic transformations are occurring in the wear/cutting test of the composites and, if so, in which extent these could affect the wear-resistant properties in microstructurally different materials. This research would be used to develop a technique for characterisation of the wear-response of PCD/PCBN at nanometric level, therefore allowing an in-depth understanding of the wear progression properties and facilitating the laser manufacture of tools in ultra-hard materials.

In conclusion, the achievement of the objectives of this research (proposed in Chapter 1) was realised as validated from the results in Chapters 4-7. Important findings on the thermal response of PCBN structures to laser ablation are proposed for the first time in literature and a relation between microstructural factors and wear properties of different PCD/PCBN arrays has been investigated for the first time. All of the proposed results have indicated that further work need to be conducted in order to achieve an in-depth understanding of the thermal reaction of PCD/PCBN to thermal excitation during pulsed laser ablation. Future research studies, by identifying the extent and causes of allotropic

transformation in PCD/PCBN structures, would allow a full control of the hardness/softness in selected sites of the ultra-hard cutting edges, therefore allowing science and technology to have benefits from it.

## References

- [1] Katchum, "Playing The Supply/Demand Gap In The Diamond Sector," *Olivut Resour.*, 2012.
- [2] R. H. J. Bundy, F. P., Hall, H. T., Strong, H. M. & Wentorf, "Man-made diamonds." *Nature*, pp. 176, 51–54, 1955.
- [3] S. N. Monteiro, A. L. D. Skury, M. G. de Azevedo, and G. S. Bobrovnitchii, "Cubic boron nitride competing with diamond as a superhard engineering material – an overview," *J. Mater. Res. Technol.*, vol. 2, no. 1, pp. 68–74, Jan. 2013.
- [4] P. W. Butler-Smith, D. A. Axinte, and M. Daine, "Preferentially oriented diamond micro-arrays: A laser patterning technique and preliminary evaluation of their cutting forces and wear characteristics," *Int. J. Mach. Tools Manuf.*, vol. 49, no. 15, pp. 1175–1184, Dec. 2009.
- [5] P. W. Butler-Smith, D. A. Axinte, and M. Daine, "Ordered diamond micro-arrays for ultra-precision grinding—An evaluation in Ti–6Al–4V," *Int. J. Mach. Tools Manuf.*, vol. 51, no. 1, pp. 54–66, Jan. 2011.
- [6] T. J. Ko and I. J. Yoon, "Mill-grinding with electroplated diamond abrasives for ceramic cutting," *Int. J. Precis. Eng. Manuf.*, vol. 13, no. 1, pp. 5–10, Feb. 2012.
- [7] Z. Shi and S. Malkin, "Wear of Electroplated CBN Grinding Wheels," *J. Manuf. Sci. Eng.*, vol. 128, no. 1, p. 110, 2006.
- [8] Y. Huang, Y. K. Chou, and S. Y. Liang, "CBN tool wear in hard turning: a survey on research progresses," *Int. J. Adv. Manuf. Technol.*, vol. 35, no. 5–6, pp. 443–453, Nov. 2006.
- [9] E. L. H. Liander, "Artificial diamonds," *ASEA J.*, vol. 28, p. 97, 1955.
- [10] M. I. Petrescu, "STRUCTURE AND PROPERTIES MODIFICATIONS IN BORON PART I : DIRECT POLYMORPHIC TRANSFORMATIONS MECHANISMS," *U.P.B. Sci. bullettin*, vol. 69, no. 1, 2007.
- [11] P. B. Mirkarimi, K. F. McCarty, and D. L. Medlin, "Review of advances in cubic boron nitride film synthesis," *Mater. Sci. Eng. R Reports*, vol. 21, no. 2, pp. 47–100, Dec. 1997.
- [12] Everyscience, "Carbon, its allotropes and structure." [Online]. Available: <http://www.everyscience.com/Chemistry/Inorganic/Carbon/a.1189.php>.

- [13] R. C. Burns and G. J. Davies, *The properties of natural and synthetic diamond*. Academic Press: London, UK, pp. 395–422.
- [14] C. a. M. Casanova, N. M. Balzaretta, G. Voronin, and J. a. H. da Jornada, “Experimental study of plastic deformation during sintering of cubic boron nitride compacts,” *Diam. Relat. Mater.*, vol. 8, no. 8–9, pp. 1451–1454, Aug. 1999.
- [15] V. L. Solozhenko, V. Z. Turkevich, and W. B. Holzapfel, “Refined Phase Diagram of Boron Nitride,” *J. Phys. Chem. B*, vol. 103, no. 15, pp. 2903–2905, Apr. 1999.
- [16] F. P. Bundy, W. A. Bassett, M. S. Weathers, R. J. Hemley, H. K. Mao, and A. F. Goncharov, “The Pressure-Temperature Phase and Transformation Diagram for Carbon,” *Carbon N. Y.*, vol. 34, pp. 141–153, 1996.
- [17] Element Six, “Synthesis of PCD/PCBN,” 2013. [Online]. Available: [http://www.e6.com/wps/wcm/connect/E6\\_Content\\_EN/Home/Materials+and+products/Synthetic+Polycrystalline+Diamond+\(PCD\)/](http://www.e6.com/wps/wcm/connect/E6_Content_EN/Home/Materials+and+products/Synthetic+Polycrystalline+Diamond+(PCD)/).
- [18] Element Six, “Synthetic polycrystalline diamond,” 2013. [Online]. Available: [http://www.e6.com/wps/wcm/connect/E6\\_Content\\_EN/Home/Materials+and+products/Synthetic+Polycrystalline+Diamond+\(PCD\)/](http://www.e6.com/wps/wcm/connect/E6_Content_EN/Home/Materials+and+products/Synthetic+Polycrystalline+Diamond+(PCD)/).
- [19] R. Edwards, *Cutting tools*. The institute of materials, 1993.
- [20] C. Sung and M. Taib, “Reactivities of Transition Metals with Carbon : Implications to the Mechanism of Diamond Synthesis Under High Pressure,” *Int. J. Refract. merals hard Mater.*, vol. 15, pp. 237–256, 1997.
- [21] G. Reisse and S. Weissmantel, “Pulsed laser deposition of hexagonal and cubic boron nitride films,” *Appl. Phys. A Mater. Sci. Process.*, vol. 69, no. 7, pp. S749–S753, Dec. 1999.
- [22] D. Sarkar, M. Chu, S.-J. Cho, Y. Il Kim, and B. Basu, “Synthesis and Morphological Analysis of Titanium Carbide Nanopowder,” *J. Am. Ceram. Soc.*, vol. 92, no. 12, pp. 2877–2882, Dec. 2009.
- [23] I. Database, “BN-Boron Nitride.” [Online]. Available: <http://www.ioffe.ru/SVA/NSM/Semicond/BN/index.html>.
- [24] P. Delhaes, *Graphite and Precursors*. Gordon and Breach Science Publisher, 2001.

- [25] F. Chen, G. Xu, C. Ma, and G. Xu, "Thermal residual stress of polycrystalline diamond compacts," *Trans. Nonferrous Met. Soc. China*, vol. 20, no. 2, pp. 227–232, Feb. 2010.
- [26] K. Bertagnoli R. Vale, "Understanding and controlling residual stresses in thick polycrystalline diamond cutters for enhanced durability," in *Proceeding of international technical conference on diamond, cubic boron nitride and their applications*, 2000.
- [27] A. Kumar, P. A. Lin, A. Xue, B. Hao, Y. K. Yap, and R. M. Sankaran, "Formation of nanodiamonds at near-ambient conditions via microplasma dissociation of ethanol vapour," *Nat. Commun.* 4, no. 2618, 2013.
- [28] T. engineering Toolbox, "Thermal expansion coefficient." [Online]. Available: [http://www.engineeringtoolbox.com/linear-expansion-coefficients-d\\_95.html](http://www.engineeringtoolbox.com/linear-expansion-coefficients-d_95.html).
- [29] W. Paszkowicz, J. B. Pelka, M. Knapp, T. Szyszko, and S. Podsiadlo, "Lattice parameters and anisotropic thermal expansion of hexagonal boron nitride in the 10 – 297 . 5 K temperature range," vol. 435, pp. 431–435, 2002.
- [30] Memsnet, "Properties of titanium carbide." [Online]. Available: <https://www.memsnet.org/material/titaniumcarbidebulk/>.
- [31] P. W. May, "Diamond thin films: A 21st century material," *Phil. Trans. R. Soc. London*, vol. A, no. 358, pp. 473–495, 2000.
- [32] J. B. Ott and J. Boerio-Goates, *Chemical thermodynamics: advanced applications*. 2000, pp. 209–212.
- [33] H. O. Pierson, *Handbook of carbon, graphite, diamond and fullerenes: properties, processing and applications*. Noyes Publications, 1993.
- [34] D. Carolan, M. Petrović, A. Ivanković, and N. Murphy, "Fracture Properties of PCBN as a Function of Loading Rate and Temperature," *Key Eng. Mater.*, vol. 452–453, pp. 457–460, Nov. 2010.
- [35] M. Akaishi, T. Ohsawa, and S. Yamaoka, "Synthesis of Fine-Grained Polycrystalline Diamond Compact and Its Microstructure," *J. Am. Ceram. Soc.*, vol. Volume 74, no. 1, pp. 5–10, 2006.
- [36] D. Miess and G. Rai, "Fracture toughness and thermal resistance of polycrystalline diamond compacts," *Mater. Sci. Eng. A*, vol. 209, no. 1–2, pp. 270–276, May 1996.

- [37] S. Goel, X. Luo, R. L. Reuben, and W. Bin Rashid, "Replacing diamond cutting tools with CBN for efficient nanometric cutting of silicon," *Mater. Lett.*, vol. 68, pp. 507–509, Feb. 2012.
- [38] M. F. Ismail, K. Yanagi, and H. Isobe, "Characterization of geometrical properties of electroplated diamond tools and estimation of its grinding performance," *Wear*, vol. 271, no. 3–4, pp. 559–564, Jun. 2011.
- [39] Element Six, "PCBN properties and applications," 2013. [Online]. Available: [http://www.e6.com/wps/wcm/connect/e6\\_content\\_en/home/materials+and+products/pcbn](http://www.e6.com/wps/wcm/connect/e6_content_en/home/materials+and+products/pcbn).
- [40] M. W. Cook and P. K. Bossom, "Trends and recent developments in the material manufacture and cutting tool application of polycrystalline diamond and polycrystalline cubic boron nitride," vol. 18, pp. 147–152, 2000.
- [41] Element six, "Synthetic Diamonds for use in Mining, Tunelling and Drilling," 2014. [Online]. Available: [http://www.e6.com/wps/wcm/connect/E6\\_Content\\_EN/Home/Applications/Drilling+crushing+sawing+and+milling/Mining,+tunnelling+and+drilling/](http://www.e6.com/wps/wcm/connect/E6_Content_EN/Home/Applications/Drilling+crushing+sawing+and+milling/Mining,+tunnelling+and+drilling/).
- [42] S. A. Catledge, Y. K. Vohra, R. Ladi, and G. Rai, "RELATED Micro-Raman stress investigations and X-ray diffraction analysis of polycrystalline diamond ( PCD ) tools," *Science (80-. )*, vol. 5, pp. 1159–1165, 1996.
- [43] J. Yan, K. Syoji, and J. Tamaki, "Some observations on the wear of diamond tools in ultra-precision cutting of single-crystal silicon," *Wear*, vol. 255, no. 7–12, pp. 1380–1387, Aug. 2003.
- [44] J. a. Arsecularatne, L. C. Zhang, and C. Montross, "Wear and tool life of tungsten carbide, PCBN and PCD cutting tools," *Int. J. Mach. Tools Manuf.*, vol. 46, no. 5, pp. 482–491, Apr. 2006.
- [45] M. Y. Tsai and J. C. Sung, "Dressing Behaviors of PCD Conditioners on CMP Polishing Pads," *Adv. Mater. Res.*, vol. 76–78, pp. 201–206, Jun. 2009.
- [46] M.-Y. Tsai, S.-T. Chen, Y.-S. Liao, and J. Sung, "Novel diamond conditioner dressing characteristics of CMP polishing pad," *Int. J. Mach. Tools Manuf.*, vol. 49, no. 9, pp. 722–729, Jul. 2009.
- [47] M.-Y. Tsai, "Polycrystalline diamond shaving conditioner for CMP pad conditioning," *J. Mater. Process. Technol.*, vol. 210, no. 9, pp. 1095–1102, Jun. 2010.

- [48] Element Six, "PCD precision cutting tools," 2014. [Online]. Available: [http://www.e6.com/wps/wcm/connect/E6\\_Content\\_EN/Home/Materials+and+products/Synthetic+Polycrystalline+Diamond+\(PCD\)//pcd+precision+cutting+tool+materials](http://www.e6.com/wps/wcm/connect/E6_Content_EN/Home/Materials+and+products/Synthetic+Polycrystalline+Diamond+(PCD)//pcd+precision+cutting+tool+materials).
- [49] A. Perveen, W. Y. San, and M. Rahman, "Fabrication of different geometry cutting tools and their effect on the vertical micro-grinding of BK7 glass," *Int. J. Adv. Manuf. Technol.*, pp. 101–115, Oct. 2011.
- [50] J. . Davim, *Machining composites materials*. Wiley, 2009.
- [51] C. C. Tsao and H. Hocheng, "Effect of tool wear on delamination in drilling composite materials," *Int. J. Mech. Sci.*, vol. 49, no. 8, pp. 983–988, Aug. 2007.
- [52] ISO 513, "Classification and application of hard cutting materials for metal removal with defined cutting edges-designation of the main groups and groups of application." 2004.
- [53] L. N. Lopez de Lacalle, A. Lamikiz, J. Fernandez de Larrinoa, and I. Azkona, "Cutting tools," in *Machining of hard materials*, J. P. Davim, Ed. Springer, 2011, pp. 33–86.
- [54] A. Zawada-Tomkiewicz, "Analysis of surface roughness parameters achieved by hard turning with the use of PCBN tools," *Est. J. Eng.*, vol. 17, no. 1, p. 88, 2011.
- [55] N. Tan, C. J. Liu, Y. J. Li, Y. W. Dou, H. K. Wang, H. Ma, Z. L. Kou, and D. W. He, "Characterization of polycrystalline cBN compacts sintered without any additives," *Eur. Phys. J. Appl. Phys.*, vol. 53, no. 1, p. 11501, Dec. 2010.
- [56] T. Halpin, G. Byrne, J. Barry, and E. Ahearne, "The performance of polycrystalline cubic boron nitride tools in continuous, semi-interrupted, and interrupted hard machining," *Proc. Inst. Mech. Eng. Part B J. Eng. Manuf.*, vol. 223, no. 8, pp. 947–953, Aug. 2009.
- [57] N. Kawasegi, H. Sugimori, H. Morimoto, N. Morita, and I. Hori, "Development of cutting tools with microscale and nanoscale textures to improve frictional behavior," *Precis. Eng.*, vol. 33, no. 3, pp. 248–254, Jul. 2009.
- [58] R. Zareena and S. C. Veldhuis, "Tool wear mechanisms and tool life enhancement in ultra-precision machining of titanium," *J. Mater. Process. Technol.*, vol. 212, no. 3, pp. 560–570, Mar. 2012.
- [59] M. Sharif Uddin, K. H. W. Seah, X. P. Li, M. Rahman, and K. Liu, "Effect of crystallographic orientation on wear of diamond tools for nano-

scale ductile cutting of silicon," *Wear*, vol. 257, no. 7–8, pp. 751–759, Oct. 2004.

- [60] W. Konrad, D. Claus, H. Marcel, and W. Christian, "Laser Prepared Cutting Tools," *Phys. Procedia*, vol. 39, pp. 240–248, Jan. 2012.
- [61] Y. K. Chou and C. J. Evans, "Cubic boron nitride tool wear in interrupted hard cutting," *Wear*, vol. 225–229, pp. 234–245, Apr. 1999.
- [62] S. Goel, X. Luo, R. L. Reuben, and H. Pen, "Influence of temperature and crystal orientation on tool wear during single point diamond turning of silicon," *Wear*, vol. 284–285, pp. 65–72, Apr. 2012.
- [63] S. Goel, X. Luo, and R. L. Reuben, "Wear mechanism of diamond tools against single crystal silicon in single point diamond turning process," *Tribol. Int.*, vol. 57, pp. 272–281, Jan. 2013.
- [64] S. Goel, X. Luo, P. Comley, R. L. Reuben, and A. Cox, "Brittle–ductile transition during diamond turning of single crystal silicon carbide," *Int. J. Mach. Tools Manuf.*, vol. 65, pp. 15–21, Feb. 2013.
- [65] S. Goel, X. C. Luo, R. L. Reuben, W. Bin Rashid, and J. N. Sun, "Single Point Diamond Turning of Single Crystal Silicon Carbide: Molecular Dynamic Simulation Study," *Key Eng. Mater.*, vol. 496, pp. 150–155, Dec. 2011.
- [66] T. W. Hwang, C. J. Evans, and E. P. Whinton, "High Speed Grinding of Silicon Nitride With Electroplated Diamond Wheels , Part 1 : Wear," vol. 122, 2000.
- [67] T. W. Hwang and C. J. Evans, "High Speed Grinding of Silicon Nitride With Electroplated Diamond Wheels , Part 2 : Wheel Topography and Grinding," vol. 122, 2014.
- [68] P. Koshy, A. Iwasaki, and M. A. Eibestaa, "Surface Generation with Engineered Diamond Grinding Wheels : Insights from Simulation," no. 1, pp. 1–4.
- [69] S. F. Miller, A. J. Shih, and J. Qu, "Investigation of the spark cycle on material removal rate in wire electrical discharge machining of advanced materials," *Int. J. Mach. Tools Manuf.*, vol. 44, pp. 391–400, 2004.
- [70] G. Spur, M. Puttrus, and U. W. Wunsch, "Wire EDM of PCD," *Ind. Diam. Rev.*, vol. 48, pp. 264–266, 1988.

- [71] Y. H. Jia, "Study on EDM Technics of Polycrystalline Cubic Boron Nitride Cutting Tool and PcBN Cutting Tool's Life," *Appl. Mech. Mater.*, vol. 120, pp. 311–315, Oct. 2011.
- [72] J. Kozak, K. P. Rajurkar, and S. Z. Wang, "Material removal in wire EDM of PCD blanks," *J. Ind. Eng.*, vol. 116, pp. 363–369, 1994.
- [73] A. Perveen, M. P. Jahan, M. Rahman, and Y. S. Wong, "A study on microgrinding of brittle and difficult-to-cut glasses using on-machine fabricated poly crystalline diamond (PCD) tool," *J. Mater. Process. Technol.*, vol. 212, no. 3, pp. 580–593, Jun. 2011.
- [74] M. Pacella, D. A. Axinte, P. W. Butler-Smith, and M. Daine, "On the Topographical/Chemical Analysis of Polycrystalline Diamond Pulsed Laser Ablated Surfaces," *Procedia CIRP*, vol. 13, pp. 387–392, 2014.
- [75] "Oxford Lasers Ltd., Abingdon Science Park, Abingdon, OX14 3YR 2 Clarendon Laboratory, University of Oxford, Oxford, OX1 4PU," pp. 3–6, 2008.
- [76] M. Pacella, P. W. Butler-Smith, D. A. Axinte, and M. W. Fay, "FIB/TEM/EELS micro/nanometric investigations of the effects of laser ablation on the diamond/binder structure in polycrystalline diamond composites," *J. Mater. Process. Technol.*, vol. 214, no. 5, pp. 1153–1161, May 2014.
- [77] P. Heyl, T. Olschewski, and R. W. Wijnaendts, "Manufacturing of 3D structures for micro-tools using laser ablation," *Microelectron. Eng.*, vol. 57–58, pp. 775–780, Sep. 2001.
- [78] C. Dold, M. Henerichs, L. Bochmann, and K. Wegener, "Comparison of Ground and Laser Machined Polycrystalline Diamond (PCD) Tools in Cutting Carbon Fiber Reinforced Plastics (CFRP) for Aircraft Structures," *Procedia CIRP*, vol. 1, pp. 178–183, Jan. 2012.
- [79] Allemen, *Laser-Beam interactions with materials*. Springer-Verlag, 1995.
- [80] Dahotre-Harimkar, *Laser fabrication and machining of materials*. Springer, 2008, pp. 248–250.
- [81] A. Dubey and V. Yadava, "Laser beam machining—A review," *Int. J. Mach. Tools Manuf.*, vol. 48, pp. 609–628, Nov. 2007.
- [82] V. Alexiades and D. Autrique, "Enthalpy model for heating, melting, and vaporization in laser ablation," vol. 19, pp. 1–13, 2010.
- [83] Bauerle, *Laser processing and chemistry*. Springer-Verlag, 2000.

- [84] M. Stafe, C. Negutu, N. N. Puscas, and I. M. Popescu, "PULSED LASER ABLATION OF SOLIDS," vol. 62, no. 4, pp. 758–770, 2010.
- [85] D. Maclellan, "Pulse length and beam shape : efficient material removal," *Spring*, no. 50, pp. 28–29, 2008.
- [86] T. Kononenko, "Ablation of CVD diamond with nanosecond laser pulses of UV–IR range," *Diam. Relat. Mater.*, vol. 7, no. 11–12, pp. 1623–1627, Dec. 1998.
- [87] T. V Kononenko, V. G. Ralchenko, I. I. Vlasov, S. V Garnov, and V. I. Konov, "Ablation of CVD diamond with nanosecond laser pulses of UV – IR rangek," *Sci. Technol.*, vol. 7, no. April, pp. 1623–1627, 1998.
- [88] J. Cheng, W. Perrie, B. Wu, S. Tao, S. P. Edwardson, G. Dearden, and K. G. Watkins, "Ablation mechanism study on metallic materials with a 10ps laser under high fluence," *Appl. Surf. Sci.*, vol. 255, no. 18, pp. 8171–8175, Jun. 2009.
- [89] S.-T. Chen, M.-Y. Tsai, Y.-C. Lai, and C.-C. Liu, "Development of a micro diamond grinding tool by compound process," *J. Mater. Process. Technol.*, vol. 209, no. 10, pp. 4698–4703, Jun. 2009.
- [90] M. Petrović, A. Ivanković, and N. Murphy, "High Rate and High Temperature Fracture Behaviour of Polycrystalline Diamond," *Key Eng. Mater.*, vol. 488–489, pp. 670–673, Sep. 2011.
- [91] M. Petrovic, A. Ivankovic, and N. Murphy, "The mechanical properties of polycrystalline diamond as a function of strain rate and temperature," *J. Eur. Ceram. Soc.*, Apr. 2012.
- [92] P. W. Butler-Smith, D. A. Axinte, M. Pacella, and M. W. Fay, "Journal of Materials Processing Technology Micro / nanometric investigations of the effects of laser ablation in the generation of micro-tools from solid CVD diamond structures," vol. 213, pp. 194–200, 2013.
- [93] H. Ohfuji, T. Okuchi, S. Odake, H. Kagi, H. Sumiya, and T. Irifune, "Micro-/nanostructural investigation of laser-cut surfaces of single- and polycrystalline diamonds," *Diam. Relat. Mater.*, vol. 19, no. 7–9, pp. 1040–1051, Jul. 2010.
- [94] E. G. Gamaly and A. V Rode, "Laser ablation of carbon at the threshold of plasma formation," *Laser Phys.*, vol. 127, pp. 121–127, 1999.
- [95] W. L. Mao, H. Mao, P. J. Eng, T. P. Trainor, M. Newville, C. Kao, D. L. Heinz, J. Shu, Y. Meng, and R. J. Hemley, "Bonding changes in compressed superhard graphite.," *Science*, vol. 302, no. 5644, pp. 425–7, Oct. 2003.

- [96] R. Gogolinsky, "Nano-sclerometry measurements of superhard materials," *Diagnostic Mater.*, vol. 6, no. 64, pp. 30–43, 1998.
- [97] C. J. Wong, "Fracture and wear of diamond cutting tools," *J. Eng. Mater. Technol.*, vol. 103(4), pp. 341–345, 1981.
- [98] P. K. Sen, M. W. Cook, and R. D. Achilles, "Various diamond cutting tool materials for the machining of HPL Wood Flooring," in *IDA Superabrasives Conference*, 1998.
- [99] M. J. Neale and M. Gee, *Guide to wear problems and testing for industry*. New York, NY, USA: William Andrew Publishing, 2001.
- [100] I. M. Hutchings, *Tribology friction and wear of engineering materials*. Oxford, UK, 1992.
- [101] X. S. Li and J. N. Boland, "The wear characteristics of superhard composite materials in abrasive cutting operations," *Wear*, vol. 259, no. 7–12, pp. 1128–1136, Jul. 2005.
- [102] J. N. Boland and X. S. Li, "Microstructural Characterisation and Wear Behaviour of Diamond Composite Materials," *Materials (Basel)*, vol. 3, no. 2, pp. 1390–1419, Feb. 2010.
- [103] H. Alehossein, X. S. Li, and J. N. Boland, "Towards improving rock cutting tools using thermally stable diamond composites," *Adv. Mater. Res.*, no. 76–78, pp. 585–590, 2009.
- [104] J. N. Boland, P. Clark, C. Harbers, S. Li, and H. Alehossein, "In proceeding European Conference on Hard Materials and Diamond Tooling," in *EURO PM*, 2002.
- [105] H. K. Tönshoff, H. Hillmann-Apmann, and J. Asche, "Diamond tools in stone and civil engineering industry: cutting principles, wear and applications," *Diam. Relat. Mater.*, vol. 11, no. 3–6, pp. 736–741, Mar. 2002.
- [106] D. F. Moore, *Principle and application of tribology*. Pergamon, Oxford, 1975.
- [107] M. C. Shaw, *Metal cutting principles*. Oxford University Press, Oxford, 1984.
- [108] B. North, "Indexable metal cutting inserts.," in *Factors influencing machining and their controls, proceedings of an international conference and workshop*, 1989, pp. 33–42.
- [109] M. Pacella, P. W. Butler-Smith, D. A. Axinte, and M. W. Fay, "FIB/TEM/EELS micro/nanometric investigations of the effects of

laser ablation on the diamond/binder structure in polycrystalline diamond composites," *J. Mater. Process. Technol.*, vol. 214, no. 5, pp. 1153–1161, May 2014.

- [110] "<https://www.memsnet.org/material/silicondioxidesio2bulk/>."
- [111] F. Jansen, M. a. Machonkin, N. Palmieri, and D. Kuhman, "Thermomechanical properties of amorphous silicon and nonstoichiometric silicon oxide films," *J. Appl. Phys.*, vol. 62, no. 12, p. 4732, 1987.
- [112] H. Kahn, R. Ballarini, and a. . Heuer, "Dynamic fatigue of silicon," *Curr. Opin. Solid State Mater. Sci.*, vol. 8, no. 1, pp. 71–76, Jan. 2004.
- [113] K. H. Song and X. Xu, "Explosive phase transformation in excimer laser ablation," pp. 111–116, 1998.
- [114] V. Babushok, F. Deluciajr, J. Gottfried, C. Munson, and a Miziolek, "Double pulse laser ablation and plasma: Laser induced breakdown spectroscopy signal enhancement," *Spectrochim. Acta Part B At. Spectrosc.*, vol. 61, no. 9, pp. 999–1014, Sep. 2006.
- [115] G. F. Zhang, B. Zhang, Z. H. Deng, and J. F. Chen, "An Experimental Study on Laser Cutting Mechanisms of Polycrystalline Diamond Compacts," *CIRP Ann. - Manuf. Technol.*, vol. 56, no. 1, pp. 201–204, Jan. 2007.
- [116] M. Marcodelucas, L. Lavissee, and G. Pillon, "Microstructural and tribological study of Nd:YAG laser treated titanium plates," *Tribol. Int.*, vol. 41, no. 11, pp. 985–991, Nov. 2008.
- [117] J. Bonse, S. Baudach, J. Krüger, W. Kautek, and M. Lenzner, "Femtosecond laser ablation of silicon – modification thresholds and," *Appl. Phys. A Mater. Sci. Process.*, vol. 25, pp. 19–25, 2002.
- [118] a. Badzian, R. Roy, T. Badzian, W. Drawl, P. Mistry, M. C. Turchan, and K. Cherian, "Decrystallization of diamond by Nd:YAG and excimer lasers and subsequent lattice relaxation," *Diam. Relat. Mater.*, vol. 14, no. 9, pp. 1562–1570, Sep. 2005.
- [119] E. Wilks and J. Wilks, *Properties and applications of diamond*. Butterworth Heinemann, 1991.
- [120] H. P. Bovenkerk, F. P. Bundy, H. T. Hall, H. M. Strong, and R. H. Wentorf, "Preparation of Diamond," *Nature*, vol. 184, no. 4693, pp. 1094–1098, Oct. 1959.
- [121] P. T. Mannion, J. Magee, E. Coyne, G. M. O'Connor, and T. J. Glynn, "The effect of damage accumulation behaviour on ablation

thresholds and damage morphology in ultrafast laser micro-machining of common metals in air," *Appl. Surf. Sci.*, vol. 233, no. 1–4, pp. 275–287, Jun. 2004.

- [122] N. M. Bulgakova and A. V Bulgakov, "Pulsed laser ablation of solids : transition from normal vaporization," vol. 208, pp. 199–208, 2001.
- [123] G. Yang, *Laser ablation in liquid: principles and applications in the preparation of nanomaterial*. Pan Stanford Publishing, 2012.
- [124] X. Liu, D. Du, and G. Mourou, "Laser Ablation and Micromachining with Ultrashort Laser Pulses," *October*, vol. 33, no. 10, pp. 1706–1716, 1997.
- [125] Crafer-Oakley, *Laser processing in manufacturing*. Chapman&Hall, 1993.
- [126] X. W. Zhang, N. Deyneka, P. Ziemann, F. Banhart, and M. Schreck, "Epitaxy of cubic boron nitride on (001)- oriented diamond," vol. 2, no. May, pp. 2–5, 2003.
- [127] H. Sachdev, R. Haubner, H. Noth, and B. Lux, "RE | . AT | D MATERIALS Investigation of the c-BN / h-BN phase transformation at normal pressure," 1997.
- [128] J. C. Sung, N. Chen, Y. Pai, C. Chou, C. Chou, S. Hu, and M. Sung, "The Pad Dressing Phenomena of Multiple Diamond Grits : Implications for The Design of CMP Pad Conditioners," in *International conference on planarization/CMP technology*, 2012, pp. 325–330.
- [129] B. Podgornik and M. Sedlacek, "Performance, Characterization and Design of Textured Surfaces," *J. Tribol.*, vol. 134, no. 4, p. 041701, 2012.
- [130] H. K. Tonshoff, "Diamond tools for wire sawing metal components," vol. 11, pp. 742–748, 2002.
- [131] R. G. Bayer, *Wear analysis for engineers*. HNB Publishing, 2002.
- [132] G. W. Stachowiak, Ed., *Wear*. John Wiley & Sons, Ltd, 2005.